Julius-Maximilians-Universität Würzburg

Fabrication of Organic Solar Cells, Screening of Non-Fullerene Acceptors and the Investigation of their Intermolecular Interactions

Dissertation zur Erlangung des

naturwissenschaftlichen Doktorgrades der

Julius-Maximilians-Universität Würzburg

vorgelegt von

Kaan Menekşe

aus Hildesheim

Würzburg, 2022

Eingereicht bei der Fakultät für Chemie und Pharmazie am

11.07.2022

Gutachter der schriftlichen Arbeit:

1. Gutachter: Prof. Dr. Frank Würthner

2. Gutachter: Prof. Dr. Jens Pflaum

Prüfer des öffentlichen Promotionskolloquiums:

1. Gutachter: Prof. Dr. Frank Würthner

2. Gutachter: Prof. Dr. Jens Pflaum

3. Gutachter: Priv.-Doz. Dr. Florian Beuerle

Datum des öffentlichen Promotionskolloquiums

07.10.2022

Doktorurkunde ausgehändigt am

_____

Danksagung

Ich danke meinem Doktorvater Prof. Dr. Frank Würthner für die Aufnahme in seinen Arbeitskreis und dafür, dass er mir die Möglichkeit gab meine Doktorarbeit in dem spannenden und zukunftsorientierten Feld der organischen Solarzellen im Rahmen des bayerischen Forschungsprogramms *„Solar Technologies Go Hybrid“* anzufertigen. Ich möchte mich bei ihm dafür bedanken, dass ich viele neue wissenschaftliche und apparative Aspekte erlernen konnte, die mir in meinem weiteren Werdegang von Nutzen sein werden. Des Weiteren möchte ich mich für das großartige und organisierte Arbeitsumfeld sowie die zahlreichen Möglichkeiten des wissenschaftlichen Austauschs auf nationaler und internationaler Ebene bedanken.

Ich danke Dr. Matthias Stolte für die Betreuung in den letzten Jahren. Durch ihn erlernte ich die Grundlagen der organischen Elektronik sowie der supramolekularen Chemie, durch die diese Arbeit erst möglich geworden ist. Ich möchte Ihm explizit für die wissenschaftliche Ausbildung, für die Korrekturen und für das stete offene Ohr danken.

Für den Rückhalt im Labor möchte ich Julius Georg Albert für die synthetischen Arbeiten und Astrid Kudzus für die Einarbeitung sowie die anlagenspezifischen Arbeiten danken. Des Weiteren danke ich Dr. Andreas Liess für die Einarbeitung und Dr. Reinhard Hecht für die Vorarbeiten zur organischen Photovoltaik in unserer Arbeitsgruppe.

Darüber hinaus gilt mein Dank Bernhard Mahlmeister für seine Arbeiten im Rahmen seines Praktikums und seiner Masterarbeit. Ihm und Tim Schembri danke ich für den stetigen wissenschaftlichen und graphischen Austausch während meiner Doktorarbeit. Ferner danke ich den beiden für das Korrekturlesen dieser Arbeit. Den weiteren Mitgliedern der Arbeitsgruppe, darunter Oliver Nagler, Felix Brust und Dr. Jinhong Kim danke ich für die großartige Zusammenarbeit und den wissenschaftlichen Diskussionen in den letzten Jahren. Ebenfalls möchte ich mich bei meinen weiteren Forschungsstudenten Lukas Stumpf und Björn Ewald und bei unserem Masteranden Fabian Grote bedanken, die ich in dieser Zeit wissenschaftlich und technisch betreuen durfte.

Ohne die Synthese von neuen Verbindungen wäre diese Arbeit in dieser Form nicht möglich gewesen. Daher möchte ich allen danken, die die hier untersuchten Moleküle synthetisiert haben: Dr. Pengzhong Chen, Olga Anhalt, Dr. Kevin Bold, Jun.-Prof. Dr. Agnieszka Nowak-Król, Franziska Schneider, Julius Georg Albert, Dr. Rodger Rausch, Dr. Santosh Panchal, Carina Mützel, Dr. Rebecca Renner, Oliver Nagler, Dr. Magnus Mahl, Dr. Kazutaka Shoyama, Dr. Alhama Arjona-Esteban, Dr. Bartlomiej Pigulski, Simon Soldner, Dr. Sabine Seifert, Ben Teichmann, Dr. Marcus Schulze und Bernhard Mahlmeister.

Olga Anhalt, Ana-Maria Krause und Dr. Kazutaka Shoyama möchte ich zusätzlich für die kristallographischen Arbeiten danken. Ferner möchte ich mich bei unseren Kooperationspartnern Prof. Dr. Takeshi Maeda, Prof. Dr. Peter Bäuerle und Prof. Dr. Ken-Tsung Wong für die Bereitstellung von neuen spannenden Materialien bedanken.

Für die gute Zusammenarbeit im Zentrum für Nanosystemchemie danke ich den Arbeitsgruppen Beuerle und Nowak-Król. Des Weiteren gilt mein Dank der kompletten Arbeitsgruppe Würthner für die großartige Atmosphäre in den letzten Jahren.

Für den sozialen Rückhalt während meiner Doktorarbeit sowie für die ausufernden Stammtische möchte ich explizit bei dem AK *Benchpress* (Tim Schlossarek, Dr. Marius Wehner, Dr. Markus Hecht und Dr. Kevin Bold) sowie bei Viktoria Leonhardt und Natalie Schäfer bedanken.

Das Weiteren möchte ich mich bei meinen langjährigen Freunden Lars Deike, Corvin Linke, Jan-Eric Sievers, Paul Uhde und Atilla Ceylan bedanken, die trotz des zeitaufwändigen Studiums stets zu mir hielten.

Mein größter Dank jedoch gilt meinen Eltern Tansu und Suat Menekşe, die mich stets auf meinem Werdegang unterstützen. Ohne ihren Rückhalt wäre weder ein Studium noch eine Doktorarbeit möglich gewesen. Ebenfalls möchte ich mich bei meinem Bruder Ozan Menekşe bedanken.

Zuletzt möchte ich mich bei meiner Partnerin Anna Tutov bedanken. Zusammen mit Luna haben wir nicht nur das nervenaufreibende Chemiestudium, sondern auch die Promotion meistern können. Danke für alles.

Abbreviations

List of abbreviations

α-6T	α-sexithiophene
A	Acceptor
ADF	Amsterdam density functional
AFM	Atomic force microscopy
Alq_3	Tris(8-hydroxyquinolinato)aluminum
BCP	Bathocuproine
BHJ	Bulk heterojunction
BPTI	Benzo[ghi]perylene trisimide
CuPc	Copper-(II)-phthalocyanine
CPTQ	Quinoidal dicyanomethylene-endcapped cyclopentadithiophenes
CT	Charge transfer
CV	Cyclic voltammetry
D	Donor
DCV5T-Me	Dicyanovinyl-endcapped methylated quinquethiophene
DFT	Density functional theory
DIPP	2,6-Di-*iso*-propylphenyl
DPP	Diketopyrrolopyrole
DSC	Differential scanning calorimetry
DTDCPB	2-[(7-{4-[*N*,*N*-Bis(4-methylphenyl)amino]phenyl}-2,1,3-benzothiadiazol-4-yl)methylene]propanedinitrile
DTPQ	Quinoidal dicyanomethylene-endcapped dithienopyrrole
ESI	Electronspray ionization
EQE	External quantum efficiency

ETL	Electron-transport layer
FOPA	Perfluorooctanephosphonic acid
FRET	Förster resonance energy transfer
GIXRD	Gracing-incident X-ray diffraction
GIWAXS	Gracing-incident wide-angle X-ray scattering
HMDS	Hexamethyldisilazane
HOMO	Highest-occupied molecular orbital
HRMS	High-resolution mass spectrometry
HTL	Hole-transport layer
ITIC-4F	3,9-bis(2-methylene-((3-(1,1-dicyanomethylene)-6,7-difluoro)-indanone))-5,5,11,11-tetrakis(4-hexylphenyl)-dithieno[2,3-d:2',3'-d']-s-indaceno[1,2-b:5,6-b']dithiophene
LUMO	Lowest-unoccupied molecular orbital
MALDI	Matrix-assisted laser desorption/ionization
MHJ	Mixed heterojunction
NAC	Naphthalimide-annulated corannulene
NDI	Naphthalene diimide
NFA	Non-fullerene acceptor
NGTI	Nanographene tetraimide
NIR	Near infrared
NMR	Nuclear magnetic resonance
OLED	Organic light-emitting diode
OSC	Organic solar cell
OPV	Organic photovoltaic
OTFT	Organic thin-film transistor
OTES	Octadecyltriethoxysilane

PADI	Polycyclic aromatic dicarboximide
PAH	Polycyclic aromatic hydrocarbon
PBI	Perylene bisimide
$PC_{61}BM$	[6,6]-Phenyl-C61-butyric acid methyl ester
$PC_{71}BM$	[6,6]-Phenyl-C71-butyric acid methyl ester
PBDB-T	Poly[(2,6-(4,8-bis(5-(2-ethylhexyl)thiophen-2-yl)-benzo[1,2-b:4,5-b']dithiophene))-alt-(5,5-(1',3'-di-2-thienyl-5',7'-bis(2-ethylhexyl)benzo[1',2'-c:4',5'-c']dithiophene-4,8-dione)
PCE-10	Poly[4,8-bis(5-(2-ethylhexyl)thiophen-2-yl)benzo[1,2-b;4,5-b']dithiophene-2,6-diyl-alt-(4-(2-ethylhexyl)-3-fluorothieno[3,4-b]thiophene-)-2-carboxylate-2-6-diyl)]
PDINO	*N*,*N*'-Bis(*N*,*N*-dimethylpropan-1-amine oxide)perylene-3,4,9,10-tetracarboxylic diimide
PHJ	Planar heterojunction
PM6	Poly[(2,6-(4,8-bis(5-(2-ethylhexyl-3-fluoro)thiophen-2-yl)-benzo[1,2-b:4,5-b']dithiophene))-alt-(5,5-(1',3'-di-2-thienyl-5',7'-bis(2-ethylhexyl)benzo[1',2'-c:4',5'-c']dithiophene-4,8-dione)]
PMMA	Poly (methyl methacrylate)
QCM	Quartz crystal monitor
SCLC	Space-charge limited current
SubPc	Subphthalocyanine
TD-DFT	Time-dependent density functional theory
TDI	Terylene diimide
TDP	3,4,5-Tris(dodecyl)phenyl
TGA	Thermogravimetric analysis
TF	Tooling factor
TL	Transport layer

TOF	Time of flight
TPA	Tetradecylphosphonic acid
UV	Ultra-violet
Vis	Visible
XRD	X-ray diffraction

Physical quantities

$A_{00}\,A_{01}^{-1}$	Intensity ratio between transitions	(1)
δ	Chemical shift	(ppm)
d	Thickness	(nm)
ε_{Max}	Molar extinction coefficient	(L mol cm^{-1})
$E_{½}^{Red}$	Reduction potential	(V)
E_{Loss}	Energy loss factor	(eV)
Φ_{Fl}	Fluorescence quantum yield	(%)
FF	Fill factor	(%)
I	Current	(A)
$I_{On}\,I_{Off}^{-1}$	On-off ratio	(1)
J	Current density	(mA cm^{-2})
J_{SC}	Short-circuit current density	(mA cm^{-2})
J	Coupling (NMR)	(Hz)
$J_{Coulomb}$	Coulomb coupling	(cm^{-1} / eV)
$J_{Coupling}$	Total coupling	(cm^{-1} / eV)
J_{CT}	Charge-transfer coupling	(cm^{-1} / eV)
L	Channel length	(µm)
L_D	Exciton diffusion length	(nm)

$\mu_{h/e}$	Mobility of holes or electrons	($cm^2\ V^{-1}\ s^{-1}$)
μ_{eg}	Transition dipole moment	(D)
λ	Wavelength	(nm)
λ_{Max}	Maximum absorption wavelength	(nm)
λ_{Ex}	Excitation wavelength	(nm)
λ_{Reorg}	Reorganization energy	(meV)
$\Delta\tilde{\nu}_{Stokes}$	Stokes Shift	(cm^{-1} / nm)
OD	Optical density	(a. u.)
p	Pressure	(mbar)
P_{Light}	Incident light power	($W\ m^{-2}$)
PCE	Power conversion efficiency	(%)
r	Deposition rate	($Å\ s^{-1}$)
R_q	Root-mean square	(nm)
θ	Incident angle	(°)
τ	Excited-state lifetime	(ns)
$t_{+/-}$	Transfer integral for holes and electrons	(meV)
T	Temperature	(°C)
T_{MP}	Melting point	(°C)
T_{SP}	Sublimation point	(°C)
T_{Target}	Target temperature	(°C)
$T_{Substrate}$	Substrate temperature	(°C)
V	Voltage	(V)
V_{DS}	Drain-source voltage	(V)
V_{GS}	Gate-source voltage	(V)
V_{OC}	Open-circuit voltage	(V)

V_{TH}	Threshold Voltage	(V)
W	Channel width	(µm)
ω_{rot}	Rotation velocity	(rpm)

Table of Content

Chapter I: Introduction & Aim of the Thesis

One of the greatest challenges of mankind is the fight against the climate change.[1] It is destroying the earth's fragile biosphere, threatening animal and plant species, human habitats, and the global availability of water and food.[2-4] While humans are responsible for the emission of greenhouse gases such as carbon dioxide and methane that have caused climate change, they too have the ability to counteract global warming. This can be done by shutting down coal- and gas-fired power plants that are harmful to the climate and by promoting renewable energies.[5] The largest available amount of usable energy is provided by sunlight, which covers the world's annual consumption manifold. However, to produce a sufficient number of solar cells for covering the electricity consumption of cities or entire countries, very large material quantities are required. In particular, this involves so-called semiconductors, which are imprinting today's world. They are used in electric circuits for calculations in computers and phones, for generating light in light-emitting diodes or for producing current in solar cells.[6-8] Nowadays, for all modern applications customized semiconducting materials are known and commercialized for the mass production, which results in a massive material consumption worldwide.[9] Generally, inorganic semiconductors like silicon, III-V compounds (e.g. GaAs or InP) or transition metal oxides (e.g. TiO_2) are utilized. These semiconductors own special properties such as their ability to transport charges, and their absorption as well as luminescence properties, which makes their application possible. Unfortunately, most of these used inorganic semiconductors need a huge amount of energy for the fabrication process, are sometimes toxic or mined under poor conditions.[10-12]

These drawbacks can be overcome with the help of ecofriendly organic semiconductors, which are often based on organic dyes and therefore accessible by organic synthetic approaches starting from small molecular precursors.[13]

However, in order to be able to use an organic dye as an organic semiconductor, it must have other characteristics (e.g. optical and electronical) that are specifically brought out by intermolecular interactions in the solid state, which is the main difference to their inorganic crystalline analogues. For organic dyes, a bottom-up approach is needed from the molecule to a supramolecular aggregate leading to the desired solid-state molecular packing, which then can be used as functional material in devices.

The optical properties of organic dyes in highly diluted solution are governed by the respective monomer. When increasing the concentration of dye molecules in such solutions, several systems tend to form supramolecular aggregates by self-assembly due to attractive intermolecular interactions between the respective dye molecules.[14] However, this molecular ensemble exhibits altered optical properties compared to the monomer species. The changed optical features originate from the coupling interaction between the respective transition dipole moments of the dye molecules in close proximity.[15-17] Therefore, the optical properties of organic semiconductors are governed by intermolecular interaction, which is the main difference to their inorganic counterparts, where the composition of the semiconductor and its particle size influences its absorption behavior.[18]

By the transition from the supramolecular aggregate to the solid-state material, even larger self-assembled particles are formed, which exhibit not only an altered absorption behavior, but also the ability to transport charges by hopping of electrons or holes. The probability of this charge-carrier transport is strongly directed by the distance and by the orientation of the respective chromophores in the solid-state structure, which is guided by intermolecular interactions.[19] In comparison to this hopping mechanism from one chromophore to another, inorganic materials exhibit a band-like transport, which occurs in the large crystalline lattice leading to high charge-carrier mobilities.[20]

For both classes of materials, organic and inorganic, the optical and electronic properties in the solid state lead to their application as functional materials in opto-electronic devices. The special feature of organic materials, however, lies in the intermolecular interactions through which the material properties are affected. The

understanding and the control over these interactions is important to develop new tailored semiconductors for specific applications.

The combination of the above mentioned properties are especially used in solar cells, which are one of the key technologies to fight against the climate change.[21] Nowadays, most of the solar cells produced are based on (poly-)crystalline silicon, leading to an energy production of about 5.3 GW in Germany in 2021.[22] With inorganic solar cell high efficiencies can be achieved but, unfortunately, they require a lot of energy and thus CO_2 for production.[21] This disadvantage can be overcome with the help of organic solar cells (OSCs), where significantly less energy is needed for the production.[21,23] Therefore, OSCs have the opportunity to become the cheapest way for generating green energy.[21] Compared with heavy-weight inorganic solar cells, their light-weight and flexible organic analogues reach places where heavy inorganic solar modules cannot be placed for safety reasons, such as on light-weight roofs.[21] Also, the installation of an organic module is significantly easier than for the inorganic ones, because the flexible multilayer film is simply attached to its destination by double-sided adhesive tape.[21,24] Another promising field in organic photovoltaics are semitransparent solar cells, where customized organic semiconductors are used in very thin-layer thicknesses, which exhibit an optical gap in the visible region.[25] These types of OSCs could be used in smart windows.[26] All in all, there are many opportunities for OSCs as a niche product in so called building-integrated photovoltaics, which will presumably lead to a worldwide multibillion € market in the next years.[21]

An OSC generally consists of at least two organic semiconductors, which absorb light and convert it into electricity. To ensure this process, materials are needed that have appropriate optical[27], energetical[28], electrical[29], and morphological[28] properties in the solid state which in turn are governed by the respective intermolecular interactions. The material properties required for OSCs with regard to the respective manufacturing methods are discussed in **Chapter II**. Two different techniques are used for the fabrication of OSCs namely the solution and the vacuum processing, which will be discussed in detail.

The simplest OSC architecture consists of two stacked n- and p-type semiconducting materials, which are sandwiched between two electrodes. These two materials,

which differ in their role with respect to the transport of the electrons (donor and acceptor), are contributing to the photocurrent. For most of the donor materials, the interactions between the respective molecules are well investigated and described in the literature. However, these interactions are not yet well described for the new emerging class of non-fullerene acceptors (NFAs). Understanding which intermolecular interactions are required and how they are controlled could pave the way for new functional materials that outperform their predecessors based on fullerene acceptors. Therefore, the aim of this thesis is to investigate the intermolecular interactions of new molecular NFAs (the workflow of this dissertation is shown in Figure 1).

To achieve this goal and to ensure a state-of-the-art investigation, first the reproduction of prominent literature-known OSCs must be conducted within our own laboratory. Accordingly, **Chapter III** deals with the new evaporation device OPTIvap-XL in combination with the glovebox line in the Center for Nanosystems Chemistry. After initial operation and calibration, literature-known organic thin-film transistors are processed, due to their rather simple one-component device architecture. The reproduction of reported OSCs is then conducted in different steps, which vary in the complexity of the resulting device architectures. First, solution-processed fullerene-based and fullerene-free OSCs will be demonstrated in conventional and inverted bulk-heterojunction architectures. The reproduction will be then completed by the refabrication of literature-known fullerene-based bulk-heterojunctions OSCs and fullerene-free planar-heterojunction OSCs through vacuum deposition.

A major part of this work is the subsequent search for suitable n-type semiconducting acceptor materials for OSCs which will be discussed in **Chapter IV**. For this purpose, materials available in the Würthner group and provided by collaboration partners will be screened in solution- as well as vacuum-processed

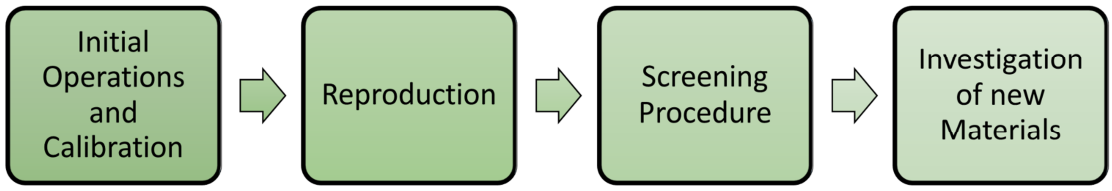

Figure 1: Workflow diagram of this thesis.

devices. To efficiently achieve this goal, laboratory intern testing-routines will be established in accordance with the available equipment for an efficient screening of manifold materials. Based on this screening, several classes of materials suitable for the study of intermolecular acceptor-acceptor interactions will be selected.

Via this screening new materials could be identified, which are composed of quinoidal dicyanomethylene-endcapped cyclopentadithiophenes as they are presented in **Chapter V**. These vacuum-sublimable materials combine a high tinctorial strength with appropriate energetic levels and n-type semiconductance as required for NFAs. Structure-property relationships will be drawn, which help to explain the observed performances in organic thin-film transistors and in vacuum-deposited planar-heterojunction OSCs.

The following **Chapter VI** deals with a new bowl-shaped naphthalimide-annulated corannulene derivative as acceptor material for solution-processed OSCs. The focus in this chapter lies on the intermolecular interactions that already exist in highly concentrated solutions and subsequently guide the thin-film formation. This investigation allows conclusions to be drawn about the molecular preorganization of the acceptor *via* self-assembly leading to the resulting active layer.

During the screening procedure of more than 90 materials in Chapter IV, a new class of NFAs could be identified, which consists of sterically shielded polycyclic aromatic dicarboximides. Therefore, **Chapter VII** focuses on the application of newly developed sterically shielded perylene bisimides and nanographene tetraimides as new solution-processable NFAs. After the discussion of the structural and optical properties in solution, in polymer matrix and in the solid state, their impact on the device performance in solution-processed OSCs will be investigated. Again, intermolecular interactions already present in the solution guide the film formation process, leading to unexpected exciton and charge transport pathways.

A conclusion that places the results of this dissertation in a larger context is addressed in **Chapter VIII** (German version **Chapter IX**).

Chapter II: State of the Art

2.1 Organic Solar Cells: Introduction & Characterization

An organic solar cell (OSC) consists of a combination of a donor and an acceptor material, which are responsible for the photocurrent generation. These materials are sandwiched between two electrodes like indium tin oxide (ITO) as transparent and a metal (Al or Ag) as reflective electrode to extract the generated charge carriers.[30] To further increase the performance of the OSC, additional transport layers (TL) are placed between the active layer (combination of donor and acceptor) and the respective electrode. These layers can be divided into electron-transport layers (ETL) and hole-transport layers (HTL).[31] Briefly, the elementary processes in an OSC (Figure 2a) can be described by the following steps: After the *absorption of light* by the donor or the acceptor an exciton is formed. The *exciton diffuses* to the interface between donor and acceptor and forms a *charge-transfer state*. The charge-transfer state undergoes a *charge separation* which leads to individual electrons and holes in the respective donor and acceptor domains. These separated charge carriers move through the active layer (*charge transport*) to the respective electrode (*charge extraction*).[32] The solar cell efficiency can be determined by measuring the *J-V* characteristics under AM1.5 G light irradiation (Figure 2b). The power conversion efficiency (PCE) is then calculated by the photocurrent density which is generated by the OSC under short-circuit conditions (J_{SC}), by the voltage under open-circuit conditions (V_{OC}), by the fill factor (FF) and the incident light power (P_{Light}) according to equation (1):

$$\mathrm{PCE} = \frac{J_{SC} \times V_{OC} \times FF}{P_{Light}}. \qquad (1)$$

When searching new materials for the application in organic photovoltaics (OPVs) like new donors or acceptors, they should combine the following properties. To gain a high J_{SC}, high tinctorial strength combined with a broadband absorption up to the

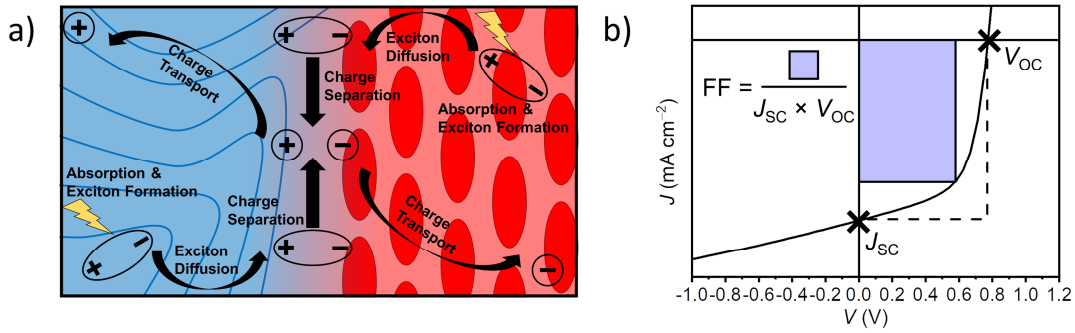

Figure 2: a) Schematic depiction of the photophysical processes in an organic solar cell at the phase boundary between a polymeric donor (blue - strands) and a small molecule acceptor (red - beats). b) Example for a *J*-*V* curve of a OSC under light irradiation with marking of J_{SC}, V_{OC} and the FF.

near infrared (NIR) is needed, to absorb the largest possible amount of photons of the solar flux for generating excitons.[27] Furthermore, a long exciton diffusion length (L_D) is needed, to allow excitons to reach the respective donor-acceptor interface and to avoid recombination.[33] To increase the charge-separation efficiency and therefore the amount of collected charge carriers, new materials should exhibit a good interface to the respective counterpart, where donor and acceptor interplay with each other. To obtain a high V_{OC} value, suitable energetic levels of the active layer materials as well as for the TL are needed, which decrease recombination as well as energy losses.[28,34] For high FFs, low recombination rates of excitons and charge carriers combined with high and balanced charge-carrier mobilities of both bulk materials are needed (donor & acceptor).[29,35] The respective mobility interfere with a high π-overlap of chromophores in the respective domains and a low reorganization energy according to Marcus' theory.[36] Experimentally, the charge-carrier mobility of the neat layer is mainly investigated by organic thin-film transistors (OTFTs), while the mobility of the solar cell's active layer is studied by space-charge limited current (SCLC) devices.[37,38]

2.2 Solution- and Vacuum-Processed Fullerene-Free OSCs

In the early 2000s fullerenes played a major role as acceptor materials in the field of OSCs.[39] They combine outstanding morphological properties with high charge-carrier mobilities in combination with small molecule and polymeric donors.[40] Furthermore, fullerenes can be used in vacuum-processed solar cells in their non-substituted form and in solution-processed solar cells after solubilization as for the fullerene derivatives **$PC_{61}BM$** and **$PC_{71}BM$**. The main drawbacks of fullerenes are their lack or only minor absorption in the visible and in the NIR-region as well as

non-tunable energetic levels, which often lead to low V_{OC} values.[39,40] Therefore, today's research focuses on new non-fullerene acceptors (NFAs) which enable higher efficiencies as for the fullerene analogues, due to their broadband absorption, their tunable energetic properties and higher charge-carrier mobilities.[41] In principle, every class of material, which combine the already described properties, can be used as a NFA in OSCs in combination with an appropriate donor material. Generally, most of the recently published scientific articles focus on two classes of materials, namely acceptor-donor-acceptor- (ADA) and rylene imide-based systems.[42,43]

On a laboratory scale, OSCs are fabricated either by spin-coating (solution processing) or by thermal evaporation (vacuum processing) as schematically shown in Figure 3. Both techniques, solution and vacuum processing are also used in commercially available OSCs. While the mass production for solution-processed OSCs is performed by a roll-to-roll printing procedure, vacuum processing is conducted by continuous thermal evaporation under reduced pressure ($p < 10^{-6}$ mbar). While the Heliatek GmbH (Germany) sells vacuum-processed OSCs, companies like Armor (France), OPVius (Germany) and Sunew (Brasil) are focusing on solution-processed devices.[21]

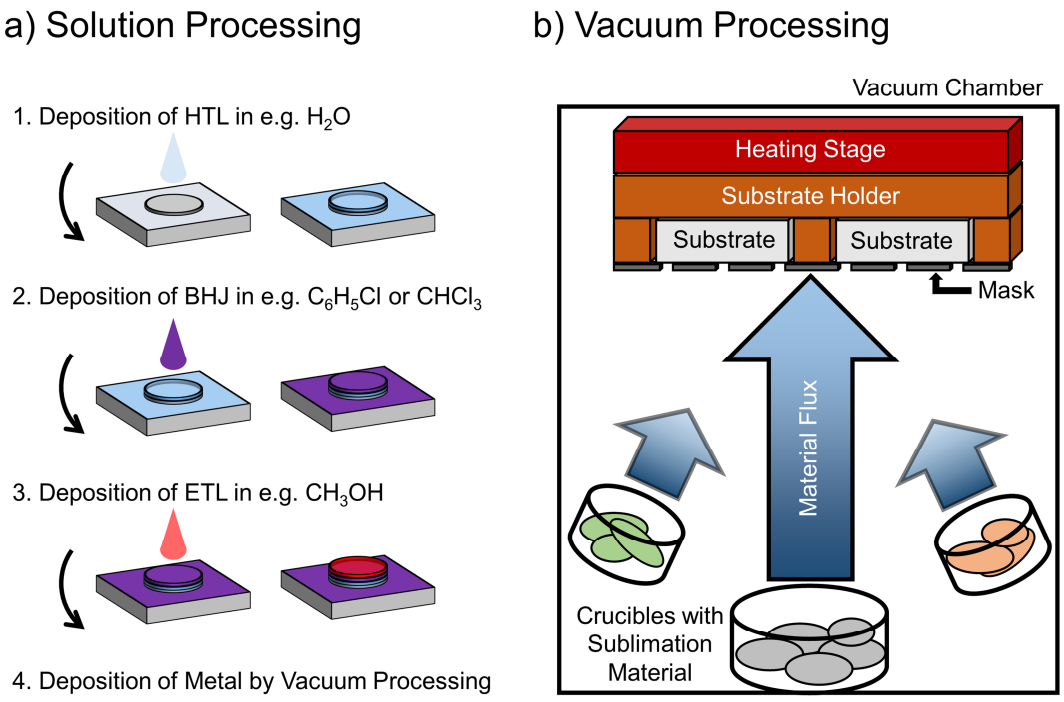

Figure 3: Schematic depiction of solution processing (a) and vacuum processing (b) for the fabrication of organic solar cells.

The most established route in academia is the solution-processing technique (Figure 3a). Here, a TL is deposited *via* spin-coating on top of an ITO-substrate. Afterwards, a blend solution of a donor and an acceptor is prepared and then spin-coated onto an ITO|TL-substrate. Usually, the first layer is soluble in aqueous solvents, while the second one is applied by using an orthogonal organic solvent (cross solubility) to avoid solubilization of the previous layers. Following layers are then applied either by further spin-coating or by thermal vacuum deposition. Finally, the OSC is completed by thermal evaporation of a reflective or semitransparent metal electrode. As for the solution-processed OSC the donor and the acceptor are deposited simultaneously, an interpenetrating network of respective donor and acceptor domains is formed, leading to percolation networks for holes and electrons. This morphology is called bulk heterojunction (BHJ).

When searching for new NFA materials for solution processing, one has to find a material, which combines the above-mentioned properties with the required solubility. Solution processing usually takes place in chlorinated solvents like chloroform or chlorobenzene with concentrations of up to 10 mg mL^{-1} per component leading to an active layer thickness of around 100 nm.[41] Fortunately, only small amounts of the D-A-blend solution are needed to coat one substrate (generally <100 µL), which makes the solution processing feasible for the initial screening of new materials.[†] This initial test can be performed with several donor polymers, to find a suitable counterpart at least from the energetic point-of-view to obtain the highest possible V_{OC} value. After finding a pair of a suitable donor and acceptor combination, the optimization can be performed by varying the general device architecture[44], the donor-acceptor ratio[45], the active-layer thickness[46], by adding different spin-coating additives[47] or by post-treatment steps like thermal or solvent vapor annealing steps[48]. Due to the rather simple processing and optimization steps many groups focus on solution-processed OSCs, which currently lead to efficiencies of up to 19.6% for ADA-type[49] (Figure 4b) and of over 11% for rylene imide-based NFAs[50] (Figure 4c). Surprisingly, both record OSCs exhibit the same device architecture (Figure 4a).

Another way to fabricate OSCs is vacuum processing from thermal sources under high vacuum. Usually, all layers are sequentially deposited onto an ITO-substrate by

[†] The given quantities are approximate values that were used in the processing, for example in the screening of new materials as shown in Chapter IV.

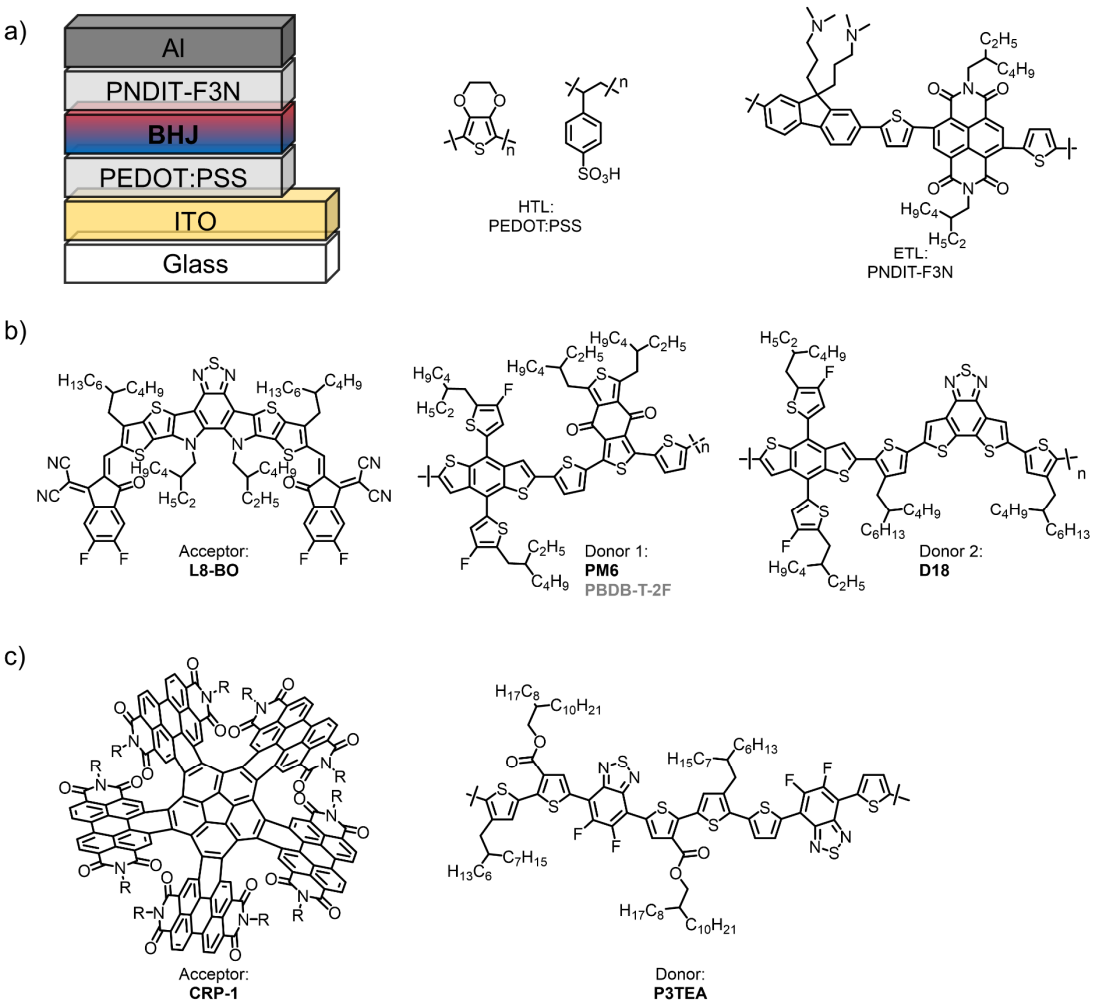

Figure 4: Schematic architecture of champion solution-processed devices in the literature and the chemical structures of the hole-transporting layer PEDOT:PSS and the electron transporting layer PNDIT-F3N (a). Chemical structures of the active layer materials for the best ADA-based (b) and rylene imide-based (c) OSCs.

thermal (co-)evaporation (Figure 3b). The vacuum sublimation allows to manufacture planar heterojunctions (PHJs)[51] by sequentially deposition of either donor and acceptor, bulk heterojunctions (BHJs) by co-evaporation of donor and acceptor[52] and so called planar-mixed heterojunctions (MHJs)[53], which combine planar donor and acceptor layers with a BHJ layer in-between.

A new NFA for vacuum-processing should combine the requirements for an OPV material combined with a low molecular mass as well as high thermal stability to allow the residual-free sublimation process.[54] The needed material quantities depend on the desired thickness of the active layer, which typically range from 40 nm to 100 nm. The material consumption for such layer thicknesses strongly depends on the used evaporation device (minimum 6 mg for 10 nm).[†] As in the case of the solution processing, the first step is the search for a suitable donor material.

[†] The given quantities are approximate values that were used in the processing, for example in the screening of new materials as shown in Chapter IV.

After finding a suitable donor-acceptor pair, this combination can be optimized by varying the active layer type[55] (PHJ, BHJ, MHJ), the general architecture[56] (TLs), the active layer thickness[57], the donor-acceptor ratio[55], the substrate temperature[58] and by post treatment like thermal annealing steps[59]. Due to the rather complicated processing and optimization steps and due to the price of such evaporation tools only less groups focus on vacuum-processed OSCs, which achieved until now efficiencies of up to 10.2%[60] for fullerene-based (Figure 5a) and of 6.0% for NFA-based[61] (Figure 5b) single-junctions OPVs. Accordingly, in contrast to solution-processed NFAs their vacuum-processable analogues were not able to surpass the performance of the fullerene-based OPVs, so far.

Both techniques have different requirements for potential NFA-candidates. A simple comparison between both techniques is listed in Table 1. When designing new materials for vacuum-processing one is limited to small pigment-like chromophores with high thermal stability for the sublimation process, which is not needed for a solution-processable NFA. Here, in turn long solubilizing chains are required, which also induce large photo-inactive volumes. This is not necessary for vacuum-processable NFAs. Nevertheless, small side groups are implemented also for vacuum-processable NFAs as well to not only ensure the synthetic access and purification but also to induce a favored packing motif in the solid state. When

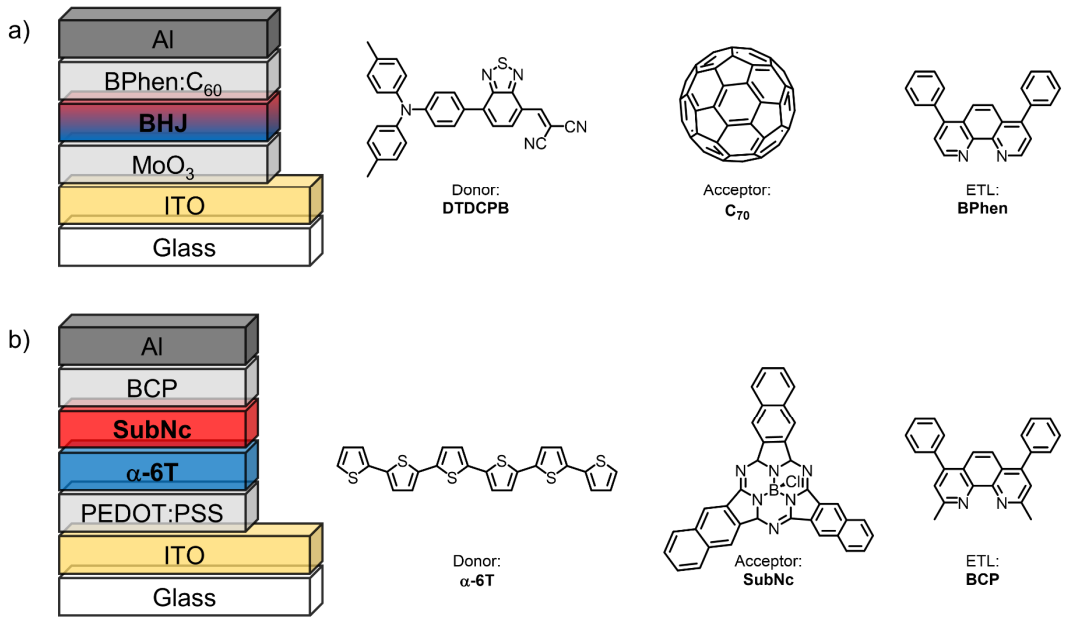

Figure 5: Device architectures and chemical structures of the active layer materials for the best fullerene-based (a) and fullerene-free (b) vacuum-processed OSCs.

searching a suitable combination of donor and acceptor for solution-processable NFAs, nowadays, a large library of donor polymers is commercially available, which can be easily and material-savingly screened by preparing the respective blend solution. As for the spin-coating process most of the solution is washed away from the substrate, this NFA-containing residual can be collected, purified by separation from the polymer, and used again for further experiments.[62] For vacuum-processable NFAs, less high potential donor molecules are commercially available, which already limits the search for a suitable NFA counterpart. Unfortunately, every donor-acceptor pair needs to be screened separately, which increase the material consumption significantly compared to the solution processing. Furthermore, no simple recycling process can be performed for both materials.

During the vacuum deposition an exact thickness increase can be constantly monitored, which significantly simplifies the reproduction of the respective solar cells. For solution processing, the resulting thickness, and the homogeneity of the BHJ layer changes for every deposition process slightly. Generally, every solution-

Table 1: Comparison between solution processing and vacuum processing for NFA screening.

	Solution processing	Vacuum processing
Material design	Solubilizing chains	Thermal stability
Quantities	1 mg / Substrate	> 10 mg / Substrate
Recycling	Yes	No
Uniformity of layers	Low	High
Optimization steps	Architecture Donor D-A ratio Thickness Additives Thermal annealing Vapor annealing	Architecture Heterojunction (PHJ etc.) Donor D-A tatio Thickness Substrate temperature
Complexity	Low	High
PHJ for NFAs	Irrelevant	Standard
BHJ for NFAs	Standard	Not realized
PCE records for NFAs	19.6%	6.0%

processed OSCs is unique, and the spin-coating process also strongly depends on the operator.[†]

As for every application of semiconducting materials, small impurities have a large impact on the respective device performance for vacuum- as well as solution-processed OSCs. Additionally to the impurities, the composition of the donor polymers as they are needed for solution-processed OSCs plays a crucial role as different molar weights and polydispersity indexes significantly influence the performance.[63]

From the morphological point-of-view, the processing in vacuum is able to control crystallinity as well as the morphology for example by changing the substrate temperature during the depositing process.[28] Structure-property relationships can be more easily drawn for example by using the respective crystal structure of a material in combination with grazing incident X-ray diffraction pattern (GIXRD).[56] For solution-processed devices, the structure-property relationships are even harder to determine, as many polymorphs are formed during the rapid spin-coating process. For further analysis, grazing incident wide angle X-ray scattering (GIWAXS) is needed, which usually requires synchrotron irradiation.[64]

From the complexity of the respective techniques, the film-formation process by vacuum deposition is rather complicated as it is connected to several growing mechanisms, which strongly depend on the interactions of the gas phase and the substrate[65], while the spin-coating process is just a quick precipitation method on a rotating substrate, which can be easily trained and optimized.

All in all, both techniques are well established in the scientific field of the organic electronics, especially in the field of OSCs. As already described, the solution-processed non-fullerene-based OSCs exhibit significant higher efficiencies than their vacuum-deposited analogues (Figure 4 and Figure 5). The historical development of the efficiencies for both techniques for fabricating NFA-based OSCs is shown in Figure 6. Interestingly, both deposition techniques show a similar increase in their efficiencies until 2014. In 2015, the discovery of large NIR-absorbing ADAs in combination with new donor polymers was a milestone for solution-processed OSCs leading to significant higher efficiencies than for their vacuum-deposited analogues.

[†] This observation was made during the extensive screening work as shown in Chapter IV.

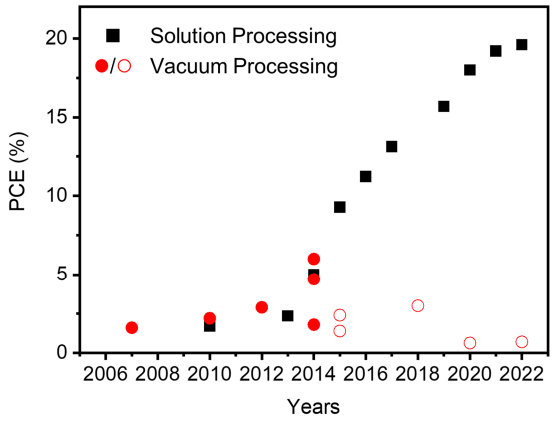

Figure 6: Development of solution- and vacuum-processed OSC based on non-fullerene acceptors from 2007 to 2022.

Every year, new record performances are obtained, all for ADA acceptors, while for vacuum-deposited OSCs a peak performance in 2014 was achieved that has not yet been surpassed. Such a milestone, as the ADAs were for the solution processing, is now also required for the vacuum processing in order to significantly increase the efficiencies and thereby allow the commercial use on equal performance level. However, in order to achieve better efficiencies, new materials have to be found first that meet the respective requirements.

Chapter III: OPTIvap-XL – Reproducing Literature-Known OTFTs and OSCs

3.1 Introduction

All optimized OTFTs and OSCs of new materials presented in this doctoral thesis were fabricated and characterized under inert conditions using the evaporation device OPTIvap-XL combined with a glovebox line (CreaPhys/MBraun) as depicted in Figure 7. This system consists of two interconnected nitrogen-filled gloveboxes, where one of them is linked to the evaporation system OPTIvap-XL. The first glovebox is equipped with a balance, heaters and stirrers, a bottle storage, a spin-coater and an UV/ozone cleaner. Therefore, this glovebox is used, whenever operating with solvents due to its installed solvent absorber, which is the difference to glovebox 2. Here, a non-solvent atmosphere is needed to avoid damage of the measurement set-ups, as glovebox 2 is only for characterization and for the access to the evaporation device OPTIvap-XL. The glovebox is equipped with a precision heat plate, an *I-V* measurement set-up in combination with a solar simulator, a measurement kit for determining the external quantum efficiency and a micromanipulator for characterizing e.g. OTFTs. The heart of the fabrication line is the evaporation system OPTIvap-XL, which is needed for the manufacture of organic electronic devices.

The evaporation device OPTIvap-XL of the Creaphys® (Dresden) is a customized system for fabricating various types of organic electronic devices. The system consists of three interconnected vacuum chambers assigned as metal, transfer and organic chamber (Figure 8, Figure 9a). The transfer chamber serves as load lock and

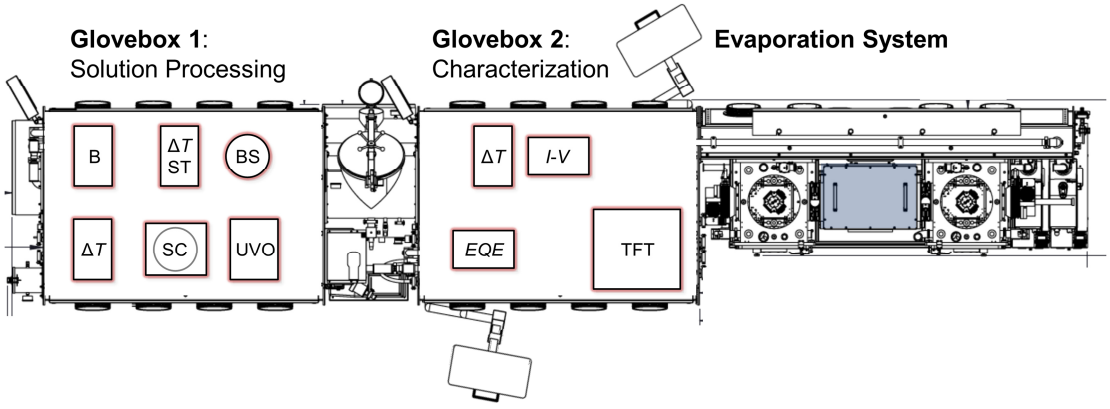

Figure 7: Technical drawing of the fabrication line for organic electronic devices in the Center for Nanosystems Chemistry consisting of two gloveboxes and one evaporation system. Glovebox 1 for solution processing owns a balance (B), heating and stirring stages (ΔT, ST), a bottle storage for solvents (BS), a spin-coater (SC) and an UV/ozone cleaner (UVO). Glovebox 2 for characterization exhibits an additional heating stage, an *I-V* measurement system under solar irradiation (*I-V*), an EQE measurement kit (EQE) and a micromanipulator for additional *I-V* measurements (TFT). Reprinted with permission from CreaPhys.

links the two other chambers. It is equipped with a semiautomatic transfer system, which allows the transfer and the change of samples and masks without breaking the vacuum. The metal and organic chambers are equipped with several thermal sources, quartz crystal monitors (QCM) and a substrate tower, which controls the deposition height and thus the distance between the evaporation source and substrate. Furthermore, several storage places for substrates are installed as well in the substrate tower.

The individual thermal sources can be divided into three types. The first type are low temperature thermal evaporators (LT; Figure 9b), which allow temperatures up to 600 °C (for organic materials). The second type are high temperature evaporators (HT) for temperatures up to 1100 °C (e. g. Ca; MoO_3). Even higher temperatures allow metal evaporators (ME; Figure 9c), consisting of ceramic (Al) or molybdenum

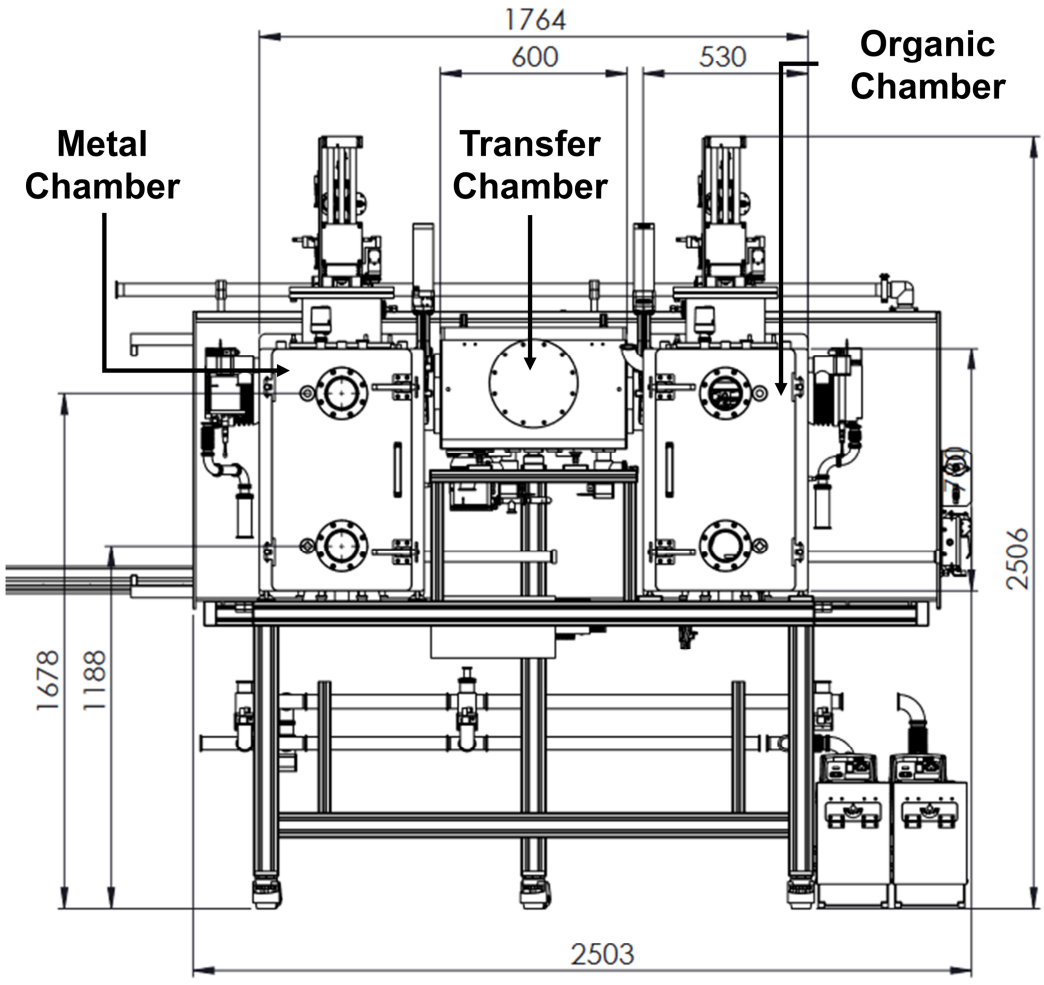

Figure 8: Technical drawing of the evaporation device OPTIvap-XL under clarification of the metal, transfer and organic chambers. All values are displayed in mm. Reprinted with permission from CreaPhys.

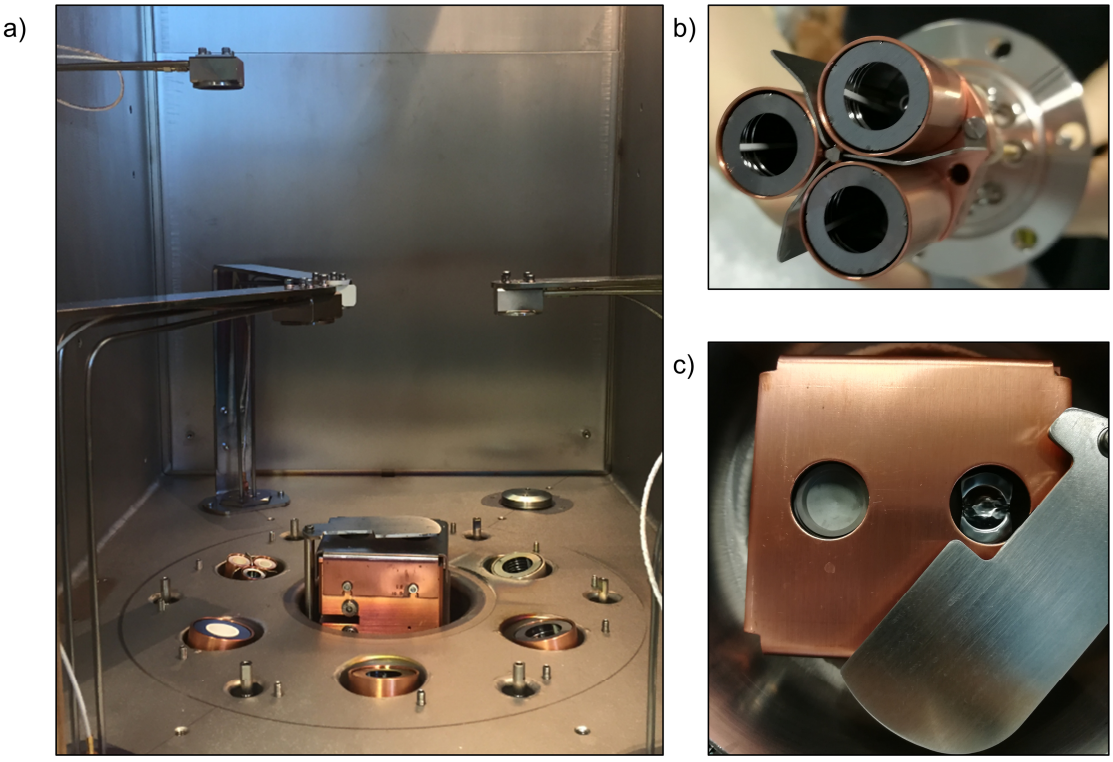

Figure 9: Photos of the organic chamber (a), a triple evaporator (b) and the metal evaporator with its two crucibles (c). For Al (left) and for Ag or Au (right).

(Ag and Au) crucibles. The metal chamber is equipped with two metal evaporators (ceramic and molybdenum crucible) and two high temperature evaporators with 4 cm^3 volume. The resulting layer thickness for each source is measured by individual QCMs. The organic chamber is constructed like the metal chamber, but it exhibits several additional features. While also two metal evaporators were installed at the center baseplate, only one high temperature evaporator (4 cm^3) is mounted. However, seven low temperature evaporators (1×4 cm^3, 3x2 cm^3 and 3x0.5 cm^3) are placed in this chamber to allow fully vacuum-processed devices as well as co- and even triple-evaporation by simultaneously using multiple QCMs and sources. Additionally, to the increased number of LT and HT evaporators other features are implemented at the substrate tower of the organic chamber. First, a wedge-tool is installed right under the substrate position, which allows thickness variations of the deposited layers allowing three different layer thicknesses in a single evaporation step. Second, substrates can be heated up to approximately 170 °C using a heating stage, which is in thermal contact to the substrates. Third, the whole tower is able to rotate during the sublimation process to enable higher homogeneity with a rotation velocity (ω_{rot}) of up to 30 rpm.

Since this system was newly set up in the Center for Nanosystems Chemistry in 2018 (University of Würzburg), the system first had to be brought into continuous operation and the reproducibility of the manufactured devices had to be checked. This was done within three steps by increasing the complexity of the respective fabrication method. First, OTFTs were fabricated based on literature-known materials. Here, in a simple OTFT architecture, two different layers, namely the organic active layer and the metal electrodes were evaporated onto the individual substrates. To double-check the reproducibility of the OTFT fabrication two different high-performance semiconducting materials were used. These experiments focused on the fine-tuning of the right semiconductor thickness as well as of the morphology control, which strongly depends on the substrate temperature. The second step targeted on solution-processed OSCs combining several solution- and vacuum-processed layers. The aim of this step was the access of new interlayers and active layer materials towards highly efficient literature-known solar cells. The last step of reproduction was fully vacuum-processed fullerene-based and fullerene-free OSCs, which were so far not processed in the group. Here, every layer of the OSCs was deposited by thermal evaporation, where single- and co-evaporation steps (e.g. for bulk-heterojunction architectures) are needed. Each of these steps is necessary to ensure a state-of-the-art investigation of new materials.

3.2 Initial Operations with the OPTIvap-XL

After first initial sublimation tests, tooling factors (TFs) were measured for all used sources. This empirical factor corrects the measured thickness difference between the substrates and the QCM as these do not have the same distance and orientation to the thermal evaporators.[66] Additional to the TFs, the density of the sublimated material and its *z*-factor is needed, to determine the actual layer thickness. The density of organic materials was fixed at 1.33 g cm^{-3}, while the *z*-factor, which describes the acoustic properties of the material with regard to the QCM is fixed at 1. When QCMs are frequently changed (lifetimes over 90%), the impact of the *z*-factors are neglectable. For all other commercially available materials (e.g. MoO_3, Al), the exact densities as well as the *z*-factor are used. Furthermore, every evaporator exhibits a different distance and angle to the substrate stage, through which the TF need to be determined for every thermal source individually.

Additionally, for several evaporators a second TF was defined for an increased distance of 130 mm instead of 30 mm. The given values do not refer to the distance to the sources but to the covered lift of the substrate tower from its own zero position. A technical drawing of the organic evaporation chamber at both positions is shown in Figure 10. An increased distance from the crucible to the substrates leads to a better homogeneity of the resulting layer especially when co-deposition is conducted. The main drawback of the increased distance is the higher material consumption up to 1 mg nm^{-1} compared to 0.72 mg nm^{-1} for the 30 mm position.[59] So the larger distance is suitable for literature-known commercially available materials, while the shorter distance is needed for sublimation tests and research materials, where only small amounts (< 20 mg) are available. For the measurement of the TF thin layers of tris(8-hydroxyquinolinato)aluminum (Alq_3) were sublimated on top of *n*-octadecyltriethoxysilane (OTES)-modified Si|SiO_2-substrates. After the sublimation, the total layer thickness was determined by scratching the layer using the micromanipulator followed by atomic-force microscopy (AFM). The resulting TFs are listed in Table 2. The tooling factors for every organic source Q1-Q8 are in the range of 20% indicating a high symmetry of the source's positions towards the substrate tower. Only the metal evaporators showed higher TFs, which can be

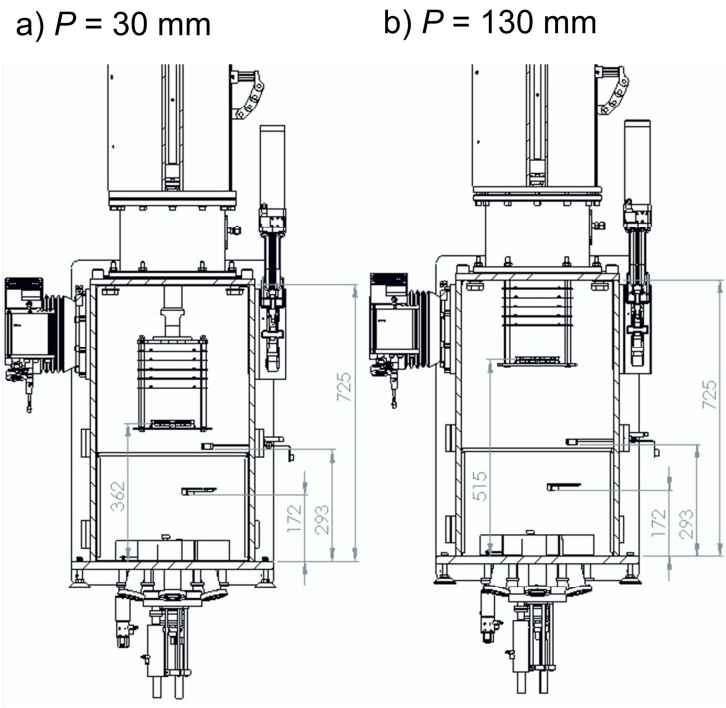

Figure 10: Schematic depiction of the sublimation process conducted at a position of 30 mm (a) and of 130 mm (b) in the metal chamber. All values are displayed in mm. Reprinted with permission from CreaPhys.

Table 2: Experimentally determined tooling factors (TFs) for every thermal evaporation source. The TFs are given for a substrate position of 30 mm, while the data in the parentheses represents the TFs for a distance of 130 mm.

Source	Type	TF (%)	Source	Type	TF (%)
Organic Chamber					
Q1	2 cm^3 - LT	18 (13)	Q5-Q7	0.5 cm^3 - LT	20 (16)
Q2	4 cm^3 - LT	24 (16)	Q8	2 cm^3 - LT	17 (14)
Q3	4 cm^3 - HT	19 (16)	Cer.	ME	52
Q4	2 cm^3 - LT	16 (12)	Mo	ME	72
Metal Chamber					
Q5	4 cm^3 - HT	- (18)	Cer.	ME	64
-	-	-	Mo	ME	71

Mo– Molybdenum crucible; Cer. – Ceramic crucible.

traced back to their location perpendicular under the substrate leading to a more focused material flux towards the substrate. By changing from the lower (30 mm) substrate position to the higher one (130 mm) a decreased TF was obtained, which is in line with the higher material consumption.

As many material properties for organic electronics are mainly connected to their crystallinity or specific intermixed morphology, the substrate temperature plays a crucial role as well. When increasing the substrate temperature, different growth mechanisms can lead to larger domain sizes of the semiconducting layer.[67] These larger domains often facilitate more efficient charge transport.[68] The main problem is to determine the exact temperature on the substrate surface. Generally, a temperature is applied at the heating stage (Figure 11a), while the temperature is directly measured at a thermocouple. Unfortunately, this temperature (T_{Target}) does not reveal the temperature, which is realized at the substrates surface ($T_{Substrate}$) transferred by the substrate holder (also called heat spread). This leads to many difficulties for reproducing literature-known data, because T_{Target} varies for different evaporation devices. $T_{Substrate}$ in comparison to T_{Target} was measured by a second thermocouple, which was fixed *via* a conductive silver varnish directly on the substrate. In Figure 11b individual temperature curves for four different substrate holders are depicted, which can be explained with a different heat conductivity as well and a changed connectivity to the heating stage for each holder. Therefore, a

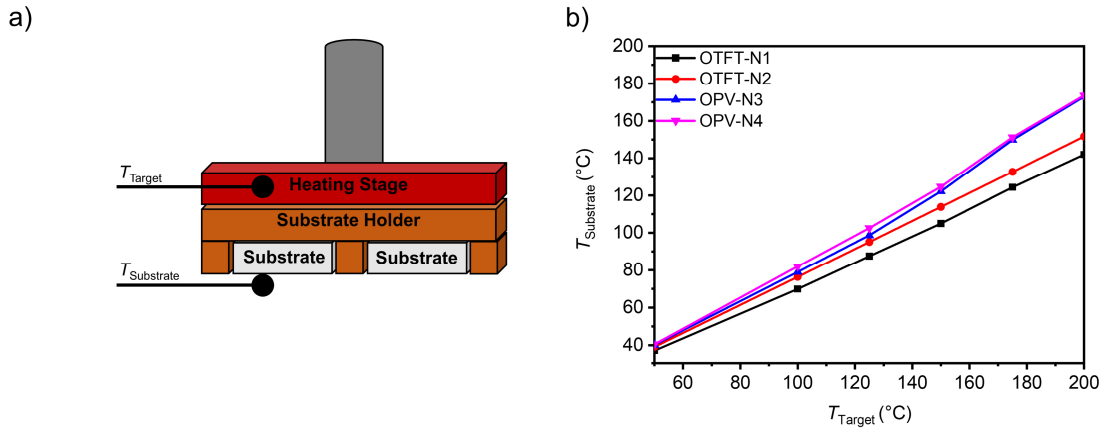

Figure 11: a) Schematic depiction of the set-up for measuring the exact substrate temperature during the evaporation processes. T_{Target} represents the temperature measured by a thermocouple at the heating stage. This temperature does not reveal the temperature, which is directly on the substrate ($T_{Substrate}$). b) Temperature curves for different substrate holders, which are used for processing OTFTs and OPVs.

characteristic heat curve was recorded for each of them, to relate T_{Target} to a specific $T_{Substrate}$. With the tooling factors and the substrate temperatures the OPTIvap-XL is now ready for reproducing efficient literature-known OTFTs and OPVs.

3.3 Reproduction of Organic Thin-Film Transistors

When reproducing OTFTs, the respective morphology as well as the layer thickness are crucial parameters. As the thicknesses are well reported for literature-known devices, the adjustment of the layer's morphology is critical. To allow a large domain growth, a low deposition rate below 0.06 Å s^{-1} without rotation was used. To adjust $T_{Substrate}$, the substrates were preheated followed by an equilibration step for approx. 30 min.

For the reproduction of literature-known OTFTs based on a material, which originates of our own group, a dichlorinated naphthalene diimide derivative with fluorinated imide substituents (**NDI 1** also known as **OFET1** or **Cl_2-NDI**) was used to elucidate the performance of the evaporation device. The OTFTs based on **NDI 1** were fabricated utilizing Si|SiO_2|AlO_x|*n*-tetradecylphosphonic acid (TPA) substrates to obtain a high mobility at a substrate temperature 50 °C analogue to Stolte *et al.*[69] The chemical structure and the schematic device architecture are shown in Figure 12a,b, while the respective transfer curve and an AFM-image of the neat **NDI 1** layer is shown in Figure 12c,d. The characteristic OTFT parameters are listed in Table 3. The transfer curve clearly shows a threshold voltage (V_{TH}) of around 0 V, indicating good turning-on behavior. Furthermore, only a small hysteresis between

Table 3: OTFT parameters of Si|SiO_2|AlO_x|TPA|**NDI 1**|Au based devices. In both cases the same architecture of the resulting OTFTs were used.

	μ_n ($cm^2\ V^{-1}\ s^{-1}$)	V_{TH} (V)	$I_{on}\ I_{off}^{-1}$ (1)
Reproduction	1.3	0	10^7
Literature[69]	1.3	5	10^7

the forward and the backwards sweep was observed, which indicates low trap state density in the resulting device. The respective mobility (μ) was calculated in the saturation regime using equation (2):

$$I_{DS} = \frac{\mu \times C_I \times W}{2 \times L} (V_{GS} - V_{Th})^2. \quad (2)$$

I_{DS} is the drain-source current, C_I the specific capacity of the substrate, W and L the width and length of the charge-transport channel respectively and V_{GS} is the gate-source voltage. Due to the high currents an extraordinary high n-type charge-carrier mobility of 1.3 $cm^2\ V^{-1}\ s^{-1}$ was observed, which is in accordance with the literature value. V_{TH} was shifted from 5 V to 0 V, which probably originates from the inert measurement conditions. Therefore, no oxidation processes of the neat organic

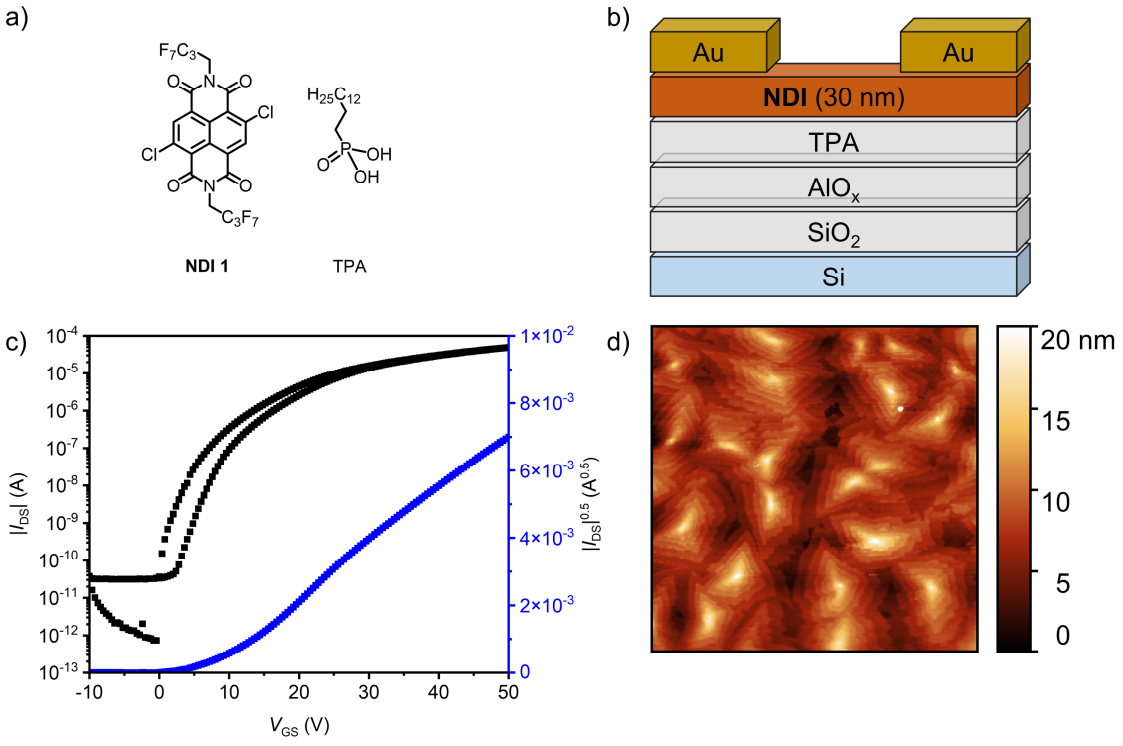

Figure 12: a) Chemical structure of the used n-type **NDI 1** and the SAM TPA. b) Schematic depiction of OTFTs in Si|SiO_2 (100 nm)|AlO_x (3.6 nm)|TPA|**NDI 1** (30 nm)|Au (30 nm) architecture. c) Transfer characteristics of **NDI 1**-based OTFTs measured at V_{DS} = 50 V with OTFT dimensions of L = 100 µm and W = 200 µm. The output characteristics are shown in Figure 21. d) 10 µm ×10 µm AFM-image of the **NDI 1** layer.

layer take place between the organic layer and the respective metal deposition, which could change their energetics. Even the on-off-ratio ($I_{on}\ I_{off}^{-1}$) showed the same value of 10^7. Both, the reproduced and the original data exhibit the same AFM morphology of large crystalline domains. This leads to the conclusion, that the OTFT was successfully reproduced.

To double-check the reproducibility of the new evaporation system OPTIvap-XL, a literature-known diketopyrrolopyrole derivative (**DPP 1**) was resynthesized and tested in an OTFT according to Qiao *et al.*[70] The literature-reported OTFT was processed on a Si|SiO_2 (300 nm)|OTES wafer at a $T_{Substrate}$ of 100 °C with a channel length and width of 8 µm and 8800 µm, respectively. In the reproduction, a $T_{Substrate}$ of 40 °C and an OTES-modified Si|SiO_2 substrate with a thinner dielectric layer of 100 nm combined with a changed channel length and width of 100 µm and 200 µm was chosen. The chemical structure of the semiconducting material, the device architecture, the transfer characteristics and the AFM morphology are shown in Figure 13 and the OTFT parameters are listed in Table 4. High currents were obtained, indicating good charge-transport properties. A n-type mobility of up to 0.41 $cm^2\ V^{-1}\ s^{-1}$, a low V_{TH} of 1 V and high on-off-ratios of 10^6 were observed.

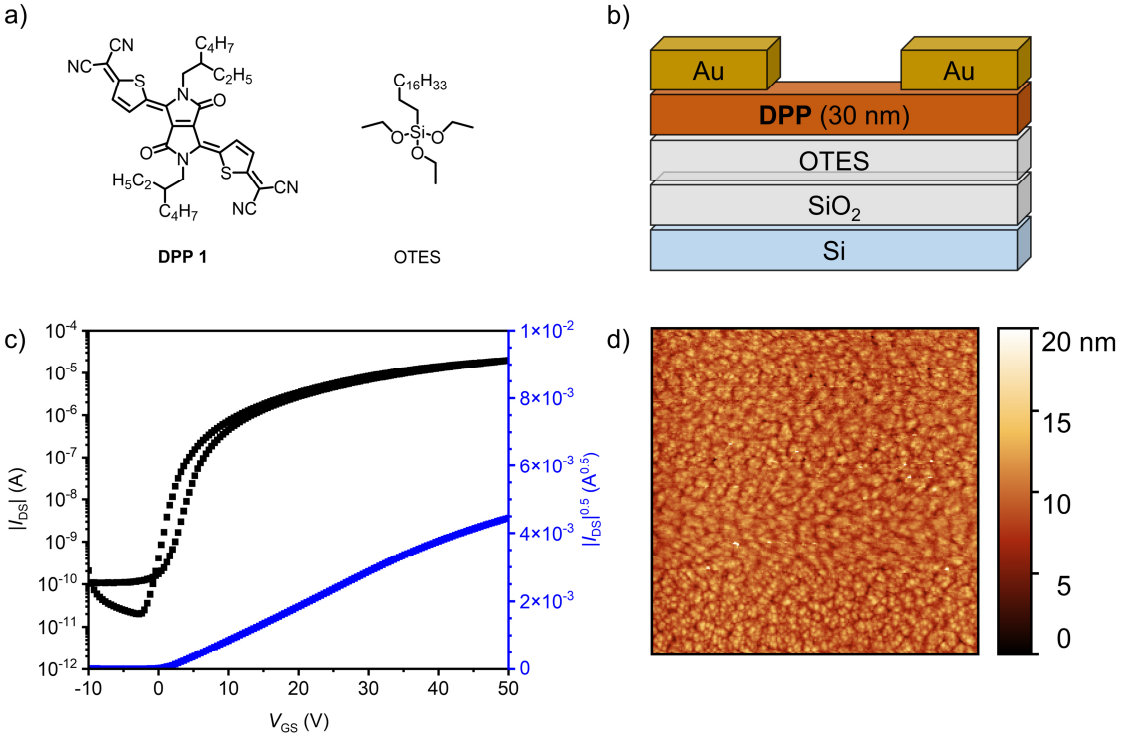

Figure 13: a) Chemical structure of the used n-type **DPP 1** and the SAM OTES. b) Schematic depiction of OTFTs in Si|SiO_2 (100 nm)|OTES|**DPP 1** (30 nm)|Au (30 nm) architecture. c) Transfer characteristics of **DPP 1**-based OTFTs measured at V_{DS} = 50 V with OTFT dimensions of L = 100 µm and W = 200 µm. The output characteristics are shown in **Figure 21**. d) 10 µm ×10 µm AFM-image of the **DPP 1** layer.

Table 4: OTFT parameters of Si|SiO_2|OTES|**DPP**|Au based devices.

	$T_{Substrate}$ (°C)	μ_n ($cm^2\ V^{-1}\ s^{-1}$)	V_{TH} (V)	$I_{on}\ I_{off}^{-1}$ (1)
Reproduction	40 °C	0.41	1	10^6
Literature[70]	100 °C	0.45	10	10^6

Compared with the literature values, the mobility and the on-off-ratio are in same range, even if different architectures and dimensions of the transistor channel were used. Only lower threshold voltages were observed in comparison to the literature, like in the case of the **NDI 1**-based OTFTs. This is probably due to the completely inert conditions. More interesting is the situation for the substrate temperature. While in our laboratory a substrate temperature of 40 °C were sufficient, the literature reported a temperature of 100 °C. By comparing the respective AFM image with the literature one, similar morphological properties were obtained.

3.4 Reproduction of Organic Solar Cells

3.4.1 Solution-Processed Organic Solar Cells

When reproducing literature-known OSCs a look in the experimental part of the respective publication is needed. Unfortunately, the experimental details are often described very scarce. Generally, only the architecture, the total blend concentration and the donor-acceptor ratio as well as the spin-coating duration and velocity are defined. Crucial parameters like the condition of the glovebox atmosphere ($c(O_2)$ / $c(H_2O)$) are often missing for whole experimental parts. For solution-processed solar cells, even the application of the first interlayer, is only reported scarce. Often the total concentration, the spin-coating parameter (acceleration, velocity, duration), and spin-coating technique (static or dynamic dispense – first drop then spin or *vice versa*) or the thermal annealing parameter are not fully described. Also, the size of the respective substrate has an impact on the spin-coating result.

For the donor-acceptor blend even more details are sometimes missing. As this solution consists of two different materials, the way this solution was produced might be relevant. Here, two different ways are possible: First, one material is dissolved and then mixed with the second one. This technique provides a good control of the respective concentration of donor and acceptor, but it also requires more material, due to the pipetting. Second, both solid materials are combined in

their solid state and solved together. This technique is more prone to weighing errors, but fewer material quantities are needed. As donor and acceptor are interacting already in solution, also the stirring time as well as possible heating periods can be important for the reproduction. Especially when operating with polymers, the respective chain length and the polydispersity are influencing the total efficiency of the device. To really reproduce literature values, the exact batches of the respective materials would be needed. Analogue to the first interlayer, also the already mentioned spin-coating parameters play a crucial role for the deposition of the active layer.

For the reproduction of the second interlayer the analogue parameters as for the first interlayer are needed. Therefore, it is necessary to deal with the reproduction of already known systems before investigating new materials. For each of the interlayers, laboratory routines were determined by trial-and-error methods to ensure their operability. For the active layer a standard spin-coating routine with a velocity of 1000 rpm with an acceleration of 3 s from 0 rpm to 1000 rpm and a duration of 60 s was chosen, while the static dispense technique was used. Here, first the spin-coating solution was deposited onto the substrate which is followed by starting the rotation.

When reproducing literature-known OSCs, the critical step is the spin-coating process, which needs to be optimized. Solution-processed OSCs were initially manufactured in the conventional architecture based on two high-performance commercially available donor polymers: **PBDB-T**[71] and **PCE-10** (also known as **PTB7-Th**)[72]. The thin-film absorption spectra as well as their chemical structures are shown in Figure 14a,b. While **PBDB-T** absorbs light up to a wavelength of 690 nm, **PCE-10** shows a more bathochromically shifted absorption up to 780 nm. Due to their energetics, both materials are suitable donors in conventional OSCs in ITO|PEDOT:PSS|BHJ|Al architecture in combination with fullerene derivatives like **$PC_{61}BM$** and **$PC_{71}BM$** (Figure 14c,d). Photovoltaic parameters of these types of OSCs are already literature-reported by several groups, as these are robust and reproducible systems. The corresponding *J*-*V* curves and parameters as well as the thin-film UV-Vis absorption and EQE spectra are shown in Figure 15 and Table 5. For all key parameters, at least five independent operating devices with an active

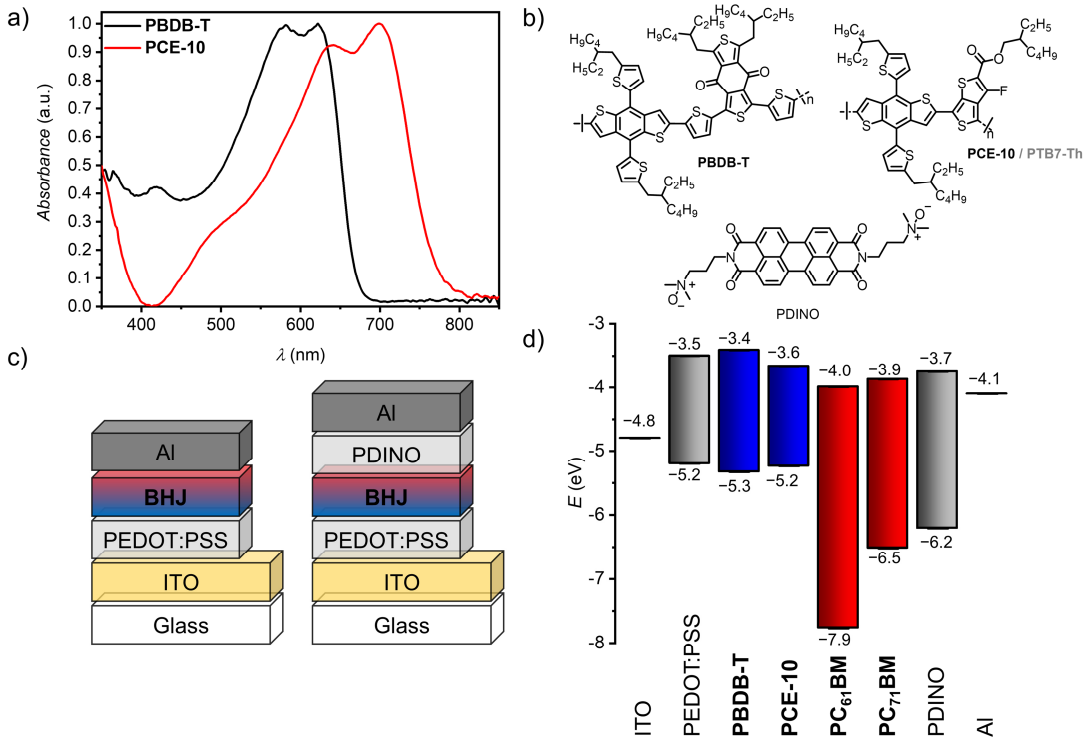

Figure 14: a) Normalized thin-film UV-Vis absorption spectra of spin-coated layers of **PBDB-T** and **PCE-10** (7.5 mg mL^{-1}; 1000 rpm, 60 s) on quartz substrates. b) Chemical structures of **PBDB-T** and **PCE-10**. c) Schematic architectures of conventional OSCs with and without PDINO as ETL. d) Energetics of used materials for conventional OSCs.

area (A) of 7.1 mm^2 were characterized for statistics. Both OSCs showed a diode-like behavior with J_{SC} values of −12.60 and −15.60 mA cm^{-2} for the **PBDB-T**:**PC$_{61}$BM** and **PCE-10**:**PC$_{71}$BM** BHJ layer, respectively. This finding can be explained with the help of the UV-Vis absorption and EQE spectra. The higher J_{SC} for the **PCE-10**:**PC$_{71}$BM** device can be traced back to the larger and therefore stronger absorbing fullerene, which absorbs more light in the visible range as the **PC$_{61}$BM** analogue and to the polymer **PCE-10** itself, which exhibits a red-shifted absorption compared to **PBDB-T**. The V_{OC} value of around 0.82 V instead of 0.61 V is higher for the **PBDB-T**-based devices, which originates from a larger HOMO$_{Do.}$-LUMO$_{Acc.}$ gap for the **PBDB-T:PC$_{61}$BM** material combination. The FF of the here shown devices are in the range from 50% to 60%, which indicates high and balanced charge-carrier mobilities in the respective OSC. Finally, the PCE is calculated by J_{SC}, V_{OC}, FF and the incident light power according to equation (1). The **PBDB-T**:**PC$_{61}$BM** devices show a maximum efficiency of 6.7%**,** while the **PCE-10:PC$_{71}$BM** heterojunctions exhibit a maximum PCE of 5.2%.

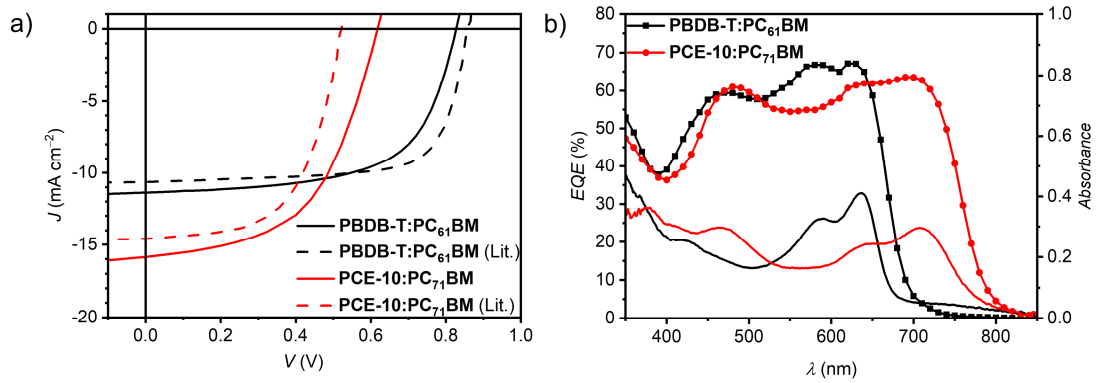

Figure 15: *J-V* curves of OSCs in ITO|PEDOT:PSS|BHJ|Al architecture based on **PBDB-T**:**PC$_{61}$BM** and **PCE-10**:**PC$_{71}$BM** BHJ layers under AM1.5 G irradiation compared with the literature data (a) as well as the corrosponding thin-film UV-Vis absorption (solid) and EQE spectra (symbols; b). Literature data adoped with permission from [71] and [72].

For the **PBDB-T**:**PC$_{61}$BM** heterojunction it was possible to reproduce the literature value of 6.7%. While V_{OC} and FF were slightly decreased, a higher J_{SC} was observed, which leads in total to the same PCE. In comparison with the respective literature, several experimental details needed to be optimized to achieve this PCE values, because a simple transfer of the details failed. In the literature, the blend solution with a total concentration of 25 mg mL^{-1} was stirred at 30 °C in *ortho*-dichlorobenzene with addition of 3% diiodoctane as additive. Unfortunately, no spin-coating parameters were given. For the reproduction, the **PBDB-T**:**PC$_{61}$BM** blend solution was stirred overnight at 90 °C with a total concentration of only 20 mg mL^{-1} in chlorobenzene without any additive. To achieve the high PCE values, it was necessary to thermally anneal the OSCs for 5 min at 150 °C, which was not reported for the literature device. Additionally, our device architecture consist of an active area of 7.1 mm^2, which is larger than the one of the reported literature device with 4.0 mm^2.

In the case of the **PCE-10**:**PC$_{71}$BM** OSCs the efficiency was increased compared to the literature value, which originates from an increase of both J_{SC} and V_{OC}. Again, in the respective literature no spin-coating parameters for the active layer was given. The main differences between the literature and the reproduction were a solvent change from *ortho*-dichlorobenzene to chlorobenzene and an increased active layer area of 7.1 mm^2 instead of 4.4 mm^2.

In both systems a decreased FF by approximately 10% was obtained. Small changes like for J_{SC} and V_{OC} could be induced by small discrepancies in the donor-acceptor

Table 5: *J-V* parameters of conventional **PBDB-T**:**PC$_{61}$BM** and **PCE-10**:**PC$_{71}$BM** based OSCs in ITO|PEDOT:PSS|BHJ|Al architecture compared with literature values. For the statistics at least five individual operating devices were used.

Donor	Acceptor	J_{SC} (mA cm^{-2})	V_{OC} (V)	FF (%)	PCE (%)	PCE^{Max} (%)	Area (mm^2)	Ref.
PBDB-T	**PC$_{61}$BM**	−12.60 ±0.25	0.82 ±0.01	63 ±1	6.3 ±0.2	6.7	7.1	-
PBDB-T	**PC$_{61}$BM**	−10.68	0.86	72	-	6.7	4.0	[71]
PCE-10	**PC$_{71}$BM**	−15.60 ±0.28	0.61 ±0.01	51 ±3	4.8 ±0.4	5.2	7.1	
PCE-10	**PC$_{71}$BM**	−14.51	0.52	59	4.2	4.4	4.4	[72]

ratio, while the larger discrepancy of the FF, which is connected to several diode properties, would need a more in-depth investigation. The main problems could be inhomogeneous layers, increased active layer areas as well as changed layer thicknesses leading to decreased charge-carrier mobilities and therefore to a decreased FF. Furthermore, contacting issues during the *J-V* measurement as well as different ITO substrates might also affect FF, which was not further investigated after several attempts.

Nevertheless, higher FF can be obtained when introducing additional electron-transporting layers. This can be done by spin-coating as in the case of the high-performance interlayer material PDINO, which is deposited on top the respective BHJ layer like **PCE-10**:**PC$_{71}$BM**. PDINO is soluble in methanol and insoluble in chlorobenzene, which is desired for multilayer fabrication with an orthogonal solvent.[72] A solution of PDINO in anhydrous methanol (1 mg mL^{-1}) was prepared and spin-coated on top of the BHJ layer at 3000 rpm *via* the dynamic dispense (first spin, then drop) method. Here, the solution is deposited on the rotating substrate. The *J-V* curves in Figure 16a show again diode-like behaviors with an increase in J_{SC} and V_{OC} compared to the sample without the PDINO interlayer. The *J-V* parameter in Table 6 show a small increase in J_{SC} from −15.60 to −16.26 mA cm^{-2} and a significant increase in FF from 51% up to 62%, which originates from a reduced recombination at the interlayers. V_{OC} was boosted from 0.61 V to 0.83 V, due to the better alignment of the energy levels. Compared with the literature, J_{SC} and V_{OC} were increased from −15.00 to −16.26 mA cm^{-2} and from 0.75 V to 0.83 V, while the FF is still lower by

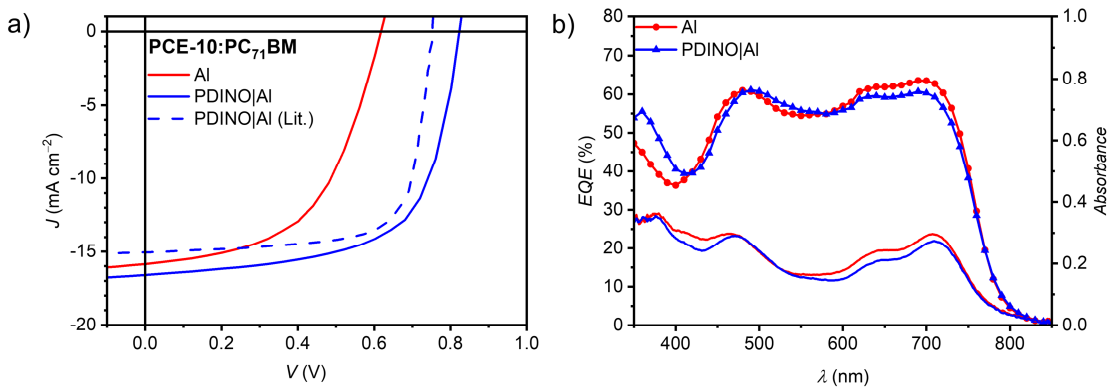

Figure 16: *J-V* curves of OPVs in ITO|PEDOT:PSS|**PCE-10**:**PC$_{71}$BM**|Al (red) and ITO|PEDOT:PSS|**PCE-10**:**PC$_{71}$BM**|PDINO|Al (blue) architecture under AM1.5 G irradiation compared with the literature data (a) as well as the corrosponding thin-film UV-Vis absorption (solid) and EQE spectra (symbols; b). Literature data adoped with permission from [72].

circa 10% similar to the samples without PDINO.[72] Due to the better V_{OC} and J_{SC} than in the reported literature, an overall higher efficiency of up to 8.7% compared with the literature value of 8.2% was obtained. The differences in the experimental procedure are the same as of the **PCE-10**:**PC$_{71}$BM**-based OSCs without the PDINO layer. For conventional OSCs it can be concluded that V_{OC} and J_{SC} are increased, while the FFs are decreased leading to overall similar PCEs in our laboratory.

Beyond the conventional device architecture an inversion can be realized as well, which is characterized by a changed position of the hole- and electron-transporting layer in the respective architecture. As a result of this change, ITO becomes the cathode, while the top electrode (Al) becomes the anode. In our laboratory, the inverted architecture was realized for the first time by applying a thin layer of ZnO on top the ITO|glass substrate according to procedures described by Sun *et al*. in 2011.[73] Onto this layer, the BHJ blend was spin-coated, followed by 10 nm MoO_3 as HTL, which was topped by Al as electrode material. The MoO_3 layer was applied by

Table 6: *J-V* parameters of conventional **PCE-10**:**PC$_{71}$BM** based OSCs in ITO|PEDOT:PSS|BHJ|Al or ITO|PEDOT:PSS|BHJ|PDINO|Al architecture compared with literature value. For the statistics at least five individual operating devices were used.

ETL	J_{SC} (mA cm^{-2})	V_{OC} (V)	FF (%)	PCE (%)	PCE^{Max} (%)	Area (mm^2)	Ref.
w/o	−15.60 ±0.28	0.61 ±0.01	51 ±3	4.8 ±0.4	5.2	7.1	-
PDINO	−16.26 ±0.26	0.83 ±0.01	62 ±1	8.46 ±0.14	8.7	7.1	-
PDINO	−15.00	0.75	73	8.15	8.2	4.4	[72]

thermal evaporation, while the ZnO layer was deposited by spin-coating. As active layer, **PCE-10**:**PC$_{71}$BM** was chosen to allow a comparison to the conventional device architecture. The schematic device architecture as well as the energetics are shown in Figure 17b and c. Analogue to the **PCE-10**:**PC$_{71}$BM** active layer, also a non-fullerene acceptor (NFA)-based blend was reproduced, which consists of the donor polymer **PM6** (also known as **PBDB-T-2F**) and **ITIC-4F** as NFA (Figure 17a).

Based on the energetics, a higher V_{OC} was expected for **PM6**:**ITIC-4F** than for **PCE-10:PC$_{71}$BM**, which is affected by the higher energetic gap between the donor's HOMO and the acceptor's LUMO levels. Accordingly, a V_{OC} of 0.84 V was obtained for the **PM6**:**ITIC-4F**-based OSC compared to 0.80 V for the **PCE-10**:**PC$_{71}$BM**-based devices. Both OSCs showed high FF in the range from 60 to 70%, which indicates good and balanced charge-transport properties (Figure 18, Table 7). The main difference of these types of OSCs is the resulting photocurrent. The **PM6**:**ITIC-4F**-based OSC showed a higher J_{SC} value of up to −17.33 mA cm^{-2} with respect to the **PCE-10**:**PC$_{71}$BM** device with −16.72 mA cm^{-2} which originates from the extended

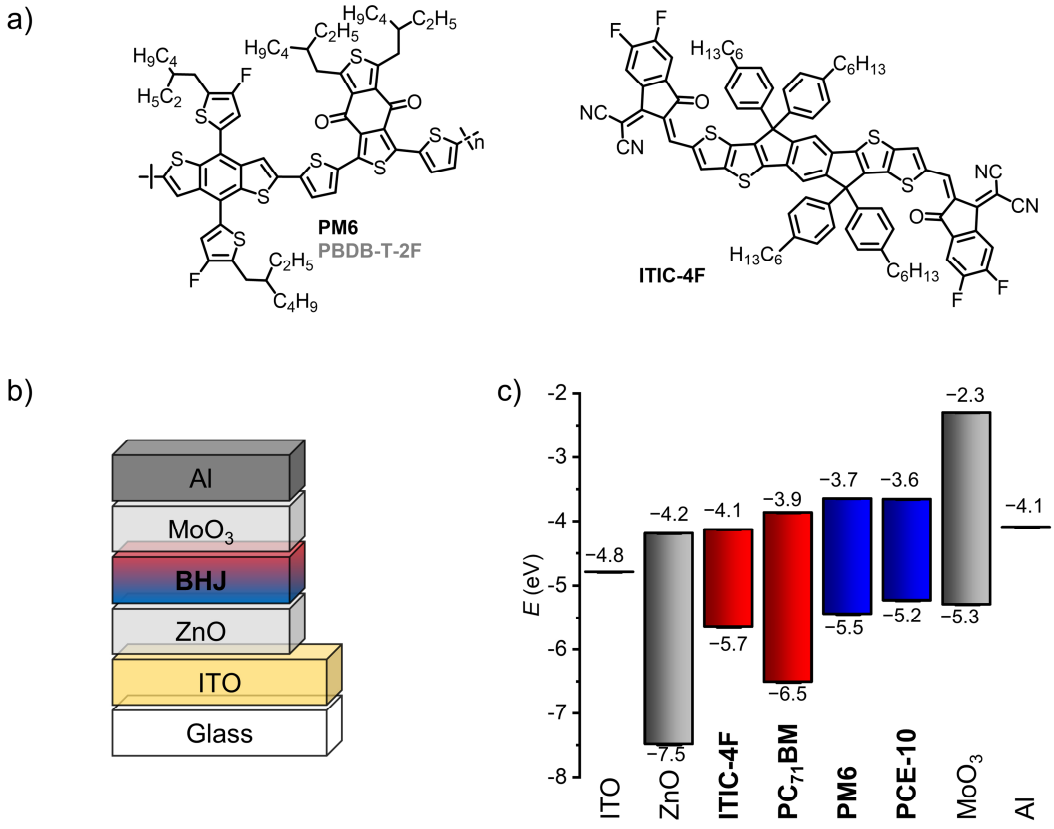

Figure 17: Chemical structures of **PM6** (also known as **PBDB-T-2F**) and **ITIC-4F** (a), schematic architecture of inverted OSC devices (b) and energetics of used materials (c).

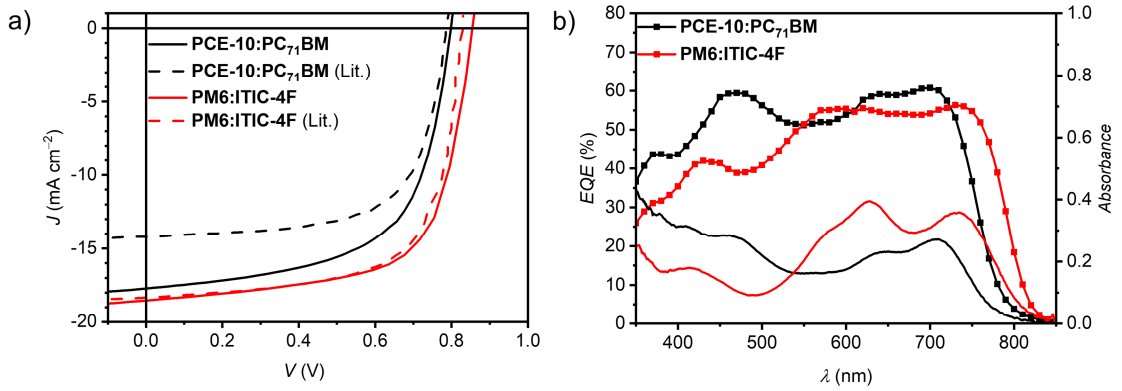

Figure 18: *J-V* curves of OPVs in ITO|ZnO|BHJ|MoO_3|Al architecture based on **PCE-10**:**$PC_{71}BM$** (black) and **PM6**:**ITIC-4F** (red) under AM1.5 G irradiation compared with the literature data (a) as well as the corrosponding thin-film UV-Vis absorption (solid) and EQE spectra (symbols; b). Literature data adoped with permission from [74] and [75].

absorption in the NIR region of the NFA **ITIC-4F**. The overall higher OSC parameters for the **PM6:ITIC-4F** device lead to an increased efficiency of up to 10.5% instead of 8.6% for the **PCE-10:$PC_{71}BM$** blend. Compared with the corresponding literature values, both OSCs were successfully reproduced. For the **PM6:ITIC-4F** device, the parameter are perfectly fitting to the literature data. Here, it was possible to directly overtake the experimental data for reproduction, except of the spin-coating parameter, which had to be adjusted. The **PCE-10:$PC_{71}BM$**-based device showed a slightly lower J_{SC} and FF which still leads to a lower PCE of up to 8.6% instead of up to 8.9% for the reported literature.[74,75] Here, a blend solution with a total concentration of 25 mg mL^{-1} was used analogue to the conventional architecture, while the literature device was made from a total concentration of 20 mg mL^{-1}. For both inverted devices, the respective active areas are comparable to our architecture with 6.0 mm^2 and 6.5 mm^2. **PCE-10:$PC_{71}BM$** devices were successfully

Table 7: *J-V* parameters of inverted OSCs in ITO|ZnO|BHJ|MoO_3|Al architecture based on **PCE-10**:**$PC_{71}BM$** and **PM6**:**ITIC-4F** compared with the corrosponding literature values. For the statistics at least five individual operating devices were used.

Donor	Acceptor	J_{SC} (mA cm^{-2})	V_{OC} (V)	FF (%)	PCE (%)	PCE^{Max} (%)	Area (mm^2)	Ref.
PCE-10	**$PC_{71}BM$**	−16.72 ±0.56	0.80 ±0.01	61 ±1	8.2 ±0.2	8.6	7.1	-
PCE-10	**$PC_{71}BM$**	−17.23	0.79	63	8.8	8.9	6.5	[74]
PM6	**ITIC-4F**	−17.33 ±0.84	0.84 ±0.01	68 ±1	9.8 ±0.4	10.5	7.1	-
PM6	**ITIC-4F**	−17.6	0.83	68	9.9	10.4	6.0	[75]

reproduced in conventional as well inverted architecture, which allows a comparison between both. For these devices, only slightly higher efficiencies were observed for the inverted OSCs. Therefore, the used architecture has only a small impact on the performance but can be used to further characterize new materials synthesized in our own laboratory.

3.4.2 Vacuum-Processed Organic Solar Cells

Instead of applying the active layer and several interlayers like ZnO or PEDOT:PSS *via* spin-coating, it is also possible to fabricate (mixed) multilayered structures by thermal evaporation. Here, freshly cleaned ITO-substrates, are placed in the evaporation chamber and every layer is deposited by thermal evaporation without breaking the vacuum. Similar as for the solution-processed OSCs, where spin-coating parameters were not reported well, also for vacuum-processed OSCs not all information are given in many publications for the sublimation process. As already mentioned before, the QCM is responsible for the thickness determination needing at least the respective material density. Often this value is not given, while a value of around 1.33 g cm^{-3} is used. While the failure of this simplification can be neglected for planar heterojunctions, discrepancies in the density have a large impact on the donor-acceptor ratio of co-evaporated bulk heterojunctions complicating their reproduction. Analogue to the OTFTs, also the right setting for $T_{\text{Substrate}}$ plays a role for material combinations, which are deposited on heated substrates. Other parameters, like the distance from the thermal source and rotation (ω_{rot}) while the sublimation are often not reported.

Still, fullerene-based planar heterojunctions (PHJs) on the basis of copper-(II)-phthalocyanine (**CuPc**) were already reproduced in our laboratory by Fabian Grote during his master thesis in 2019.[59] Therefore, it was still necessary to reproduce fullerene-based BHJ and non-fullerene-based PHJ OSCs. The BHJ architectures were reproduced by using two high-performance donor molecules, which were supplied by Prof. Dr. Peter Bäuerle (University of Ulm) and by Prof. Dr. Ken-Tsung Wong (University of Taiwan). The material from Prof. Dr. Peter Bäuerle is a dicyanovinyl-endcapped quinquethiophene (**DCV5T-Me**) with an ADA-type structure.[56] The material from Prof. Dr. Ken-Tsung Wong is a DAA-type chromophore (**DTDCPB**; Figure 19b).[55] Both materials show different HOMO levels of −5.3 eV (**DTDCPB**)

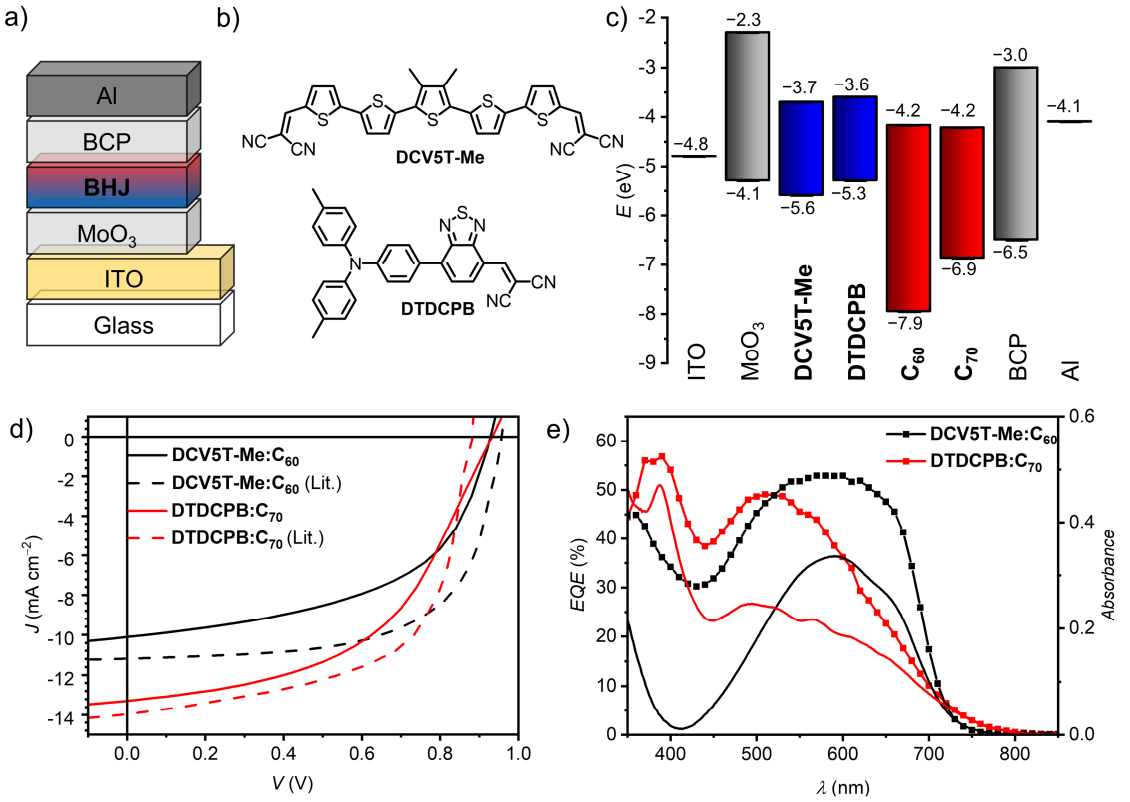

Figure 19: Schematic devices architecture of fullerene-based vacuum-processed BHJ OSCs (a), chemical structures of donor materials **DCV5T-Me** and **DTDCPB** (b), energetics of used materials (c), *J*-*V* curves of OSCs in ITO|MoO_3 (6 nm)|BHJ|BCP (10 nm)|Al architecture based on **DCV5T-Me:C$_{60}$** (40 nm; black) and **DTDCPB:C$_{70}$** (80 nm; red) under AM1.5 G irradiation compared with the literature data (d) as well as the corresponding thin-film UV-Vis absorption (solid) and EQE spectra (symbol; e). Literature data adoped with permission from [55] and [56].

and −5.6 eV (**DCV5T-Me**), respectively. This leads to the presumption, that **DCV5T-Me** should show a higher V_{OC} in the resulting device in combination with fullerene as **DTDCPB**. For comparison, both materials were tested in the same conventional device architecture ITO|MoO_3|BHJ|BCP|Al, knowing that the literature-reported best-performing devices consist of a different one. The **DTDCPB**-based literature-reported device consists of the same architecture but with an increased MoO_3 layer thickness of 10 nm instead of 6 nm. For the **DCV5T-Me** based device, the literature-reported OSC exhibit an inverted architecture with several additional layers. However, since the reproduction is performed with regard to the testing of new materials, a simpler architecture was used for both materials for a more general screening routine (Figure 19, Table 8). While **DCV5T-Me** was blended with **C$_{60}$** at a substrate temperature of 90 °C, **DTDCPB** was co-sublimated with **C$_{70}$** as acceptor at a substrate temperature of only 20 °C. The resulting devices showed both diode-like behavior as well as excellent photocurrents. J_{SC} values of up to −10.09 mA cm^{-2} for the **DCV5T-Me**:**C$_{60}$** OSC and

−13.26 mA cm^{-2} for the **DTDCPB**:**C$_{70}$**-based device were obtained. The higher J_{SC} for the **DTDCPB**:**C$_{70}$** can be traced back to the bathochromically shifted absorption of **C$_{70}$** compared to **C$_{60}$**. Both OSCs showed high V_{OC} values of around 0.9 V. This seems to contract the presumption of the V_{OC} dependence from the energetics but one have to note, that both solar cells consists of different mass ratios between donor and acceptor material, which have a strong influence to the resulting V_{OC}. While for the **DCV5T-Me**:**C$_{60}$** layer a 2:1 ratio was chosen, the **DTDCPB**:**C$_{70}$** solar cell consist of 1:2 ratio. The mass ratio is connected to the respective exciton diffusion length (L_D) and to the charge-carrier mobility of the donor. When a lower L_D was observable for example in PHJ experiments, it can be recommended to use a higher ratio of fullerene to decrease the domain size of the donor in the BHJ. This should allow excitons to reach the respective interface for charge separation.[55] Both solar cells showed similar FF of about 50% which led to high PCE values of 5.0% for **DCV5T-Me**:**C$_{60}$** and 6.3% for **DTDCPB**:**C$_{70}$** OSCs, respectively.

Both solar cells showed in the EQE as well as in the respective UV-Vis absorption spectra similar structureless band shapes, which emphasizes that both compounds are equally contributing to the respective photocurrent. A closer look to the corresponding EQE and UV-Vis absorption spectra resemble a strange behavior. While the **DTDCPB**-based OPV shows a significantly higher J_{SC} in the *J-V* measurement under AM1.5 G conditions, the area under the EQE spectra, which corresponds to the J_{SC} is lower as for the **DCV5T-Me**-based OPV. This finding was

Table 8: *J-V* parameters of experimentally observed conventional OSCs in ITO|MoO_3|BHJ|BCP|Al architecture based on **DCV5T-Me:C$_{60}$** (2:1 – 40 nm) and **DTDCPB**:**C$_{70}$** (1:2 – 80 nm) compared with literature-known OSCs based on the same active layer compounds. For the statistics at least five individual operating devices were used.

Donor	Acceptor	J_{SC} (mA cm^{-2})	V_{OC} (V)	FF (%)	PCE (%)	PCE^{Max} (%)	Area (mm^2)	Ref.
DCV5T-Me	**C$_{60}$**	−10.09 ±0.12	0.92 ±0.01	51 ±1	4.7 ±0.3	5.0	7.1	-
DCV5T-Me[a]	**C$_{60}$**	−11.50	0.96	63	-	6.1	n. a.	[56]
DTDCPB	**C$_{70}$**	−13.26 ±0.21	0.93 ±0.02	48 ±1	5.9 ±0.2	6.3	7.1	-
DTDCPB	**C$_{70}$**	−13.90	0.89	62	7.5	-	n. a.	[55]

a) **DCV5T-Me** in ITO|C_{60} (15 nm)|**DCV5T-Me**:C_{60} (2:1, 30 nm, 90 °C)|BPAPF (5 nm)|BPAPF:NDP9 (9:1, 50 nm)|Au (50 nm) and under 115 mW cm^{-2} intensity.

traced back to a reduced stability of the **DTDCPB**-based OPV in our laboratory. Accordingly, the device is degrading even under inert conditions during the EQE measurement, which takes up to 20 min.

In the case of the **DCV5T-Me:C_{60}**-based OSC the literature-reported device was processed in the inverted architecture with several doped and undoped transport layers to optimize this system, which resulted in an efficiency of 6.1% at an increased light intensity of 115 mW cm^{-2}. In this context, the obtained efficiency of 5.0% is even more surprising, as only a simple conventional device architecture with a light intensity of 100 mW cm^{-2} was chosen. For the **DTDCPB**-based OPV also a higher PCE value of 7.5% was shown in the literature, which mainly originates again from an increased FF. In the respective literature significant higher deposition rates of up to 2 Å s^{-1} were used to achieve 70 nm layers. In the reproduction, the best results were obtained using a 80 nm active layer at a deposition rate of 0.2 Å s^{-1}.

For both solar cells, a decreased FF was observed with respect to the literature. As this failure is present for both, solution- and vacuum-processed OSCs, contacting issues or the ITO-substrate are the most likely sources of errors. The often observed slightly increased J_{SC} values cannot be related to discrepancies of the incident light power as this is checked before every measurement using a calibrated silicon solar cell.

As fullerene-based OSCs can be manufactured reproducibly, the last step is now to manufacture an efficient vacuum-processed non-fullerene OSC with the OPTIvap-XL. Therefore, a system based on commercially available α-sexithiophene (**α-6T**) and subphthalocyanine (**SubPc**) was chosen, which was first described by Cnops *et al*. in 2014 (Figure 20a,b).[61] As **SubPc** is usually used as donor in vacuum-processed OPVs it shows high-lying HOMO- and LUMO-levels of −3.6 eV and −5.6 eV, respectively. In this case, **SubPc** was used as acceptor by mixing with **α-6T** as electron donor, which exhibits even higher energetic levels of −3.1 eV and −5.3 eV. Therefore, a high V_{OC} and due to the complementary absorption of both materials, a high J_{SC} was expected. The *J*-*V* curve and the photovoltaic parameters of a PHJ OSC with a **SubPc** thickness of 20 nm is shown in Figure 20c,d and Table 9, respectively**.** A remarkably high J_{SC} for a PHJ of up to −7.09 mA cm^{-2} was obtained. Due to the high $HOMO_{Do.}$-$LUMO_{Acc.}$ gap and the well-balanced charge-carrier mobilities in each neat

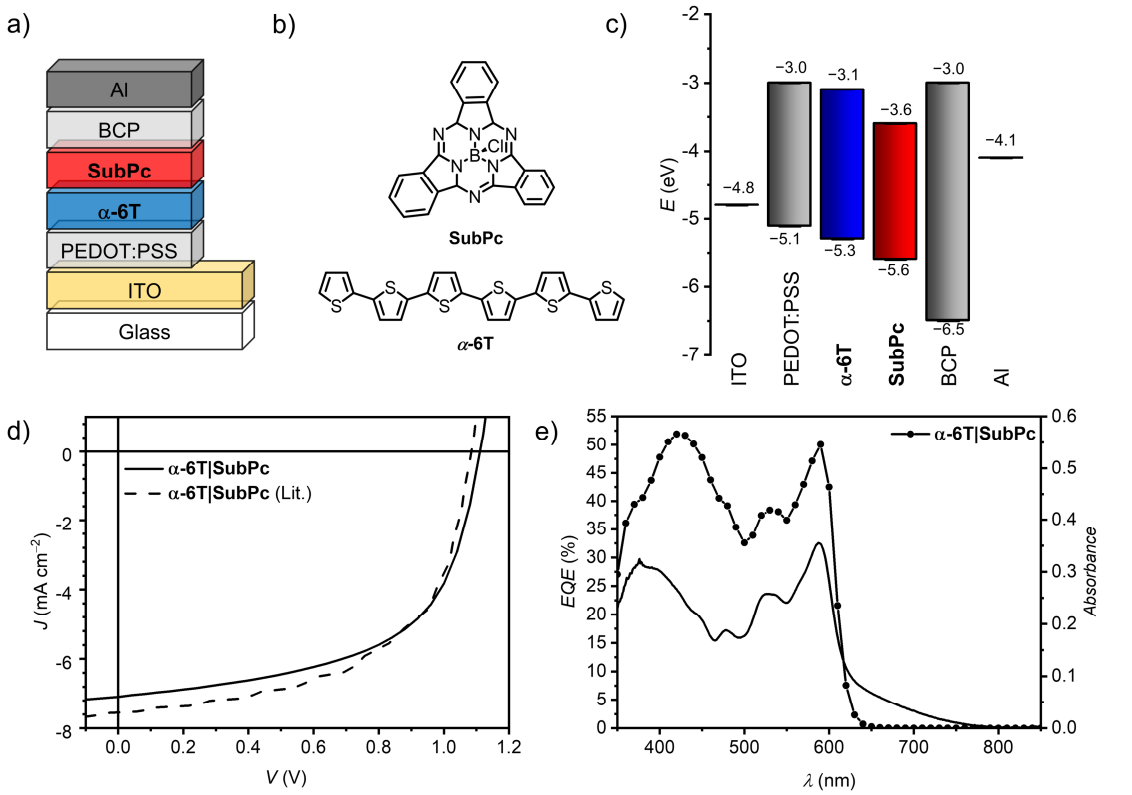

Figure 20: Schematic devices architecture of fullerene-free vacuum-processed PHJ OSCs (a), chemical structures of **α-6T** and **SubPc** (b), energetics of used materials (c), *J-V* curves of OSCs in ITO|PEDOT:PSS|**α-6T** (60 nm)|**SubPc** (20 nm)|BCP (5 nm)|Al (100 nm) architecture under AM1.5 G irradiation compared with the literature-reported data (d) as well as the corrosponding thin-film UV-Vis absorption (solid) and EQE spectra (symbol; e). Literature data adoped with permission from [61].

layer a high V_{OC} of 1.12 V and a high FF of 57% was observed, respectively, which leads to an overall performance of up to 4.5%. The respective EQE- and UV-Vis absorption spectra showed almost the same shape, which indicated that again both materials are equally contributing to the photocurrent. In this special case, it is also simple to distinguish between each compound. While **α-6T** shows its absorption maximum in the range under 450 nm the absorption of the **SubPc** is bathochromically shifted at 500 nm to 650 nm. Compared with the literature data, a smaller J_{SC} was obtained while V_{OC} was increased. A similar FF of around 57% was

Table 9: *J-V* parameters of experimentally observed conventional OSCs in ITO|PEDOT:PSS|PHJ|BCP|Al architecture based on **α-6T** (60 nm) and **SubPc** (20 nm) compared with literature-known OSCs based on the same active layer compounds. For the statistics at least five individual operating devices were used.

Donor	Acceptor	J_{SC} (mA cm^{-2})	V_{OC} (V)	FF (%)	PCE (%)	PCE^{Max} (%)	Area (mm^2)	Ref.
α-6T	**SubPc**	−6.88 ±0.1	1.12 ±0.01	57 ±1	4.4 ± 0.2	4.5	7.1	-
α-6T	**SubPc**	−7.49	1.09	58	-	4.7	13.4	[61]

observed, which leads to a similar efficiency of up to 4.5% compared to the literature value of 4.7%.[61] The main experimental differences, which were applied, was a reduced deposition rate of 0.2 Å s^{-1} instead of 1 Å s^{-1} and decreased active area of 7.1 mm^2 instead of 13.4 mm^2.

3.5 Conclusion

In this chapter the glovebox line in combination with the evaporation device OPTIvap-XL was introduced and tested towards its capability for manufacturing organic thin-film transistors (OTFTs) and organic solar cells (OSCs). Before the fabrication of those complex device structures, tooling factors were determined to allow the control over the respective layer thicknesses, which are monitored during the deposition process. Furthermore, specific temperature curves for each substrate holder were measured to carefully adjust the substrate temperature. This is needed for reproducing especially OTFTs, where the crystallinity of the active layer has a large impact on the respective device performance. This crystallinity can be guided with the respective substrate temperature. The first OTFTs, which were processed with the OPTIvap-XL were based on dichlorinated naphthalene diimide (**NDI 1**) and on diketopyrrolopyrole (**DPP 1**) derivatives. It could be shown, that both devices can be reproduced, when applying the right substrate temperature. While the mobility as well as the I_{on} I_{off}^{-1} ratios matches the respective literature values, significant reduced threshold voltages were obtained for these OTFTs, due to the complete handling under inert or vacuum conditions. This avoids oxidation processes of the active layers and at the interfaces.

Afterwards, OSCs were carefully reproduced beginning from polymer-based solution-processed devices based on fullerenes in conventional architectures. The impact of interlayers was demonstrated, which were not used in this laboratory so far. Fullerene and non-fullerene-based OSCs were studied in combination with the inverted device architecture and afforded state-of-the-art PCE values of up to 10.5% as for the **PM6:ITIC-4F**-based device. The last step of reproduction focused on vacuum-processed fullerene-based bulk-heterojunction (BHJ) and fullerene-free planar-heterojunction (PHJ) devices, where single- and co-evaporation techniques were used to successfully achieve values of up to 6.3% for **DTDCPB:C_{70}** (2:1) or up to 4.5% for the **α-6T|SubPc** literature-reported OSCs. In the reproduction work, the

respective PCEs could be obtained, but decreased FFs and slightly increased J_{SC} and V_{OC} values were frequently observed. The reason for this discrepancy could not be conclusively elucidated. The most likely sources of error are contacting problems during the measurement or a different nature of the ITO-substrate.

After these studies the OPTIvap-XL in combination with the glovebox line was fully operational for fabricating OTFTs and OSCs. Due to these findings, it can be concluded that also complex architectures for organic light-emitting diodes, photodiodes and phototransistors can be processed, too. Therefore, utilization of this fabrication line for new and innovative materials synthesized at the University of Würzburg became possible and first results will be presented in **Chapter IV**.

3.6 Supporting Information for Chapter III

3.6.1 Experimental Part

Materials: **NDI 1** (Laboratory intern synthesis), **DPP 1** (Laboratory intern resynthesis), PEDOT:PSS (Heraeus, Clevios O VO Ak 4083), PDINO (Laboratory intern resynthesis), **PBDB-T** (1-Material Inc.; M_w = 50000-100000 kg mol^{-1}), **PCE-10** (1-Material Inc.; M_w = 125000 kg mol^{-1}), **PM6** (Brilliant Matters, $M_w \geq$ 70000 kg mol^{-1}), **PC$_{61}$BM** (Solenne), **PC$_{71}$BM** (Solenne), **ITIC-4F** (Ossila), Zinc-acetate dihydrate (Sigma Aldrich), Ethanolamine (TCI), Methylglycole (Sigma Aldrich), MoO_3 (Abcr), BCP (Sigma Aldrich), **DTDCPB** (received from Prof. Dr. Ken-Tsung Wong), **DCV5T-Me** (received from Prof. Dr. Peter Bäuerle), **C$_{60}$** (CreaPhys), **C$_{70}$** (CreaPhys).

Organic Thin-Film Transistors were fabricated by cleaning the substrates with toluene, acetone and isopropanol followed by an UV/ozone treatment for 5 min. OTES-wafers were obtained using thermally grown SiO_2 (100 nm) on Si (SIEGERT WAFER), which were treated with an OTES-monolayer according to Ito *et al.*[76] TPA-wafers were received from Hagen Klauk (MPI Stuttgart) in the architecture Si|SiO_2 (100 nm)|AlO_x (3.6 nm)|TPA with a specific capacitance of C_i = 32.4 nF cm^{-2}. Afterwards, the substrates were placed with in vacuum chamber and the organic layer (d = 30 nm, r = 0.06 Å s^{-1}, ω_{rot} = 0 rpm, $p < 10^{-6}$ mbar) and gold (d = 30 nm, r = 0.3 Å s^{-1}, ω_{rot} = 0 rpm, $p < 10^{-6}$ mbar) were sequentially evaporated on top of the substrates. The organic and the gold layer were deposited through

different shadow masks, which lead to desired electrode configuration with a channel length (L) of 100 µm and a channel width (W) of 200 µm. The transfer characteristics were measured with a drain-source voltage (V_{DS}) of +50 V.

Organic Solar Cells were prepared by cleaning ITO-glass substrates (Soluxx GmbH) by sonication in acetone (1×15 min), detergent solution (mucasol®; 1×15 min), deionized water (3×10 min) and isopropanol (1×15 min). After an UV/ozone cleaning treatment for 30 min the ITO-glass substrates were covered with polymer (First Contact™ Polymer) to avoid contamination by particles. After applying the polymer coating, the substrates were dried overnight under ambient conditions.

Conventional solution-processed OSCs:

PEDOT:PSS layers were fabricated by allowing the PEDOT:PSS suspension (Heraeus Clevios™) warm up to room temperature followed by ultrasonication for at least 20 min at 30 °C. The PEDOT:PSS suspension is drawn up with a syringe and then added directly to the substrate through a syringe filter (0.45 µm). The spin-coating is performed using 6-7 drops (until the whole substrate is covered with PEDOT:PSS) followed by starting the spin-coating process (2500 rpm, 60 s, 4000 rpm s^{-1}). Afterwards, the substrates were annealed at 150 °C on a precision heat stage in the flow box for 15 min. The substrates were transferred into a nitrogen-filled glovebox (MBraun Inertgas-Systeme GmbH, UNIlad Pro, $c(O_2)$ < 1 ppm, $c(H_2O)$ < 1 ppm).

Active Layer: After weighing the respective donor and acceptor quantities under ambient conditions, the respective vials were transferred into the glovebox in which also the polymer:fullerene blend solutions were prepared. **PBDB-T**-based BHJ layers were fabricated by solubilizing **$PC_{61}BM$** in anhydrous chlorobenzene (10 mg mL^{-1}; Sigma Aldrich) while stirring at 30 °C for 3 h. This fullerene solution was added to the **PBDB-T** in 1:1 ratio (total concentration 20 mg mL^{-1}) and stirred overnight at 90 °C. The blend solution was spin-coated (80 µL, 1000 rpm, 60 s, 3 s from 0 to 1000 rpm) on top of the PEDOT:PSS layer *via* static dispense technique. In the case of **PCE-10:$PC_{71}BM$** layer, the blend solution was prepared analogue to **PBDB-T**:**$PC_{61}BM$** except of a 1:1.5 (D:A) ratio with a total concentration of 25 mg mL^{-1}, which was stirred at 30 °C overnight. For the **PCE-10:$PC_{71}BM$** blend, it

is necessary to add 3 % diiodoctane as spin-coating additive approx. 30 min before the spin-coating process to the respective solution.

For a PDINO ETL, PDINO was synthesized as shown in the literature[72] and dissolved in anhydrous methanol (1 mg mL^{-1}; Sigma Aldrich) by stirring for 10 min. The filtered PDINO solution (0.22 µm) was spin-coated on top of the **PCE-10:PC_{71}BM** layer *via* dynamic dispense technique (3-4 drops, 3000 rpm, 30 s) under inert conditions. In all cases, Al was used as top electrode, which was deposited in the OPTIvap-XL (d = 100 nm, r = 1-2 Å s^{-1}, $p < 10^{-6}$ mbar) *via* a shadow-mask to obtain seven individual operating solar cells with an area of 7.1 mm^2.[59,77] In the case of the **PBDB-T**:**PC_{61}BM** based OSCs, an additional thermal annealing step for 5 min at 150 °C was performed.

Inverted solution-processed OSCs:

ZnO-layers were fabricated on top of precleaned ITO-glass substrates by spin-coating a colloidal ZnO solution. This solution is prepared by dissolving zinc acetate dihydrate (400 mg, Sigma-Aldrich) in anhydrous methoxy glycol (4 mL, Sigma-Aldrich) under addition of ethanolamine (115 µL, Carl-Roth) followed by stirred (1000 rpm) overnight at room temperature.[73] The filtered colloidal ZnO suspension (0.45 µm) was spin-coated (2500 rpm, 30 s, 3000 rpm s^{-1}) on top of the ITO-glass substrates and annealed for 1 h at 200 °C in air on a precision heat plate in a flow box. Notably, better layer qualities are obtained by using syringes with a lower total volume like 3 or 5 mL.

The **PCE-10**:**PC_{71}BM** layer was prepared as for the conventional BHJ device architecture. For the non-fullerene **PM6**:**ITIC-4F** combination the acceptor was dissolved in chlorobenzene (10 mg mL^{-1}) by stirring 3 h at 60 °C. This solution was added to the polymer in 1:1 ratio to obtain a blend solution with an overall concentration of 20 mg mL^{-1}, which was stirred overnight at 60 °C. 30 min before the spin-coating 1% diiodoctane was added. Both blend solutions were spin-coated *via* static dispense technique (80 µL, 1000 rpm, 60 s, 3 s from 0 to 1000 rpm) and transferred into the OPTIvap-XL.

The HTL MoO_3 was deposited (Q3, d = 10 nm, r = 0.1 Å s^{-1}, ω_{rot} = 10 rpm, $p < 10^{-6}$ mbar) followed by Al (d = 100 nm, r = 1-2 Å s^{-1}, $p < 10^{-6}$ mbar) without

breaking the vacuum to obtain seven individual operating OSCs with an area of 7.1 mm^2.

Conventional vacuum-processed bulk-heterojunction OSCs:

These OSCs were fabricated by placing precleaned ITO substrates into the OPTIvap-XL. Afterwards MoO_3 is sublimated on top as hole-transporting layer (d = 6 nm, r = 0.1 Å s^{-1}, ω_{rot} = 10 rpm, p < 10^{-6} mbar) followed by a bulk-heterojunction layer, which is deposited by co-sublimation of the respective donor material and the fullerene derivative (**DCV5T-Me:C_{60}**: d = 40 nm, r = 0.2 Å s^{-1}:0.1 Å s^{-1}, ω_{rot} = 10 rpm, p < 10^{-6} mbar, $T_{Substrate}$ = 90 °C; **DTDCPB:C_{70}** = d = 80 nm, r = 0.1 Å s^{-1}:0.2 Å s^{-1}, ω_{rot} = 10 rpm, p < 10^{-6} mbar, $T_{Substrate}$ = 20 °C). After an additional cool down step (for **DCV5T-Me**-based OPVs), bathocuprione (BCP; d = 10 nm, r = 0.1 Å s^{-1}, ω_{rot} = 10 rpm, p < 10^{-6} mbar) was used as electron-transporting layer followed by Al (d = 100 nm, r = 1-2 Å s^{-1}, p < 10^{-6} mbar) as electrode material.

Conventional vacuum-processed planar-heterojunction OSCs:

Fullerene-free PHJ devices were fabricated by applying a PEDOT:PSS layer on top of the ITO-substrate analogue to the fabrication of conventional solution-processed OSCs. Afterwards, the substrates were placed in the evaporation device OPTIvap-XL, where **α-6T** (d = 60 nm, r = 0.2 Å s^{-1}, ω_{rot} = 10 rpm, p < 10^{-6} mbar, $T_{Substrate}$ = 20 °C) and **SubPc** (d = 60 nm, r = 0.2 Å s^{-1}, ω_{rot} = 10 rpm, p < 10^{-6} mbar, $T_{Substrate}$ = 20 °C) were deposited on top of the PEDOT:PSS layer. Afterwards, the OSCs were completed by thermal evaporation of BCP (d = 10 nm, r = 0.1 Å s^{-1}, ω_{rot} = 10 rpm, p < 10^{-6} mbar) and Al (d = 100 nm, r = 1-2 Å s^{-1}, p < 10^{-6} mbar).

Measurements and Characterization: *I-V* characteristics of OTFTs were measured on a Cascade EPS150 probe station using an Agilent 4055C parameter analyzer. All thin-film UV-Vis absorption spectra were recorded either on a Jasco V770 or on a Perkin-Elmer Lambda 950 spectrometer equipped with an integration sphere. OPV *J-V* characteristics were measured using a parameter analyzer (Botest Systems GmbH) combined with a AM1.5 G Oriel Sol3ATM class AAA solar simulator (Newport®) which was calibrated with a standard silicon solar cell with a KG filter (ISE Freiburg). The respective EQE spectra were recorded using a Quantum

Efficiency/IPCE Measurement Kit (Newport®) by using a 300 W Xe lamp combined with a Cornerstone monochromator. The measurement was recorded either using a SR810 Lock-In Amplifier or a Merlin Lock-In amplifier. AFM morphologies were investigated with a NT-MDT Next Solver System combined with SCOUT 350 RAI silicon cantilever (Nu Nano Ltd; spring constant = 42 N m^{-1}, resonance frequency = 350 kHz) in semi-contact mode.

3.6.2 OTFT Output Characteristics

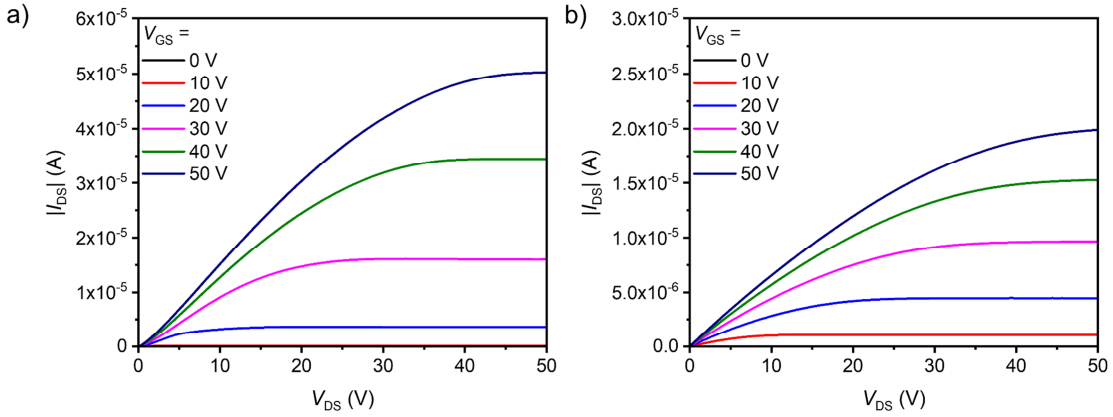

Figure 21: Output characteristics of OTFTs based on **NDI 1** (a) and on **DPP 1** (b).

Chapter IV: Screening of New Materials

The following chapter describes the search of new acceptor materials for vacuum- as well as solution-processed OSCs. Due to the vast number of investigated compounds, only the respective PCE values as well as the key parameter leading to the observed performances are discussed. For vacuum-processed OSCs, the characteristic data are shown in Table 12, while the data for solution-processed OSCs are listed in Table 13 at the end of this chapter.

4.1 Screening of Vacuum-Processable Materials

The screening procedure for new NFAs for vacuum sublimation was performed in two steps, which are visualized in Figure 22**.** The first step is an initial sublimation test in a Boc Edwards AUTO306 evaporation device. In this device only small material amounts of approximately 3 mg for 30 nm thick layers are needed for initial tests. Out of these 3 mg, five different OTFT devices can be generated by using a set of partially modified wafer substrates like Si|SiO_2, Si|SiO_2|OTES, Si|SiO_2|HMDS, Si|SiO_2|AlO_x|FOPA and Si|SiO_2|AlO_x|TPA. Furthermore, a quartz substrate is used for a thin-film solid-state UV-Vis absorption spectra (and additional spectroscopic measurements) as well as an ITO|ZnO or an ITO|MoO_3 substrate for potential acceptor or donor molecules, respectively. These ITO|TL-substrates can be further completed to obtain fully operating OSCs to gain a first insight for the potential of a

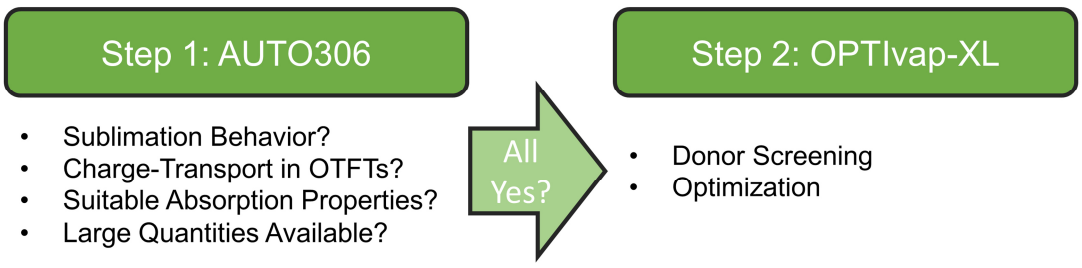

Figure 22: Schematic diagram of the two steps for screening of vacuum-processable materials.

new candidate. With this first step, a new compound can be material-savingly characterized towards its spectroscopic (UV-Vis measurement), morphologic (AFM measurement), energetic (*I-V* measurement: n- or p-type) and charge-transport properties (*I-V* measurement: $\mu_{e/h}$). After identifying a potential NFA candidate for OSCs, it is necessary to find a suitable counterpart using the new evaporation device OPTIvap-XL, which allow for inert processing and characterization. Here, donor materials are separately used in PHJ architecture to identify a suitable donor-acceptor combination for optimization. For this screening procedure the architecture was fixed (ITO|MoO_3|Donor|Acceptor|Bathocuproine (BCP)|Al). The search of a suitable donor is the most material and time consuming step towards the identification and optimization of a new vacuum-processed NFA material. In our laboratory, several donor materials are available, which differ in their optical and their energetics i.e. **α-6T**, **CuPc**, **DCV5T-Me**, **DTDCPB** and several merocyanine dyes (Figure 23). These materials must match the acceptor not only in terms of electronic and optical properties, but also in terms of morphological properties. In addition, it is known that the respective previous vacuum-deposited layer (e.g. donor)

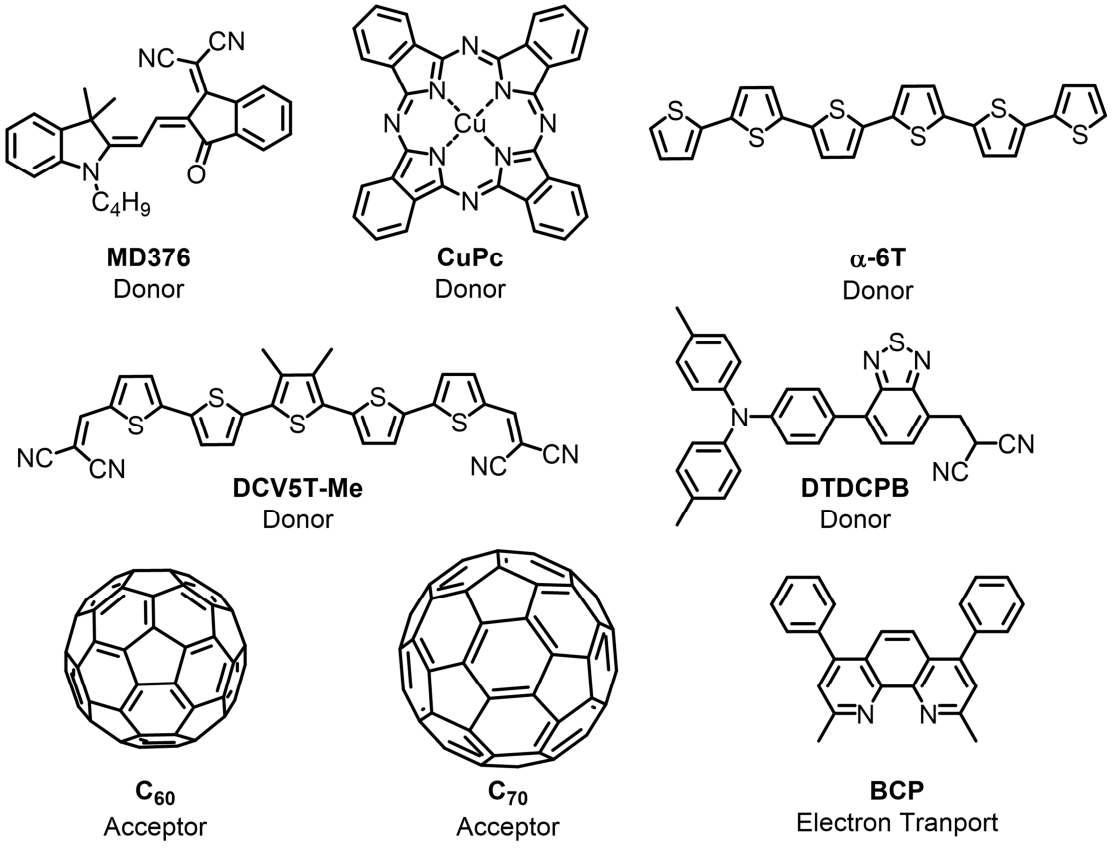

Figure 23: Chemical structures of donor materials and interlayer materials, which were used for the screening procedure of vacuum-sublimable compounds.

influences the growth of the subsequent layer (e.g. acceptor). Therefore, several donors must be tried for the most promising acceptor candidates.

In order to better classify the results from the material screening, the most important literature on vacuum-processable NFAs will be summarized beforehand (Figure 24 and Table 10). In the respective reports, only few examples for vacuum-processable NFAs are known until now. The first reported OSC made by Tang *et al.* is based on copper-(II)-phthalocyanine and a perylenetetracarboxylic bisbenzimidazole (**PTCBI**), which led to an efficiency of about 1%.[30] Since then, several material classes were investigated towards their use in vacuum-processed OSCs. As already mentioned before, the highest efficiency for a vacuum-processed single-junction NFA-based OSC was obtained by Cnops *et al*. by using a subnaphthalocyanine (**SubNc**) derivative in a single-junction OSC, which afforded an impressive efficiency of 6.0%.[61] In a cascade OSC in combination with **SubPc**, they were additionally able to achieve efficiencies up to 8.4%. Other promising routes led to efficiencies of up to 2.4% for ADA-based acceptors (**DCV3T** and **EBB**)

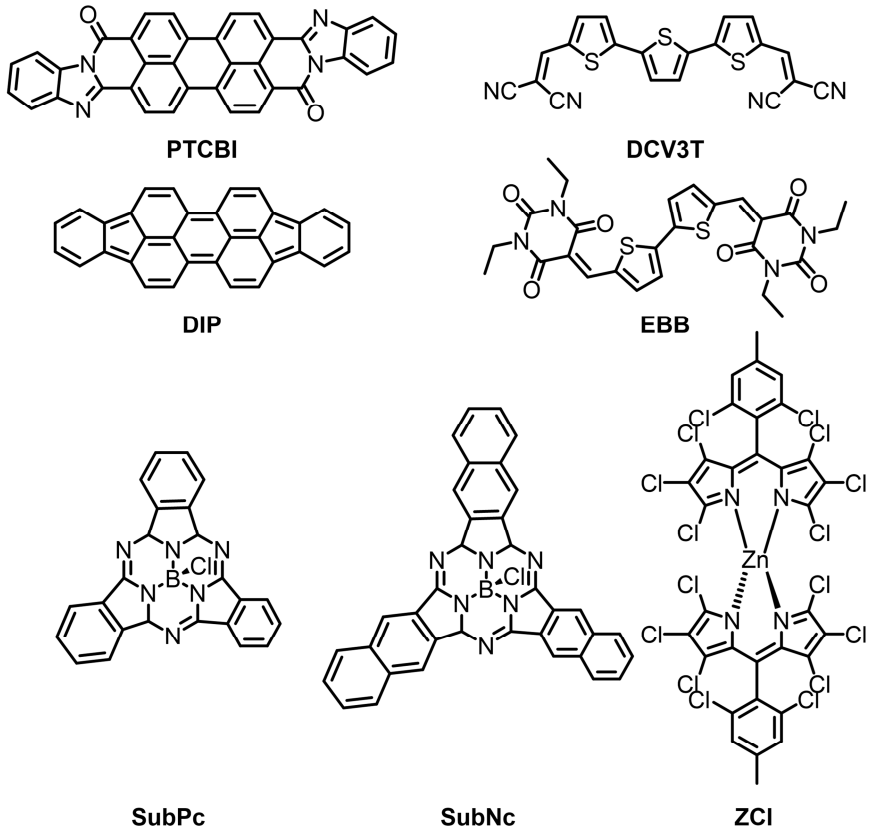

Figure 24: Molecular structures of the mentioned literature-known materials for vacuum-processed fullerene-free OSCs.

Table 10: Photovoltaic properties reported in literature for devices based on NFAs shown in **Figure 24**.

Donor	Acceptor	J_{SC} (mA cm^{-2})	V_{OC} (V)	FF (%)	PCE (%)	Ref.
CuPc	**PTCBI**	−2.3	0.45	65	1.0	[30]
α-6T	**DIP**	−1.4	1.22	57	1.8	[28]
4P-TPD	**DCV3T**	−5.1	0.71	40	1.6	[78]
SubPc	**EBB**	−3.8	1.24	50	2.4	[79]
α-6T	**SubPc**	−7.5	1.09	58	4.7	[61]
α-6T	**SubNc**	−12.0	0.94	54	6.0	[61]
DBP	**ZCl**	−2.4	1.33	42	1.4	[81]

[78-80], 1.8% for PAH-based molecules (**DIP**)[28] and of up to 1.4% for metal complexes (**ZCl**)[81] in combination with the respective donor molecules.

4.1.1 ADA-type Chromophores

The first set of ADA-type molecules were designed by using a cyclopentadithiophene (CPDT) central donor core combined with dicyanomethylene (**1**), indandione (**2**) and dicyanomethyleneindanone (**3**) moieties as acceptor units, which are depicted in Figure 25. Various derivatives of these materials were synthesized by introducing different groups like *n*-octyl (**a**), 2-ethyl-hexyl (**b**), *n*-propyl (**c**), phenyl (**d**) and methyl (**e**) at the central CPDT carbon atom. The molecules **2b** and **3b** were already reported before by our group.[82]

The initial vacuum sublimation for **1a-e**[83] could be performed successfully, which led to OTFTs with an n-type mobility in the range of 10^{-5} to 10^{-2} cm^2 V^{-1} s^{-1}. To get insights into the photovoltaic behavior of these materials, a donor screening for the octyl-substituted **1a** was performed, due to its best n-type semiconductance, using **MD376**, **35** and **2a** (Figure 23 and Figure 30). The decision for these donors were made, due to their low-lying HOMO levels, which should enable high V_{OC} values. High FFs of up to 50% and efficiencies of up to 0.64% were obtained in PHJ architectures, in combination with merocyanine **MD376** as donor material. The other derivatives showed significant lower efficiencies in OSC devices of 0.11% (**1b**), 0.05% (**1c**) and 0.10% (**1d**), while for **1e** it was not possible to obtain an operating device.

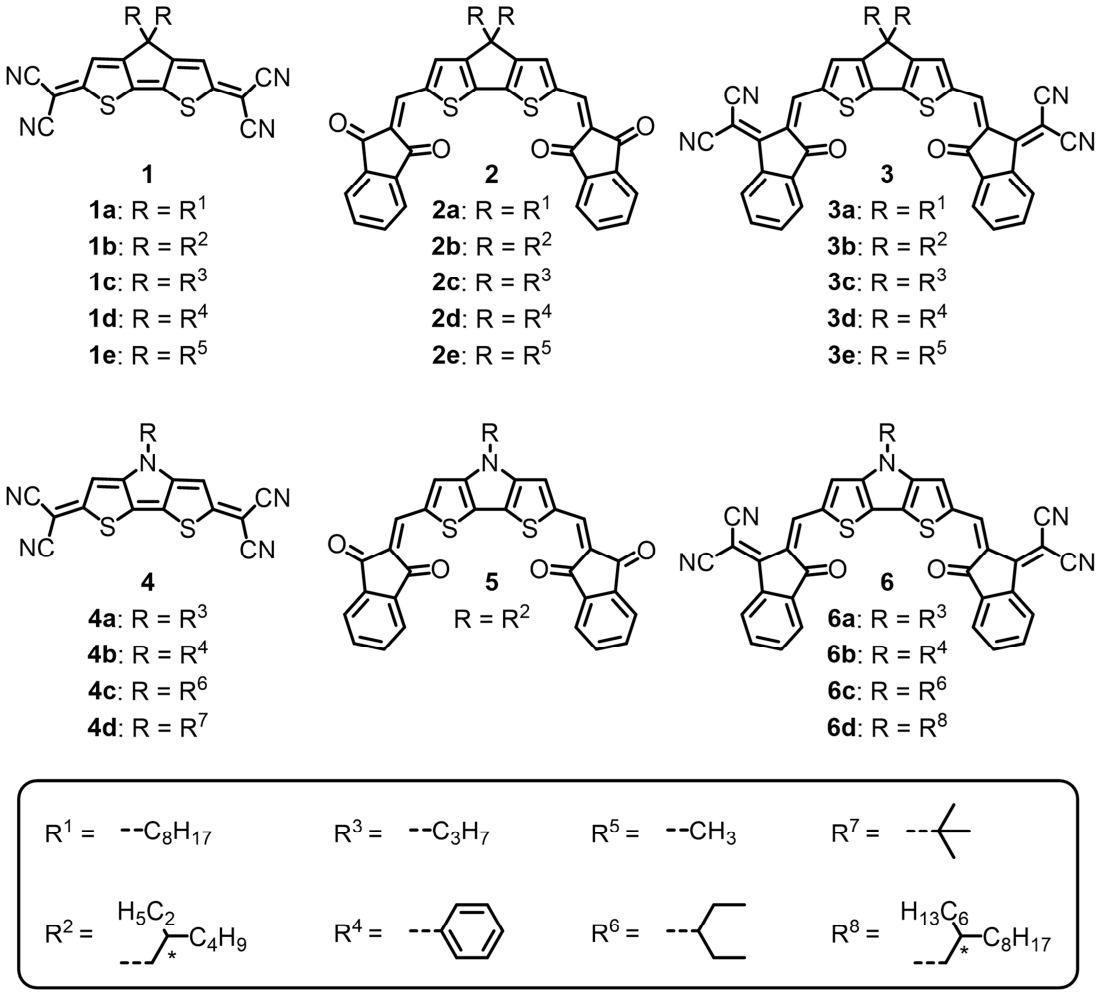

Figure 25: Chemical structures for ADA-type materials based on a cyclopentadithiophene or a dithienopyrrole core as donor unit combined with dicyanomethylene (**1**, **4**), indandione (**2**, **5**) or dicyanomethyleneindanone (**3**, **6**) moieties as acceptor units. Chiral centers are marked with *. In all cases racemic starting materials were used.

Approaches towards a BHJ failed. A detailed investigation of these materials can be found in **Chapter V**.

All materials based on the indandione-containing chromophore **2** showed p-type semiconductance in OTFT experiments. Vacuum-processed OTFTs of derivatives of **2** were already described in the literature.[84] Therefore, they were investigated as new donor molecules in OSCs in combination with **C_{70}**. Due to the relatively high V_{OC} values ranging from 0.90 V up to 1.12 V, good PCEs of 1.18% (**2a**), 1.26% (**2d**) and 1.80% (**2e**) could be realized in PHJ architectures. Additionally, to fullerene-based OPVs **2b** and **2c** were used as donor materials for NFA-based OPVs in combination with **3b** and **3d**, respectively. Here, only marginal PCEs of 0.02% (**2b**|**3b**) and 0.17% (**2c**|**3d**) were obtained, which can be traced back to a poor FF and to a low J_{SC}. Besides the use as donor molecule, the methyl-substituted **2e** was used as NFA in

Literature-unknown materials were synthesized by Dr. Pengzhong Chen (**2**,**3**) and Dr. Kevin Bold (**4**,**6**).

combination with the electron-rich donor molecule **α-6T** as well, where an PCE of 1.08% was observed. This originates from a good J_{SC} value of −2.71 mA cm^{-2} in combination with a FF of 53%. The low V_{OC} value of 0.64 V seems to limit the efficiency.

The largest CPDT-based materials **3a-e** with their dicyanomethyleneindanone endgroups exhibited appreciable high n-type semiconductance from 10^{-3} to 10^{-2} cm^2 V^{-1} s^{-1} in OTFTs. Derivatives of **3** in solution-processed OPV studies were already reported in the respective literature.[84,85] However, in our OPV experiments, only PCEs of 0.02% (**3a** and **3b**), 0.10% (**3c**), 0.21% (**3d**) and 0.79% (**3e**) were obtained in the PHJ architecture in combination with a donor molecule. These low PCEs originate from low V_{OC} values and therefore from too low LUMO levels of these materials. Therefore, for the **3e-**based device the high-performance donor molecule **DCV5T-Me** with its significant lower HOMO level was used as well, leading to higher efficiencies of up to 0.79% compared with the other **3**-based devices.

Additionally to the vacuum-processed devices, **1a**, **3a** and **3b** were implemented as acceptor molecules in solution-processed inverted BHJ OSCs in combination with the high-performance donor polymer **PM6** due to their higher solubility in organic solvent compared to other derivatives. These devices exhibit PCEs of 0.86%, 0.22% and 0.91% for **1a**, **3a** and **3b** in BHJ architecture, respectively.

Analogue to the ADAs based on the cyclopentadithiophene core, similar molecules based on the dithienopyrrole (DTP) core (**4-6**) were synthesized. While chromophore **4** was already described by Pappenfuss *et al*. in 2008,[86] **5** and **6d** were reported by our group in 2016.[82] For derivatives of **4** *n*-propyl (**4a**), phenyl (**4b**), *iso*-pentyl (**4c**) or *tert.*-butyl (**4d**) were introduced at the central nitrogen atom, while **6** was decorated with *n*-propyl (**6a**), phenyl (**6b**), *iso*-pentyl (**6c**) or 2-hexyl-decyl (**6d**) substituents. In the case of **5** only a 2-ethyl-hexyl derivative was available in our laboratory.

Analogue to **1a-e**, the quinoidal materials **4a-d** exhibited n-type charge-transport behavior with mobilities of about 10^{-3} cm^2 V^{-1} s^{-1} in OTFTs. Due to insufficient material amounts only the *iso*-pentyl substituted **4c** was tested in OPV devices in

combination with merocyanine **35** as donor, where an efficiency of 0.27% was obtained, similar to the derivatives based on **1**. Again, a low J_{SC} value of −1.32 mA cm^{-2} and low FF of 36% seem to limit the device's performance.

Due to its p-type semiconductance **5** was used as a donor material in fully vacuum-processed devices in combination with **C_{70}**, which afforded an efficiency of 2.43% in the PHJ architecture. In an initial test for BHJ architectures (1:1) an increased efficiency of up to 3.65% was obtained. Further optimization could not be performed due to low material quantities.

The dicyanomethyleneindanone-endcapped dithienopyrroles **6a-d** exhibited appreciable high n-type charge-transport mobilities of up to 10^{-2} cm^2 V^{-1} s^{-1} in OTFTs. In vacuum-processed OSCs efficiencies of 0.41% (**35**|**6a**), 0.19% (**CuPc**|**6b**) and 0.32% (**α-6T**|**6c**) with good FFs up to 55% were obtained. The low efficiencies originate either from a reduced V_{OC} or from an insufficient J_{SC} values. Due to its solubilizing chains, **6d** was tested as NFA in solution-processed OPVs in combination with the donor polymer **PCE-10**, as well. Here, a PCE of 1.50% was observed.

Based on the dicyanomethyleneindanone moiety, molecules **7**-**13** (Figure 26) were synthesized by combining the acceptor unit with several known bis-aldehyde donor units like phenyl (**7**), dimethoxyphenyl (**8**), furan (**9**), thiophene (**10**), bithiophene (**11**), benzodithiophene (**12**) and a thiophene-functionalized DPP (**13**). Due to their poor solubility, these materials were initially tested in vacuum-processed OSCs after thermal gradient sublimation in combination with **α-6T** as donor material.

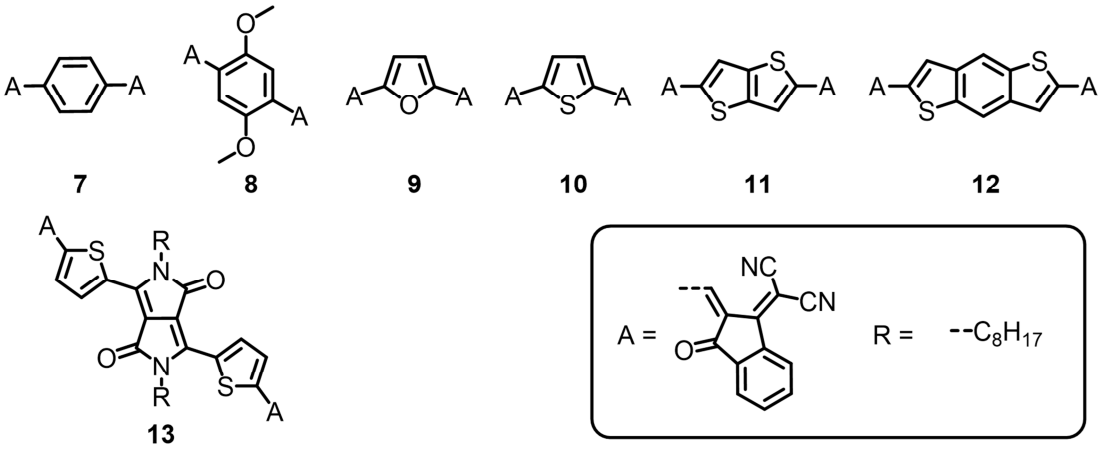

Figure 26: Chemical structures of additional dicyanomethyleneindanone-functionalized ADA-type materials.

Literature-unknown materials were synthesized by Julius Albert (**7-12**) and Dr. Rodger Rausch (**13**). For **7-12**, the crude material was directly used for device experiments without further characterization.

Chromophore **13** was already described in the literature as an OTFT material.[87] While **7** and **9** could not be sufficiently purified *via* thermal gradient sublimation, **13** was not sublimable at all and decomposed. In contrast to these materials, **8**, **10**, **11** and **12** are well sublimable. However only **8** and **11** showed a n-type semiconductance of 10^{-5} cm^2 V^{-1} s^{-1} in OTFT devices. All OPV devices based on **8**, **10**, and **12** in combination with **α-6T** as donor material in PHJ architecture were non-operational.

Chromophores **14-17** (Figure 27) exhibit different donor core units like cyclopentadithiophene (**14**), dithienopyrrole (**15**), dithienyl thienothiadiazole (**16**) or boron dipyrromethene (**17**) in combination with accepting dicyanovinyl groups. **14** and **15b**, which are based on the CPDT and DTP core were already described by Yassin *et al.* as potential donor materials in vacuum-deposited PHJ OSCs.[88] **14** bears a *n*-octyl chain, **15a** exhibits a 2-ethyl-hexyl group while **15b** owns a *n*-propyl chain. All three materials are sublimable. **14** showed n-type semiconductance of 10^{-5} cm^2 V^{-1} s^{-1} in OTFTs, while no OPVs could be fabricated due to low available amounts. **15a** and **15b**, which were provided by Prof. Dr. Peter Bäuerle, led appreciable PHJ OSC efficiencies of 0.99% and 0.56% in combination **α-6T** as donor molecule. The relatively high PCE of the **15a|α-6T** heterojunction originates from a good J_{SC} value of −3.40 mA cm^{-2}. Analogue to these molecules, **16** and **17** also show an ADA-type structure with dicya novinyl groups. **16**, which was also provided by

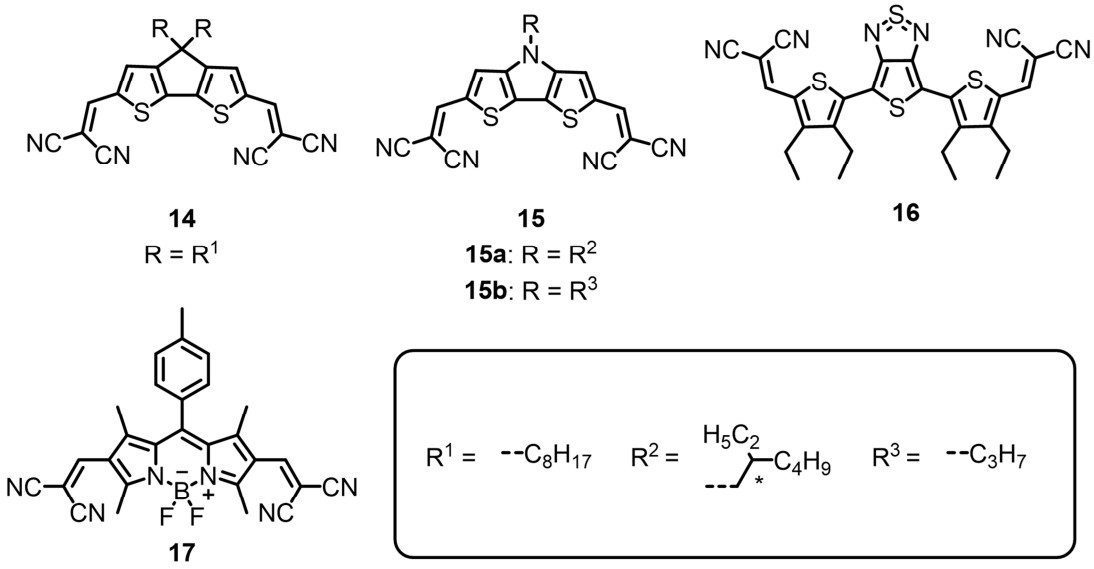

Figure 27: Chemical structures of addtional dicyanovinyl-functionalized ADA-type materials. Chiral centers are marked with *. In all cases racemic starting materials were used.

Literature-unknown materials were synthesized by the laboratory of Prof. Dr. Peter Bäuerle, (**15**, **16**) and Dr. Santosh Panchal (**17**).

Prof. Dr. Peter Bäuerle, showed an OPV performance of 0.32% in combination with **α-6T**. For **17** the sublimation was possible, but no OTFT performance was observed.

To summarize, these strong absorbing ADAs exhibit good sublimation properties in combination with promising n-type semiconductance in OTFTs, but they tend to afford very low V_{OC} values in PHJ OSCs, which limit their efficiency. This could be improved with suitable donors. Furthermore, although acceptable FF could be observed for some derivatives, these OSCs are then limited by low photocurrents. The best-performing NFA-based device was based on a combination of **α-6T** and **2e** in PHJ architecture, leading to an efficiency of up to 1.08%.

4.1.2 Boron-doped Polycyclic Aromatic Hydrocarbons

All boron-doped PAHs **18**-**23** were synthesized by Carina Mützel and coworkers (Figure 28).[89,90,91,92] With the exception of the hydroxy-containing material **18**[90] all molecules are well sublimable, while **18** is probably prone to condensation upon heating. Out of these materials, only the larger molecules **21** and **23** exhibited charge-transport behavior. While the mesitylene-substituted material **21** showed n-type charge transport in OTFTs with mobilities up to 10^{-3} cm^2 V^{-1} s^{-1}, the annulated **23**[92] exhibited an ambipolar behavior with mobilities of 10^{-1} (p) and 10^{-3} cm^2 V^{-1} s^{-1} (n) on TPA-modified substrates. Unfortunately, only for **21** the material quantities were high enough for OSC experiments. In proof-of-principle solution-processed OSCs a PCE of 3.10% in combination with the donor polymer **PCE-10** was obtained.[91] For vacuum-processed OPV, a donor screening was performed using **CuPc** (0.02%), **DCV5T-Me** (non-operational), **DTDCPB** (0.22%) and **α-6T** (0.77%) in PHJ architecture. The good efficiency in combination with **α-6T**

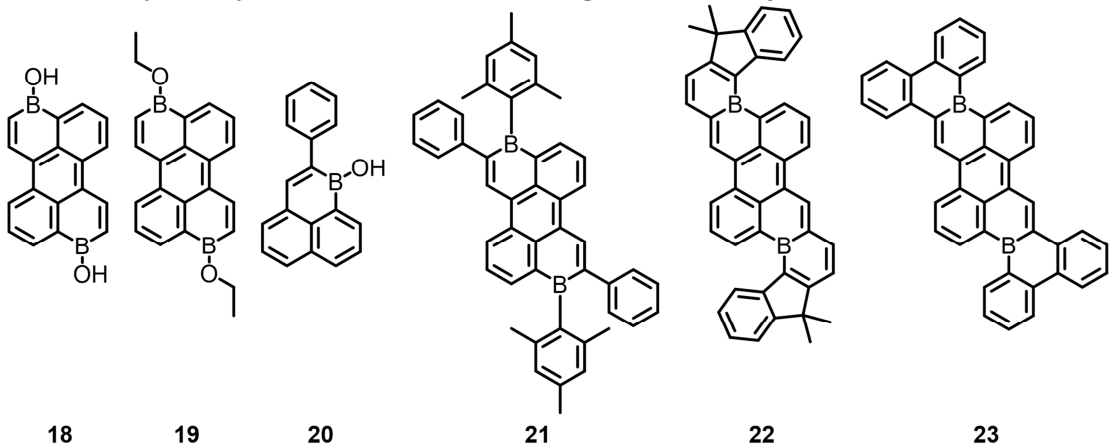

Figure 28: Chemical structures of boron-doped PAHs.

Literature-unknown materials were synthesized by Carina Mützel (**19**, **22**).

originated from a good FF of 50% in combination with a J_{SC} value of −2.10 mA cm^{-2} and a V_{OC} of 0.72 V. Inspired by the PHJ, a BHJ device of **21** in combination with **α-6T** was fabricated. Unfortunately, a decreased efficiency of only 0.11% compared with the 0.77% of the PHJ device, was obtained. Additionally, to the use of **21** as acceptor material, its performance as a donor material in combination with fullerene **C_{70}** was tested, too. In a PHJ architecture an efficiency of 0.69% was obtained, while again only 0.37% for the BHJ device could be realized.

4.1.3 PBI-based Chromophores

Bay-substituted perylene bisimide (PBI) dyes, which were used for vacuum sublimation are shown in Figure 29. All displayed materials were vacuum sublimable. The phenyl-bearing tetraarylated PBIs (**24**[93,94]) except of **24d** showed a n-type semiconductance of up to 10^{-3} cm^2 V^{-1} s^{-1} in OTFTs. In initial OSC studies, which were fabricated using **α-6T** as donor material in PHJ architecture, these materials showed efficiencies below 0.5%, which originated from low V_{OC} and low J_{SC} values. The most potent candidate was **24c** with its H-atom in imide-position, due to its FF of 54%, which indicated good charge-transport properties in its thin film. Therefore, **24c** was used as an electron-transport layer for vacuum-processed **α-6T:C_{70}**-based BHJ solar cells, which yielded PCEs of 3.34%. This efficiency was surprisingly good compared to the literature value of 2.4% for a conventional BHJ OSCs.[95] Unfortunately, these **24c**-based OSCs show heavy light-soaking effects limiting their use.[96] The naphthyl substitution in bay position as for **25** and **26** led only to lower mobilities and due to insufficient material quantities the photovoltaic performance could not be further tested. The most electron-poor chlorinated PBIs **27**[97] and **28**[98] did not show any solar cells performance in **α-6T**-based PHJ OSCs. Like the tetraarylated PBIs, the tetraphenoxy PBI **29a**[99] afforded only a low efficiency of 0.27%, which originates from a low J_{SC} value of −0.92 mA cm^{-2}. Surprisingly, it was possible for **29a** to turn a monomeric vacuum-sublimated film into its J-aggregate by washing with a mixture of chlorobenzene and diiodoctane (97:3).[100] This J-aggregate showed in the same device architecture a significantly increased V_{OC} from 0.68 V to 0.92 V but a slight reduction in J_{SC} yielding a PCE of 0.29%. The diphenylmethylene-bridged PBI **30** was used as an electron-

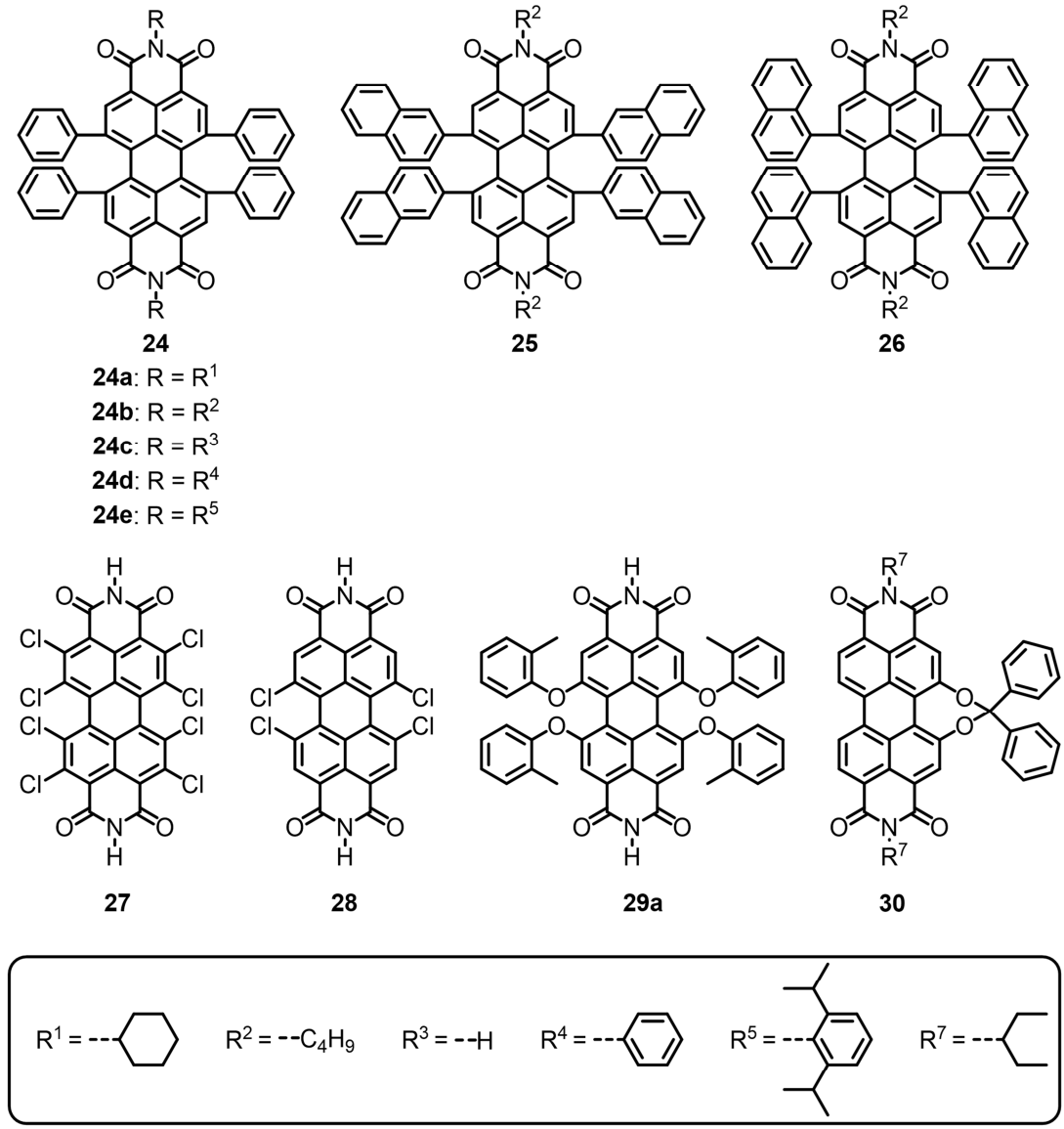

Figure 29: Chemical structures of PBI-based materials for vacuum processing. For molecules **24**-**26** racemic starting materials were used.

transporting layer in **α-6T**:**C$_{70}$**-based OSCs, which showed an efficiency of 1.98%. Like for **24c** heavy light-soaking effects were observed.

4.1.4 DA- and DAD-type materials

All following materials **31**-**37** are well sublimable (Figure 30). For **31**-**34** either the mobility in OTFT experiments (**33**[101] and **34**) or the material quantity (**31** and **32**) were too low for further OSC investigations. The merocyanines **35** and **36**[102] were directly tested in vacuum-processed OSCs. In PHJ architecture in combination with **α-6T** an efficiency of 0.04% for **35** and a significant higher efficiency of 0.56% for **36** were obtained. The squaraine-based DAD materials **37a** and **37b** were provided by Prof. Dr. Takeshi Maeda.[103] These materials are characterized by a rigidification

Literature-unknown materials were synthesized by Dr. Rebecca Renner (**24c**) and by Oliver Nagler (**30**).

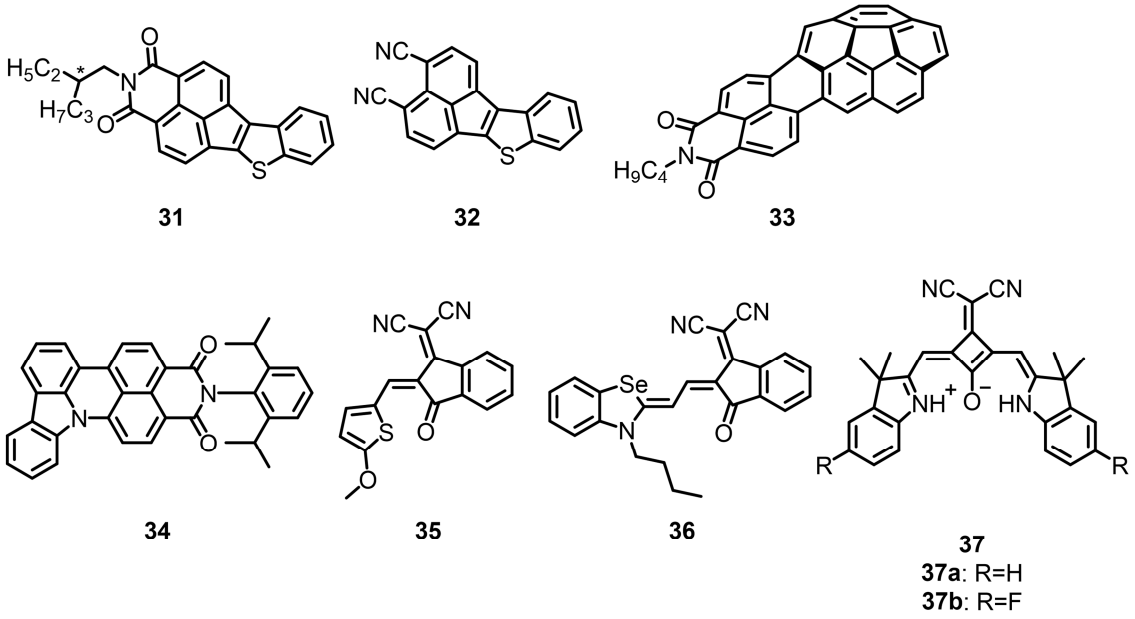

Figure 30: Chemical structures of addtional DA- and DAD-type materials. Chiral centers are marked with *. In all cases racemic starting materials were used.

of the π-system due to intramolecular hydrogen bonds. Due to their energetic levels, they were used as donor materials in PHJ and BHJ solar cells in combination with the fullerene **C_{70}**. In combination with **37a** an efficiency of 2.10% (PHJ) and 2.39% (BHJ) was achieved, while for the fluorinated analogue **37b** only 1.80% (BHJ) was obtained. The increased efficiency for **37a** can be traced back to an increased FF of 54%, instead of 38% for **37b**.

4.2 Screening for Solution-Processable Materials

For the screening of solution-processable materials three commercially available high-performance donor polymers were used, namely **PCE-10**, **PBDB-T** and **PM6** (Figure 31a). Combined with the inverted device architecture a new laboratory-intern screening method for new potential NFA candidates was established. With the three polymers the V_{OC} can be varied in about 0.1 V steps, which originates from these respective different HOMO levels for each polymer. This trend from **PCE-10** over **PBDB-T** up to **PM6** in V_{OC} should be observed in every NFA screening, which also serves as indicator for the functionality of a NFA candidate. Discrepancies from this trend could indicate morphological problems, due to phase separation, that would be indicative of poor reproducibility. An exemplary NFA screening-procedure of the well-established fullerene acceptor **$PC_{71}BM$** with the energetic diagram of all components and the respective *J-V* curve is shown Figure 31b and c. For the

Literature-unknown materials were synthesized by Dr. Magnus Mahl (**31**, **32**) and Dr. Xiaoqi Tian (**34**).

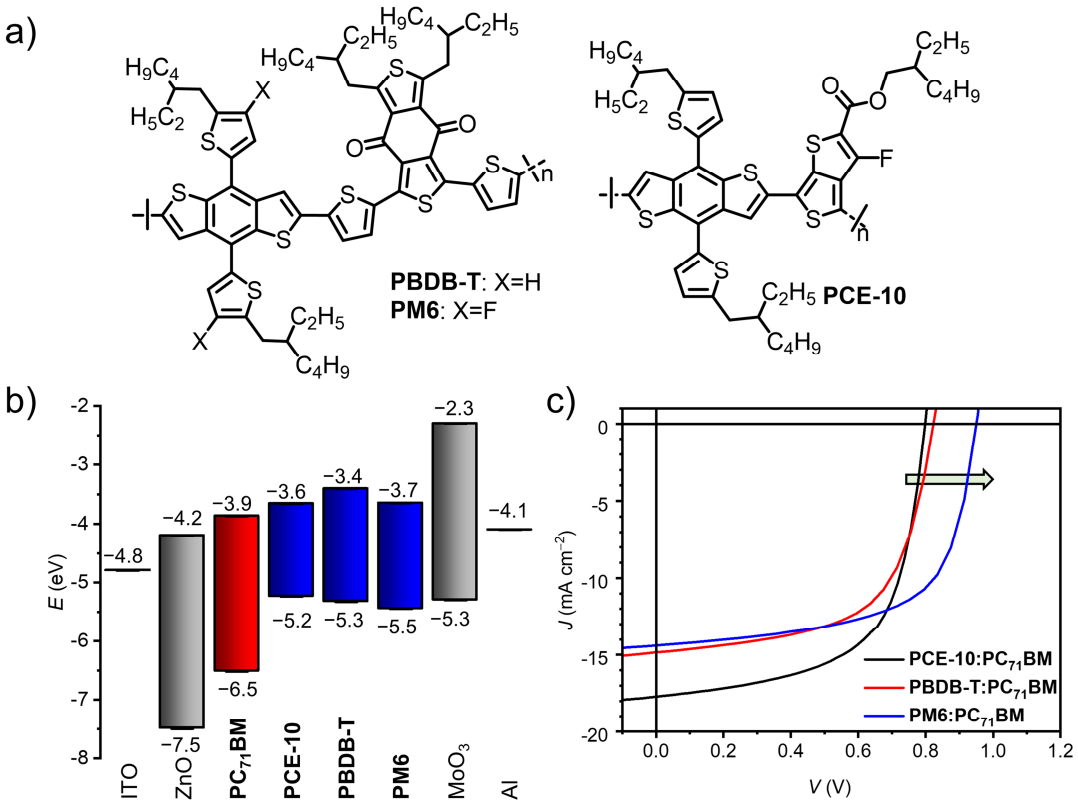

Figure 31: Chemical structures of donor polymer **PBDB-T**, **PM6** and **PCE-10** (a), Energetics of used materials (b) and *J-V* curves of OPVs in ITO|ZnO|BHJ|MoO_3|Al architecture based on **PCE-10** (black), **PBDB-T** (red) and **PM6** (blue) in combination with **$PC_{71}BM$** under AM1.5 G irradiation (c).

upcoming screening section of this thesis for new solution-processable NFA candidates exemplary the best material combination is shown in Table 13. To ensure that also materials with a lower solubility (< 10 mg mL^{-1}) could be investigated, a total concentration of 15 mg mL^{-1} for a 1:1 mixture of donor and acceptor was used for the initial spin-coating process, which occurs at 1000 rpm for 60s. For the initial screening, no additives or post treatment steps like thermal or solvent vapour annealing were performed.

This subchapter mainly focusses on the use of polycyclic aromatic dicarboximides (PADIs) for solution-processed OSCs. The most reported PADI for solution-processed OPVs in the literature are based on PBIs (Figure 32 and Table 11). Single PBIs without any chemical modification in ortho or bay position (**PBI-*i*Pent**) exhibit PCEs up to 3.7% in combination with a high-performance donor polymer.[104] Hernett *et al.* further investigated the substitution in ortho position (**PBI-3,7-DMO**), which lead to an similar efficiency of 3.6%.[105] Cai *et al.* and Mahlmeister *et al.* synthesized bay-substituted single PBIs (**TP-PBI**), which enabled efficiencies of up

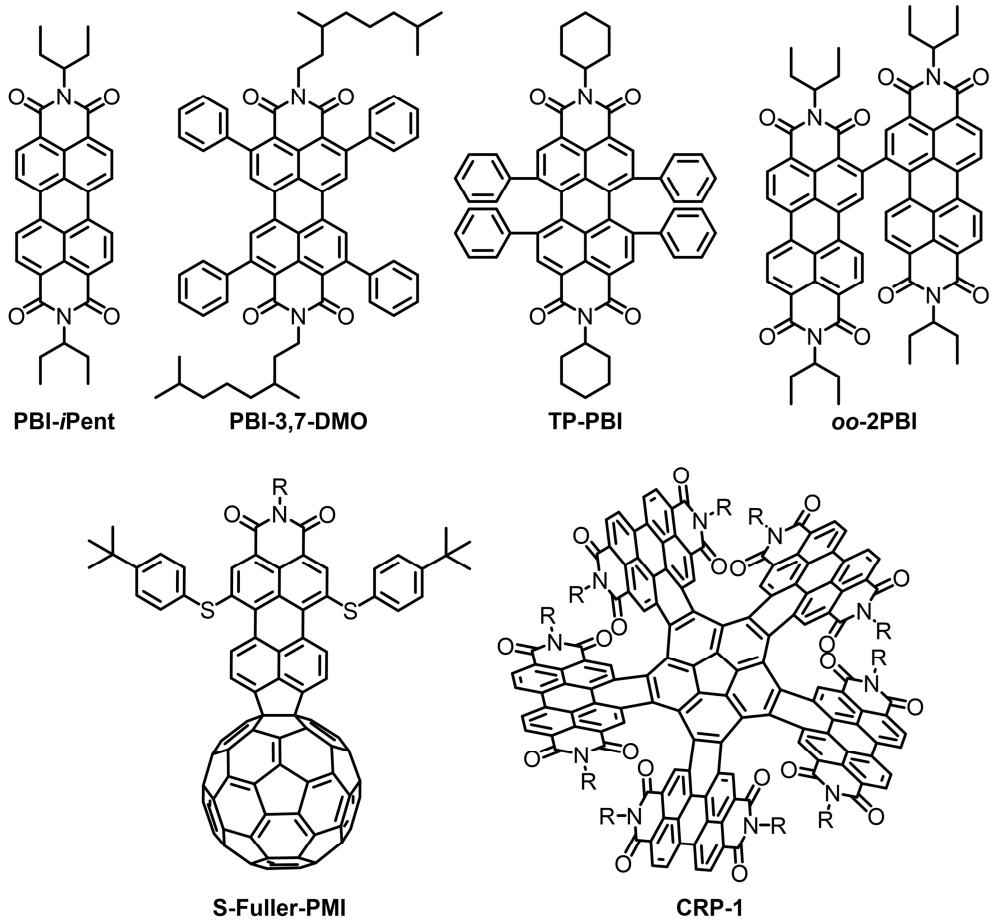

Figure 32: Molecular structures of the literature-known materials for solution-processed OSCs based on PADIs.

to 4.4% and 4.3%, respectively.[94,106] To further improve the efficiency, the next step was the extension of the π-surface by bridging or by fusing two PBI units (***oo*-2PBI**). With this approach, it was possible to improve the OSCs efficiencies up to 8.3%, as it was demonstrated by Wang *et al*. in 2017.[107] Recent research focusses on the fusion of several PBI units and/or the combination with different chromophores as it was shown by e.g. Meng *et al*. with their corannurylene pentapetalae (**CRP-1**),

Table 11: Photovoltaic properties reported in literature for devices based on NFAs shown in **Figure 32**.

Donor	Acceptor	J_{SC} (mA cm^{-2})	V_{OC} (V)	FF (%)	PCE (%)	Ref.
PBDTTT-CT	**PBI-iPent**	−8.1	0.80	52	3.6	[104]
PBDTT-FTTE	**PBI-3,7-DMO**	−9.2	0.81	48	3.6	[105]
PCE-10	**TP-PBI**	−9.7	0.87	46	4.1	[106]
PCE-10	***oo*-2PBI**	−18.6	0.80	55	8.1	[107]
PBDB-T	**S-Fuller-PMI**	−12.6	0.91	68	7.8	[109]
P3TEA	**CRP-1**	−15.5	1.06	67	11.0	[50]

which led to efficiencies of up to 11.1% or with their fullerylene derivative affording 7.8% (**S-Fuller-PMI**).[50,108,109]

4.2.1 Tetraphenoxy-substituted PBIs

Bay-substituted PBIs (**29a-g**) with an H-atom at imide position were substituted with different groups at the bay tetraphenoxy moiety (**29a**[99],**29g**[110]) and tested in BHJ architecture combined with the donor polymer **PBDB-T** (Figure 33). All of these solar cells exhibit modest FF in range of 30-40% and low J_{SC} and V_{OC} values, which led to low efficiencies of below 0.5%. Additional to these dyes, the commercially available 2,6-di-*iso*-propylphenyl imide substituted tetraphenoxy PBI (**38**) was tested in BHJ OSCs in combination with the donor polymer **PBDB-T**, too. This OSC showed a similar poor efficiency of only 0.24%, which can be traced back mainly to the low V_{OC} value of 0.26 V.

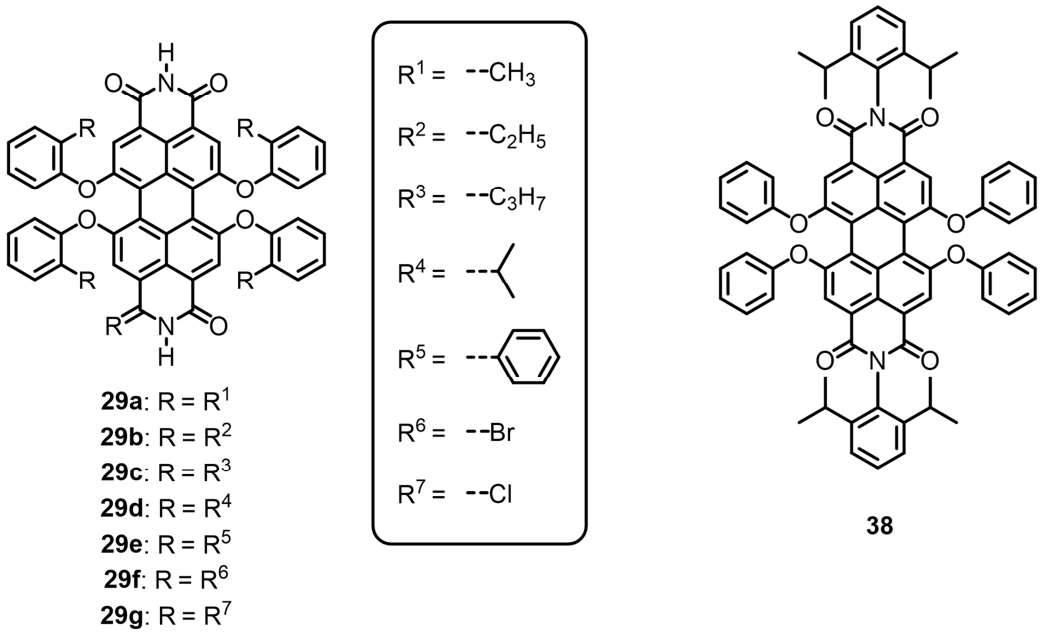

Figure 33: Chemical structures of tetraphenoxy-substituted PBIs for solution-processed OSCs.

4.2.2 Shielded Polycyclic Aromatic Dicarboximides

Shielded electron-poor polycyclic aromatic dicarboximides (PADIs) based on PBIs, terrylene diimides (TDI) and the nanographene tetraimides (NGTI) with different imide substituents, which were combined with the donor polymer **PM6** are shown in Figure 34. The shielding of the respective chromophore's π-core from the imide substituted should prevent over-aggregation and therefore too strong phase separation of these materials during spin-coating. Chemically, the shielding was

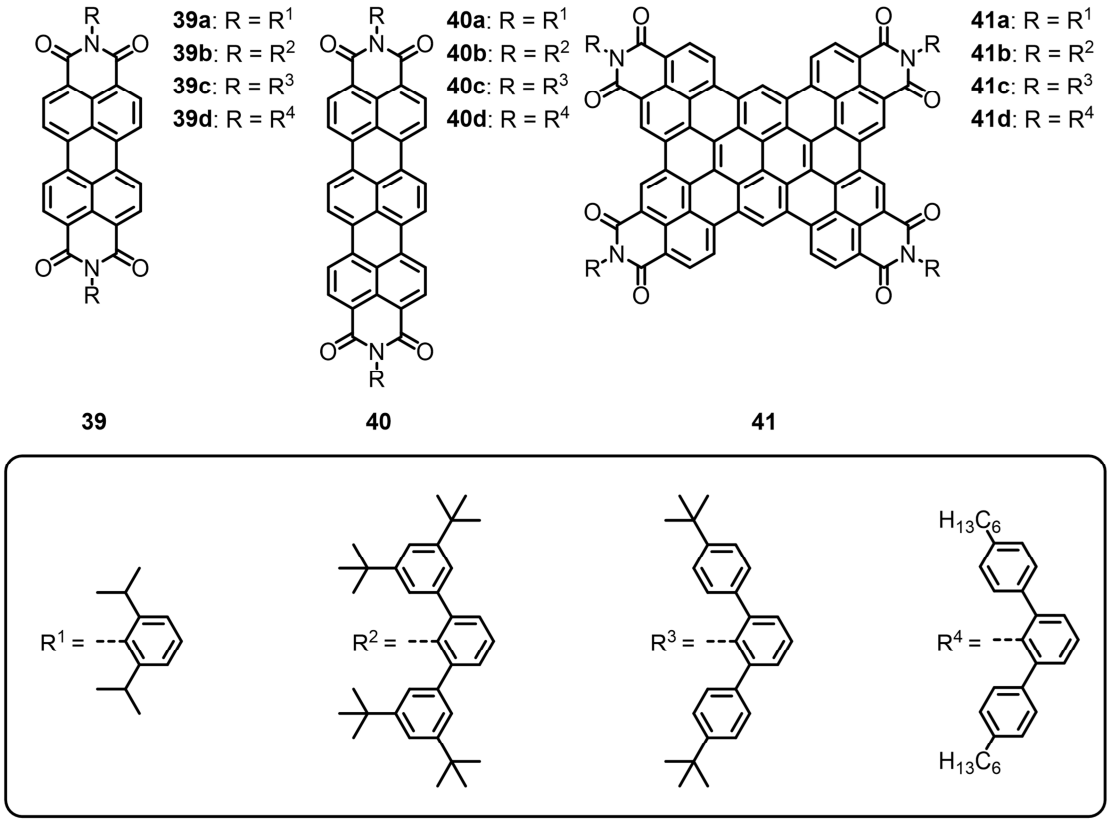

Figure 34: Chemical structures of imide-substituted PADIs.

performed by introducing bulky imide substituents like 2,6-di-*iso*-propylphenyl (DIPP) or a diphenylphenyl which was further decorated with *tert*. butyl or *n*-hexyl substituents. The various imide substitution should affect the solubility and enable the control of the shielding as well as the aggregation behavior. The PBIs **39b-d**[111,112] exhibit an efficiency of about 2.4%, which is close to the best literature values for single PBIs of around 3.7% as mentioned above. The efficiency of 2.4% can be traced back to an impressive V_{OC} over 1 V combined with medium FF of 30-40%. Only **39a** and showed a lower efficiency of 2.13%, due to decreased V_{OC} and J_{SC}, respectively. The OSCs based on TDIs **40a** and **40b** were not operating, due to insufficient film-formation properties. The at para-position substituted **40c** and **40d** showed better film-formation and efficiencies of 2.09% and 2.34% were obtained, respectively.[112,113] Compared with the PBIs, higher FFs of 40-45% but lower V_{OC} of about 0.95 V were observed. The NGTI **41a**[114] yielded non-operational devices to the same reasons as for the TDIs, while **41b**, **41c**[115] and **41d** led to operating OSCs. The highest efficiency was obtained for the hexyl-functionalized NGTI **41d** with a peak performance of 7.10%, followed by *tert*. butyl-containing derivatives **41c** and **41b** with efficiencies of 6.42% and 4.20%, respectively. The increased efficiency of

Literature-unknown materials were synthesized by Dr. Magnus Mahl (**41b**) and Julius Albert (**41d**).

41d compared with the other derivatives originated from an increased FF of up to 56% and from an increased J_{SC} of up to −10.79 mA cm^{-2}. The impressive efficiencies of over 7%, which were obtained even when shielding the respective π-surface through bulky imide substituents cannot be explained with the help of the classical doctrine in organic electronics, where π-π stacked aggregates are responsible for exciton- and charge transport. This result will be further elaborated and discussed in **Chapter VII**.

4.2.3 PBI- and Benzo[ghi]perylene trisimide-based Materials

As the bridging of PBIs often leads to higher PCEs as shown in der literature, in following, Bis-PBIs and their monomeric analogues as well as benzo[ghi]perylenes trisimides (BPTIs) are investigated (Figure 35). Single and Bis-PBIs **42** and **43**(*R*)[116] led in combination with **PBDB-T** to efficiencies of 0.67% and 2.91%, respectively. The main difference between these two devices was the remarkable higher J_{SC} value of −7.86 mA cm^{-2} for **43**(*R*) in comparison to the single PBI **42** with only −1.88 mA cm^{-2}. Similar BPTIs **44**[117] and **45**[117] feature analogue substitution as for **43**(*R*). **44**- and **45**-based OSCs yielded efficiencies of 0.87% and 1.62% in combination with **PM6**, respectively. Both BPTIs exhibit similar FFs of about 35%, but significantly changed V_{OC} and J_{SC} values, which had the most impact on the respective performance. **46** and **47** are both pyridine-bridged Bis-PBIs.[118] While the single-pyridine bridge containing **46** led to an efficiency of 2.52%, the double-pyridine bridged **47** did not show any photovoltaic performance, due to insufficient film-formation properties. The relatively high PCE for **46** originates from a high V_{OC} of 1.04 V in combination with a medium J_{SC} of −6.71 mA cm^{-2}. Only the low FF of 35% seems to limit the device's efficiency. The "exotic" NFA candidates **48** and **49** are based on a dihydroxy PBI, which are either connected to one silicon endgroup or interconnected by a boron bridge towards a PBI, respectively. In the case of **49** tetrabutylammonium was used as anion. The silicon-containing PBI **48** afforded a PCE of 1.23%, while a Bis-boron-containing PBI **49** afforded a PCE of only 0.68%. Both materials exhibited the same V_{OC} of about 0.7 V and FF of about 35% but significantly different J_{SC} values of −4.57 mA cm^{-2} for **48** and of −2.14 mA cm^{-2} for **49**. The here presented single and Bis-PBIs and Bis-BPTIs show good V_{OC} values in

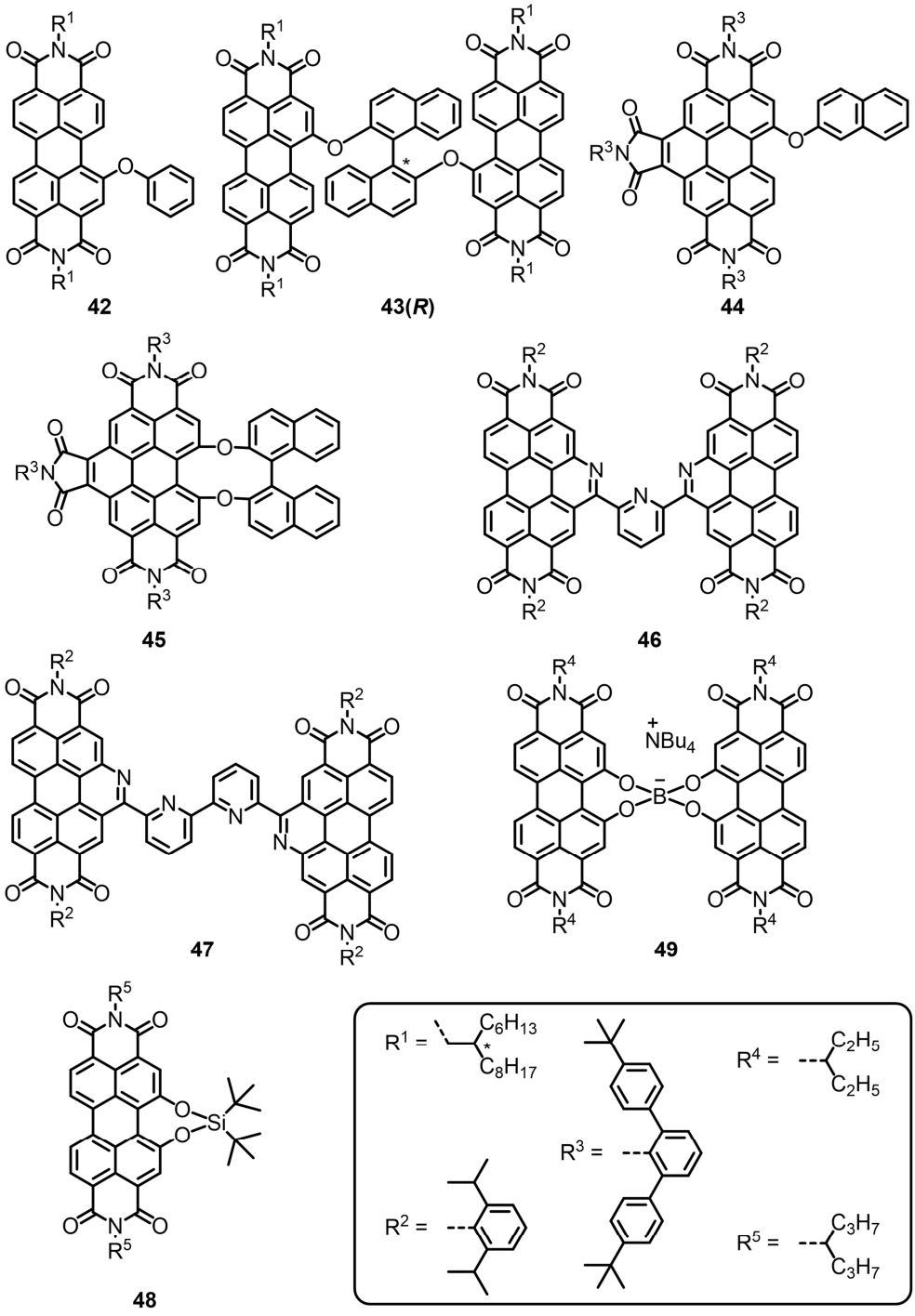

Figure 35: Chemical structures of single and bridged PBI- and BPTI-based materials. Chiral centers are marked with *. In case of **46** the *R* enantiomer was used.

solution processed OSCs. Unfortunately, low J_{SC} values and FFs limiting their efficiencies.

4.2.4 Miscellaneous Polycyclic Aromatic Dicarboximides

All remaining PADIs are shown in Figure 36. The fullerylene-based polycyclic aromatic dicarboximide **50** afforded an efficiency of 1.31% in combination with

Literature-unknown materials were synthesized by Oliver Nagler (**48**, **49**).

PCE-10. The mixture with **PM6** led to a lower efficiency of only 1.14%. Both OSCs exhibited good V_{OC} values of 0.87 V and 1.08 V, respectively, but unfortunately, low FFs below 30%, which limit the overall device efficiencies. A OSC based on a PADI with a central corannulene unit (**51**) achieved a PCE of 2.0% in combination with **PM6** and an efficiency of 2.1% with **PCE-10**.[119] The good efficiencies can be traced back to good J_{SC} value of up −6.71 mA cm^{-2} (+**PCE-10**) in combination with good V_{OC}

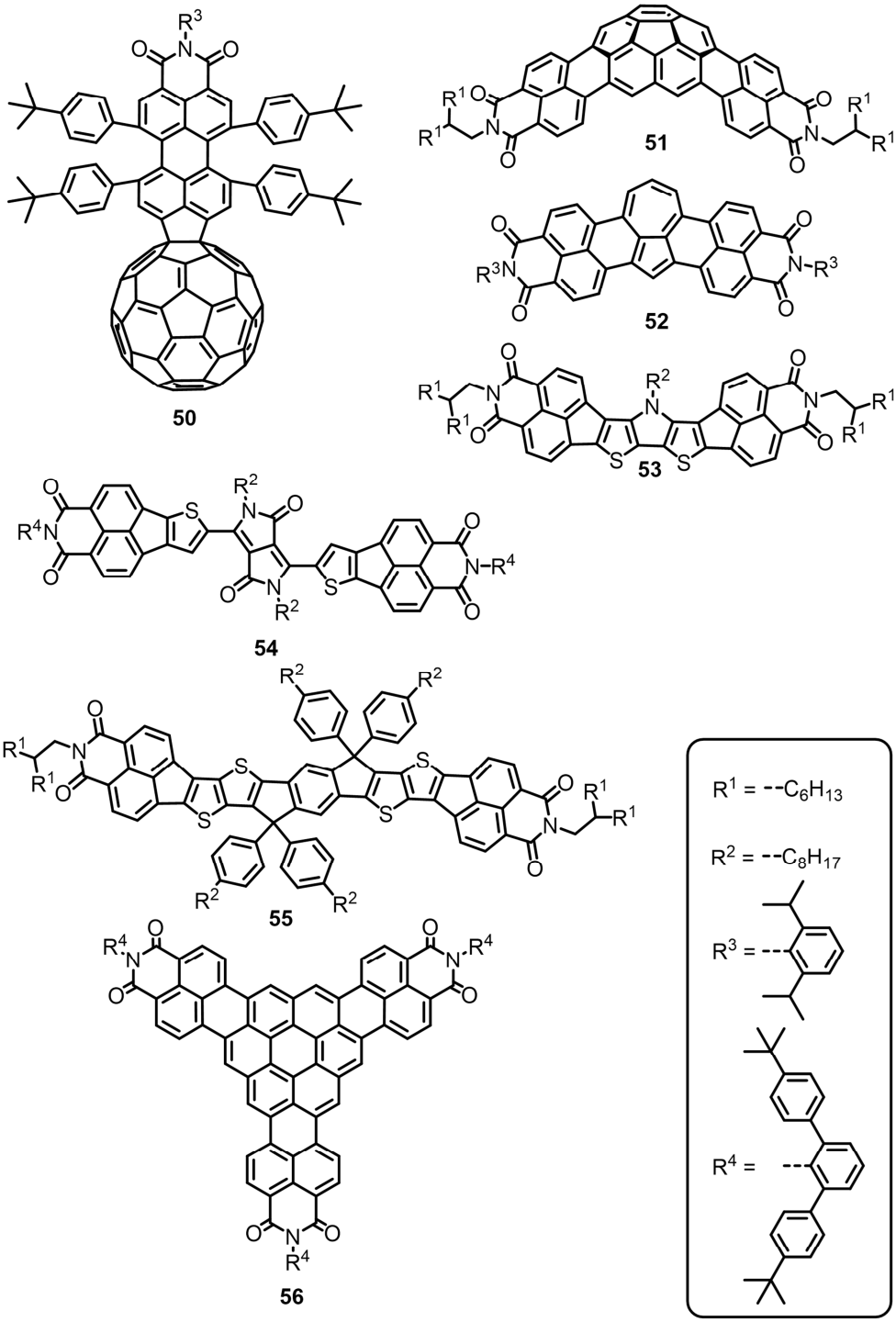

Figure 36: Chemical structures of additional PADIs.

Literature-unknown materials were synthesized by Bernhard Mahlmeister (**50**) and Dr. Magnus Mahl (**53**-**55**).

values of up to 1.02 V (+**PM6**). **55** is today the second best corannulene based molecular system as NFA in solution-processed OSCs. This acceptor was therefore further investigated as it is shown in **Chapter VI**. Analogue molecular structures based on PADIs, but with changed central donor units, led to lower efficiencies. The azulene-containing material **52**[120] was not operational in BHJ OSCs, while the DTP-based **53** containing devices afforded an efficiency of only 0.02%, which can be traced back to poor V_{OC} and FF. The DPP-based polycyclic aromatic dicarboximide (PADI) **54** and the indacenodithienothiophene containing **55** afforded low PCEs of 0.22% and 0.28%, respectively, in combination with **PCE-10**. In both cases the low PCEs originate from a low FF of about 30% and from low J_{SC} values. The triangle shaped naphthalimide-annulated coronene **56**[121] afforded an efficiency of 0.51% in combination with **PM6.** Like in the most cases of this class of dyes, low J_{SC} and FF are again limiting the PCE.

4.4 Conclusion

Within this chapter, new material screening testing routines were established for the search for new non-fullerene acceptors (NFAs) for solution- and vacuum-processed organic solar cells (OSCs). New candidates for vacuum-processing are first tested towards their sublimation behavior and their charge-transport properties in organic thin-film transistors (OTFTs), before initial trials in OSCs in combination with small molecule donors are conducted. For solution-processable materials, the screening was directly performed *via* the fabrication of inverted BHJ OSCs in combination with three donor polymers e.g. **PCE-10**, **PBDB-T** and **PM6**.

This chapter gave an overview on more than 90 molecules, which were tested in organic electronic devices with the aim to find suitable NFA candidates for OSCs. The achieved PCE values in dependence on the observed J_{SC} values, which is in most of the cases the bottleneck towards efficient devices, is illustrated in Figure 37. For vacuum-processed NFAs six material yielded efficiencies above 0.5%, while 18 materials exhibit an OTFT mobility of 10^{-3} cm^2 V^{-1} s^{-1} or higher. It is noticeable that among the vacuum-processed OSCs, most of the functional devices were each made in combination with **α-6T**. Therefore, it can be assumed that **α-6T** forms a good interface to many different acceptors. Nevertheless, its use is limited by its relatively high HOMO and LUMO levels. For solution-processed NFAs 14 materials achieved

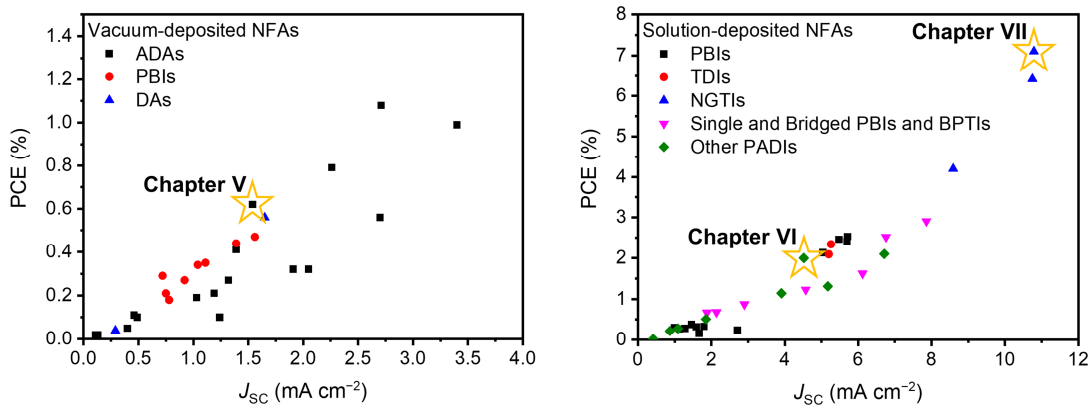

Figure 37: PCE-J_{SC} plot for vacuum-deposited (a) and solution-deposited (b) NFA based OSCs.

efficiencies above 2.0%. For many of the here presented NFA-based OSCs it was possible to achieve decent V_{OC} values and FFs reaching maximum values of 1.12 V and 57%, respectively. The main bottleneck towards efficient OSCs is the limitation of the J_{SC}, which originates presumably from large recombination rates. Generally, the vacuum-processed NFAs yielded efficiencies of up to 1.08%, while for solution-processed NFAs it was possible to achieve PCEs of up to 7.10%. However, four material classes stood out from the others due to morphological and opto-electronic factors and were therefore investigated in more detail.

Thus, the well-sublimable and strong absorbing small quinoidal cyclopentadithiophenes **1a-d** showed a high charge-carrier mobility of up to 10^{-2} cm^2 V^{-1} s^{-1} in OTFTs and an efficiency of up to 0.64% in OSCs for **1a** in combination with the small molecular donor **MD376**. These new materials were investigated towards their optoelectronic properties, which finally led to the results discussed in **Chapter V**.

Furthermore, the boron-doped polycyclic aromatic hydrocarbon **21** showed one of the highest charge-carrier mobilities for a boron-doped PAHs so far and was therefore tested in solution-processed OSCs, which yielded in an efficiency of up to 3.10% in combination with the donor polymer **PCE-10**. This proof-of-principle showed that boron-doped PAHs are suitable candidates for non-fullerene acceptors. This result was published by Farell *et. al* in 2020.[91] Unfortunately, it was not possible to exceed the efficiencies of this initial solution-processed OSCs by additional vacuum-processed devices.

The shielded perylene bisimides (PBIs) **39a-d** and nanographene tetraimides (NGTIs) **41a-d** showed OSC efficiencies of up to 2.5% for the PBIs and up to 7.1% for NGTIs, respectively. These remarkable high efficiencies are even more surprising when considering that the large imide substituents of these dyes should prevent intimate acceptor-acceptor interactions, which are deemed necessary for charge transport. To clarify this observation a systematic study of the optical, structural, and photovoltaic properties was conducted, which led to the results discussed in **Chapter VII**.

Furthermore, PADI **51** showed an efficiency of up to 2.1% in solution-processed BHJ solar cells. At this time, this was the highest reported efficiency of a corannulene-based NFA. Therefore **51** was further studied by self-assembly experiments and device optimization, which led to the results shown in **Chapter VI**.

All in all, new laboratory intern screening methods were established, yielding in a fast and material-savingly screening procedure of several different molecular structures. While various new and interesting material systems were found, it remains elusive to predict the OSC performance based on molecular properties.

4.5 Overview of Photovoltaic Properties

4.5.1 Materials studied in Vacuum-Processed Devices

Table 12: Overview of materials which were applied in vacuum-processed organic solar cells (* racemic starting materials, [a] purification not possible, [b] not sublimable, [c] deposited as monomer, [d] deposited as J-aggregate). Donors are marked in blue while acceptors are marked in red.

Material (Initial Name)	Ref.	OTFT		OPV							
		Substrate	μ ($cm^2\ V^{-1}\ s^{-1}$)	Process	Usage		Architecture	J_{SC} ($mA\ cm^{-2}$)	V_{OC} (V)	FF (%)	PCE^{Max} (%)
1a (**PC-1-Oc**)	[83]	TPA	10^{-2} (n)	V	A	PHJ	ITO|MoO_3|**MD376**|**1a**|BCP|Al	−1.54	0.86	47	0.62
				V	A	PHJ	ITO|MoO_3|**35**|**1a**|BCP|Al	−1.10	0.64	52	0.36
				V	A	PHJ	ITO|MoO_3|**2a**|**1a**|BCP|Al	−0.88	0.88	36	0.28
				S	A	BHJ	ITO|ZnO|**PM6**:**1a**|MoO_3|Al	−3.31	0.56	44	0.86
1b (**PC-1-Ethex**)*	[83]	TPA	10^{-4} (n)	V	A	PHJ	ITO|MoO_3|**MD376**|**1b**|BCP|Al	−0.46	0.88	27	0.11
1c (**PC-1-Pr**)	[83]	TPA	10^{-5} (n)	V	A	PHJ	ITO|MoO_3|**MD376**|**1c**|BCP|Al	−0.40	0.74	17	0.05
1d (**PC-1-Ph**)	[83]	TPA	10^{-5} (n)	V	A	PHJ	ITO|MoO_3|**2-Oc**|**1d**|BCP|Al	−0.49	0.91	22	0.10
1e (**PC-1-Me**)		TPA	10^{-4} (n)	V	A	PHJ	ITO|ZnO|**1e**|**CuPc**|MoO_3|Al	Non-operational			
2a (**PC-2-Oc**)	[82]	Bare	10^{-3} (p)	V	D	PHJ	ITO|MoO_3|**2a**|**C_{70}**|BCP|Al	−2.18	1.12	46	1.18
2b	[82]	-	-	V	D	PHJ	ITO|MoO_3|**2b**|**3b**|BCP|Al	−0.13	0.50	25	0.02
				S	D	BHJ	ITO|ZnO|**2b**:**1a**| MoO_3|Al	−0.75	0.70	33	0.18
2c (**PC-2-Pr**)	[82]	Bare	10^{-5} (p)	V	D	PHJ	ITO|MoO_3|**2c**|**3d**|BCP|Al	−0.72	0.74	27	0.17
2d (**PC-2-Ph**)	[82]	Bare	10^{-5} (p)	V	D	PHJ	ITO|MoO_3|**2d**|**C_{70}**|BCP|Al	−2.98	0.90	44	1.26
2e (**PC-2-Me**)	[82]	Non-operational		V	D	PHJ	ITO|MoO_3|**2e**|**C_{70}**|BCP|Al	−3.94	0.92	45	1.80
				V	A	PHJ	ITO|MoO_3|**α-6T**|**2e**|BCP|Al	−2.71	0.64	53	1.08
3a (**PC-3-Oc**)	[82]	TPA	10^{-3} (n)	V	A	PHJ	ITO|ZnO|**3a**|**2a**|MoO_3|Al	−0.11	0.56	31	0.02

Material (Initial Name)	Ref.	OTFT		OPV							
		Substrate	μ ($cm^2\ V^{-1}\ s^{-1}$)	Process	Usage		Architecture	J_{SC} ($mA\ cm^{-2}$)	V_{OC} (V)	FF (%)	PCE^{Max} (%)
				S	A	BHJ	ITO|ZnO|**PM6**:**3a**|MoO_3|Al	−1.43	0.37	41	0.22
3b	[82]	-	-	V	A	PHJ	ITO|MoO_3|**2b**|**3b**|BCP|Al	−0.13	0.50	25	0.02
				S	A	BHJ	ITO|ZnO|**PM6**:**3b**|MoO_3|Al	−2.27	0.79	45	0.91
3c (PC-3-Pr)	[82]	TPA	10^{-3} (n)	V	A	PHJ	ITO|ZnO|**3c**|**CuPc**|MoO_3|Al	−1.24	0.24	34	0.10
3d (PC-3-Ph)	[82]	TPA	10^{-2} (n)	V	A	PHJ	ITO|ZnO|**3d**|**CuPc**|MoO_3|Al	−1.19	0.23	51	0.21
3e (PC-3-Me)	[82]	TPA	10^{-3} (n)	V	A	PHJ	ITO|MoO_3|**DCV5T-Me**|**3e**|BCP|Al	−2.26	0.76	45	0.79
4a (KB-1-Pr)	[86]	TPA	10^{-3} (n)	-	-	-	-	-	-	-	-
4b (KB-1-Ph)	[86]	TPA	10^{-3} (n)	-	-	-	-	-	-	-	-
4c (KB-1-iPent)	[86]	TPA	10^{-3} (n)	V	A	PHJ	ITO|MoO_3|**35**|**4c**|BCP|Al	−1.32	0.56	36	0.27
4d (KB-1-Bu)	[86]	TPA	10^{-3} (n)	-	-	-	-	-	-	-	-
5 (FK03)	[82]	-	-	V	D	PHJ	ITO|MoO_3|**5**|**C_{70}**|BCP|Al	−5.26	0.77	58	2.43
				V	D	BHJ	ITO|MoO_3|**5**:**C_{70}**|BCP|Al	−7.04	1.08	45	3.65
6a (KB-3-Pr)	[82]	TPA	10^{-3} (n)	V	A	PHJ	ITO|MoO_3|**35**|**6a**|BCP|Al	−1.39	0.80	34	0.41
6b (KB-3-Ph)	[82]	TPA	10^{-4} (n)	V	A	PHJ	ITO|ZnO|**6b**|**CuPc**|MoO_3|Al	−1.03	0.34	50	0.19
6c (KB-3-Pent)	[82]	TPA	10^{-2} (n)	V	A	PHJ	ITO|MoO_3|**α-6T**|**6c**|BCP|Al	−1.91	0.32	50	0.32
6d*	[82]	-	-	S	A	BHJ	ITO|ZnO|**PCE-10**:**6d**|MoO_3|Al	−4.20	0.65	54	1.50
7[a]			-	-	-	-	-	-	-	-	-
8		TPA	10^{-3} (n)	V	A	PHJ	ITO|MoO_3|**α-6T**|**8**|BCP|Al	Non-operational			
9[a]			-	-	-	-	-	-	-	-	-
10		Non-operational		V	A	PHJ	ITO|MoO_3|**α-6T**|**9**|BCP|Al	Non-operational			

Material (Initial Name)	Ref.	OTFT		OPV							
		Substrate	μ ($cm^2\ V^{-1}\ s^{-1}$)	Process	Usage		Architecture	J_{SC} ($mA\ cm^{-2}$)	V_{OC} (V)	FF (%)	PCE^{Max} (%)
11		TPA	10^{-5} (n)	-	-	-	-	-	-	-	-
12		-	-	V	A	PHJ	ITO|MoO_3|**α-6T**|**12**|BCP|Al	Non-operational			
13 (RR242)[b]	[87]	-	-	-	-	-	-	-	-	-	-
14 (PC-19)	[88]	TPA	10^{-5} (n)	-	-	-	-	-	-	-	-
15a (DCV-DTP-Ethex)*	[88]	-	-	V	A	PHJ	ITO|MoO_3|**α-6T**|**15a**|BCP|Al	−3.40	0.60	44	0.99
15b (DCV-DTP-Pr)	[88]	-	-	V	A	PHJ	ITO|MoO_3|**α-6T**|**15b**|BCP|Al	−2.70	0.49	38	0.56
16 (TDA2T(Et)-DCV)		-	-	V	A	PHJ	ITO|MoO_3|**α-6T**|**16**|BCP|Al	−2.05	0.32	47	0.32
17 (SP-B-4)		Non-operational		-	-	-	-	-	-	-	-
18 (CM218)[a]	[90]	-	-	-	-	-	-	-	-	-	-
19 (CM236)		Non-operational		-	-	-	-	-	-	-	
20 (CM255)	[91]	Non-operational		-	-	-	-	-	-	-	
21 (CM064)	[91]	TPA	10^{-3} (n)	S	A	BHJ	ITO|ZnO|**PCE-10**:**21**|MoO_3|Al	−8.44	0.87	40	3.10
				V	A	PHJ	ITO|MoO_3|**CuPc**|**21**|BCP|Al	−0.07	0.60	31	0.02
				V	A	PHJ	ITO|MoO_3|**DCV5T-Me**|**21**|BCP|Al	Non-operational			
				V	A	PHJ	ITO|MoO_3|**DTDCPB**|**21**|BCP|Al	−0.74	1.04	22	0.22
				V	A	PHJ	ITO|MoO_3|**α-6T**|**21**|BCP|Al	−2.10	0.72	50	0.77
				V	A	BHJ	ITO|MoO_3|**α-6T**:**21**|BCP|Al	−0.51	0.64	32	0.11
				V	D	PHJ	ITO|MoO_3|**21**|**C_{70}**|BCP|Al	−2.64	0.72	36	0.69
				V	D	BHJ	ITO|MoO_3|**21**:**C_{70}**|BCP|Al	−1.42	1.04	23	0.37
22		Non-operational		S	A	BHJ	ITO|ZnO|**PCE-10**:**22**| MoO_3|Al	Non-operational			

Material (Initial Name)	Ref.	OTFT		OPV							
		Substrate	μ ($cm^2\ V^{-1}\ s^{-1}$)	Process	Usage		Architecture	J_{SC} ($mA\ cm^{-2}$)	V_{OC} (V)	FF (%)	PCE^{Max} (%)
23 (**CM200**)	[92]	TPA	10^{-3} (n)	-	-	-	-	-	-	-	-
		TPA	10^{-1} (p)	-	-	-	-	-	-	-	-
24a (**ReRe255**)*	[93,94]	TPA	10^{-4} (n)	V	A	PHJ	ITO|ZnO|**24a**|α-6T|MoO_3|Al	−1.39	0.76	42	0.44
24b (**ReRe173**)*	[93,94]	TPA	10^{-3} (n)	V	A	PHJ	ITO|ZnO|**24b**|α-6T|MoO_3|Al	−0.78	0.61	34	0.18
24c (**ReRe246**)*		TPA	10^{-3} (n)	V	A	PHJ	ITO|ZnO|**24c**|α-6T|MoO_3|Al	−0.75	0.52	54	0.21
				V	A	PHJ	ITO|MoO_3|α-6T|**24c**|BCP|Al	−1.56	0.56	52	0.47
				V	ETL[c]	BHJ	ITO|MoO_3|α-6T:C_{70}|**24c**|Al	−10.32	0.80	41	3.34
24d (**JA175**)*	[93,94]	Non-operational		V	A	PHJ	ITO|ZnO|**24d**|α-6T|MoO_3|Al	−1.11	0.67	42	0.35
24e (**ReRe307**)*	[93,94]	TPA	10^{-4} (n)	V	A	PHJ	ITO|ZnO|**24e**|α-6T|MoO_3|Al	−1.04	0.68	47	0.34
25 (**ReRe174**)*	[93,94]	Non-operational		-	-	-	-	-	-	-	
26 (**ReRe175**)*	[93,94]	TPA	10^{-5} (n)	-	-	-	-	-	-	-	-
27 (**BERPSE-60**)	[97]	-	-	V	A	PHJ	ITO|MoO_3|α-6T|**27**|BCP|Al	Non-operational			
28 (**Cl8-PTCDI**)	[98]	-	-	V	A	PHJ	ITO|MoO_3|α-6T|**28**|BCP|Al	Non-operational			
29a[c] (**JT03**)	[99]	-	-	V	A	PHJ	ITO|ZnO|**29-M**|α-6T|MoO_3|Al	−0.92	0.68	44	0.27
29a[d] (**JT03**)	[99]	-	-	V	A	PHJ	ITO|ZnO|**29-J**|α-6T|MoO_3|Al	−0.72	0.92	44	0.29
30 (**ON126**)		TPA	10^{-5} (n)	V	ETL[c]	BHJ	ITO|MoO_3|α-6T:C_{70}|**30**|Al	−8.52	0.61	32	1.98
31 (**MM482**)*		FOPA	10^{-3} (p)	-	-	-	-	-	-	-	-
32 (**MM430**)		FOPA	10^{-4} (p)	-	-	-	-	-	-	-	-
33 (**C32-Bu**)	[101]	TPA	10^{-4} (n)	-	-	-	-	-	-	-	-
34 (**XT-4c**)		Non-operational		-	-	-	-	-	-	-	

Material (Initial Name)	Ref.	OTFT		OPV							
		Substrate	μ ($cm^2\ V^{-1}\ s^{-1}$)	Process	Usage		Architecture	J_{SC} ($mA\ cm^{-2}$)	V_{OC} (V)	FF (%)	PCE^{Max} (%)
35 (**AAE060**)		-	-	V	A	PHJ	ITO|MoO_3|**α-6T**|**35**|BCP|Al	−0.29	0.25	28	0.04
36 (**AAE031**)	[102]	-	-	V	A	PHJ	ITO|MoO_3|**α-6T**|**36**|BCP|Al	−1.65	0.75	43	0.56
37a (**HA077**)	[103]	-	-	V	D	PHJ	ITO|MoO_3|**37a**|**C_{70}**|BCP|Al	−6.71	0.55	54	2.10
				V	D	BHJ	ITO|MoO_3|**37a**:**C_{70}**|BCP|Al	−7.74	0.72	41	2.39
37b (**TS10701**)	[103]	-	-	V	D	BHJ	ITO|MoO_3|**37b**:**C_{70}**|BCP|Al	−6.69	0.71	38	1.80

4.5.2 Materials studied in Solution-Processed Devices

Table 13: Overview of materials for the application in solution-processed organic solar cells (* racemic starting materials). Donors are marked in blue while acceptors are marked in red. For those materials (**39a-d**, **41a-d** and **51**) which are further described in the upcoming chapters the optimized parameters are given and the screening PCE^{Max} is given in brackets.

Material (Initial Name)	Ref.	Process	Usage		Architecture	J_{SC} (mA cm^{-2})	V_{OC} (V)	FF (%)	PCE^{Max} (%)
29a	[99]	S	A	BHJ	ITO|ZnO|**PBDB-T**:**29a**|MoO_3|Al	−1.28	0.60	37	0.28
29b	[110]	S	A	BHJ	ITO|ZnO|**PBDB-T**:**29b**|MoO_3|Al	−1.13	0.64	38	0.27
29c	[110]	S	A	BHJ	ITO|ZnO|**PBDB-T**:**29c**|MoO_3|Al	−0.99	0.76	40	0.30
29d	[110]	S	A	BHJ	ITO|ZnO|**PBDB-T**:**29d**|MoO_3|Al	−1.46	0.68	38	0.38
29e	[110]	S	A	BHJ	ITO|ZnO|**PBDB-T**:**29e**|MoO_3|Al	−1.59	0.52	39	0.32
29f	[110]	S	A	BHJ	ITO|ZnO|**PBDB-T**:**29f**|MoO_3|Al	−1.67	0.32	30	0.16
29g	[110]	S	A	BHJ	ITO|ZnO|**PBDB-T**:**29g**|MoO_3|Al	−1.80	0.52	35	0.33
38		S	A	BHJ	ITO|ZnO|**PBDB-T**:**38**|MoO_3|Al	−2.71	0.26	28	0.24
39a		S	A	BHJ	ITO|ZnO|**PM6**:**39a**|MoO_3|Al	−5.04	0.95	40	2.13(1.68)
39b (**SiSo-1c**)	[111]	S	A	BHJ	ITO|ZnO|**PM6**:**39b**|MoO_3|Al	−5.71	1.09	38	2.53(1.71)
39c (**SiSo-1b**)	[111]	S	A	BHJ	ITO|ZnO|**PM6**:**39c**|MoO_3|Al	−5.48	1.02	37	2.46(1.55)
39d (**SiSo-1d**)	[112]	S	A	BHJ	ITO|ZnO|**PM6**:**39d**|MoO_3|Al	−5.70	1.03	37	2.41
40a (**SiSo-2a**)	[113]	S	A	BHJ	ITO|ZnO|**PM6**:**40a**|MoO_3|Al		Non-operational		
40b (**SiSo-2c**)	[112]	S	A	BHJ	ITO|ZnO|**PM6**:**40b**|MoO_3|Al		Non-operational		
40c (**SiSo-2b**)	[112]	S	A	BHJ	ITO|ZnO|**PM6**:**40c**|MoO_3|Al	−5.20	0.95	41	2.09
40d (**SiSo-2d**)	[112]	S	A	BHJ	ITO|ZnO|**PM6**:**40d**|MoO_3|Al	−5.26	0.96	44	2.34
41a (**SS197**)	[114]	S	A	BHJ	ITO|ZnO|**PM6**:**41a**|MoO_3|Al		Non-operational		
41b (**MM420**)		S	A	BHJ	ITO|ZnO|**PM6**:**41b**|MoO_3|Al	−8.59	1.08	44	4.20(3.44)

Material (Initial Name)	Ref.	Process	Usage		Architecture	J_{SC} (mA cm^{-2})	V_{OC} (V)	FF (%)	PCE^{Max} (%)
41c (**MM421**)	[115]	S	A	BHJ	ITO|ZnO|**PM6**:**41c**|MoO_3|Al	−10.75	1.02	54	6.42 (3.74)
41d (**JA343**)		S	A	BHJ	ITO|ZnO|**PM6**:**41d**|MoO_3|Al	−10.79	1.04	56	7.10(6.99)
42	[116]	S	A	BHJ	ITO|ZnO|**PBDB-T**:**42**|MoO_3|Al	−1.88	0.96	32	0.67
43(R)	[116]	S	A	BHJ	ITO|ZnO|**PBDB-T**:**43**|MoO_3|Al	−7.86	0.84	42	2.91
44 (**BT-127b**)	[117]	S	A	BHJ	ITO|ZnO|**PM6**:**44**|MoO_3|Al	−2.90	0.87	34	0.87
45 (**BT_MJL_30H**)	[117]	S	A	BHJ	ITO|ZnO|**PM6**:**45**|MoO_3|Al	−6.12	0.70	36	1.62
46 (**MS69**)	[118]	S	A	BHJ	ITO|ZnO|**PM6**:**46**|MoO_3|Al	−6.76	1.04	35	2.52
47 (**MS70**)	[118]	S	A	BHJ	ITO|ZnO|**PM6**:**47**|MoO_3|Al		Non-operational		
48 (**ON99**)		S	A	BHJ	ITO|ZnO|**PCE-10**:**48**|MoO_3|Al	−4.57	0.72	35	1.23
49 (**ON57**)		S	A	BHJ	ITO|ZnO|**PM6**:**49**|MoO_3|Al	−2.14	0.73	36	0.68
50 (**BM65**)		S	A	BHJ	ITO|ZnO|**PCE-10**:**50**|MoO_3|Al	−5.17	0.87	29	1.31
					ITO|ZnO|**PM6**:**50**|MoO_3|Al	−3.91	1.08	27	1.14
51 (**C44-C6**)	[119]	S	A	BHJ	ITO|ZnO|**PM6**:**51**|MoO_3|Al	−4.52	1.02	40	2.0
					ITO|ZnO|**PCE-10**:**51**|MoO_3|Al	−6.71	0.82	36	2.1(1.5)
52 (**BPW-199**)	[120]	S	A	BHJ	ITO|ZnO|**PBDB-T**:**52**|MoO_3|Al		Non-operational		
53 (**MM419**)		S	A	BHJ	ITO|ZnO|**PCE-10**:**53**|MoO_3|Al	−0.41	0.17	32	0.02
54 (**MM287**)		S	A	BHJ	ITO|ZnO|**PCE-10**:**54**|MoO_3|Al	−0.87	0.74	30	0.22
55 (**MM327**)		S	A	BHJ	ITO|ZnO|**PCE-10**:**55**|MoO_3|Al	−1.09	0.75	32	0.28
56 (**BPW286**)	[121]	S	A	BHJ	ITO|ZnO|**PM6**:**56**|MoO_3|Al	−1.85	0.8	34	0.51

Chapter V: Quinoidal Dicyanomethylene-Endcapped Cyclopentadithiophenes as Vacuum-processable n-type Semiconductors

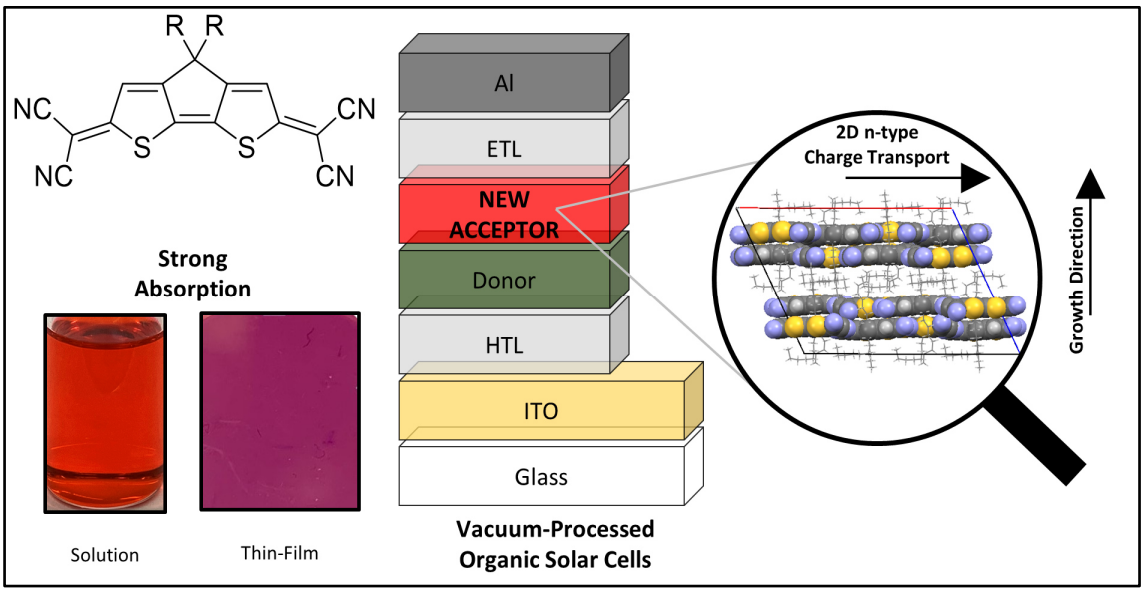

A series of new quinoidal cyclopentadithiophene-based vacuum-processable n-type semiconductors were synthesized and characterized both in solution and in their solid state followed by their successful application in organic thin-film transistors and initial studies in organic solar cells.

This Chapter was published by

K. Menekşe, P. Chen, B. Mahlmeister, O. Anhalt, A. Kudzus, M. Stolte and F. Würthner

in *Journal of Material Chemistry C*

2020, *8*, 15303-15311. Reprinted with Permissions.

5.1 Abstract

Current research in the field of organic photovoltaics (OPVs) is mainly focusing on the application of non-fullerene acceptors (NFAs) in solution-processed materials. Another promising area for their commercial application is all-vacuum-processed organic solar cells (OSCs) enabling not only the formation of homogenous thin films but also the construction of very complex multi-layered architectures. In this field fullerenes **C_{60}** and **C_{70}** still play the major role as acceptor materials, while alternatives with better optical features still remain rarely reported. One fascinating class of materials is quinoids, due to their interesting energetic properties, which enable not only n-type charge transport but also strong absorption in the visible spectral region even for low molecular weight molecules. Here, we report the synthesis of a series of new vacuum-processable organic pigments based on dicyanomethylene-endcapped cyclopentadithiophenes. This new class of materials is characterized by a high tinctorial strength and a low-lying LUMO level enabling n-type charge transport with mobilities of up to 10^{-2} cm^2 V^{-1} s^{-1}. Crystal engineering was performed by introducing different residues at the cyclopentadithiophene, which tunes the solid-state molecular packing and thin-film formation. Supramolecular interactions are the dominating structural forces, which help in explaining the organic thin-film transistor (OTFT) performance along with the film morphologies. As a proof of principle, a power conversion efficiency (PCE) of up to 0.62% was observed in a fully vacuum-processed planar-heterojunction (PHJ) device architecture combining our new quinoidal non-fullerene acceptors with a merocyanine dye as the donor material.

5.2 Introduction

After the initial demonstration of organic light-emitting diodes (OLEDs) in the middle of the last century[122], this first offspring of the field of organic electronics has recently manifested itself in the mass market as a multi-billion dollar business worldwide. Its sister technology, the organic photovoltaics, is today at the brink to the market due to its appealing light-weight and flexible configuration in times with strong interest in energy preservation and environment-friendly energy generation. Since the first all-vacuum-processed organic solar cells reported by Tang *et al.* in 1986,[30] designing new and more efficient organic semiconducting absorber

materials moved rapidly in the focus of this promising research.[41] Nowadays literature-known best but only solution-processable non-fullerene acceptors (NFAs) achieve efficiencies of up to 18% in combination with high-molecular weight donor polymers.[123,†] This clearly shows the beneficial impact of new NFAs to the device performance compared to previously preferred fullerenes. In comparison to fullerene-based systems, more light is accumulated by the device due to the complementary absorption of both materials, which leads to higher photocurrents.[124] NFAs allow tailor-made OPVs by energetic and optical fine tuning with respect to optimized donor materials as well as interfaces.[125,126] While many NFAs are reported for solution-processed systems, which nowadays outperform the fullerene-based predecessors, NFAs are still rather the exception for vacuum-processed systems, which lag behind in power conversion efficiency (PCE). Contrary to the polymer|NFA devices, sublimation in vacuum enables not only the formation of solvent-free sustainable thin films of high homogeneity but also the construction of sophisticated multi-layered architectures, which is already well established for commercial OLEDs. However, NFAs have not yet met the performance level to replace fullerenes in vacuum-processed OSCs. Thus, the reported most efficient single-junction vacuum-processed OSC exhibits a PCE of 9.8% using fullerene C_{70} as the acceptor and a small-molecule donor-acceptor-acceptor-type (D-A-A´) donor material.[127,‡] Even higher efficiencies were observed for vacuum-processed tandem cells, similar to those based on fullerene acceptors.[128,129] The ideal molecular properties for an efficient sublimable NFA should combine a high absorbance with low molecular weight for generating high amounts of excitons in thin layers[123] as well as suitable low-lying HOMO and LUMO levels, to enable not only n-type charge transport but also high open-circuit voltages (V_{OC})[130]. On the nanoscopic scale high exciton and electron mobilities are desired to avoid recombination effects and to obtain a high fill-factor,[131,132] which is as important as an appropriate morphology, that interplays with the donor to lower the energy loss factor.[133] However, this morphology as well as the suitable interface to the donor need to be formed instantly during the rapid deposition process (0.1-1.0 Å s^{-1}) already at a low substrate temperature. Therefore, a preferential face-on orientation of chromophores on the substrate with a high tinctorial strength is desired to allow strong absorption in the already thin layers as well as high exciton generation.[134]

† In 2022 the most efficiency NFA-based OSCs yielded 19.6%.[49]
‡ Higher efficiency were already reported yielding 10.2%.[60]

Best performing non-fullerene planar-heterojunction (PHJ) solar cells based on two active layer materials were fabricated by Cnops *et al.* using a subphthalocyanine as the NFA and a sexithiophene (**α-6T**) as the donor with an efficiency up to 6.0%.[61] Vacuum-processable oligothiophene systems like a barbituric acid-endcapped bithiophene and a dicyanovinyl-endcapped oligothiophene achieve efficiencies of up to 2.4% and 1.6% in a PHJ, respectively.[78,79] Therefore, the idea of using rigid π-scaffolds instead of a flexible oligothiophene bridge is reasonable.[135] Also the fusion between the donor (D) and the acceptor (A) moieties seems to be a way to further tune the energetics as demonstrated for a library of efficient p-type ADA small-molecule donors by the Marks' group.[136,137] and several other groups[56,88,138,139]. Inspired by the work of Pappenfuss *et al.*, describing both the synthesis and the molecular properties of a low-molecular weight quinoidal dicyanomethylene-endcapped dithienopyrrole (**DTPQ**), suitable candidates based on this structural motif can be imagined for application in organic electronics.[86] Pappenfuss *et al.* well demonstrated through the conversion of the aromatic dithienopyrrole to the quinoidal **DTPQ** along with decoration with the electron-rich dicyanomethylene groups by an unexpected reaction pathway, that the absorption is strongly bathochromically shifted as well as intensified. MARDER and coworkers reported firstly on the synthesis, characterization and charge-carrier properties of similar diselenopheno-[3,2-b:2′,3′-d]pyrrole derivatives. However, only an n-type field effect mobility (μ_n) of 8.7×10^{-4} $cm^2\ V^{-1}\ s^{-1}$ was observed in spin-cast layers.[140] Along this line, Li and coworkers synthesized a dicyano-substituted quinoidal oligothiophene bearing a cyclopentadithiophene core unit, which shows ambipolar behavior with almost balanced electron (2×10^{-2} $cm^2\ V^{-1}\ s^{-1}$) and hole (3×10^{-3} $cm^2\ V^{-1}\ s^{-1}$) mobilities.[141] The quinoidal ADA motif was used by serval groups in organic transistors[142-144] but its application as a NFA in OSCs is still rare. Ie and coworkers synthesized a dicyanomethylene-endcapped oligothiophene and due to the low-lying HOMO and LUMO levels it was used as the electron acceptor in solution-processed OPVs.[145] In the inverted architecture combined with the high-performance donor polymer **PBDB-T** an efficiency of 1.39% was achieved. All these compounds have in common that either large alkyl chains were implemented to allow the necessary solubility or the chromophore´s π-system was significantly extended. Both measures are rather undesired for vacuum-processed applications

due to their detrimental impact on the sublimation behavior. Thus, we have decided to design a new vacuum-sublimable pigment, which should crystallize in a layer-like structure with slipped-stacked packing and a face-on orientation on the substrate. Accordingly, we synthesized pigment-like chromophores based on quinoidal dicyanomethylene-endcapped cyclopentadithiophenes (**CPTQ**), which should likewise enable high absorbance and n-type charge-transport behavior. Theoretical studies from Shen *et al.* regarding the chromophore unit show low-lying HOMO (−6.5 eV) and LUMO levels (−4.2 eV) as well as a diradical character of 0.286.[146] To induce a face-on orientation on the substrate and a slipped-stacked packing in the solid state we chose different substituents with varying flexibility and steric demand at the central **CPDT** carbon atom like *n*-octyl (**CPTQ-Oc**), 2-ethylhexyl (**CPTQ-EH**), *n*-propyl (**CPTQ-Pr**) or phenyl (**CPTQ-Ph**) to tune the molecular arrangement. Herein, we report on the synthesis and molecular characterization of this so far not reported series of quinoidal pigments along with their implementation as vacuum-processable n-type semiconductors in OTFTs and NFAs in OSCs.

5.3 Results and Discussion

5.3.1 Synthesis and Molecular Properties

The synthesis of the here reported series of **CPTQs** was performed according to literature-known procedures. First, cyclopentadithiophene derivatives (**CPDT-R**) bearing either *n*-octyl, 2-ethylhexyl, *n*-propyl or phenyl substituents were synthesized. To gain access to the desired quinoidal structure **CPTQ-R**, a condensation step was performed by adding tetracyanoethene to the respective cyclopentadithiophene derivative in dimethylformamide (DMF) as described by Pappenfuss *et al.* (Scheme 1).[86]

All target molecules were obtained in decent yields from 18 to 31% and could be purified not only using column chromatography but also using thermal gradient

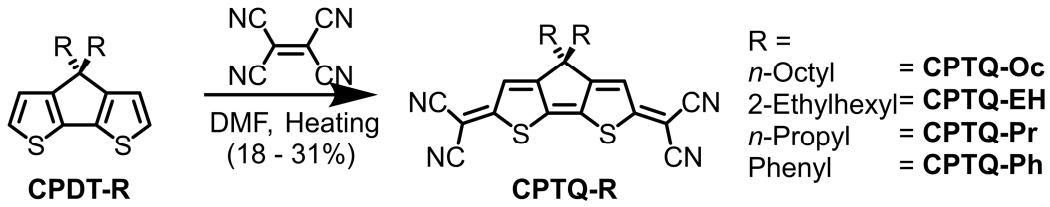

Scheme 1: Synthetic route for **CPTQ-Oc**, **CPTQ-EH**, **CPTQ-Pr** and **CPTQ-Ph**.

sublimation in vacuum. These new materials were characterized *via* ^{1}H and ^{13}C NMR, UV-Vis and fluorescence spectroscopy as well as high-resolution mass spectrometry, cyclic voltammetry (CV), differential scanning calorimetry (DSC) and thermal gravimetric analysis (TGA) (for details see Chapter 5.5). All dyes are decently soluble in dichloromethane, wherein the UV-Vis, fluorescence and CV measurements could be performed (Figure 38 and Table 14). As expected for these dyes bearing the same π-scaffold, similar absorption spectra are observed with a pronounced vibronic structure and maxima (λ_{Max}) at about 530 nm, corresponding to optical band gaps of approximately 2.34 eV. Fluorescence studies reveal almost mirror image-like emission profiles with maxima at about 550 nm and very low quantum yields ($\Phi_{Fl} < 1\%$) as well as short fluorescence lifetimes (< 0.5 ns) (Figure 57 and Table 17). The molar extinction coefficients (ε_{Max}) for all derivatives are in the range of 80000-90000 $M^{-1}\,cm^{-1}$, which is very promising for application in organic photovoltaics. Indeed, their absorption densities ($\mu_{eg}^2\,M^{-1}$) defined by the square of the transition dipole-moment (μ_{eg}) per molar mass (M_W) are in the range of 0.19-0.28 $D^2\,mol\,g^{-1}$, which is comparable to other strong absorbers that are applied as donor components in OSCs.[147]

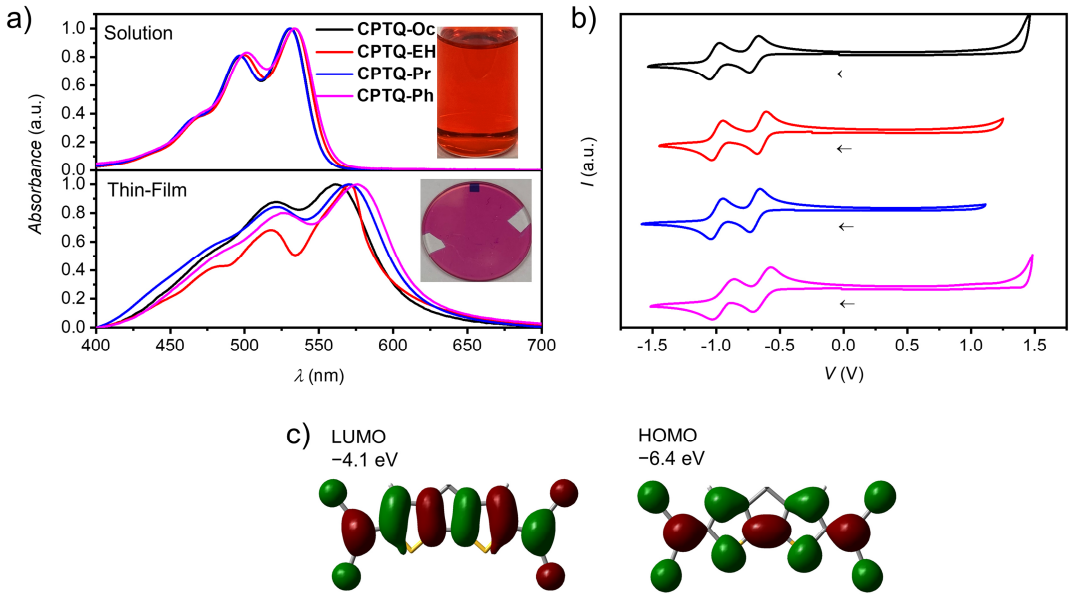

Figure 38: a) UV-Vis absorption spectra of **CPTQ-R** derivatives in dichloromethane (top, photo of a 0.5 mg mL^{-1} **CPTQ-EH** solution) and of vacuum-deposited thin films (30 nm, photo **CPTQ-EH**) on quartz (bottom) at room temperature. b) Cyclic voltammograms (relative to Fc/Fc^+) measured in dichloromethane (2.5×10^{-4} M) at room temperature with addition of Bu_4NPF_6. c) Calculated frontier molecular orbitals and their energies of the **CPTQ** chromophore.

The thin-film UV-Vis spectra were obtained by thermal evaporation of the materials as a 30 nm thick layer on top of a quartz substrate at 20 °C, like for later the OPV fabrication. The rather low sublimation temperature is increasing in the order **CPTQ-EH** (80 °C), **CPTQ-Pr** (90 °C), **CPTQ-Oc** (95 °C) and **CPTQ-Ph** (115 °C), which might be governed by the amount of intramolecular interactions (*vide infra*) and increasing M_W. All materials show excellent thermal stability up to 320 °C, which was proven using DSC and, for **CTPQ-Oc**, using TGA experiments (Figure 58, Figure 59). The absorption profiles of these thin films are broader with respect to the observed spectra in solution and their optical densities (OD) are observed to be up to 0.6, which is appreciably high. The absorption band exhibits a small bathochromic shift in the solid state of 30 nm (**CPTQ-Oc**), 36 nm (**CPTQ-EH**), 39 nm (**CPTQ-Pr**) and 42 nm (**CPTQ-Ph**). The molecular HOMO and LUMO levels were experimentally obtained *via* CV in CH_2Cl_2 with the addition of Bu_4NPF_6 (Figure 38b, Table 14). Two reversible reduction potentials were observed at almost the same voltage for all derivatives. The first reduction potential ($E_{½}^{Red\ 1}$) was found to be in the range from −0.64 to −0.70 V versus Fc/Fc^+. The second reduction potential ($E_{½}^{Red\ 2}$) was observed from −0.94 to −1.01 V. Considering the energetic level for the

Table 14: Results of UV-Vis and CV experiments in CH_2Cl_2 as well as DSC and thermal evaporation experiments for **CPTQ-R**.

	λ_{Max}^{Sol} (nm)	λ_{Max}^{TF} (nm)	ε_{Max} ($M^{-1}\,cm^{-1}$)	$\mu_{eg}^2\,M^{-1}$ ($D^2\,mol\,g^{-1}$)	E_g (eV)
CPTQ-Oc	531	561	88200	0.20	2.32
CPTQ-EH	534	570	81400	0.19	2.33
CPTQ-Pr	531	570	89100	0.28	2.32
CPTQ-Ph	534	576	83200	0.23	2.33
	$E_{½}^{Red\ 2}$ (V)	$E_{½}^{Red\ 1}$ (V)	E_{LUMO}^{CV} (eV)	E_{HOMO}^{CV} (eV)	T_{MP} (°C)	T_{SP} (°C)
CPTQ-Oc	−1.01	−0.70	−4.45	−6.77	142	95
CPTQ-EH	−0.99	−0.64	−4.51	−6.84	202	80
CPTQ-Pr	−0.98	−0.69	−4.46	−6.78	271	95
CPTQ-Ph	−0.94	−0.64	−4.51	−6.84	331	115

UV-Vis data were measured in CH_2Cl_2 solution and at room temperature. CV data were measured in CH_2Cl_2 (2.5×10^{-4} M) with the addition of Bu_4NPF_6. The energy levels are according to Fc/Fc+ (−5.15 eV).[82] Melting (T_{MP}) and sublimation (T_{SP}) points were obtained using DSC and an evaporation device (10^{-6} mbar), respectively.

Fc/Fc^+ oxidation at −5.15 eV the LUMO levels of the dyes were estimated. [82] All materials show low-lying LUMO levels at about −4.5 eV. Using the optical band gap of around 2.3 eV a HOMO level of about −6.8 eV was determined. DFT-calculations yielded the HOMO and LUMO levels around −6.4 eV and −4.1 eV (Figure 13c), respectively, which is in good accordance with the experimental CV data and to the literature values.[146] Compared to the commonly used fullerene **C_{60}**, which is still the state-of-the-art material in highly-efficient vacuum-processed OSCs, the LUMO levels here reported for our **CPTQs** are even 0.3 eV lower in energy, which should be beneficial for charge separation at the donor-acceptor interface and will have an impact on the open-circuit voltage of the device (*vide infra*).

5.3.2 Crystal Structure

Solvent-free single crystals of all compounds were successfully grown either by the diffusion method of methanol into a chloroform solution (10^{-4} M) followed by slow solvent evaporation (**CPTQ-Oc**) or by sublimation (10^{-6} mbar) on top of $Si|SiO_2$ wafers in vacuum (**CPTQ-EH**, **CPTQ-Pr** and **CPTQ-Ph**). In the case of **CPTQ-EH**, the alkyl-chains could be refined as disordered conformations of *RR*, *SS* and *RS* ethylhexyl stereoisomers (see Chapter 5.5).

The chromophores are displayed in side view in Figure 39 (for additional information see Table 18) and well depict the expected rigid π-scaffold as well as the increasing steric demand at the central cyclopentyl moiety. While **CPTQ-Oc** and **CPTQ-EH** with long and flexible alkyl chains show an almost planar π-system, **CPTQ-Pr** and **CPTQ-Ph** are slightly distorted from planarity. The shielding character of the long alkyl chains in the case of **CPTQ-Oc** and **CPTQ-EH** prevents a part of the chromophore from additional in-plane interactions. The resulting space in those derivatives is filled by alkyl chains. Derivatives with less flexible substituents (**CPTQ-Pr** and **CPTQ-Ph**) exhibit a shorter distance between the chromophores, which leads to more interactions and to a distortion of the π-scaffold. For all derivatives, the molecular packing within the crystal structures is governed by specific molecular interactions (Figure 40). Different types of non-covalent interactions include directional dipole-dipole interactions, the coordination of the

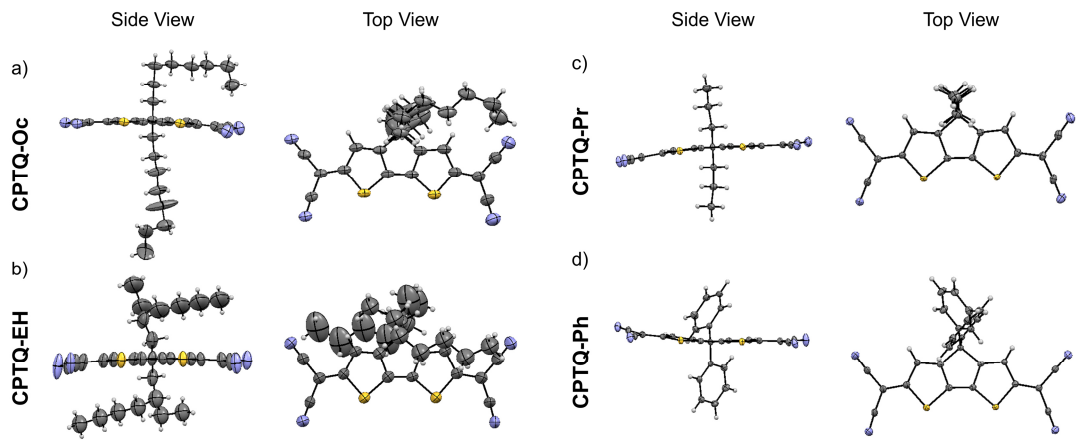

Figure 39: Solid-state molecular structures of **CPTQ-Oc** (a), **CPTQ-EH** (b), **CPTQ-Pr** (c) and **CPTQ-Ph** (d) within their single-crystal structures in side (left) and top (right) view determined by single-crystal X-ray analysis. Disorder of the **CPDT** residues are omitted and thermal ellipsoids are set at 50% probability.

electron poor nitrile groups to hydrogen or sulfur (CN···S/H), i.e. chalcogen bonding,[148] and the antiparallel orientation of the partial dipole moments between CN···CN along with π-π stacking. Dipole-dipole interactions become obvious from the antiparallel alignment of neighboring molecules within one layer but also of π-stacked chromophores, which originates from the ground state dipole moment (μ_g) of about 5.5 D (obtained from DFT). Additionally, the directional force of the nitrile units by coordination to the sulfur atoms of the **CPDT** cores directs the layer-like arrangement of molecules within the crystal structures. Those interactions are similar to previously reported CN···Se interactions of squaraine dyes.[149] The two-dimensional structures (**CPTQ-Oc**, **CPTQ-EH** and **CPTQ-Pr**) are additionally characterized by CN···H interactions (2.4-2.7 Å) between the nitrile groups as well as the **CPDT** core. In the case of **CPTQ-Ph** these interactions are missing and the CN···S (2.9-3.0 Å) interactions combined with the steric cumbersome phenyl residues lead to a tilted arrangement of multiple neighboring molecules. For all derivatives CN···CN interactions (3.1-3.2 Å) were observed, which originate from the cancelation of the partial dipole moments. Especially for **CPTQ-EH** and **CPTQ-Ph** those nitrile groups get in close contact to each other whereby polarization interactions can be suspected. Within a layer of **CPTQ-Oc**, **CPTQ-EH** and **CPTQ-Pr**, high hole-transfer integrals (for details see Chapter 5.5) were calculated to the CN···S bonded neighbors, achieving values of up to 133 meV (t_+) for **CPTQ-EH**. For **CPTQ-Ph** the charge-transfer integrals are much lower. Therefore, we assume that the tilted arrangement is unfavorable for charge transport. To the next layer, similar

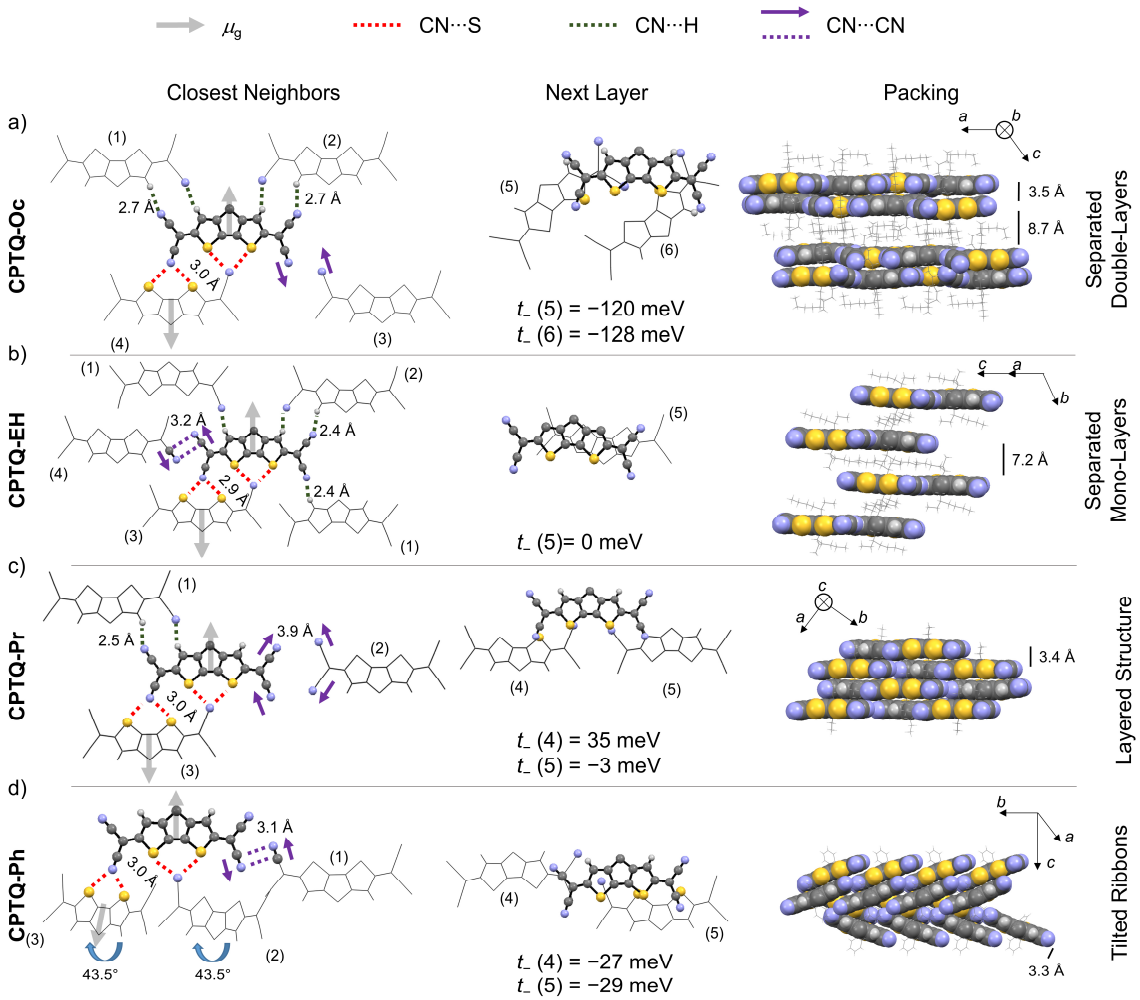

Figure 40: Solid-state molecular packing of neighboring molecules of **CPTQ-Oc** (a), **CPTQ-EH** (b), **CPTQ-Pr** (c) and **CPTQ-Ph** (d) within their single-crystal structures indicating the most relevant supramolecular interactions (left) like dipole-dipole interactions (arrows), hydrogen or chalcogen bonding involving nitrile groups (dotted lines) as well as π-π interaction (middle and right, solid lines). Selected transfer integrals are given (middle) and further data to all next neighboring molecules are listed in Table 20 (grey-carbon, blue-nitrogen, yellow-sulfur, white-hydrogen).

interactions based on CN···S forces can be observed. While **CPTQ-Oc**, **CPTQ-Pr** and **CPTQ-Ph** show a slipped arrangement of chromophores, **CPTQ-EH** crystallizes in a columnar stacking. The highest electron-transfer integral to the closest molecule of the next layer was observed for **CPTQ-Oc** with values of −120 and −128 meV (t_-). For **CPTQ-Pr** and **CPTQ-Ph** the charge-transfer integrals are much lower, while for **CPTQ-EH** it is almost 0 meV. This suggests that **CPTQ-Oc** shows good electron-transport properties within one layer and to the next layer, while **CPTQ-EH** shows almost no charge transport to the next layer.

In the side view of the packing of the chromophores of **CPTQ-Oc**, two different π-π distances were observed: firstly, two neighboring molecules with a close π-π contact of 3.5 Å and secondly, a neighboring layer of molecules with a distance of about

8.7 Å, which originate from the spatial orientation of the space-demanding octyl-chains. Hence, a double-layered structure is formed in which excellent percolation pathways for electrons should exist according to the high transfer integrals. In **CPTQ-EH**, all layers are separated by a π-π distance of 7.4 Å, which is detrimental for charge transport. In contrast to **CPTQ-Oc**, monolayers of **CPTQ-EH** are formed. In **CPTQ-Pr**, all monolayers stack at an equal π-π distance of only 3.4 Å, unfortunately with only a minor π-π overlap leading to small transfer integrals (t-). Unlike **CPTQ-Oc**, **CPTQ-EH** and **CPTQ-Pr**, **CPTQ-Ph** exhibits a continuous three-dimensional packing motif. Two ribbons of chromophores were observed with a π-π distance of 3.3 Å and tilted to each other at 43.5°. Comparing the different crystal structures and the calculated values for the charge-transfer integral with regards to possible charge-transport properties in the thin film, the mobility should decrease in the order of **CPTQ-Oc**, **CPTQ-Pr**, **CPTQ-Ph**, and **CPTQ-EH**.

5.3.3 Charge Transport and Thin-Film Morphology

Subsequently, organic thin-film transistors (OTFTs) were fabricated in a bottom-gate-top-contact architecture by sublimation of a 30 nm thick layer of **CPTQ-R** on top of (heated) *n*-tetradecylphosphonic acid (TPA)-modified $Si|SiO_2|AlO_x$ substrates. All rapidly grown layers deposited at a substrate temperature of 20 °C, similar to the later OSC production, showed n-type charge-transport behavior under inert conditions in accordance with their low-lying LUMO levels (Figure 41, Figure 60, Figure 61, Table 15). All devices unfortunately exhibit a rather significant hysteresis between the bidirectional sweeps, which is probably caused by trapped states at the surface or between the many grain boundaries. Only subtle differences with the exception of **CPTQ-Oc** can be observed in their respective morphologies visualized using atomic force microscopy (AFM), showing smooth layers composed of small domains and accordingly the minor impact of the side chains on the thin-film formation at a substrate temperature of 20 °C (Figure 42, Figure 62). Thin films of **CPTQ-EH** exhibit the highest charge-carrier mobility (μ_n) of 10^{-4} $cm^2 V^{-1} s^{-1}$, a threshold voltage (V_{TH}) of 5 V and an on/off-current ratio ($I_{on} I_{off}^{-1}$) of about 10^3 within this series. All other derivatives showed a slightly smaller n-type mobility of about 10^{-5} $cm^2 V^{-1} s^{-1}$ and an $I_{on} I_{off}^{-1}$ value around 10^2. While all materials behave very similarly when deposited onto the substrates at 20 °C, their respective thin-

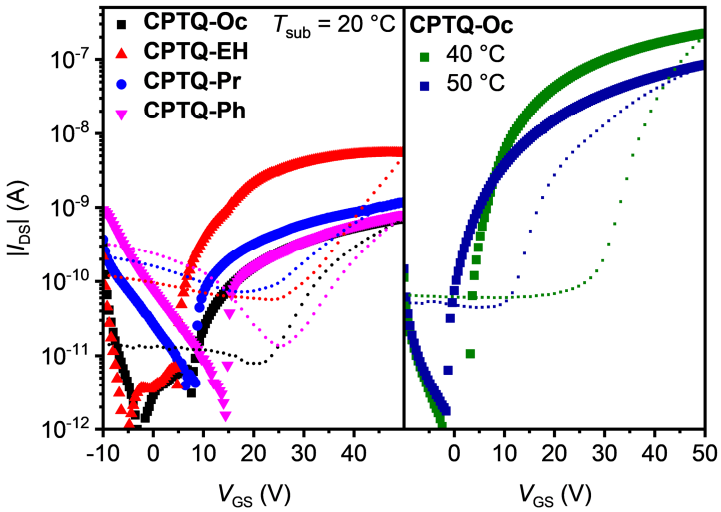

Figure 41: Transfer characteristics of vacuum-processed OTFTs of **CPTQ-Oc** (black), **CPTQ-EH** (red), **CPTQ-Pr** (blue) and **CPTQ-Ph** (pink) on TPA-modified Si|SiO_2|AlO_x substrates (L = 100 µm, W = 200 µm, V_{GS} = 50 V, forward (symbols) and backward (dotted) sweep). Transfer characteristics for optimized OTFTs based on **CPTQ-Oc** were obtained by increasing substrate temperature up to 40 °C (green) and 50 °C (dark blue) while decreasing semiconductor layer thickness to 15 nm.

film growth changed significantly at elevated substrate temperatures. Already at substrate temperatures of 40 °C thin films of **CPTQ-EH**, **CPTQ-Pr** and **CPTQ-Ph** became discontinuous although larger domains were formed (Figure 62) and no charge transport was detected. Only in the case of **CPTQ-Oc**, it was possible to further increase the OTFT performance up to 10^{-2} cm^2 V^{-1} s^{-1} by elevating substrate temperature, by varying of the layer thickness and by optimizing the architecture (L = 1000 µm, W = 20 µm, V_{DS} = 70 V). This value is one order of magnitude higher than that for the previously reported diselenophenodithiophene in spin-coated thin films by Getmanenko *et al.*[140] and in good accordance with other quinoidal

Table 15: Characteristic values for OTFTs of **CPTQ-Oc**, **CPTQ-EH**, **CPTQ-Pr** and **CPTQ-Ph** in Si|SiO_2|AlO_x|TPA|**CPTQ-R**|Au architecture (L = 100 µm, W = 200 µm) deposited onto heated substrates ($T_{Substrate}$) with varying layer thickness ($d_{Ac.}$). The field-effect mobility was calculated in the saturation regime (V_{GS} = 50 V).

	$T_{Substrate}$ (°C)	$d_{Ac.}$ (nm)	μ_n (cm^2 $V^{-1}s^{-1}$)	V_{Th} (V)	I_{on} I_{off}^{-1} (1)
CPTQ-EH	20	30	1×10^{-4}	5	10^3
CPTQ-Pr	20	30	2×10^{-5}	8	10^2
CPTQ-Ph	20	30	1×10^{-5}	14	10^2
CPTQ-Oc	20	30	1×10^{-5}	7	10^2
	40	15	5×10^{-3}	5	10^5
	50	15	1×10^{-3}	−2	10^5

semiconductors.[150,151] The observed mobility values seem at first glance to contradict the assumptions that resulted from the crystal-structure analysis, where the expected mobility should decrease in the order of **CPTQ-Oc**, **CPTQ-Pr**, **CPTQ-Ph**, and **CPTQ-EH**. This discrepancy can be explained with the help of AFM images, revealing the morphologies of the sublimated thin films, which provide insights into their inherent tendency for crystallization guided by their **CPTQ** residues (Figure 42a-d). At a substrate temperature of 20 °C, **CPTQ-Ph** forms a smooth homogeneous layer on the substrate. Individual domains cannot be observed as these are estimated to be in the lower nanometer scale. The low root mean square (R_q) value of 2.6 nm indicates low crystallinity. **CPTQ-Pr** exhibits already at 20 °C de-wetting character. Spherical domains are visible, which form a closed layer on top of the substrate with a R_q value of 3.1 nm. The domains have an average size of 145 nm. In contrast, **CPTQ-EH** displays already domains with a needle-like shape with an average size of up to 180 nm. The defined shape of the particles might indicate higher crystallinity in contrast to the other derivatives, which would support the highest charge-carrier mobility obtained for deposition at 20 °C. In comparison to **CPTQ-Ph** and **CPTQ-Pr** the R_q value for **CPTQ-EH** has increased to 6.5 nm. The thin-film morphology of **CPTQ-Oc** shows a closed layer, which is covered by larger domains with an ill-defined shape. These undefined domains show an average size of 650 nm which leads to a high R_q value of 20.8 nm. Except **CPTQ-EH**, all other derivatives showed undefined surface morphologies, which are

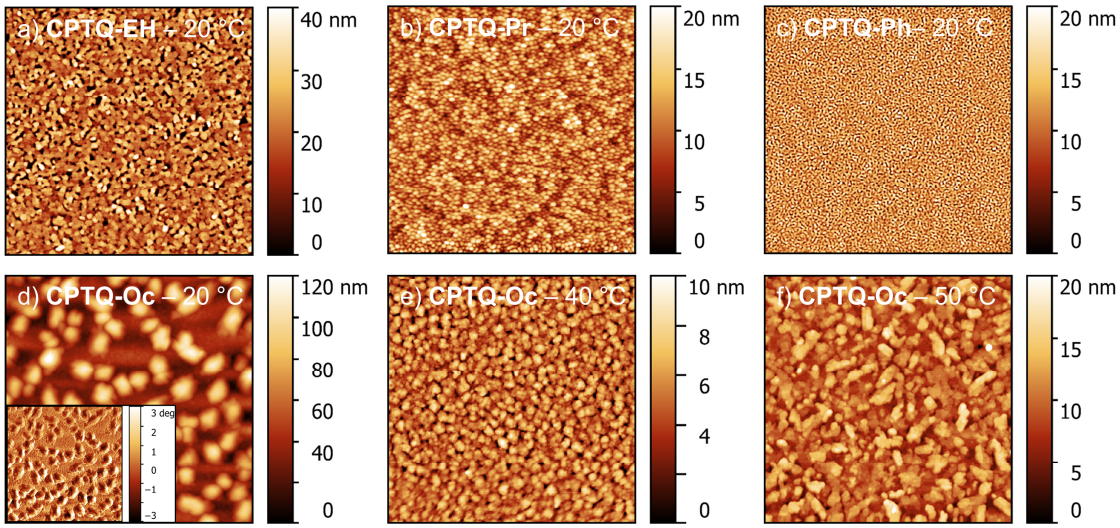

Figure 42: AFM images of vacuum-processed layers of **CPTQ-EH** (a), **CPTQ-Pr** (b), **CPTQ-Ph** (c) and **CPTQ-Oc** (d-f) on TPA-modified Si|SiO_2|AlO_x substrates deposited at a substrate temperature of 20 °C and at elevated substrate temperatures of 40 °C (e) and 50 °C (f) for **CPTQ-Oc**. 10×10 µm².

probably unfavorable for charge transport. This explains the slightly lower mobilities of these derivatives of about 10^{-5} cm^2 V^{-1} s^{-1} in contrast to **CPTQ-EH**. By heating the substrate, the molecular motion on the substrate surface is increased and less nucleation sites are formed, facilitating more homogeneous layers. Accordingly, for **CPTQ-Oc** an increased number of particles (Figure 42e,f) and decreased R_q values to 2.3 nm to 2.8 nm for the substrate temperatures of 40 °C and 50 °C, respectively, were obtained. This coincides with the highest mobility of 10^{-2} cm^2 V^{-1} s^{-1}, which is just one order of magnitude lower than that of **C$_{60}$** in OTFTs.[152,153] Unfortunately, this is not the case for all the other derivatives which in contrast de-wet from the TPA-modified surface giving rise to discontinuous films without any OTFT performance. For these **CPTQ** derivatives the formation of extended crystalline domains, which is needed for high-performance OTFTs, might be hindered due to the disorder caused by stereoisomers (**CPTQ-EH**) or the bulky (**CPTQ-Ph**) or rigid (**CPTQ-Pr**) residues. In contrast, the aliphatic chains of **CPTQ-Oc** interdigitate well (Figure 40a) which leads to extended layer-like growth. Comparing the experimental X-ray diffraction (XRD) pattern of the thin film of **CPTQ-Oc** on a TPA-modified Si|SiO$_2$|AlO$_x$ substrate (40 °C) with the simulated XRD-pattern of the single crystal, the orientation of the chromophores on the substrate can be derived (Figure 43). The experimental XRD pattern shows diffraction peaks (2Θ) at 4.8, 6.4, 7.0, 14.4, 19.3, 21.2, 24.2, 28.4 and 29.2°, where most of the them can be assigned to the simulated XRD pattern of the single crystal along the {h00} (one peak), {hk0} (one peak) and the {00l} (four peaks) net plane shear (Table 19). Three diffraction peaks could not be indexed, probably due to nanocrystalline phases, and might relate to a polymorph of **CPTQ-Oc**. We assume that **CPTQ-Oc** is growing in a

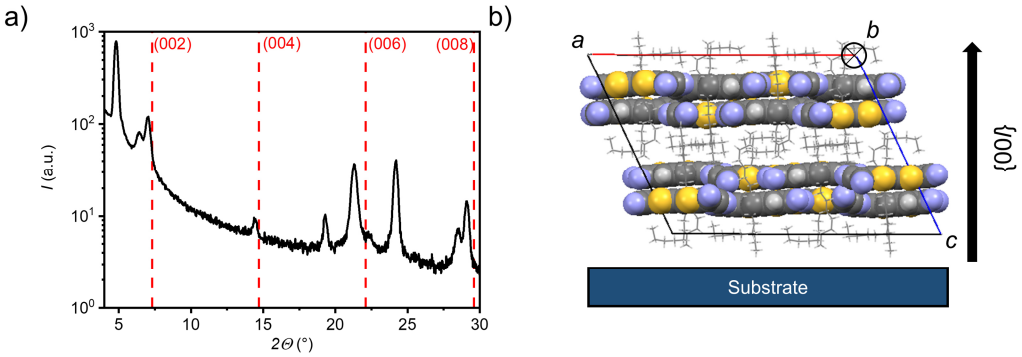

Figure 43: a) Powder X-ray diffraction pattern of vacuum-deposited thin film of **CPTQ-Oc** on TPA-modified Si|SiO$_2$|AlO$_x$ substrate at temperature of 40 °C (black solid) compared with simulated XRD reflexes of the {00l} net plane shear of **CPTQ-Oc** single crystals (red dashed). b) Spatial orientation of **CPTQ-Oc** on a substrate with view along the *b*-axis.

layer-like fashion along the 00*l*-direction on top of a TPA-modified Si|SiO_2|AlO_x substrate. The alkyl chains are pointing towards the substrate and due to the orientation of the chromophore, the π-surfaces are lying almost parallel to the substrate, resulting in the desired face-on orientation. This also explains the high tinctorial strength of up to 0.6 in the thin film on a quartz substrate.

5.3.4 Organic Photovoltaics

As for these new quinoidal molecules **CPTQ-R** all prerequisites for vacuum-sublimable NFAs like strong thin-film absorption as well as n-type semiconductance are met, we attempted their initial application in OSCs in comparison with the standard acceptor **C_{60}**. Schematics of the planar-heterojunction (PHJ) device architecture and the chemical structure of a previously reported donor material **MD376**[54, 102,154] are shown in Figure 44a,b, respectively. The merocyanine **MD376** was chosen as it should not only enable applicable open-circuit voltages (V_{OC}) but also inherit complementary thin-film absorption at a higher wavelength (Figure 63). V_{OC} should however be lower than that of the corresponding **C_{60}**-based OSC, due to the lower LUMO level of the compounds reported here. The fully vacuum-processed OSCs in an ITO|MoO_3|**MD376**|acceptor|BCP|Al architecture were optimized by varying the thickness of the active layer materials as well as the substrate temperature. The representative *J-V* curves of comparable OSCs based on **CPTQ-Oc** or **C_{60}** as the acceptor as well as their UV-Vis and EQE spectra are shown in Figure 44c,d and the photovoltaic parameters are listed in Table 16 (for other derivatives see Figure 64 and Table 21). Devices processed at 20 °C based on **CPTQ-Oc** showed the highest performance yielding a power conversion efficiency (PCE) of up to 0.64%. In contrast, the optimized **C_{60}** containing OSC exhibits a PCE of up to 1.25%. **CPTQ-EH**, **CPTQ-Pr** and **CPTQ-Ph** afforded devices with lower efficiencies of 0.11%, 0.05% and 0.004%, respectively (see chapter 5.5), which are presumably caused by the inferior film formation as well as the corresponding poor interface and low charge carrier mobility (*vide supra*). These OSCs mainly suffer from low electron mobility, which leads to a high series resistance. Appreciable fill-factors (FF) of 47% and V_{OC} of up to 0.86 V could be realized for **CPTQ-Oc** with an energy loss factor of about 0.5 eV, which is in good accordance with the analogue **C_{60}**-based OSCs. The highest short-circuit current density (J_{SC}) of −1.54 mA cm^{-2} was

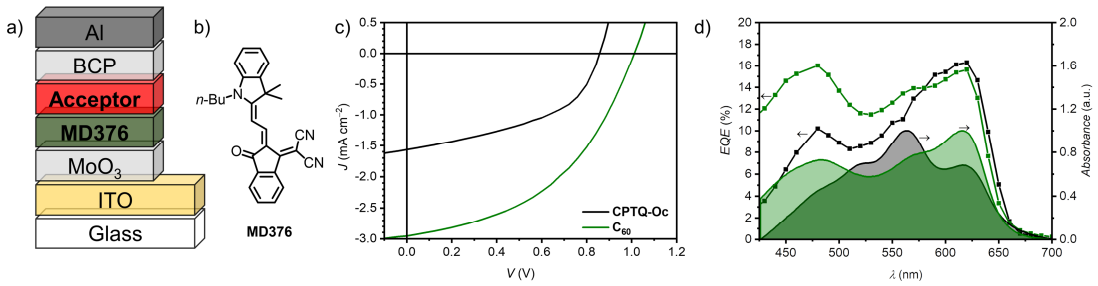

Figure 44: a) Schematic representation of the architecture of the vacuum-processed planar-heterojunction (PHJ) organic solar cells. b) Chemical structure of merocyanine **MD376** used as donor material. c) *J-V* curves of vacuum-processed PHJ organic solar cells based on **MD376** as donor and **CPTQ-Oc** (black) or **C60** (green) as acceptor materials, which were measured under AM 1.5G conditions. d) EQE and normalized UV-Vis spectra of **MD376**|**CPTQ-Oc** or **C60**-based PHJ solar cells.

also obtained for **CPTQ-Oc**, while all other derivates show only less than a third of J_{SC}. The short-circuit current density determined by the integration of the EQE (J_{SC}^{EQE}) of −1.54 mA cm^{-2} equals the one calculated using *J-V* curves. Comparing the shapes of the UV-Vis and EQE-spectra of the **CPTQ-Oc** based OSCs, it becomes obvious that their profiles are not equal, especially in the spectral region of the NFA (Figure 44d). The EQE spectra of the NFA based OSC exhibit almost the same shape as the UV-Vis spectra of the neat **MD376** solid-state film with a maximum EQE value of 16% at about 620 nm. Due to the missing EQE signature of the NFA, we conclude that almost all excitons generated by **CPTQ-Oc** do not reach the interface with the donor **MD376**. While excitons can presumably move freely in each conducting double-layer of **CPTQ-Oc**, their transport from one double-layer to another is hindered due to the large layer spacing (8.7 Å, Figure 40a) and recombination takes place. Accordingly, the EQE signals originate almost solely from excitons, which were generated by **MD367** and can reach the donor-acceptor interface of **CPTQ-Oc** resulting in efficient charge separation with a low loss-factor. Only the EQE of OSCs based on **CPTQ-Pr** with a continuous packing arrangement (Figure 40c) shows a

Table 16: Photovoltaic parameters of optimized planar-heterojunction OSCs in ITO|MoO_3|**MD376**|acceptor|BCP|Al architecture measured under inert conditions and under AM 1.5G irradiation. Layer thicknesses of donor **MD376** ($d_{Do.}$) and acceptor ($d_{Ac.}$) are given as well.

Acceptor	$d_{Ac.}$ (nm)	$d_{Do.}$ (nm)	J_{SC} (mA cm^{-2})	V_{OC} (V)	FF (%)	PCE (%)	PCE^{Max} (%)
CPTQ-Oc[a]	20	20	−1.54 ±0.04	0.86 ±0.02	47 ±1	0.62 ±0.01	0.64
C60[b]	10	10	−2.90 ±0.10	1.02 ±0.03	43 ±2	1.25 ±0.08	1.39

similar shape as the UV-Vis spectrum of the active layer and both materials contribute to the generated photocurrent (Figure 64c). However, the bad film-forming ability results in a poor interface with the donor as well as mediocre electron transport and the overall device performance is strongly diminished. Comparing the **CPTQ-Oc** based OSC with the fullerene-based one (Figure 65, Table 22), V_{OC} and J_{SC} were decreased due to a smaller $E_{HOMO}(D)-E_{LUMO}(A)$ gap and due to the discussed recombination losses. The FF was slightly increased due to a more balanced charge transport in **CPTQ-Oc** (47%) compared with **C_{60}** (43%) with respect to **MD376**.

5.4 Conclusion

Here, we have reported the synthesis and characterization of a series of four new n-type semiconductors based on quinoidal dicyanomethylene-endcapped cyclopentadithiophene core units with different residues at the center of the π-scaffold. We investigated their opto-electronic properties in both solution and the solid state. Our new materials exhibit high molar extinction coefficients and low molar weights, which make these pigments feasible for vacuum-sublimation at low temperatures. Through cyclic voltammetry and DFT-calculations, we were able to determine the low-lying LUMO levels of about −4.5 eV, which enable n-type charge transport in vacuum-processed OTFTs with mobilities of up to 10^{-2} cm^2 V^{-1} s^{-1}. The XRD pattern of thin films in combination with the individual single-crystal structures proved a preferential face-on orientation of the small molecules on substrates. However, the charge transport ability of each derivative depends not only on the molecular packing but also strongly on the individual tendency for thin-film formation. Finally, we fabricated vacuum-processed planar-heterojunction solar cells with all new non-fullerene acceptors in combination with a previously reported merocyanine dye **MD376** as the donor material yielding moderate power conversion efficiencies of up to 0.62% for **CPTQ-Oc**. All devices suffer mainly from low short-circuit current densities, which stem from poor exciton migration within the new layered acceptor material, as was proven using UV-Vis and EQE measurements. Further careful fine-tuning of the packing arrangement in the solid state may enable more efficient exciton transport in this new class of thermally stable and colorful pigments to fully meet their potential as efficient NFA in all-

vacuum-processed OSC. The manufacture of bulk-heterojunction OSCs might be promising as well.

5.5 Supporting Information for CHAPTER V

5.5.1 Materials and Methods

UV-vis spectroscopy in CH_2Cl_2 were measured at room temperature on a Jasco V770 spectrophotometer in 10 mm cuvettes (SUPRASIL®, Hellma® Analytics). For the thin-film spectra on quartz substrates (SUPRASIL®, Hellma® Analytics) as well as of the active layer of the OSC, the same spectrometer with an integration sphere was used. Thin films of investigated compounds were fabricated by thermal sublimation of 30 nm thick layer on quartz substrates analogue to the OTFTs fabrication, while the substrate was not heated.

Fluorescence spectroscopy in CH_2Cl_2 solution (10^{-7} M, $A^{Max} < 0.05$, spectroscopic grade, Uvasol®, Merck) were measured at room temperature on an Edinburgh Instruments FLS980-D2D2-ST spectrometer and were corrected against the photomultiplier sensitivity and the lamp intensity. Fluorescence lifetimes were determined with an EPL picosecond pulsed diode laser (λ_{Ex} = 505.8 nm) for time correlated single photon counting (TCSPC) with the same spectrometer. Fluorescence quantum yields were measured in CH_2Cl_2 on a Hamamatsu Absolute PL Quantum Yield Measurement System CC9920-02.

Cyclic voltammetry was performed with an electrochemical analyser (EC epsilon; BAS Instruments) with a three-electrode single component cell. CV data was measured in CH_2Cl_2 (2.5×10^{-4} M) with addition of Bu_4NPF_6 versus Fc/Fc^+ standard. The working and the auxiliary electrodes consist of Pt and the reference electrode of Ag/AgCl.

NMR spectroscopy was performed on a Bruker *Avance III HD* 400 MHz NMR spectrometer relative to residue undeuterated solvent signals. The chemical shifts (δ) are listed in parts per million (ppm). Multiplicities for proton signals are abbreviated as s, d, t and m for singlet, doublet, triplet and multiplet, respectively.

Mass spectrometry was performed in the negative mode *via* MALDI-TOF on a Bruker Daltonics Autoflex *II* with 2-[(2*E*)-3-(4-*tert*-butylphenyl)-2-methylprop-2-enylidene]malononitrile) (DCBT) as matrix.[†]

[†] Instead of a Bruker Daltonics Autoflex II a Bruker Daltonics UltrafleXtreme was used.

Thermogravimetric analysis was performed using a Perkin Elmer STA 6000 Simultaneous Thermal Analyzer under nitrogen atmosphere at a heating rate of 5 °C min^{-1} up to a maximum temperature of 500 °C.

Differential scanning calorimetry thermograms were recorded using a DSC 8000 (Perkin Elmer) equipped with an Intracooler 2 refrigerated cooling system at a scan rate of 10 °C min^{-1}.

DFT calculations for HOMO and LUMO energies as well as for the ground state dipole moments were performed with GAUSSIAN 09.[155] Start structures were energy minimized by using B3LYP[156-158] functional and 6-31G**[159-161] basis set.

ADF (Amsterdam Density Functional) calculation[162-164] for the transfer integral was performed employing the TZP[165] basis set and the PW91[166] functional.

Single crystal X-ray diffraction for compounds **CPTQ-Oc**, **CPTQ-EH**, **CPTQ-Pr** and **CTPQ-Ph** was measured at 100 ± 1 K on a Bruker D8 Quest Kappa diffractometer with a Photon II CMOS detector and multi-layered mirror monochromated $Cu_{K\alpha}$ radiation. The solved structure was obtained with Fourier techniques and the Shelx software package.[167] Crystallographic data are deposited with the Cambride Crystallographic Data Centre as supplementary publication no. CCDC 2011168 (**CPTQ-Oc**), CCDC 2011165 (**CPTQ-EH**), CCDC 2011167 (**CPTQ-Pr**) and CCDC 2011166 (**CPTQ-Ph**).

Thin-film X-ray diffraction data were collected on a Bruker D8 Discover diffractometer with a LynxEye-1D-Detecter and $Cu_{K\alpha}$ radiation.

Organic thin-film transistors were fabricated on Si|SiO_2 (100 nm)|AlO_x (8 nm)|*n*-tetradecylphosphonic acid (TPA, 1.7 nm) substrates with a capacitance C_i = 32.4 nF cm^{-2}. The precleaned wafers were placed in the vacuum chamber. For OTFTs fabricated at room temperature, the wafer was placed into the thermal evaporation system Auto306 (BocEdwards) followed by depositing 30 nm of the respective compound (r = 0.02 – 0.05 Å s^{-1}) at a pressure of about 10^{-6} mbar from a quartz crucible enclosed by a ceramic boat. On top of the organic material 30 nm gold as electrode material was deposited through a shadow mask (r = 0.2 Å s^{-1}) to obtain the device geometry (L = 100 µm, W = 200 µm). Each resulting film growth

was monitored by a quartz crystal microbalance. OTFTs, which were fabricated with higher substrate temperature were processed in the OPVIvap-XL (Creaphys GmbH). The semiconductor layer was deposited (15 nm, r = 0.04 Å s^{-1}) from a quartz crucible enclosed by a ceramic boat at a pressure below 10^{-6} mbar followed by the evaporation of gold electrodes (30 nm, r = 0.2 Å s^{-1}). The resulting transfer and output characteristics were measured under inert conditions (M. Braun Inertgas Systeme GmbH; c(O_2) < 0.1 ppm, c(H_2O) < 0.1 ppm) with an Agilent 4055C parameter analyzer and a Cascade EPS150 probe station.

AFM morphologies of thin films were investigated with NT-MDT Next Solver System in semi-contact mode by using a SCOUT 350 RAI (Nu Nano Ltd) silicon cantilever (spring constant = 42 N m^{-1}; resonance frequency = 350 kHz).

Organic Photovoltaics were processed on ITO-glass substrates (Soluxx GmbH), which were cleaned by sonication with acetone, detergent solution (mucasol®), deionized water and isopropanol followed by an UV/ozone treatment for 30 min. The substrates are placed into the evaporation system OPTIvap-XL and MoO_3 (d = 6 nm, r = 0.1 Å s^{-1}, ω_{rot} = 10 rpm, p < 10^{-6} mbar) were sublimated on top of the ITO as hole-transporting layer followed by a thickness variation of merocyanine dye **MD376** (r = 0.1 Å s^{-1}, ω_{rot} = 10 rpm, p < 10^{-6} mbar) and the acceptor molecules **CPTQ-R|C_{60}** (r = 0.1 Å s^{-1}, ω_{rot} = 10 rpm, p < 10^{-6} mbar). Bathocuproine (BCP, d = 10 nm, r = 0.1 Å s^{-1}, ω_{rot} = 10 rpm, p < 10^{-6} mbar) and aluminum (d = 100 nm, r = 1-2 Å s^{-1}, p < 10^{-6} mbar) was used as electron transport layer and top electrode. *J-V*-characteristics were measured after calibration with a standard silicon solar cell with a KG filter (ISE Freiburg) under an AM1.5G Oriel Sol3ATM Class AAA solar simulator (Newport®) by a parameter analyzer (Botest Systems GmbH). EQE measurements were carried out with a Quantum Efficiency/IPCE Measurement Kit (Newport®) by using a 300 W Xe lamp and a Cornerstone monochromator with a Merlin Lock-In Amplifier for detection.

5.5.2 Synthesis

Synthesis of precursor compounds **CPDT-R**

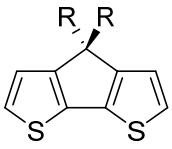

CPDT-R

R =
n-Octyl = **CPDT-Oc**
2-Ethylhexyl = **CPDT-EH**
n-Propyl = **CPDT-Pr**
Phenyl = **CPDT-Ph**

The precursors were synthesized analogue to literature-known procedure. **CPDT-Oc** and **CPDT-Pr** were reported by Zotti *et al.*,[168] **CPDT-EH** by Zhu *et al.*,[169] and **CPDT-Ph** by Hanamura *et al.*[170] The structure of the synthesized precursors were confirmed by ^{1}H NMR spectroscopy.

Synthesis of target compounds **CPTQ-R**:

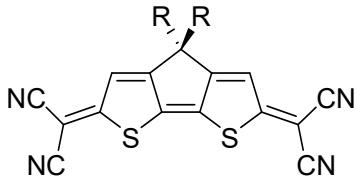

CPTQ-R

R =
n-Octyl = **CPTQ-Oc**
2-Ethylhexyl = **CPTQ-EH**
n-Propyl = **CPTQ-Pr**
Phenyl = **CPTQ-Ph**

Synthesis of **CPTQ-Oc** (as general procedure): Compound **CPDT-Oc** (200 mg, 0.49 mmol) was dissolved in anhydrous DMF (3 mL), and tetracyanoethylene (TCNE, 145 mg ,1.99 mmol) was added to the reaction solution. The color of the reaction solution changed into dark red immediately after addition of TCNE. The reaction mixture was heated at 100 °C for 30 min. TLC analysis showed that the complete consumption of starting materials and the formation of monotricyanovinyl product (upper fraction) and quinoidal target compound **CPTQ-Oc** (second fraction) as major product. After cooling down to room temperature, water was added to the mixture. The aqueous phase was extracted with diethyl ether four times. The combined organic phase was washed with brine to remove residual DMF, dried over Na_2SO_4, and evaporated under reduced pressure. The crude product was purified *via* column chromatography by using hexane/chloroform (2/1 to 1/4, *V*/*V*) as eluent to afford the final product **CPTQ-Oc** as a dark solid with the yield of 31% (83 mg, 0.16 mmol).

2,2'-(4,4-Dioctyl-*2H*-cyclopenta[2,1-*b*:3,4-*b*']dithiophene-2,6(*4H*)-diylidene)dimalono-nitrile (**CPTQ-Oc**):

Yield = 31%

^{1}H NMR ($CDCl_3$, 400 MHz): δ 6.88 (s, 2H), 1.82 (m, 4H), 1.3-1.2 (m, 20H), 1.02 (m, 4H), 0.87 (t, *J* = 7.2 Hz, 6H).

^{13}C NMR ($CDCl_3$, 100 MHz): δ 177.5, 175.6, 145.6, 119.1, 112.6, 112.3, 73.2, 53.0, 38.8, 31.7, 29.6, 29.2, 24.8, 22.6, 14.1.

HRMS (MALDI-TOF, neg. mode, DCTB:$CHCl_3$ (3:1)): *m*/*z* calculated for $C_{31}H_{36}N_4S_2^-$ [M^-] = 528.24, found: = 528.23.

UV-Vis absorption (CH_2Cl_2): λ_{Max} = 531 nm; ε_{Max} = 88200 M^{-1} cm^{-1}

MP = 142 °C (DSC)

Sublimation temperature = 95 °C ($p < 10^{-6}$ mbar)

2,2'-(4,4-Bis(2-ethylhexyl)-*2H*-cyclopenta[2,1-*b*:3,4-*b*']dithiophene-2,6(*4H*)-diylidene)dimalononitrile (**CPTQ-EH**):

Yield: 25%

^{1}H NMR ($CDCl_3$, 400 MHz): δ 6.88 (s, 2H), 1.90 (m, 4H), 1.1 (m, 16H), 0.92 (m, 2H), 0.85 (t, *J* = 7.2 Hz, 6H), 0.74 (t, 6H).

^{13}C NMR ($CDCl_3$, 100 MHz): δ 176.8, 175.7, 145.9, 119.5, 112.5, 112.1, 73.2, 52.5, 44.1, 35.9, 33.8, 28.2, 27.2, 22.9, 14.0, 10.4.

HRMS (MALDI-TOF, neg. mode, DCTB:$CHCl_3$ (3:1)): *m*/*z* calculated for $C_{31}H_{36}N_4S_2^-$ [M^-] = 528.24, found: = 528.23.

UV-Vis absorption (CH_2Cl_2): λ_{Max} = 534 nm; ε_{Max} = 81400 M^{-1} cm^{-1}

MP = 202 °C (DSC)

Sublimation temperature = 80 °C ($p < 10^{-6}$ mbar)

2,2'-(4,4-Dipropyl-*2H*-cyclopenta[2,1-*b*:3,4-*b*']dithiophene-2,6(*4H*)-diylidene)-dimalononitrile (**CPTQ-Pr**):

Yield = 18%

^{1}H NMR ($CDCl_3$, 400 MHz): δ 6.89 (s, 2H), 1.9 (m, 4H), 1.15 - 1.05 (m, 4H), 0.9 (t, J = *7*.2 Hz, 6H),

^{13}C NMR ($CDCl_3$, 100 MHz): δ 177.5, 175.6, 145.7, 119.2, 112.6, 73.2, 53.1, 40.8, 18.2, 14.1.

HRMS (MALDI-TOF, neg. mode, DCTB:$CHCl_3$ (3:1)): *m*/*z* calculated for $C_{21}H_{16}N_4S_2^-$ [M^-] = 388.08, found: = 388.08.

UV-Vis absorption (CH_2Cl_2): λ_{Max} = 531 nm; ε_{Max} = 89100 M^{-1} cm^{-1}

MP = 271 °C (DSC)

Sublimation temperature = 90 °C ($p < 10^{-6}$ mbar)

2,2'-(4,4-Diphenyl-*2H*-cyclopenta[2,1-*b*:3,4-*b*']dithiophene-2,6(*4H*)-diylidene)-dimalononitrile) (**CPTQ-Ph**)

Yield = 29%

^{1}H NMR (400 MHz, CD_2Cl_2): δ 7.4 (m, 6H), 7.15 (m, 4H), 6.94 (s, 2H).

^{13}C NMR (100 MHz, $CDCl_3$): δ 175.7, 173.1, 143.8, 138.6, 128.6, 126.4, 120.6, 111.4, 111.0, 73.1, 59.9.

HRMS (MALDI-TOF, neg. mode, DCTB:$CHCl_3$ (3:1)): *m*/*z* calculated for $C_{27}H_{12}N_4S_2^-$ [M^-] = 456.05, found: = 456.05.

UV-Vis absorption (CH_2Cl_2): λ_{Max} = 534 nm; ε_{Max} = 83200 M^{-1} cm^{-1}

MP = 331 °C (DSC)

Sublimation temperature = 115 °C ($p < 10^{-6}$ mbar)

5.5.3 ^{1}H NMR Spectra

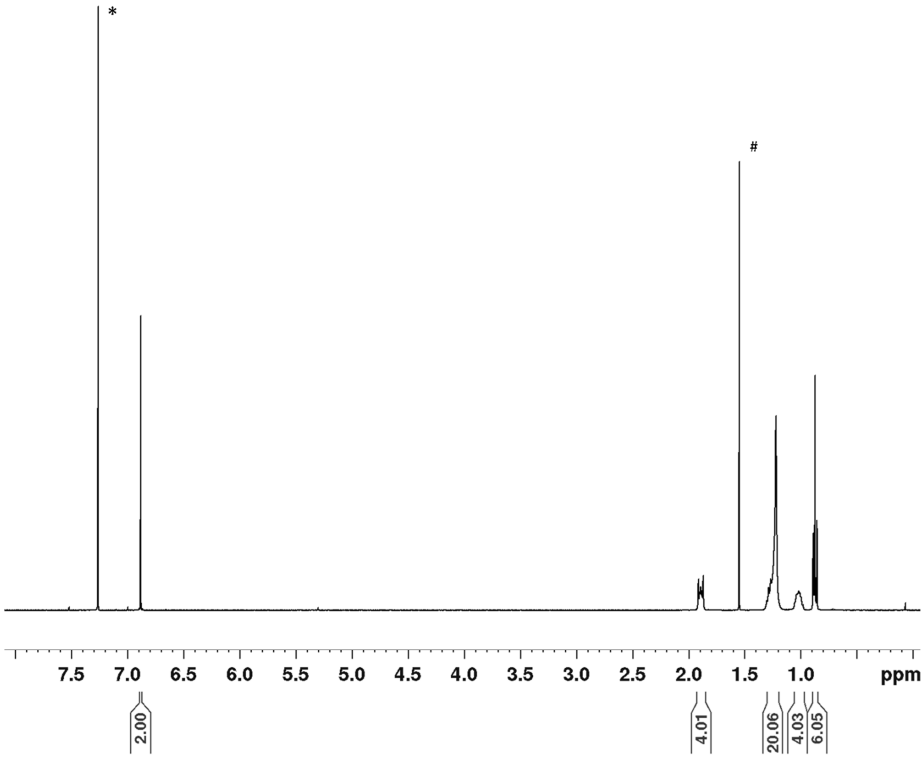

Figure 45: ^{1}H NMR spectrum (400 MHz) of **CPTQ-Oc** measured in $CDCl_3$ at room temperature. * $CHCl_3$, # H_2O.

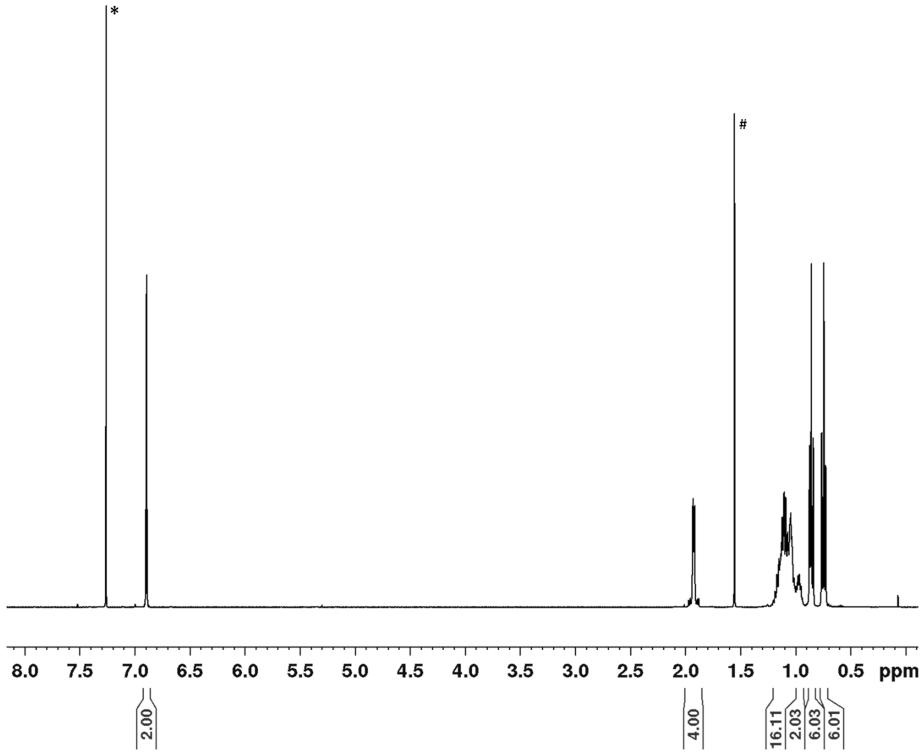

Figure 46: H NMR spectrum (400 MHz) of **CPTQ-EH** measured in $CDCl_3$ at room temperature. * $CHCl_3$, # H_2O.

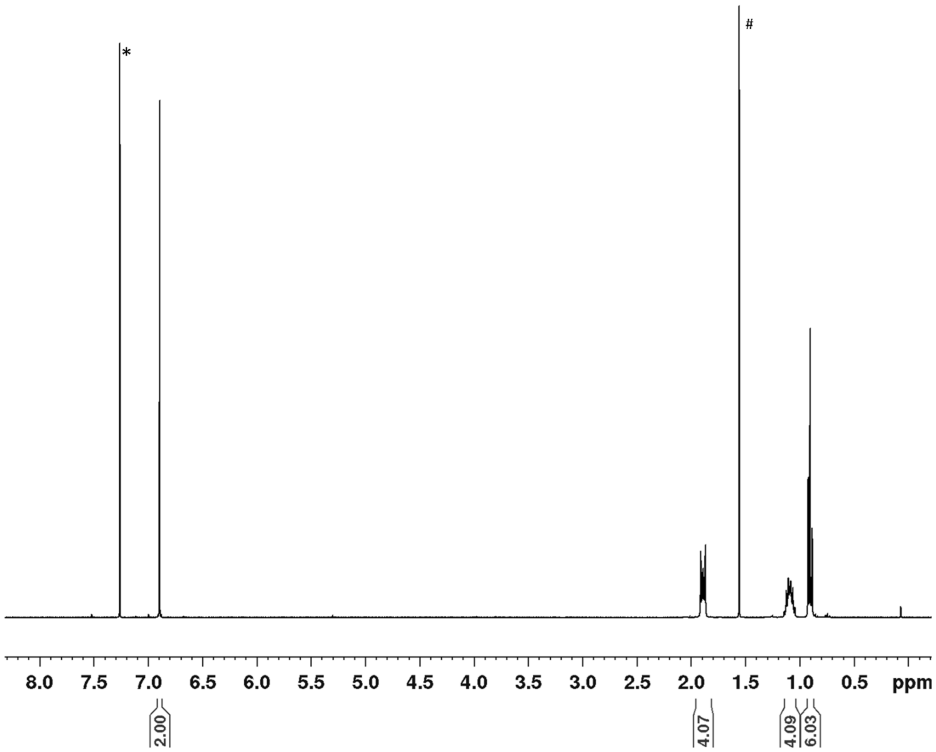

Figure 47: ^{1}H NMR spectrum (400 MHz) of **CPTQ-Pr** measured in $CDCl_3$ at room temperature. * $CHCl_3$, # H_2O.

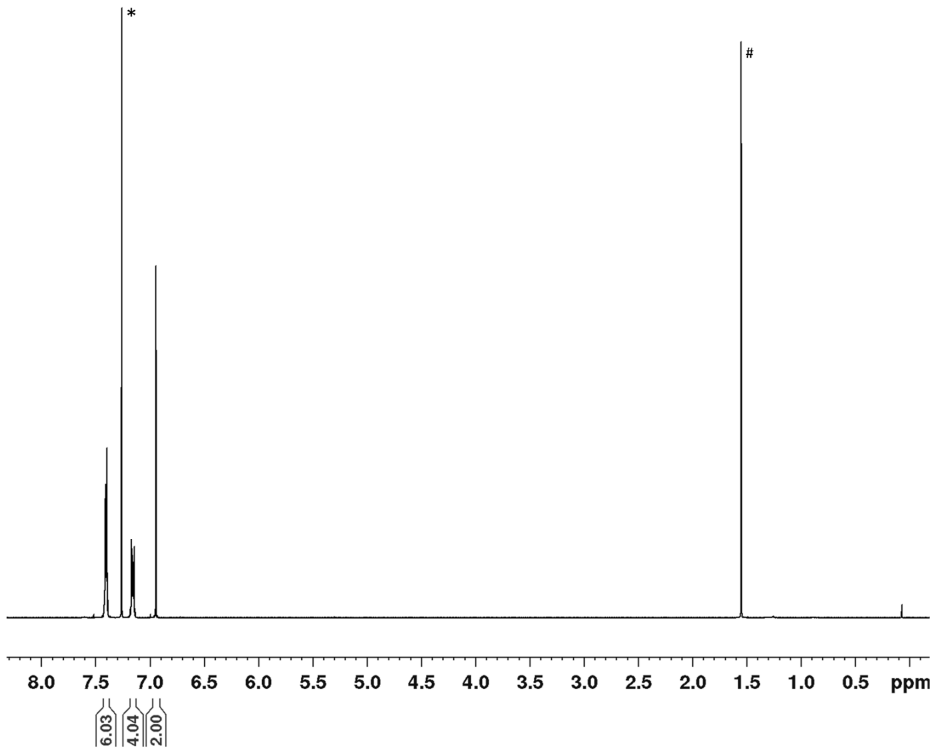

Figure 48: ^{1}H NMR spectrum (400 MHz) of **CPTQ-Ph** measured in $CDCl_3$ at room temperature. * $CHCl_3$, # H_2O.

5.5.4 ^{13}C NMR Spectra

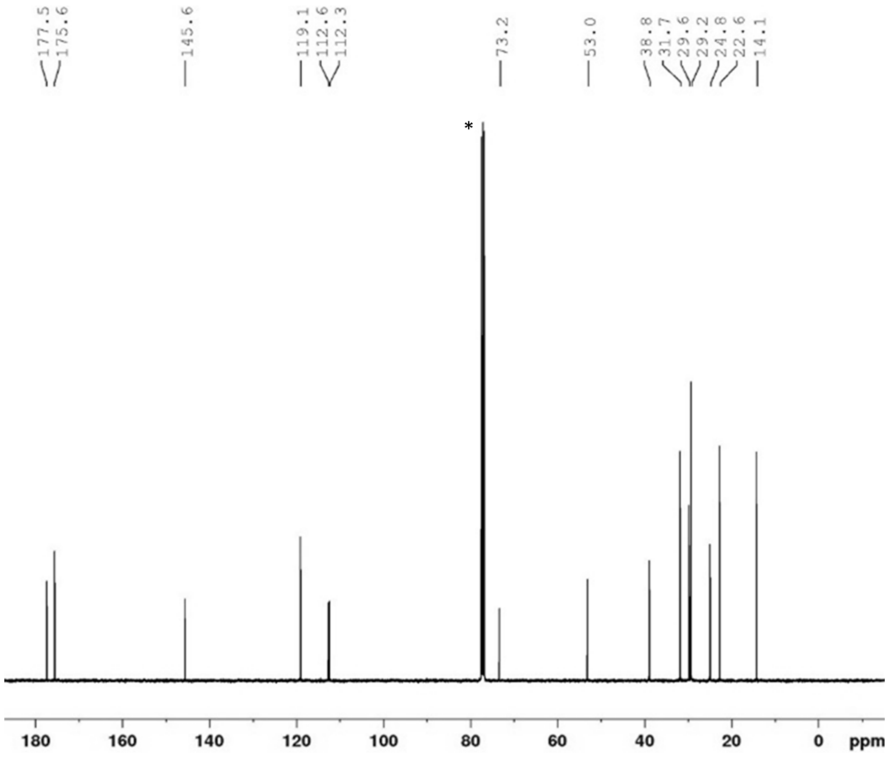

Figure 49: ^{13}C NMR spectrum (100 MHz) of **CPTQ-Oc** measured in $CDCl_3$ at room temperature. * $CHCl_3$.

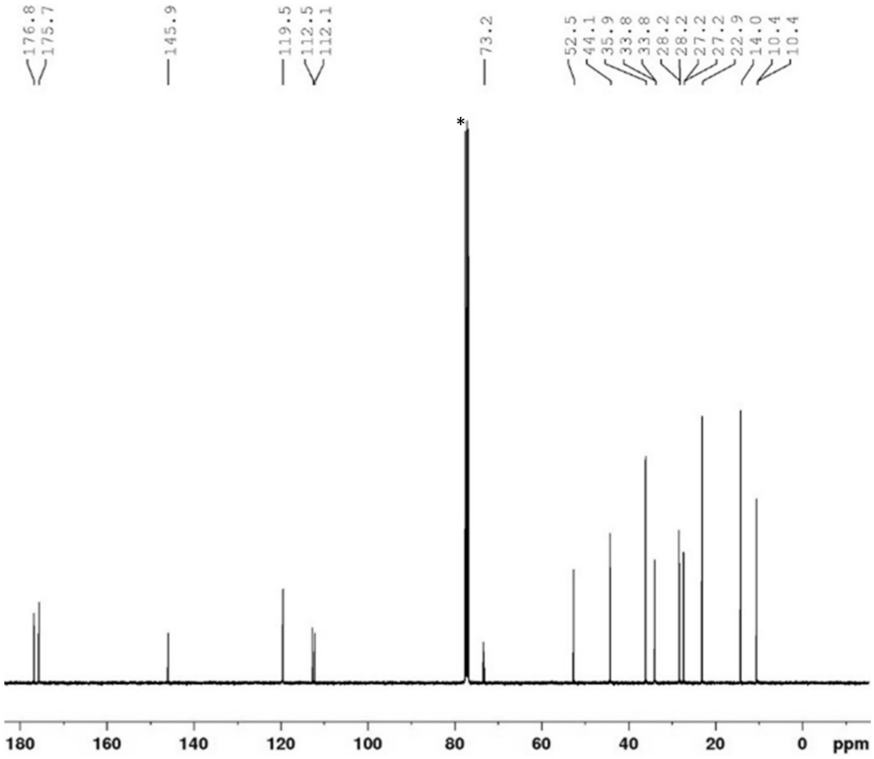

Figure 50: ^{13}C NMR spectrum (100 MHz) of **CPTQ-EH** measured in $CDCl_3$ at room temperature. * $CHCl_3$.

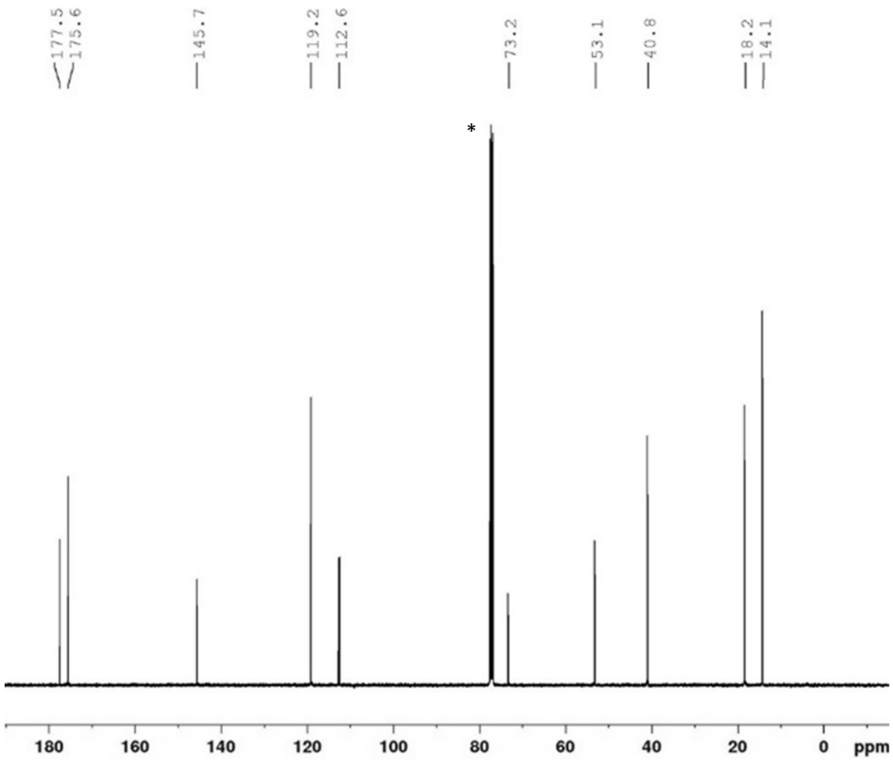

Figure 51: ^{13}C NMR spectrum (100 MHz) of **CPTQ-Pr** measured in $CDCl_3$ at room temperature. * $CHCl_3$.

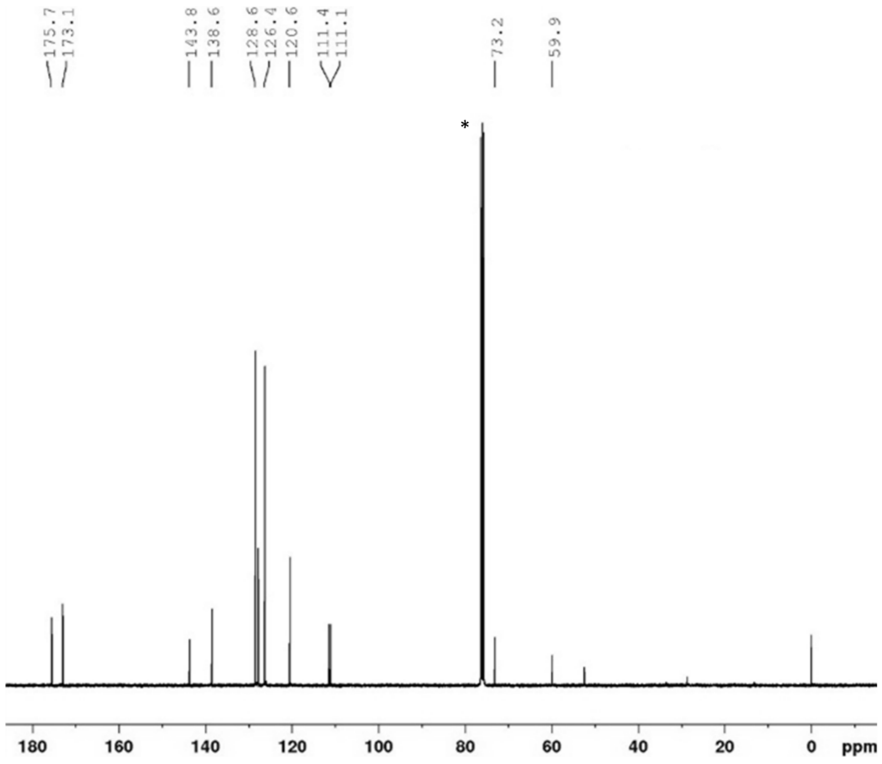

Figure 52: ^{13}C NMR spectrum (100 MHz) of **CPTQ-Ph** measured in $CDCl_3$ at room temperature. * $CHCl_3$.

5.5.5 High-Resolution Mass Spectra

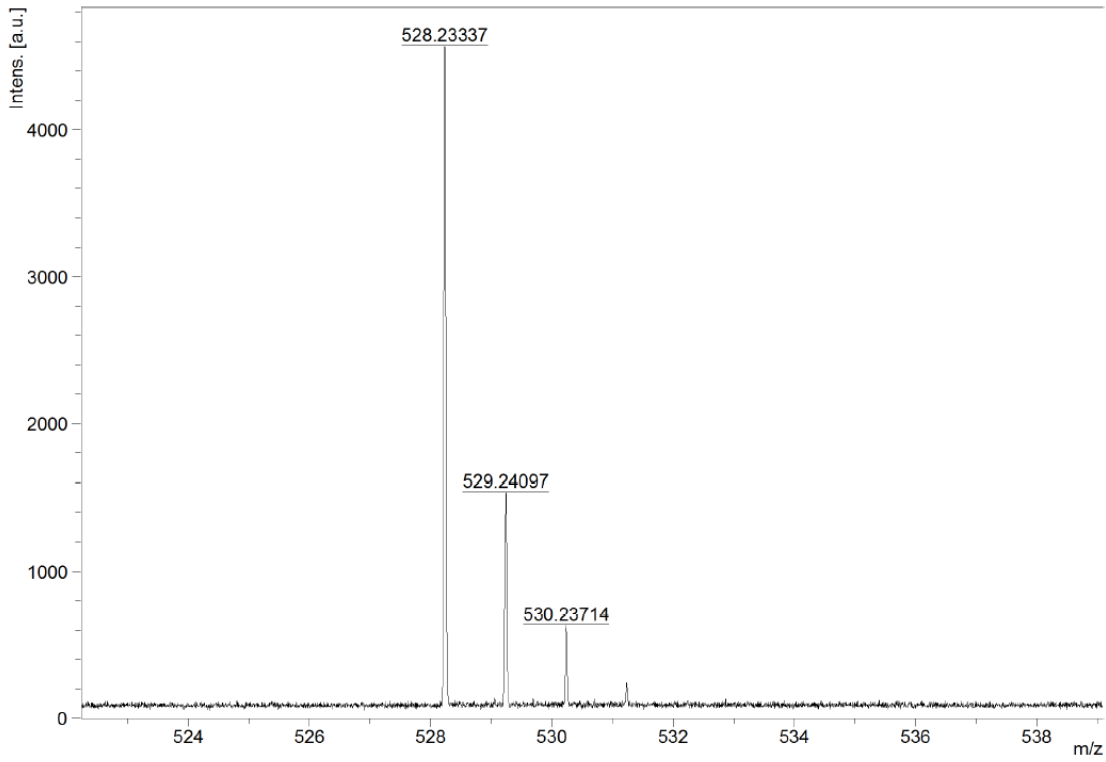

Figure 53: Mass spectrum of **CPTQ-Oc** measured by MALDI-TOF in DCTB:$CHCl_3$ (3:1).

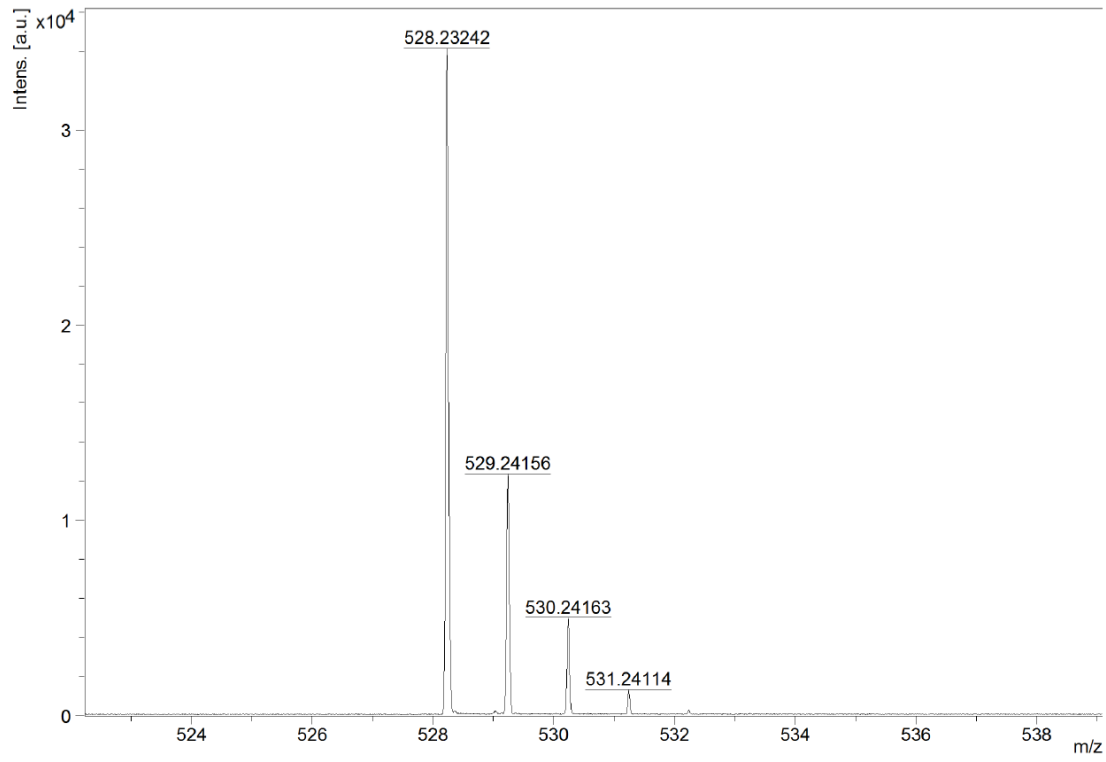

Figure 54: Mass spectrum of **CPTQ-EH** measured by MALDI-TOF in DCTB:$CHCl_3$ (3:1).

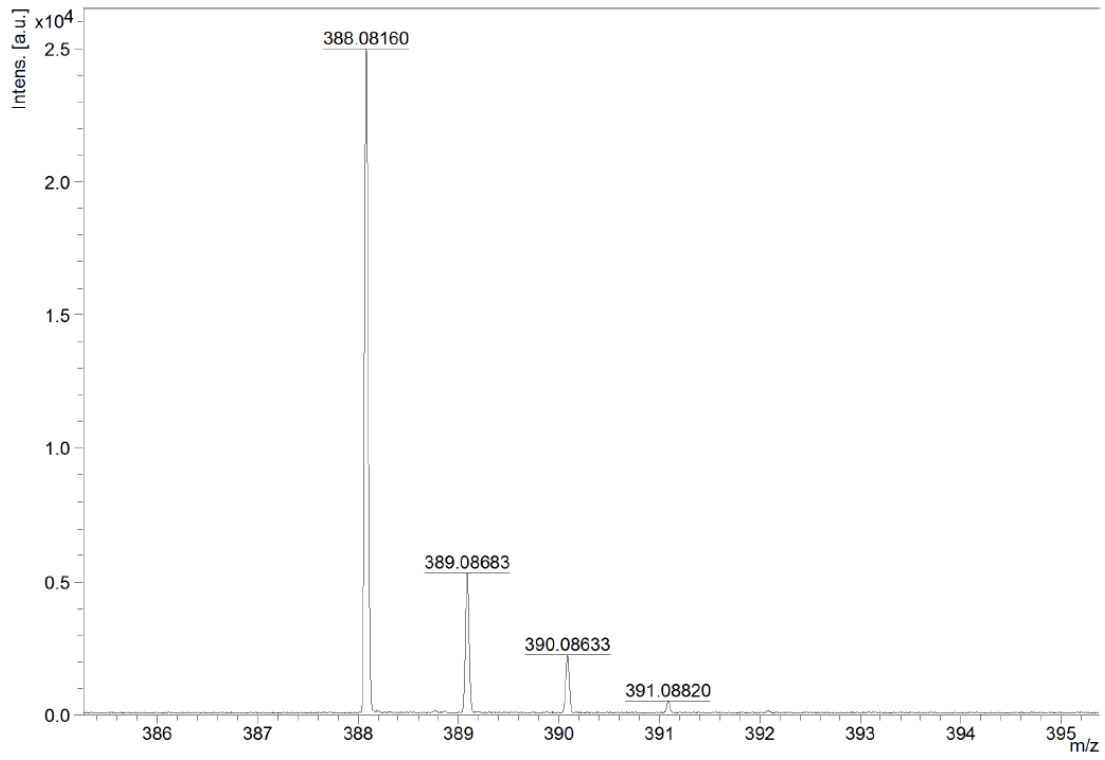

Figure 55: Mass spectrum of **CPTQ-Pr** measured by MALDI-TOF in DCTB:$CHCl_3$ (3:1).

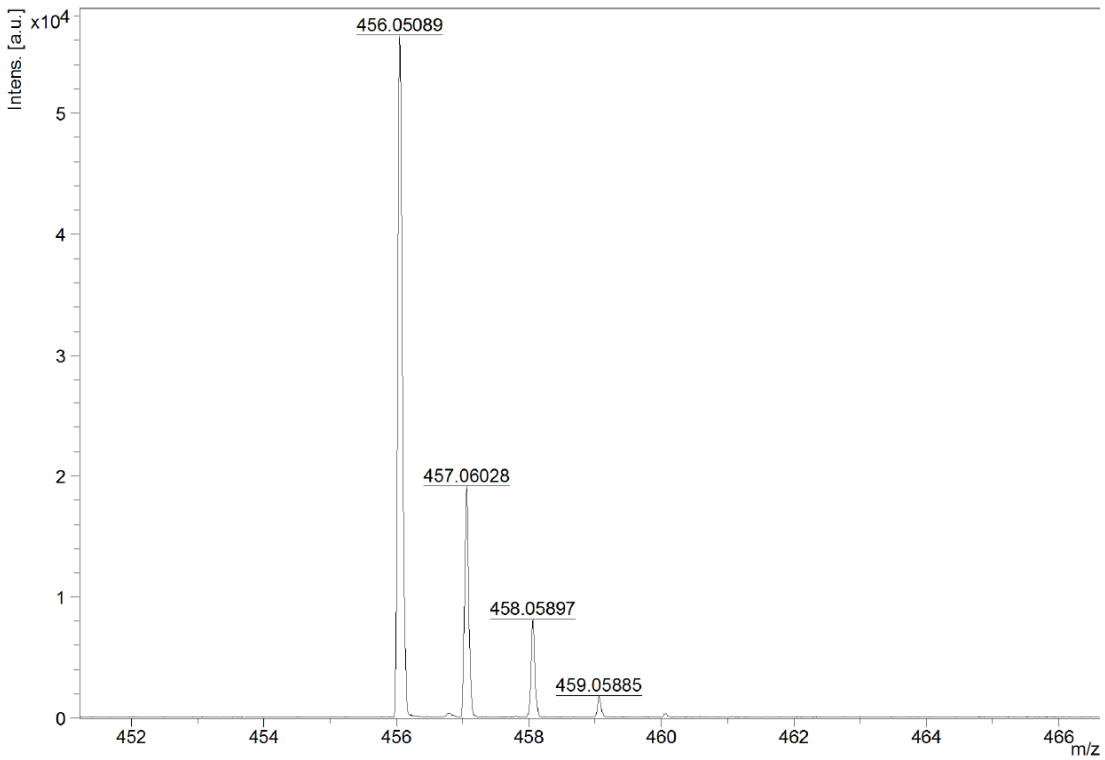

Figure 56: Mass spectrum of **CPTQ-Ph** measured by MALDI-TOF in DCTB:$CHCl_3$ (3:1).

5.5.6 Fluorescence

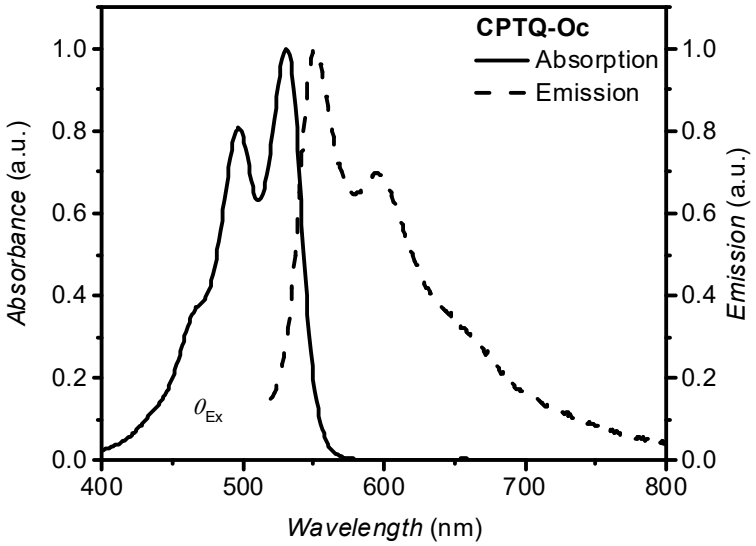

Figure 57: UV-Vis (solid line) and fluorescence (dashed line) spectra of **CPTQ-Oc** measured in CH_2Cl_2.

Table 17: Results from fluorescence measurements for **CPTQ-R** derivatives in CH_2Cl_2 giving rise to emission maxima (λ_{Em}), Stokes shifts, fluorescence quantum yields (Φ_{Fl}) as well as fluorescence lifetimes (τ).

	λ_{Em} (nm)	Stokes Shift (cm^{-1})	Φ_{Fl} (%)	τ^a (ns)
CPTQ-Oc	551	680	< 1	< 0.5
CPTQ-EH	549	510	< 1	< 0.5
CPTQ-Pr	549	620	< 1	< 0.5
CPTQ-Ph	549	510	< 1	< 0.5

[a] The fluorescence lifetimes are below the instrument response time of the TCSPC setup.

5.5.7 X-Ray

Table 18: X-ray structure characteristics for **CPTQ-R** derivatives.

	CPTQ-Oc	**CPTQ-EH**	**CPTQ-Pr**	**CPTQ-Ph**
Empirical formula	$C_{31}H_{36}N_4S_2$	$C_{31}H_{36}N_4S_2$	$C_{21}H_{16}N_4S_2$	$C_{27}H_{12}N_4S_2$
$M_{empirical}$ (g mol^{-1})	528.76	528.76	388.50	456.53
Wavelength (Å)	1.54178	1.54178	1.54178	1.54178
T (K)	100	100	100	100
Description of the crystal				
Color	Red	Red	Red	Red
Habit	Needle	Block	Block	block
Crystal System	Monoclinic	Triclinic	Triclinic	Monoclinic
Space group	C2/c	P-1	P-1	P 21/c
Unit cell dimension				
a (Å)	36.1243	11.2766	8.0883	15.1209
b (Å)	13.4326	14.5164	9.7191	10.3600
c (Å)	26.6643	19.2705	12.9959	16.1591
α (°)	90	81.129	95.349	90
β (°)	115.541	78.6665	103.060	117.608
γ (°)	90	88.437	96.387	90
Volume (Å^3)	11674.3	3056.0	981.6	2243.1
Z	16	2	2	4
$p_{calc.}$ (g cm^{-3})	1.203	1.149	1.314	1.352
F(000)	4512	1128	404	936
Range of θ (°)	2.71 – 71.91	2.36 – 68.45	3.51 – 72.52	3.29 – 72.16
Goodness of Fit	1.051	1.109	1.063	1.062
CCDC	2011168	2011165	2011167	2011166

Table 19: Indexed thin-film diffraction reflexes for sublimated thin film of **CPTQ-Oc** on TPA-modified $Si|SiO_2|AlO_x$ substrates with a substrate temperature of 40 °C.

$2\Theta_{TF}$ (°)	$2\Theta_{SC}$ (°)	h	k	l
4.8	5.4	2	0	0
6.4	7.1	1	1	0
7.0	7.3	0	0	2
14.4	14.7	0	0	4
19.3	-	-	-	-
21.2	22.1	0	0	6
24.2	-	-	-	-
28.4	29.6	0	0	8
29.2	-	-	-	-

Table 20: Calculated transfer integrals for holes (t_+) and electrons (t_-) between closest neighbors in **CPTQ-R** single-crystal structures via ADF. For the indexed neighbors see Figure 40.

CPTQ-R	Neighbor	t_+ (meV)	t_- (meV)	**CPTQ-R**	Neighbor	t_+ (meV)	t_- (meV)
CPTQ-Oc	(1)	−27	24	**CPTQ-Pr**	(1)	38	32
	(2)	−26	23		(2)	8	5
	(3)	−106	1		(3)	105	−1
	(4)	−3	1		(4)	27	35
	(5)	−17	−120		(5)	37	−3
	(6)	198	−128		-	-	-
CPTQ-EH	(1)	−22	19	**CPTQ-Ph**	(1)	5	−6
	(2)	4	1		(2)	−34	1
	(3)	133	1		(3)	−34	1
	(4)	−1	−4		(4)	24	−28
	(5)	5	0		(5)	22	−29

5.5.8 DSC & TGA

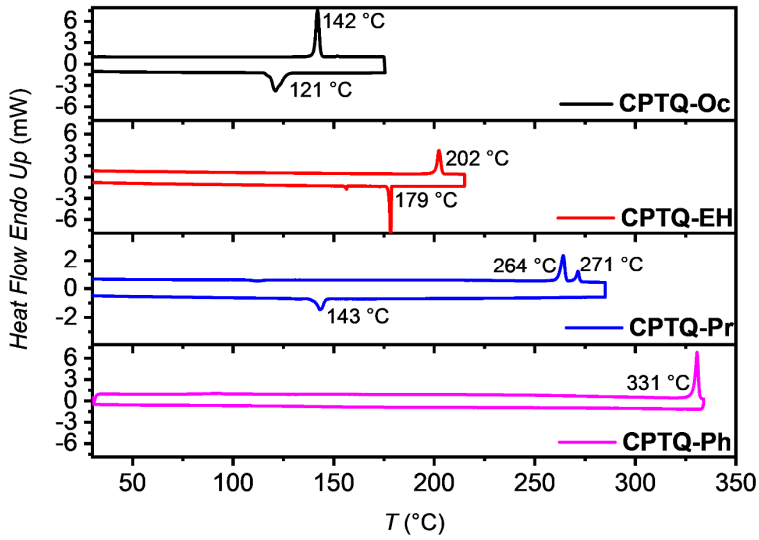

Figure 58: Differential scanning calorimetry traces of **CPTQ-Oc** (black), **CPTQ-EH** (red), **CPTQ-Pr** (blue) and **CPTQ-Ph** (pink) in second heating process. The heating and cooling rates were 10 °C min^{-1}. **CPTQ-Ph** shows a decomposition directly after its melting point at 331 °C.

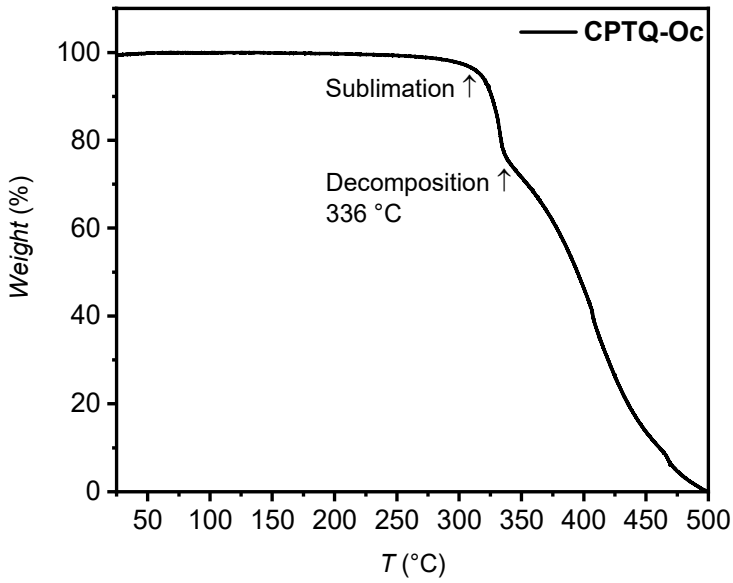

Figure 59: Representative TGA trace of **CPTQ-Oc**. The measurement was performed with ceramic pans under a flow of N_2 with a heating rate of 5 °C min^{-1}. Due to the sublimation process, which also occurs at 1 atm, the informative value of TGA experiments is limited.

5.5.9 OTFT

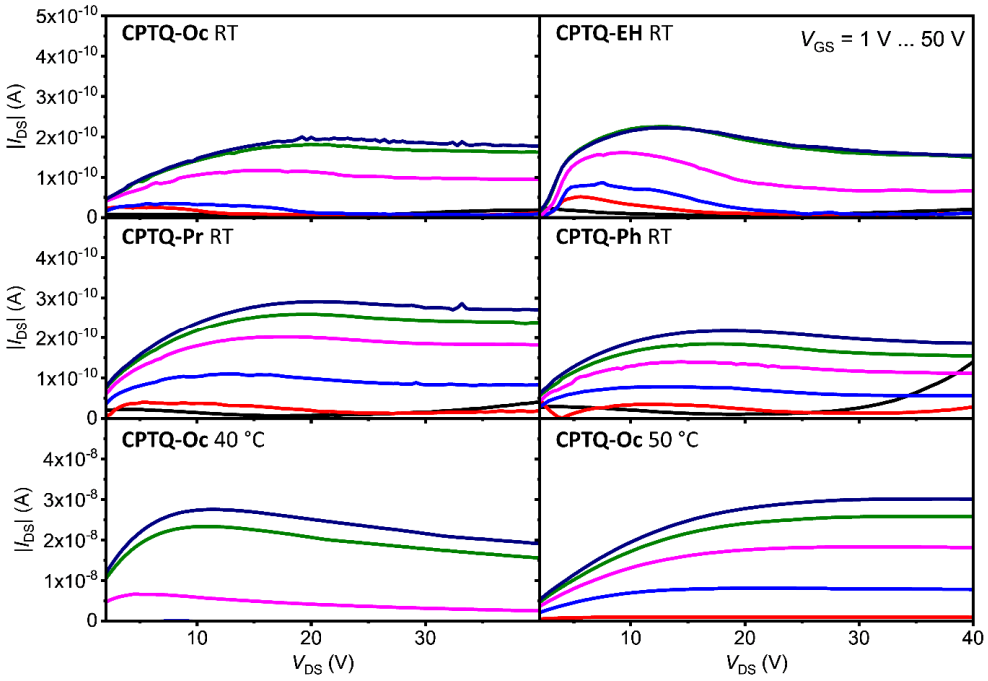

Figure 60: Output characteristics for Si|SiO_2|AlO_x|TPA|**CPTQ-R**|Au based OTFTs processed at different substrate temperatures. For OTFTs at elevated substrate temperature, the semiconductor layer thickness was decreased from 30 nm to 15 nm.

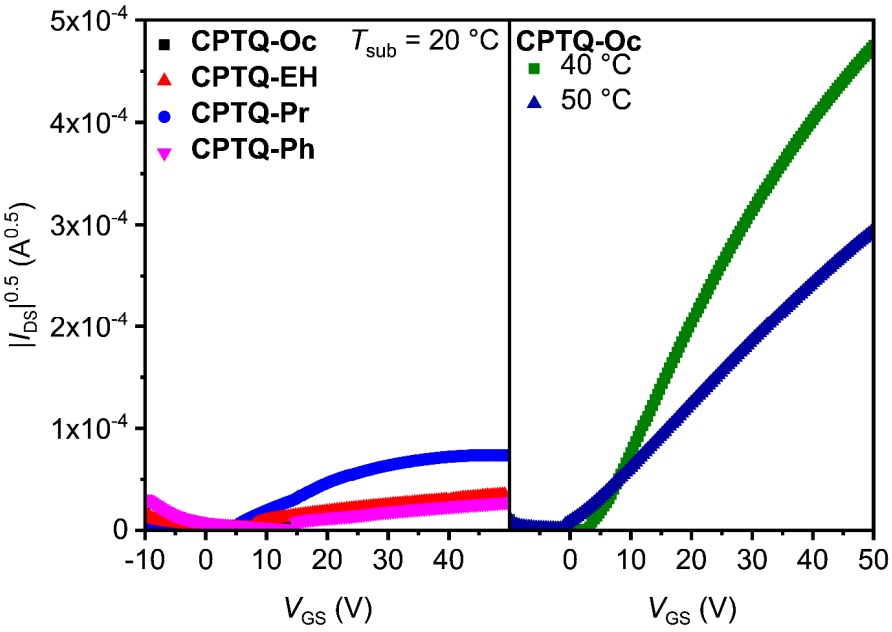

Figure 61: Square-root plot for Si|SiO_2|AlO_x|TPA|**CPTQ-R**|Au based OTFTs processed at different substrate temperatures and layer thicknesses (left: 30 nm, right: 15 nm).

5.5.10 AFM

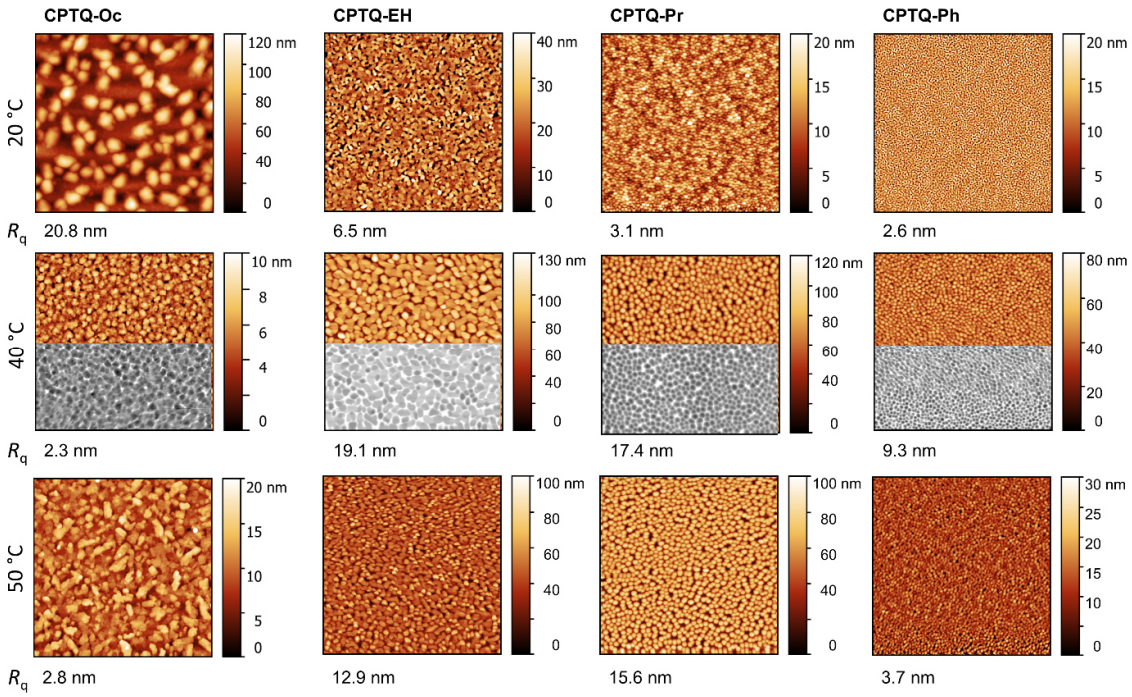

Figure 62: AFM images of vacuum-processed layers of **CPTQ-R** on TPA-modified Si|SiO_2|AlO_x substrates deposited at different substrate temperatures of 20 °C (top), 40 °C (middle) or 50 °C (bottom, 10×10 µm²). The negative images (40 °C) clearly show the substrate stage as white background for all thin films. However, while the domains of **CPTQ-Oc** increase in size and are in contact with each other to maintain charge percolation pathways, the domains of the other derivatives at elevated substrate temperatures are not connected and accordingly this discontinuous thin films only show minor or no charge transport.

5.5.11 OPV

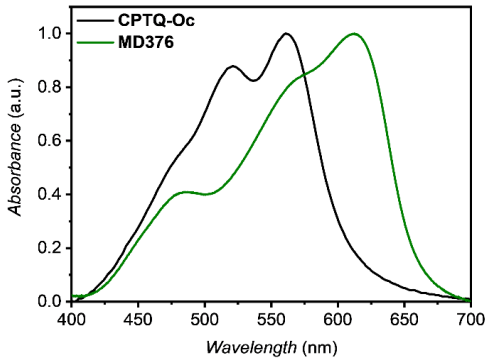

Figure 63: Thin-film absorption spectra of a 30 nm layer obtained by sublimation of **CPTQ-Oc** (black line) compared with **MD376** (green line).

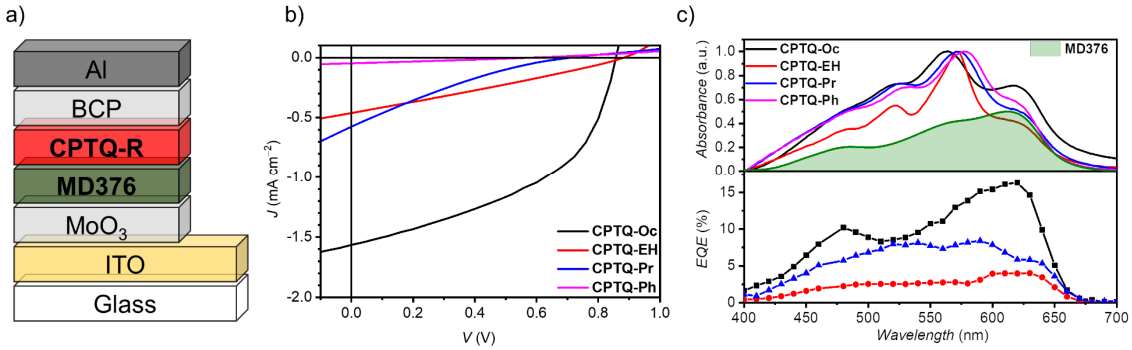

Figure 64: a) Schematic representation of the architecture of the vacuum-processed planar-heterojunction (PHJ) organic solar cells. b) *J-V* curves of vacuum-processed PHJ organic solar cells based on **MD376** as donor and **CPTQ-Oc** (black), **CPTQ-EH** (red), **CPTQ-Pr** (blue) and **CPTQ-Ph** (pink) as acceptor materials, which were measured under AM 1.5G conditions. c) EQE (bottom) and UV-Vis (top) spectra of **CPTQ-R** based OSC combined with merocyanine dye **MD376** as donor and its thin-film absorption (green). EQE spectra could not be obtained for **CPTQ-Ph** due to insufficient J_{SC}.

Table 21: Photovoltaic parameters[a] for ITO|MoO_3|**MD376**|**CPTQ-R**|BCP|Al based OPVs measured under inert conditions and under AM 1.5G irradiation.

Acceptor	$d_{Do.}$ (nm)	$d_{Ak.}$ (nm)	J_{SC} (mA cm^{-2})	V_{OC} (V)	FF (%)	PCE (%)	PCE^{Max} (%)
CPTQ-EH[a]	15	15	−0.46 ± 0.01	0.88 ± 0.01	27 ± 1	0.11 ± 0.01	0.11
CPTQ-Pr[a]	20	20	−0.40 ± 0.1	0.74 ± 0.04	17 ± 1	0.05 ± 0.02	0.08
CPTQ-Ph[b]	10	10	−0.02 ± 0.001	0.48 ± 0.01	28 ± 1	0.004 ± 0.001	0.06

Average of at least five[a] or three[b] independent working devices.

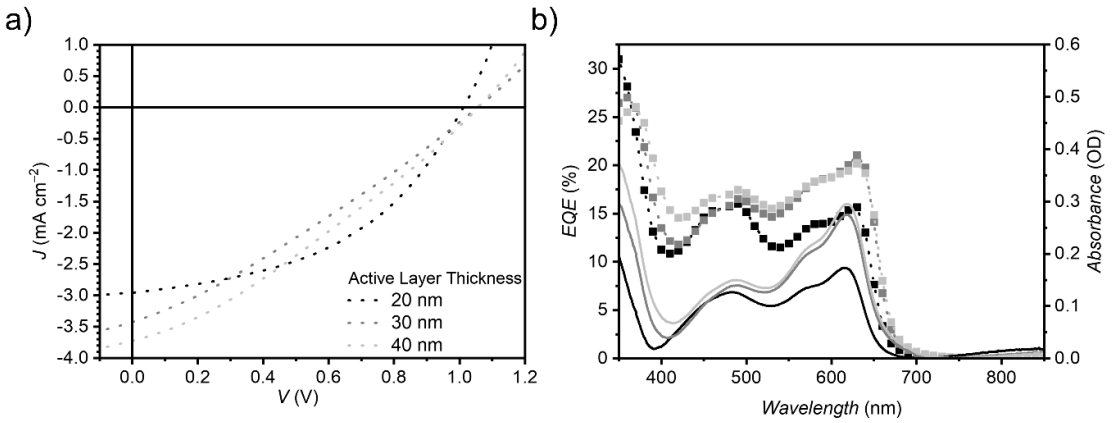

Figure 65: *J-V* curves (a) and EQE and UV-Vis spectra (b) of vacuum-processed planar-heterojunction organic solar cells based on different layer thicknesses of **MD376** as donor and of **C_{60}** as acceptor (20 nm, 30 nm, 40 nm), which were measured under AM 1.5G conditions.

Table 22: Photovoltaic parameters[a] for ITO|MoO_3|**MD376**|**C_{60}**|BCP|Al based OPV measured under inert conditions and under AM 1.5G irradiation.

$d_{Do.}$ (nm)	$d_{Ak.}$ (nm)	J_{SC} (mA cm^{-2})	V_{OC} (V)	FF (%)	PCE (%)	PCE^{Max} (%)
10	10	−2.9 ± 0.1	1.02 ± 0.03	43 ± 2	1.25 ± 0.08	1.39
15	15	−2.8 ± 0.1	1.04 ± 0.01	26 ± 2	0.79 ± 0.17	1.05
20	20	−3.1 ± 0.1	1.04 ± 0.01	26 ± 2	0.82 ± 0.22	1.20

[a] Average of at least five independent working devices.

Chapter VI: Bowl-Shaped Naphthalimide Annulated Corannulene as Non-Fullerene Acceptor in Organic Solar Cells

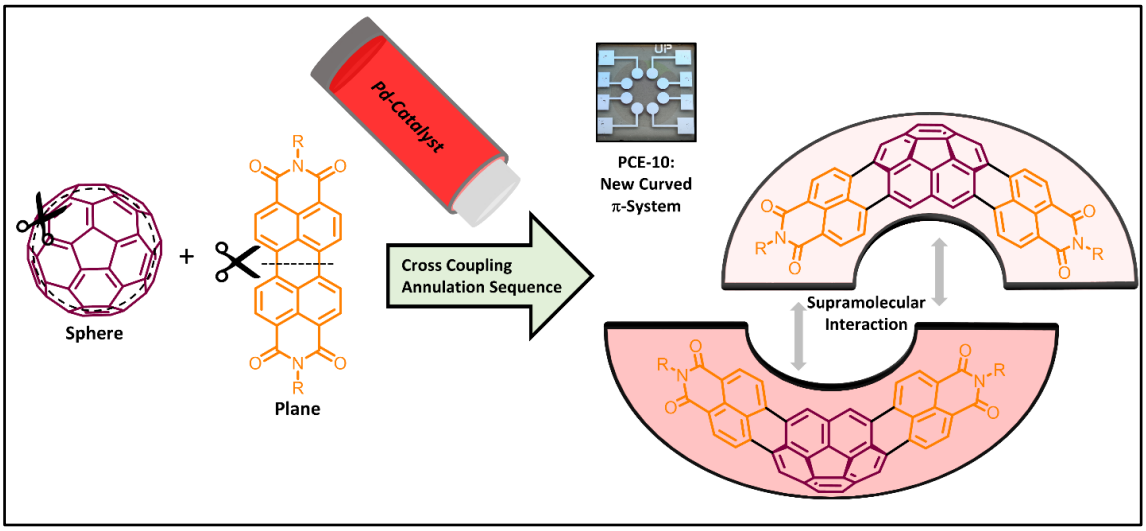

This Chapter was published by

K. Menekşe, R. Renner, B. Mahlmeister, M. Stolte and F. Würthner

in *Organic Materials,*

2020, *3*, 229-234. Reprinted with Permission.

6.1 Abstract

An electron-poor bowl-shaped naphthalimide-annulated corannulene with branched alkyl residues in the imide position was synthesized by a palladium-catalyzed cross-coupling annulation sequence. This dipolar compound exhibits strong absorption in the visible range along with a low-lying LUMO level at–3.85 eV, enabling n-type charge transport in organic thin-film transistors (OTFTs). Furthermore, we processed inverted bulk-heterojunction (BHJ) solar cells in combination with the two donor polymers **PCE-10** and **PM6** to achieve open-circuit voltages (V_{OC}) up to 1.04 V. By using a blend of the self-assembled naphthalimide-annulated corannulene and **PCE-10**, we were able to obtain a power conversion efficiency (PCE) of up to 2.1%, which is to the best of our knowledge the highest reported value for a corannulene-based organic solar cell to date.

6.2 Introduction

Nonplanar polycyclic aromatic hydrocarbons (PAHs) have started to gain more attention as alternative electron acceptor materials in organic electronics to replace fullerenes and their soluble derivatives.[171-175] Due to their improved solubility compared to their planar PAH counterparts along with the possibility to tune the electronic properties by substitution, these molecules are promising candidates for application in organic photovoltaics (OPVs).[176,177] These nonplanar molecules are commonly implemented in bulk-heterojunction organic solar cells (OSCs) by derivatives of three dimensional perylene bisimide (PBI) architectures[178-180] or the bowl-shaped subphthalocyanine family.[176,181,182]

Corannulene, which is another example of bowl-shaped PAHs and a subunit of fullerene C_{60}, has been used in organic electronics after the first synthesis in 1966 by Lawton and Barth, repeatedly.[183,184] Its derivatives have been applied in organic field-effect transistors (OFETs),[185-187] organic light-emitting diodes (OLEDs)[188,189] and in nonlinear optics.[190] Due to its structural similarity to fullerenes, which are still the state-of-the-art acceptor materials in OPVs,[191] OSCs using corannulene and its derivatives have been fabricated by different groups.[192] By substituting the phenyl group in the widely used phenyl-C_{61}-butyric acid methyl ester (**$PC_{61}BM$**) with corannulene, a new fullerene-corannulene dyad has been successfully

† In 2022 the most efficiency corannulene-based OSCs yielded 11.1%.[51]

synthesized. This new molecule was implemented in the device using the donor polymer **P3HT**, resulting in a power conversion efficiency (PCE) of 1.05%.[193] Furthermore, a series of decakis(arylthiol)corannulenes was used as electron-accepting materials achieving the highest reported PCE for corannulene-based BHJ OSCs to date of 1.23%.[194] The first reported example of a corannulene-based solar cell, however, utilizes a derivative, in which the electron accepting abilities are enhanced by coupling the bowl-shaped PAH to either a phthalimide or a naphthalimide, respectively. By this means, Lu *et al.* were able to show a significant lowering of the LUMO level to –3.24 eV and better miscibility with **P3HT** compared to pristine corannulene, leading to a PCE of up to 1.03%.[195]

Recently, we reported the synthesis[196] and self-assembly[197] of new dipolar naphthalimide-annulated corannulene (NAC) derivatives. Both, mono- and disubstituted NAC derivatives exhibit beneficial optoelectronic properties for use as non-fullerene acceptors (NFA) in OSCs, such as the broad absorption between 400 and 600 nm and a low lying LUMO level of −3.88 eV. The so-far introduced residues in the imide position, 2,6-2,6-di-*iso*-propylphenyl (Dipp) and 3,4,5-tris(dodecyl)phenyl (TDP) proved to be less suitable to the use in OSCs due to the extensive inactive alkyl content of the latter and the prevention of intimate π-π interactions and thus suboptimal charge transport of the former. Thus, we decided to synthesize a new derivative, which combines the optoelectronic advantages of the double NAC motif with high solubility and proper aggregation properties. By introduction of a branched alkyl chain, the desired solubility could be maintained and the new material was successfully implemented as a NFA in inverted BHJ OSCs.

6.3 Results and Discussion

Corannulene derivative **4** was synthesized according to Scheme 2 by a palladium-catalyzed Suzuki cross-coupling using tri(*m*-tolyl)phosphine as a ligand followed by a Heck-type annulation reaction using tri(1-adamantyl)phosphine as a ligand and at a significantly higher temperature of 170 °C, as reported previously, to enable the annulation reaction.[195,196] By applying this sequential two-step synthesis,[198] it was possible to obtain **4** in an adequate yield of 41% to get a sufficient amount of highly-soluble material for the use in OSCs. In toluene, up to 51 mg mL^{-1} could be dissolved.

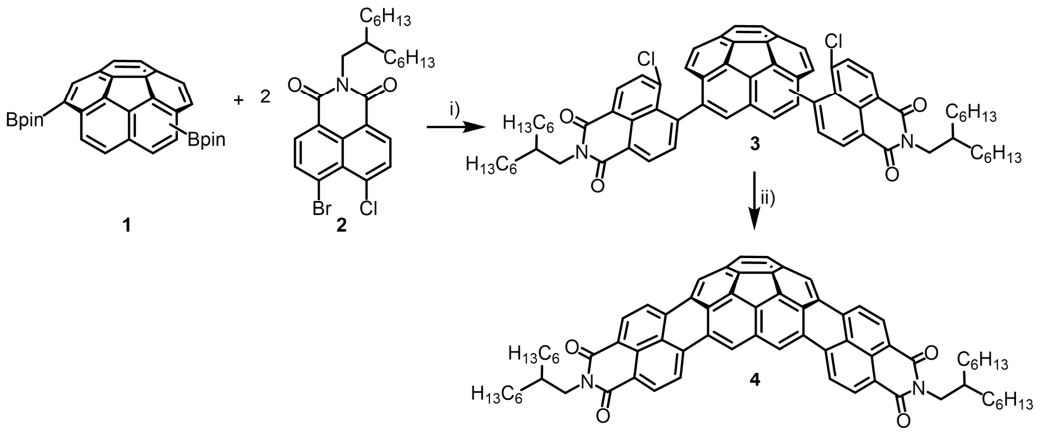

Scheme 2: Synthetic scheme for corannulene derivative **4**: (i) $[Pd_2(dba)_3]\cdot CHCl_3$,P(m-tolyl)$_3$, Cs_2CO_3, 1-chloronaphthalene, 110 °C, 2d; (ii) $[Pd_2(dba)_3]\cdot CHCl_3$, PAd_3, Cs_2CO_3, Bu_4NCl, 1-chloronaphthalene, 170 °C, 16 h. Detailed synthetic procedures are reported in Chapter 6.5.

The new derivative was characterized using nuclear magnetic resonance spectroscopy (NMR) and high-resolution mass spectrometry (HRMS). The optical properties were measured by using UV-Vis and fluorescence spectroscopy in dichloromethane solution, to avoid any possible aggregation, similar to a previously reported derivative[196] (Figure 66, for details see chapter 6.5.3). The absorption maximum (λ_{Max}) is observed at 503 nm with an extinction coefficient of 44600 L mol^{-1} cm^{-1} (Table 24). Due to the electron-poor naphthalimide annulation of the electron-rich corannulene core, which leads to an extension of the π-system, the absorption is significantly red-shifted compared to the parent corannulene and Suzuki-coupled derivatives,[194] as well as the monoannulated derivative.[195] Even more important is the huge increase in absorptivity with respect to the benchmark acceptor **C_{60}**, which should augment the light-harvesting ability in an OSC (Figure 66). The optical band gap has been estimated to be 2.17 eV from the onset of the absorption band in solution. The emission maximum (λ_{Ex}) at 572 nm as well as the fluorescence quantum yield (Φ_{Fl}) of 46% and fluorescence lifetime (τ) of 5.19 ns are also in good accordance with previously reported values for the Dipp derivative, given the fact that the imide substituent has only minor impact on optoelectronic properties but influences the solubility, self-assembly as well as the solid state packing (Table 24).

Further studies of the self-assembly of the new derivative **4** by UV-Vis spectroscopy in toluene revealed the ability to form defined aggregates in this aromatic solvent at high concentrations (Figure 70). The process could be ascribed to an anti-

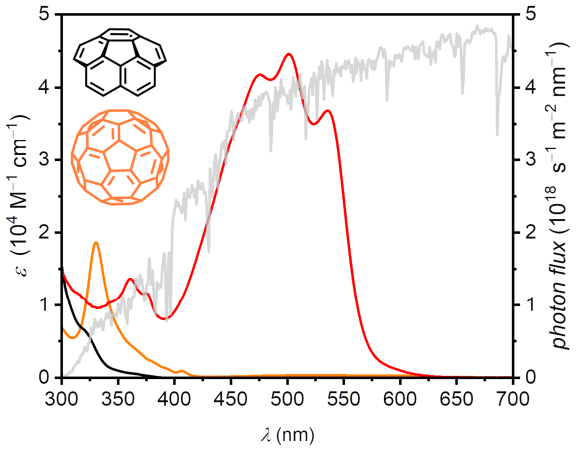

Figure 66: UV-Vis absorption spectra of **C$_{60}$** (orange), corannulene (black), and the new corannulene derivative **4** (red) at 10^{-5} M in CH_2Cl_2 in comparison to solar photon flux under AM 1.5G conditions (grey).

cooperative nucleation-elongation mechanism of **4**, where the formation of dimers is highly favored over the formation of extended structures. In toluene, the application of the K_2-K aggregation model[199] using a nucleus size of two gave $K = 6.5\times10^2\,M^{-1}$, $K_2 = 5.2\times10^3\,M^{-1}$ and a cooperativity factor $\sigma = 8$, indicating only slightly lower tendency to aggregate compared to the previously reported TDP system.[197] This preorganization into well-defined small aggregate entities with high tinctorial strength and electron affinity in solution will affect the morphology of thin films and the efficiency as a NFA in OPV (*vide infra*).

The optical signature of the spin-cast thin film of **4** on quartz (Figure 67b) resembles the hypsochromically-shifted features of aggregated NAC chromophores with an absorption maximum at about 465 nm of the previously investigated NAC dimer species in solution (Figure 71).[197] However, this hypsochromically shifted absorption of **4** in the thin film enables excellent complementary absorption of solar light with the most common donor polymers in the visible up to the near-infrared spectral region (Figure 67a,b). The donor polymer **PM6** absorbs light in the range from 570 to 700 nm. **PCE-10** shows an even more bathochromically-shifted absorption in comparison to **PM6** up to 800 nm. The electrochemical properties were characterized by cyclic and square wave voltammetry in dichloromethane (Figure 78). The molecule showed three reversible reduction processes, of which the first two could not be observed completely separated at approximately −1.25 V, −1.37 V and −1.74 V, and two irreversible oxidation processes at 1.00 V and 1.24 V. The HOMO and LUMO energy levels were calculated to be at −6.10 eV and −3.85 eV,

respectively according to the assumption that the energy level of the Fc/Fc^+ redox couple is −5.1 eV relative to vacuum.[200] With this the prerequisites for the use of the new compound as a NFA in OSC are given. Additionally, the LUMO-level of **4** is also comparable to that of commonly used **$PC_{61}BM$**. Due to a slightly higher LUMO-level for **4** compared with **$PC_{61}BM$** higher open-circuit voltages (V_{OC}) are expected. Solution-processed solar cells based on **PCE-10** and **PM6** (Figure 2c) demonstrate the influence of the HOMO of the donor polymer to the V_{OC}, due to their difference in E_{HOMO} and the resultant gap to the LUMO level of the acceptor of 1.4 eV (**PCE-10**) and 1.6 eV (**PM6**) respectively. The photovoltaic properties were investigated under optimized conditions in an inverted device architecture (ITO|ZnO|Polymer:**4**|MoO_3|Al). The architecture of the OSC, the representative *J-V* curves as well as the UV-Vis and external quantum efficiency (EQE) spectra for the best-performing devices are depicted in Figure 67. The photovoltaic parameters are listed in detail in Table 23. We optimized the processing parameters of the total concentration, donor-acceptor ratio and additives for the **PCE-10**:**4** based OPV (Figure 79-87) to achieve the highest so far reported PCE of a corannulene-based

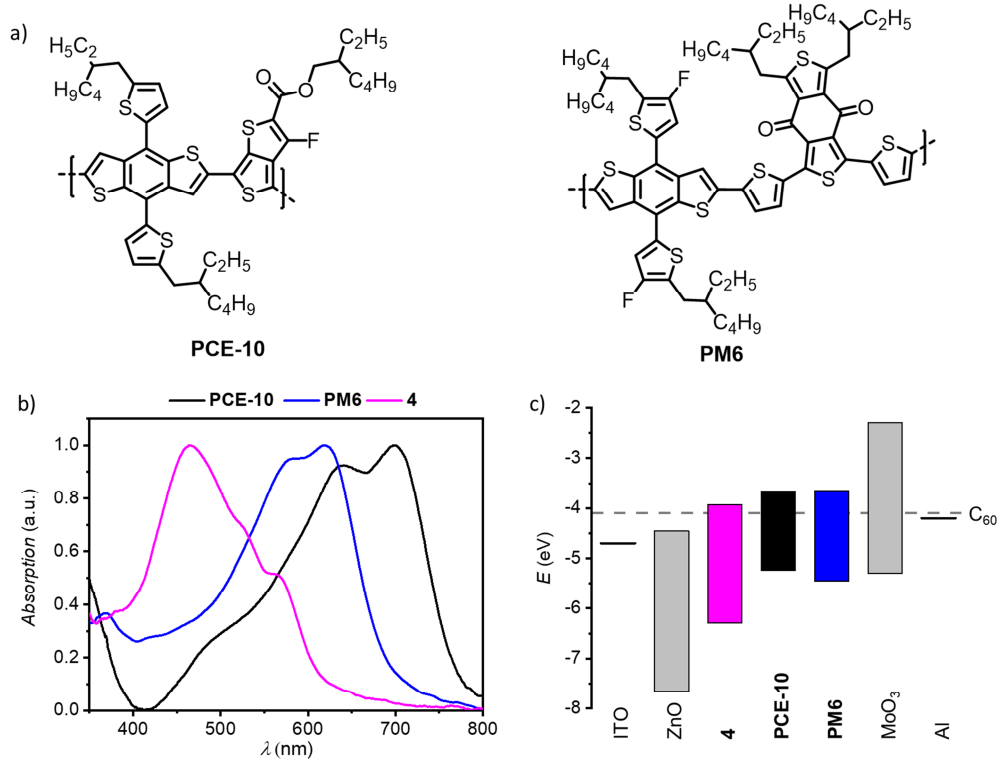

Figure 67: (a) Chemical structures of donor polymers **PCE-10** and **PM6**. (b) Normalized UV-Vis spectra of spin-coated thin films of donor polymers **PCE-10** (black), **PM6** (blue) and corannulene derivative **4** (pink) on quartz (chlorobenzene, 7.5 mg mL^{-1}). (c) Schematic diagram of the electrical band gaps for all materials used in OPV experiments. The E_{LUMO} of fullerene **C_{60}** is given as reference (−4.1 eV).

NFA of up to 2.1%. The best performing blend for processing the active layer with a thickness of about 60 nm was prepared by dissolving the polymers (7.5 mg mL^{-1}) in chlorobenzene followed by mixing with **4** in a 1:1 ratio. All steps were performed under inert conditions. This blend solution was spin-cast without additives at 1000 rpm for 60 s on a freshly prepared ITO|ZnO substrate, without any further treatment by thermal or solvent-vapor annealing. The devices were completed by thermal evaporation of 10 nm MoO_3 as hole-transporting layer as well as a 100 nm aluminum electrode and measured under AM 1.5G irradiation. The OSCs showed maximum PCEs of 2.1% (**PCE-10**) and 2.0% (**PM6**), respectively. While OSCs of **PCE-10** exhibit a 33% higher short-circuit current density (J_{SC}) of −6.71 mA cm^{-2}, devices based on **PM6** compensate this deficiency by a 25% increase in the V_{OC} value up to 1.04 eV. In comparison to devices processed under identical conditions with the unsubstituted corannulene, the OPV performance was significantly enhanced for our new annulated derivative (Figure 82, Figure 83 and Table 25). This is caused by a tenfold higher J_{SC} value due to the significantly shifted strong absorption of **4** in the visible region. Additionally, a higher V_{OC} due to better energetic alignment of **4** with the donor polymer could be realized. However, for all OSCs using **PCE-10** only moderate FF could be achieved. The **PCE-10**:**4** based OSC generates a higher J_{SC} of −6.71 mA cm^{-2} compared to the **PM6**:**4** based OSC, which exhibits a J_{SC} of −4.52 mA cm^{-2}. This is attributed to the more bathochromically shifted absorption of **PCE-10** in comparison to **PM6**, enabling more light accumulation (Figure 67b). The contribution of **PCE-10** and **4** to the photocurrent of the solar cell could be determined by comparing both EQE and UV-Vis spectra of the **PCE-10:4** based OSC (Figure 68c). The highest photocurrent in the range from 400 to 550 nm is mainly generated by **4**, while above 550 nm it originates solely from **PCE-10**. The OPV

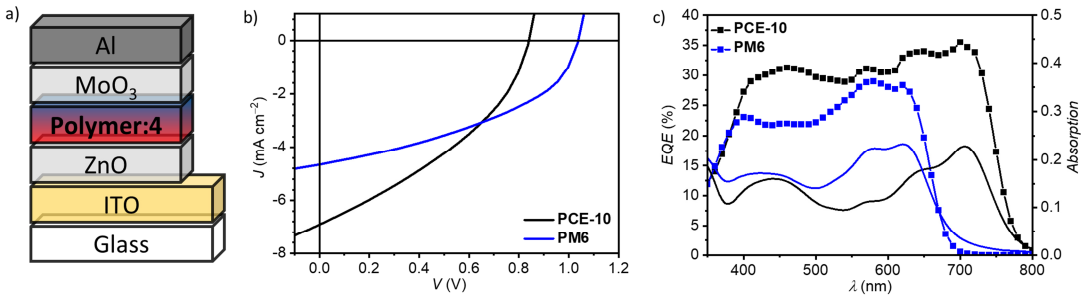

Figure 68: Device architecture of inverted BHJ OSC (a). *J-V* curves of ITO|ZnO(30 nm)|BHJ|MoO_3(10 nm)|Al (100 nm) of NAC **4** in 1:1 ratio with donor polymers **PCE-10** (black) and **PM6** (blue) measured under inert conditions and under AM 1.5G irradiation (b). EQE (symbols) UV-Vis (solid lines) spectra of polymer:**4** based OSC (c).

Table 23: Photovoltaic parameters of OSCs based on **4** in combination with donor polymers **PCE-10** and **PM6** in 1:1 ratio in the architecture ITO|ZnO|BHJ|MoO_3|Al.

Donor	J_{SC} (mA cm^{-2})	V_{OC} (V)	FF (%)	PCE (%)	PCE^{Max} (%)
PCE-10	−6.71 ±0.1	0.82 ±0.02	36 ±1	2.0 ±0.1	2.1
PM6	−4.52 ±0.2	1.02 ±0.02	40 ±2	1.9 ±0.1	2.0

[a]Average of at least seven independent devices.

shows a continuous high EQE over 30% in a broad spectral range from 400 nm to 720 nm. The highest EQE was observed in the range of the **PCE-10** of 35%. Due to the stronger overlap of the absorption of **PM6** and **4**, the generated short-circuit current density and the EQE are lower. The calculated J_{SC}^{EQE} values, which were obtained by the integration of the EQE, are −4.28 mA cm^{-2} and −7.35 mA cm^{-2} for the **PM6:4** and the **PCE-10**:**4** cells, respectively, and are in accordance with the *J-V* measurements. Furthermore, both OSCs exhibit a continuous high EQE due to the absorption of **4**, which perfectly fits in the absorption window between the two absorption peaks of both polymers. The similar efficiency of the **PM6:4** OSCs originates from an increased open-circuit voltage of up to 1.04 V, which is caused by the larger HOMO(Donor)-LUMO(Acceptor) gap of about 1.6 eV. In contrast, **PCE-10**:**4** based OSC exhibits an V_{OC} of 0.84 V and a HOMO(Donor)-LUMO(Acceptor) gap of about 1.4 eV. Both OSCs showed the same energy loss factors (E_{loss}) of about 0.6 V, which is in good accordance with other corannulene-based OSCs.[193,194] The moderate FFs, which are an indicator for an unbalanced charge-transport (36% for **PCE-10**:**4** and 40% for **PM6**:**4**) for both OSCs are the limiting OPV parameter. This seems to be mainly caused by the poor electron mobility of **4**, which was further characterized in organic thin-film transistors (OTFTs). Annealed solution-processed thin-films (5 min at 100 °C) of **4** on OTES-treated Si|SiO_2 substrates only exhibit a modest n-type field-effect mobility of 10^{-5} cm^2 V^{-1} s^{-1}, a threshold voltage of 14 V and an I_{on} I_{off}^{-1} ratio of 10^2 in bottom-gate-top-contact OTFTs (transfer- and output-characteristics in Figure 84, Figure 85). Accordingly, we deduce from AFM images of the thin-film of **4** on OTES-treated Si|SiO_2 substrates (Figure 86) that also compound **4** tends to aggregate in an anti-cooperative fashion without the

formation of an extended aggregate domain under the investigated conditions, due to cancellation of the molecular dipole moments upon dimer formation.[201] As this low-crystalline thin-film is composed of randomly arranged dimers of **4** this might explain the rather poor performance in OTFTs. This assumption is corroborated by the AFM images of blend films of **PCE-10**:**4** and **PM6**:**4** (Figure 69) which exhibit spherical particles, that form a homogenous surface. The **PCE-10**:**4** active layer morphology showed a root mean square (R_q) of 0.8 nm and for the **PM6**:**4** based OSC the R_q value was increased to 1.4 nm. As we could prove that prior to the spin-coating already a preorganization of **4** into dimers takes place in chlorobenzene solution (Figure 71), we assume that these dimer agglomerates were spin-coated on the substrate from the donor-acceptor blend. Due to the absence of higher aggregates, homogenous thin-films with low R_q values are formed. This leads to a good blending into small domains of donor and acceptor, which can explain the high open-circuit voltage and the low energy loss factor. However, due to the low electron mobility of the NAC dimer in contrast to the used donor polymers, the FF decreases and probably recombination takes place. In accordance with the earlier examples, also the preorganized dimers of **4** give rise to only moderate FF, presumably due to unbalanced charge transport. However, V_{OC} could be significantly increased up to 1.04 V (**PM6:4**) for our new NFA, due to a larger HOMO(Donor)-LUMO(Acceptor)-gap and J_{SC} was increased up to −6.71 mA cm^{-2} (**PCE-10**:**4**) due to the better interplay of the absorption properties between the donor and our new NFA **4**.

6.4 Conclusions

In conclusion, a new electron-poor NAC derivative **4** was synthesized which inherits good solubility due to the curved π-system along with the two branched imide substituents. The molecule exhibits a low-lying LUMO level of −3.85 eV similar to

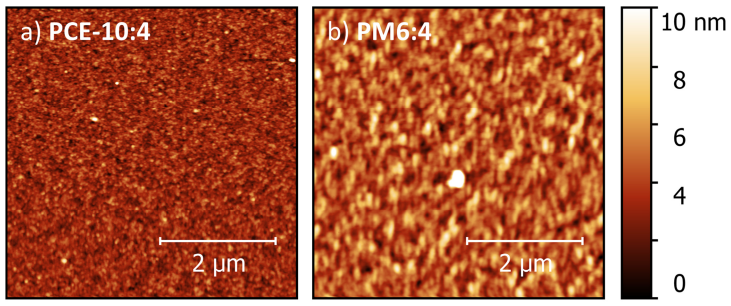

Figure 69: AFM height images of active layers of **4** in 1:1 ratio with **PCE-10** (a) and **PM6** (b) of inverted BHJ OSC on ITO|ZnO (5 x 5 µm²).

fullerene **C_{60}** but a much broader and more intense absorption in the visible range than the fullerene. This new NFA **4** self-assembles in an anti-cooperative fashion into dimer aggregates in the blend solutions with two different donor polymers and was successfully implemented in inverted BHJ OSCs. The best performing blend was identified as a 1:1 mixture of **4** and **PCE-10**, which showed a maximum power conversion efficiency of 2.1%, while with **PM6** a PCE of 2.0% with V_{OC} up to 1.04 V could be achieved. This is to the best of our knowledge the highest reported value for a corannulene-based NFA in OSCs. [†]

† In 2022 the most efficiency corannulene-based OSCs yielded 11.1%.[51]

6.5 Supporting Information for CHAPTER VI

6.5.1 Synthesis

General Methods: Reagents were purchased from commercial suppliers and used as received without further purification. Dichloromethane and ethylacetate were distilled prior to use. All reactions were carried out under nitrogen atmosphere. Column chromatography was performed with commercial glass columns using silica gel 60 M (particle size 0.04 – 0.063 mm; Merck KGaA) as stationary phase. Size-exclusion chromatography was performed on BioBeads S-X1 using HPLC grade solvents. NMR spectra were recorded on a Bruker *Avance III HD* 400MHz NMR spectrometer and are calibrated to the residual proton signal of the used deuterated solvent. The chemical shifts (δ) are reported in parts per million (ppm) and coupling constants *J* in Hertz (Hz). Multiplicities for proton signals are abbreviated as s, d, t and m for singlet, doublet, triplet and multiplet, respectively. MALDI-TOF mass spectra were recorded with an *Autoflex II* mass spectrometer (Bruker Daltonics GmbH) using DCBT (2-[(2*E*)-3-(4-*tert*-butylphenyl)-2-methylprop-2-enylidene]malononitrile) as matrix.[†] High resolution mass spectra (ESI) were recorded with an *ESI microTOF Focus* mass spectrometer (Bruker Daltonics GmbH). UV/Vis absorption spectra were recorded in cuvettes (SUPRASIL®, Hellma® Analytics) on a Perkin-Elmer Lambda 950 or Jasco V-770 spectrometer and fluorescence spectra on a FLS980 fluorescence spectrometer (Edinburgh Instruments) and were corrected against the photomultiplier sensitivity and the lamp intensity.

Synthetic Procedures: 4-Bromo-5-chloronaphthalene-1,8-dicarboxylic anhydride[196] and 2-hexyloctylamine[202] were synthesized according to procedures reported in literature.

*Synthesis of **2**:* A solution from 2-hexyloctylamine (500 mg, 2.34 mmol) and 4-bromo-5-chloronaphthalene-1,8-dicarboxylic anhydride (663 mg, 2.13 mmol) in degassed *n*-propanol (20 mL) and H_2O (1 mL) was stirred under nitrogen for 2 d at 100 °C. The solid was removed by filtration and washed with *n*-propanol. After evaporation of the solvent the crude product was purified by column chromatography (Hex: CH_2Cl_2 1:2) and reprecipitated from CH_2Cl_2 and MeOH to give 573 mg (1.13 mmol, 53%) of yellow crystalline needles.

[†] Instead of a Bruker Daltonics Autoflex II a Bruker Daltonics UltrafleXtreme was used.

^{1}H-NMR (400 MHz, $CDCl_3$): δ *[ppm]* = 8.51 (d, *J* = 8.0 Hz, 1H), 8.39 (d, *J* = 8.0 Hz, 1H), 8.17 (d, *J* = 8.0 Hz, 1H), 7.90 (d, *J* = 8.0 Hz, 1H), 4.07 (d, *J* = 7.3 Hz, 6H),1.96 (m, 1H), 1.38-1.23 (m, 20 H), 0.84 (t, *J* = 7 Hz, 6H).

^{13}C-NMR (100 MHz, $CDCl_3$): δ *[ppm]* = 163.7, 163.5, 139.0, 136.2, 131.8, 131.71, 131.70, 131.49, 127.0, 126.7, 123.0, 122.6, 44.8, 36.6, 31.9, 31.7, 29.8, 26.5, 22.7, 14.2.

HRMS (ESI-MS, pos. mode, MeCN/$CHCl_3$): *m*/*z* calculated for $C_{26}H_{33}BrClNNaO_2^+$ $[M+H]^+$: 528.1275, found: 528.1291.

Melting point: 104 °C.

*Synthesis of **3**:* Corannulenediboronicacidbis(pinacol)ester **1** (100 mg, 200 µmol), 4-bromo-5-chloronaphthalene-1,8-dicarboximide derivative **2a** (223 mg, 440 µmol), tris(dibenzylideneacetone) dipalladium(0)-chloroform adduct (10.4 mg, 10.0 µmol), tri(*m*-tolyl)phosphine (12.2 mg, 40.0 µmol), cesium carbonate (391 mg, 1.20 mmol) and 6 mL 1-chloronaphthalene were charged in a Schlenk tube. The reaction mixture was stirred at 110 °C for 2 d. After cooling to room temperature, cyclohexane was added and the mixture was purified by column chromatography with cyclohexane and followed by a mixture of 10% acetone in CH_2Cl_2 as eluent and size-exclusion chromatography on BioBeads S-X1 (CH_2Cl_2/MeOH 9:1) to give **3** as a red solid (164.7 mg, 78%). The product was isolated as a mixture of atropisomers.

MS (MALDI-TOF, neg. mode, DCTB in $CHCl_3$): *m*/*z* calculated for $C_{72}H_{73}ClN_2O_4^-$ $[M]^-$: 1064.526, found: 1064.526.

*Synthesis of **4**:* A Schlenk tube was charged with **3** (22.0 mg, 20.0 µmol), tris(dibenzylideneacetone) dipalladium(0)-chloroform adduct (2.07 mg, 2.00 µmol), tri(1-adamantyl)phosphine (2.49 mg, 6.00 µmol), cesium carbonate (39.1 mg, 120 µmol), tetrabutylammonium chloride (2.78 mg, 10.0 µmol) and 1 mL 1-chloronaphthalene. The reaction mixture was stirred at 170 °C for 16 h. After cooling to room temperature, 3 mL cyclohexane were added and the mixture was purified successively by column chromatography (cyclohexane:dichloromethane:ethylacetate gradient = 1:0:0 to 0:1:0 then 0:98:2) to yield **4** as a dark red powder (25.1 mg, 41%).

^{1}H-NMR (400 MHz, TCE-d_2, 390 K): δ [ppm]= 8.52 (d, J = 7.9 Hz, 2H), 8.43 (d, J = 7.9 Hz, 2H), 8.28 (d, J = 7.9 Hz, 2H), 7.20 (d, J = 7.9 Hz, 2H), 8.04 (s, 2H), 8.01 (s, 2H), 7.65 (s, 2H), 4.10 (d, J = 7.4 Hz, 4H), 2.02 (bs, 2H), 1.37 – 1.23 (m, 40H), 0.83 (t, J = 6.8 Hz, 12H).

^{13}C-NMR (100 MHz, TCE-d_2, 390 K): δ [ppm]= 163.8, 163.6, 137.2, 136.32, 135.2, 136.29, 133.7, 133.6, 133.0, 132.8, 132.6, 131.1, 131.0, 129.8, 129.0, 128.5, 128.4, 127.1, 123.2, 123.0, 122.8, 121.8, 120.6, 45.2, 37.2, 32.5, 31.9, 29.9, 26.8, 22.7, 14.0.

MS (MALDI-TOF, neg. mode, DCTB in $CHCl_3$): m/z calculated for $C_{72}H_{72}N_2O_4^-$ $[M]^-$: 1028.549, found: 1028.544.

HRMS (ESI-TOF, pos. Mode, acetonitrile/chloroform 1/1) m/z: calculated for $C_{72}H_{73}N_2O_4^+$: 1029.5565 $[M+H]^+$, found: 1029.5539.

Melting point: 267 °C.

UV-Vis (c = 2×10^{-6} M, CH_2Cl_2, 293 K): $\varepsilon_{Max}(\lambda_{Max})$ = 44600 M^{-1} cm^{-1} (503 nm).

Fluorescence (CH_2Cl_2): λ_{Max} (λ_{Ex}) = 573 nm (501 nm); Φ = 0.46±0.03.

6.5.2 Device Fabrication

Organic solar cells were prepared by cleaning ITO substrates (Soluxx GmbH) with acetone (VWR, semiconductor grade), detergent, deionized water, and isopropanol (VWR, semiconductor grade) for 15 min each, followed by an UV/ozone treatment for 30 min. The ZnO layer was deposited by spin-coating ZnO nanoparticles on top of the substrates (3000 rpm, 30 s) followed by an annealing step (200 °C, 1 h). The donor–acceptor blends were prepared by stirring a 1:1 mixture with a total concentration of 15 mg mL^{-1} of donor (**PCE-10** obtained from 1-Material Inc.; **PM6** obtained from Brilliant Matters Inc.) and **4** in chlorobenzene for 3 h at room temperature under inert conditions followed by spin-coating at 1000 rpm for 60 s (M.Braun Inertgas-Systeme GmbH, UNIlab Pro, c(O_2) < 1 ppm, c(H_2O) < 1 ppm). The substrates were placed in the evaporation system (OPTIvap-XL, Creaphys GmbH) and MoO_3 (d = 10 nm, r = 0.1 Å s^{-1}, p < 10^{-6} mbar, ω_{rot} = 10 rpm) and aluminum (d = 100 nm, r = 1-2 Å s^{-1}, p < 10^{-6} mbar) were deposited on top of the active layer to obtain the inverted BHJ organic solar cells. The device area was 7.1 mm^2. J-V

characteristics were measured after calibration with a standard silicon solar cell with a KG filter (ISE Freiburg) under an AM1.5G OrielSol3ATM Class AAA solar simulator (Newport®) by a parameter analyzer (Botest Systems GmbH). EQE measurements were carried out with a quantum efficiency/IPCE measurement kit(Newport®) by using a 300 W Xe lamp and a Cornerstone monochromator with a Merlin lock-in amplifier for detection. Thin-film UV-Vis spectra were measured on a Jasco V770 spectrometer using an integration sphere. AFM images were obtained by a NT–MDT Next Solver system in semi-contactmode by using a SCOUT 350 RAI (Nu Nano Ltd) silicon cantilever (spring constant = 42 N m^{-1}; resonance frequency = 350 kHz). The high-resolution AFM image was measured at a AXS Multimode Nanoscope IV instrument in the tapping mode using a silicon cantilever from Olympus (OMCL-AC160TS) with a spring constant of 42 N m^{-1} and a resonance frequency of 300 kHz.

Organic thin film transistors were fabricated on wafer substrates based on Si|SiO_2(100 nm)|octadecyltriethoxysilane(OTES) with a capacitance of 32.4 nF cm^{-2}, which were rinsed prior to use with toluene (p.a. grade, VWR chemicals), acetone, and isopropanol (semiconductor grade, VLSI PURANALTM, Aldrich® Chemistry), successively. After drying under nitrogen flow, the substrates were placed into a nitrogen-filled glovebox (M. Braun Inertgas-Systeme GmbH, UNIlab Pro, c(O_2) < 1 ppm, c(H_2O) < 1 ppm) and a freshly prepared solution of **4** (5 mg mL^{-1} in chloroform) was spin-coated on top of the substrate (1000 rpm, 60 s) followed by an annealing step (100 °C, 5 min). The substrates were placed into an evaporation system (OPTIvap-XL, Creaphys GmbH) and gold was deposited on top of the organic layer through a shadow mask (d = 30 nm, r = 0.2 Å s^{-1}, $p < 10^{-6}$ mbar). The resulting transfer and output characteristics were measured under inert conditions with an Agilent 4055C parameter analyzer and a Cascade EPS150 probe station (W = 1000 µm, L = 20 µm).

6.5.3 Optical Properties

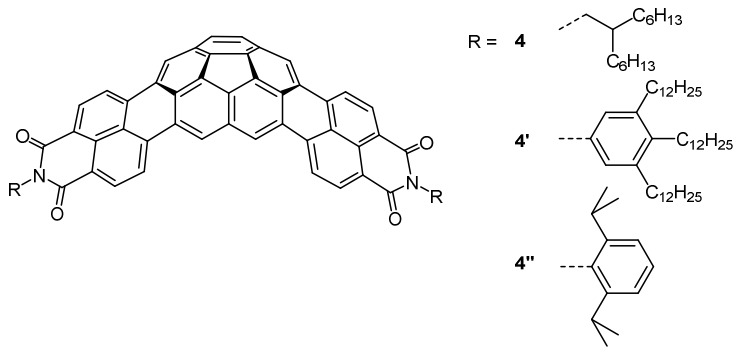

Table 24: Optical properties of **4** and the previously reported double annulated corannulene derivatives **4'** and **4''** in dichloromethane at 25 °C.

R =	λ_{Abs} (nm)	ε_{Max} (M^{-1} cm^{-1})	λ_{Em} (nm)	Φ_{Fl}[a] (%)	τ (ns)	Stokes shift (cm^{-1})
4	536, 503, 476	36900, 44600, 41800	572	46	5.19	1140
4'[197]	536, 503, 477	52500, 56200, 44900	572	43	4.92	1140
4''[196]	538, 504, 478	45900, 51300, 42500	573	48	5.00	1140

[a] Fluorescence quantum yields were determined relative to (*N*,*N*'-bis(2,6-di-*iso*-propylphenyl)-3,4:9,10-perylenetetracarboxylic diimide).[203]

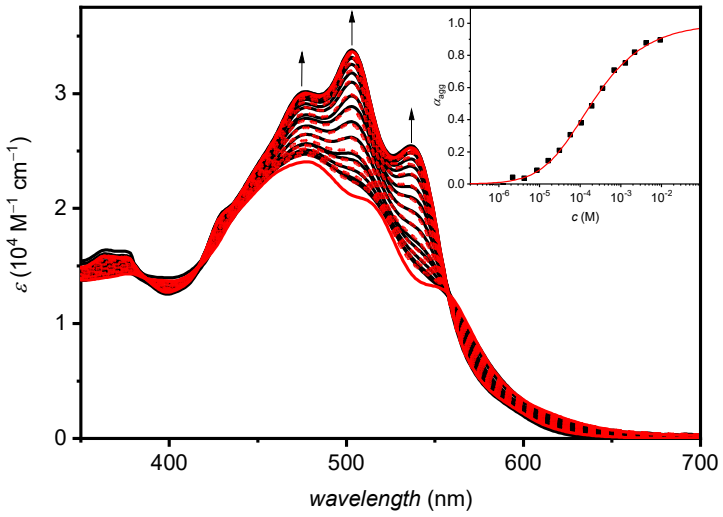

Figure 70: Concentration-dependent UV-Vis spectra at 25 °C of **4** (black, c = 2.2×10^{-2} – 1.6×10^{-6} M) in toluene, the global fit analysis according to the monomer-dimer model for **4** (red, dashed lines) and the ideal monomer and dimer spectra (red solid lines). Inset: Molar fraction of aggregated molecules α_{agg} as a function of concentration of **4** fitted with the dimer model.

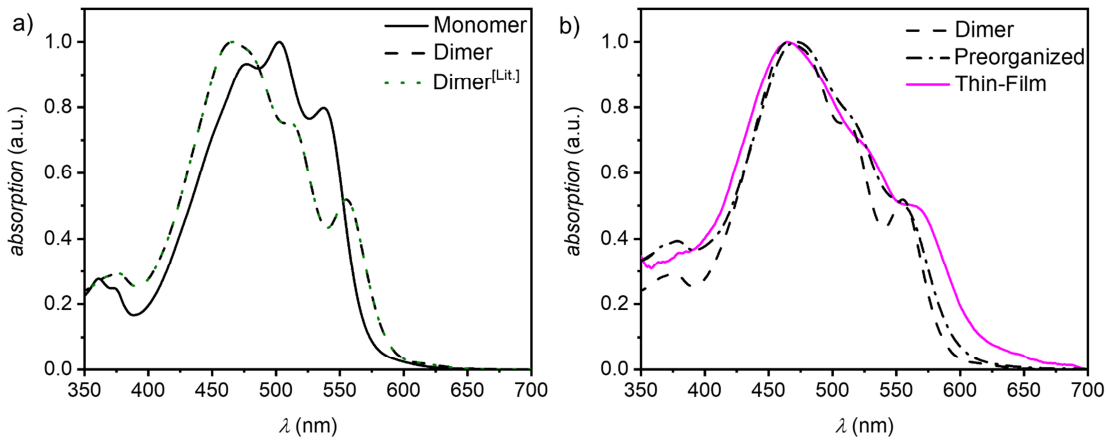

Figure 71: (a) UV-Vis spectra of **4** in solution as monomer (2.0×10^{-5} M in CH_2Cl_2; black - solid), as dimer (2.2×10^{-2} M in toluene; black - dashed) compared with the previously reported dimer spectra of **4'** (green - dotted).[197] (b) UV-Vis spectra of **4** as dimer (2×10^{-2} M in toluene; black - dashed), preorganized dimer for OPV processing (7.5 mg mL^{-1} in chlorobenzene; black – dashed and dotted) and thin-film absorption of a spin-coated film on quartz (pink - 7.5 mg mL^{-1} in chlorobenzene spin-coated at 1000 rpm for 60 s).

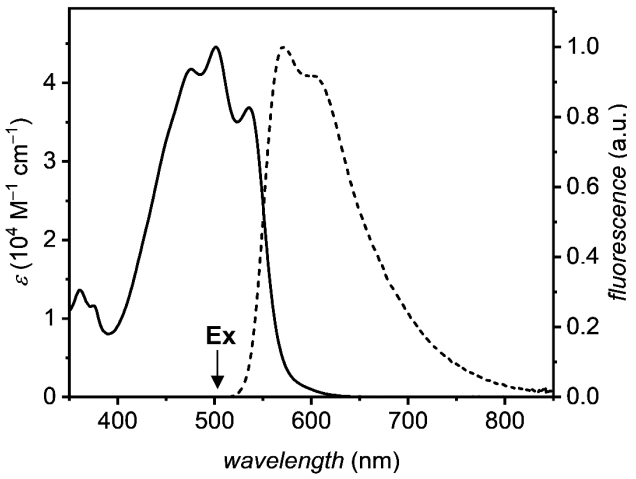

Figure 72: UV-Vis absorption (solid line) and emission spectra (dashed line) of **4** in dichloromethane.

6.5.4 NMR Spectra

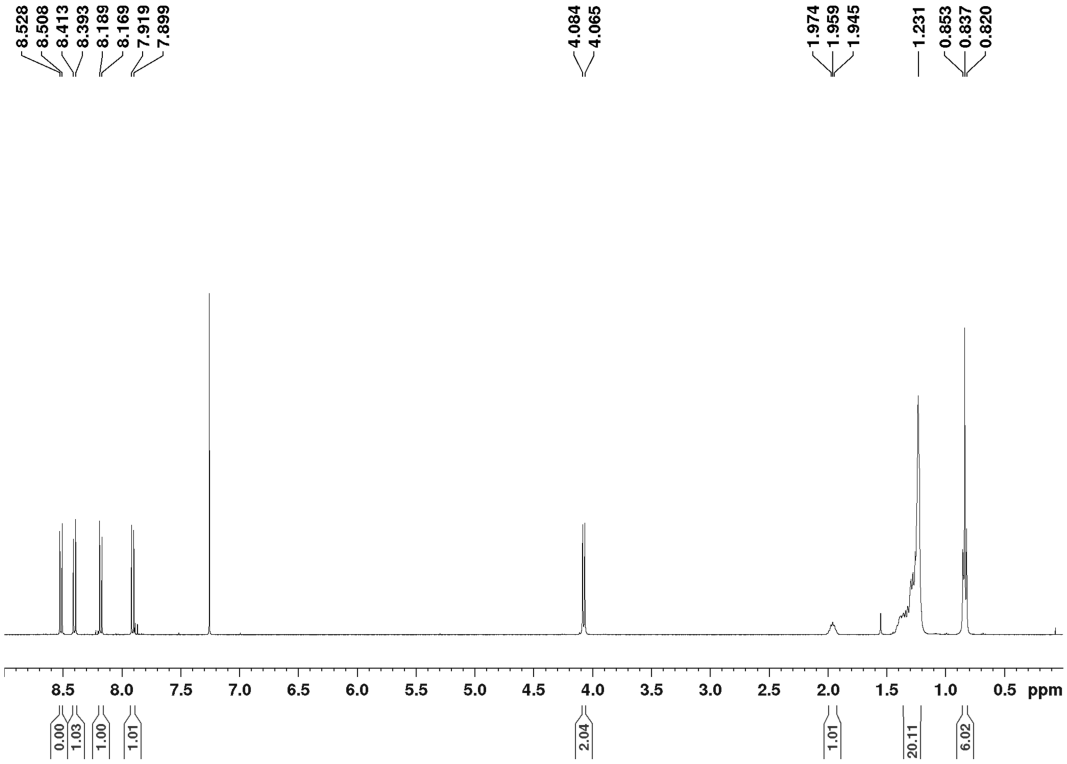

Figure 73: 400 MHz ^{1}H-NMR spectrum of **2** in $CDCl_3$ recorded at 295 K.

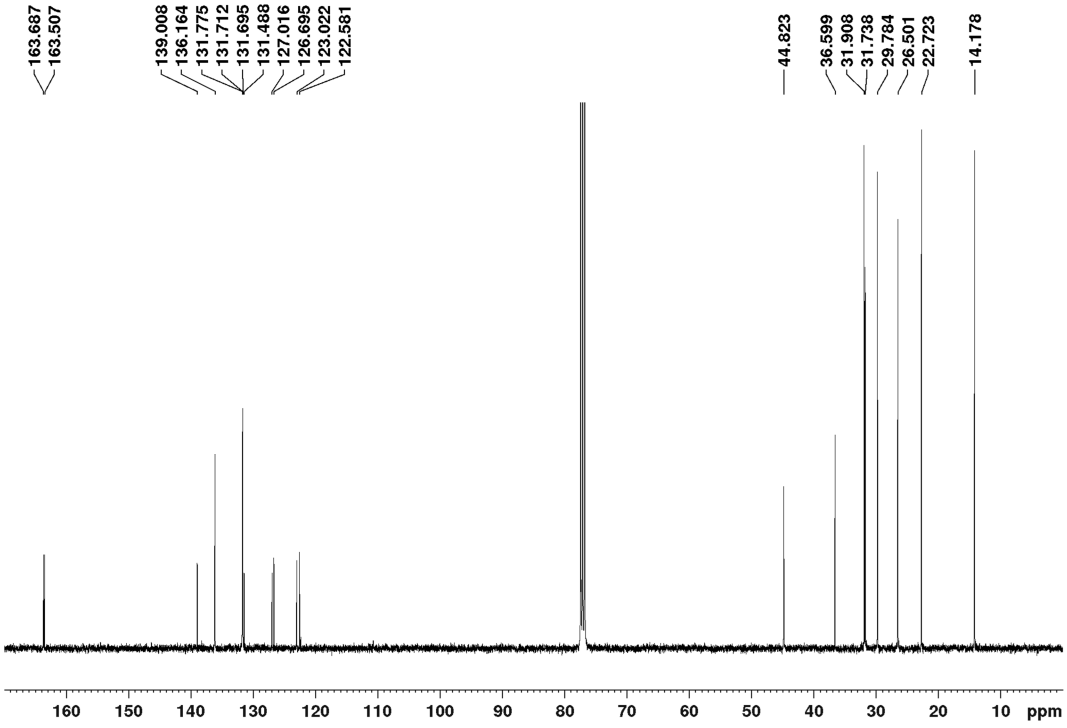

Figure 74: 100 MHz ^{13}C NMR spectrum of **2** in $CDCl_3$ recorded at 295 K.

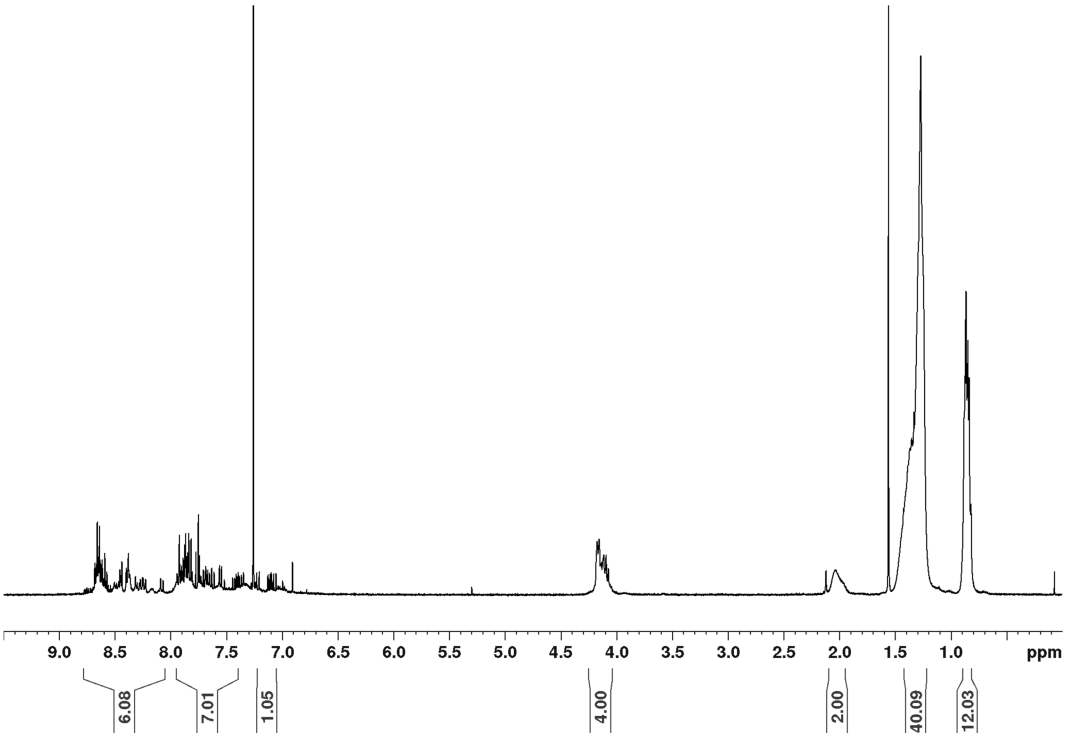

Figure 75: 400 MHz ^{1}H-NMR spectrum of the mixture of atropisomers of **3** in $CDCl_3$ recorded at 295 K.

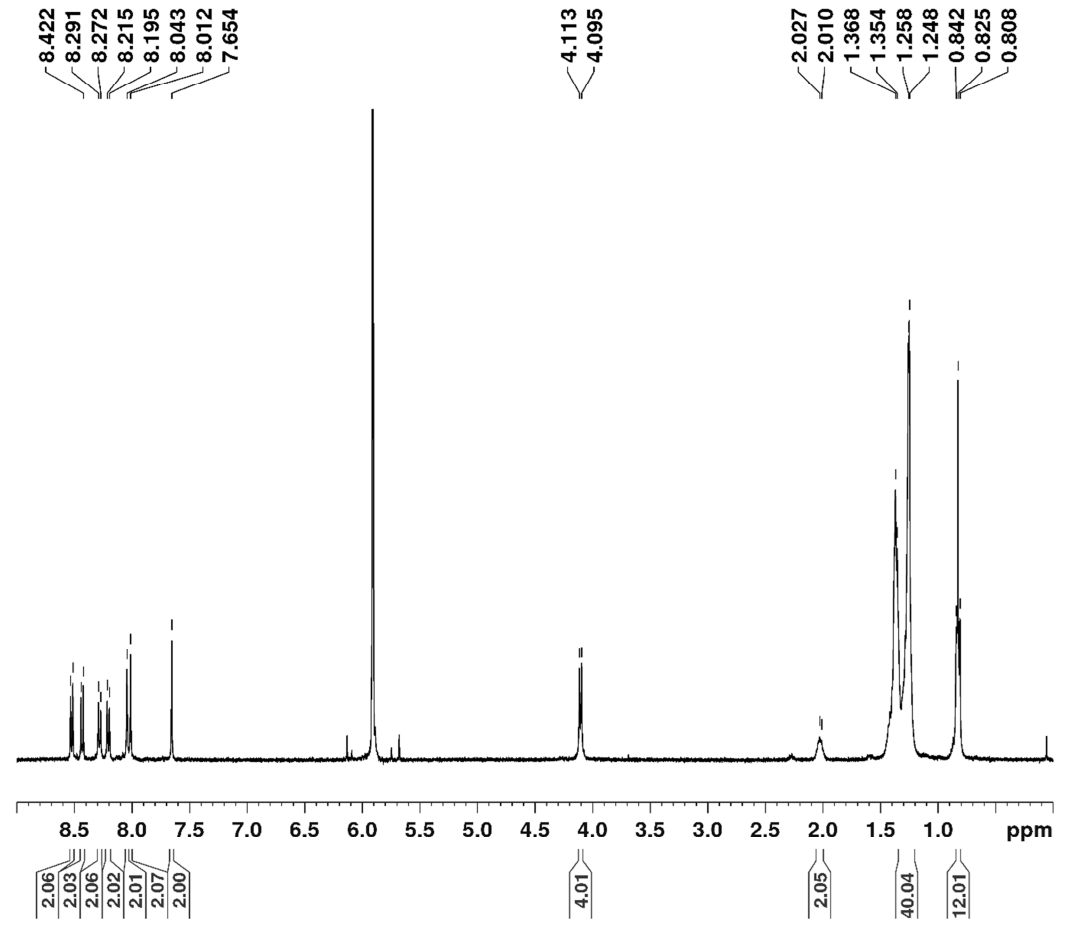

Figure 76: 400 MHz ^{1}H NMR spectrum of **4** in TCE-d_2 recorded at 390 K.

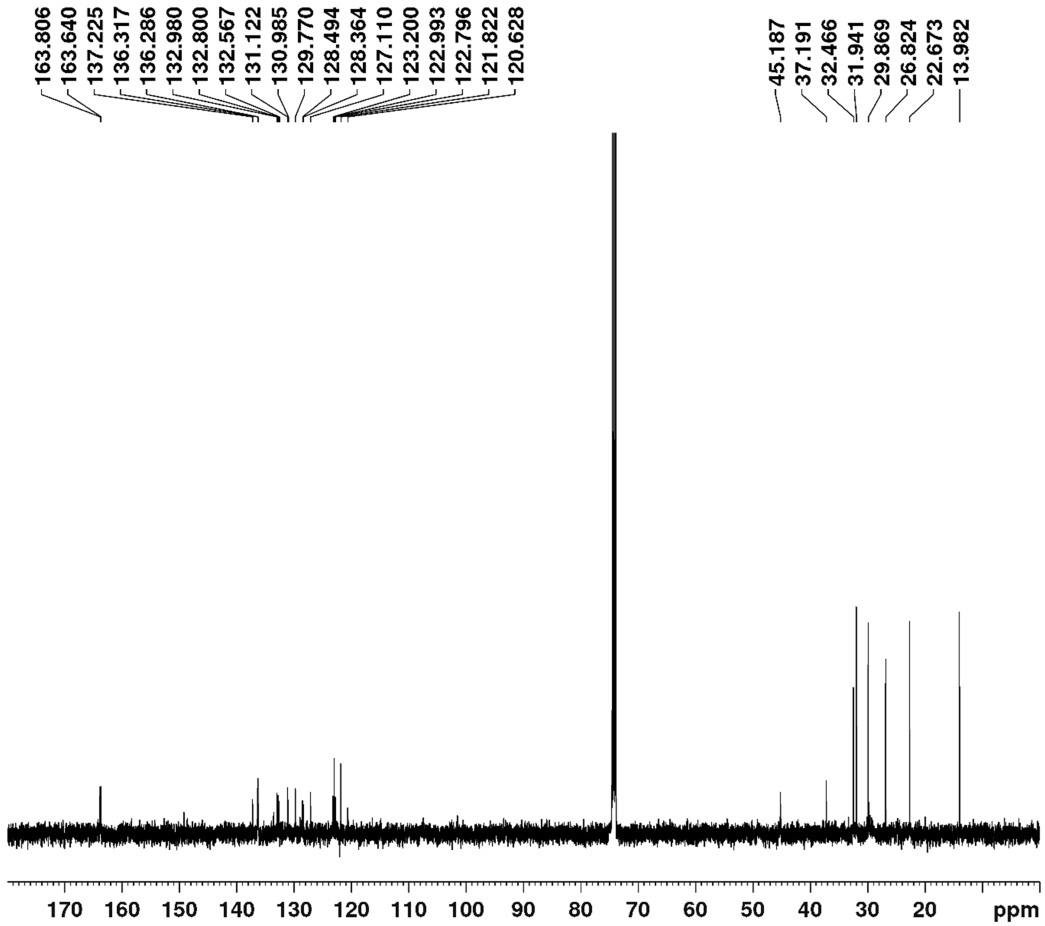

Figure 77: 100 MHz ^{13}C NMR spectrum of **4** in TCE-d_2 recorded at 390 K.

6.5.5 CV Data

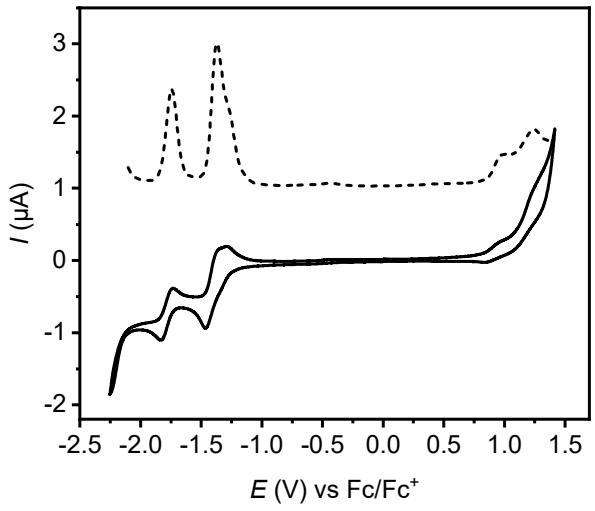

Figure 78: Cyclic voltammetry (solid line) and square wave voltammetry (dashed line) traces of **4**. Measurement was performed using dichloromethane solutions at room temperature using tetrabutylammonium hexafluorophosphate (0.1 M) as electrolyte.

6.5.6 OPV Optimization

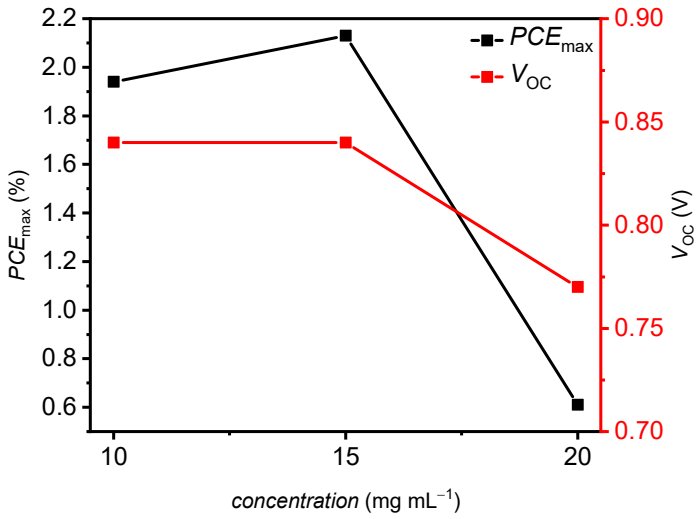

Figure 79: PCE^{Max} (black) and V_{OC} (red) of **PCE-10:4** based OPV in ITO|ZnO|BHJ|MoO_3|Al architecture. The mass ratio of donor and acceptor was kept at 1:1 ratio, while the total concentration was changed between 10 - 20 mg mL^{-1} in chlorobenzene as solvent. The OSCs were measured under inert conditions and under AM 1.5G irradiation.

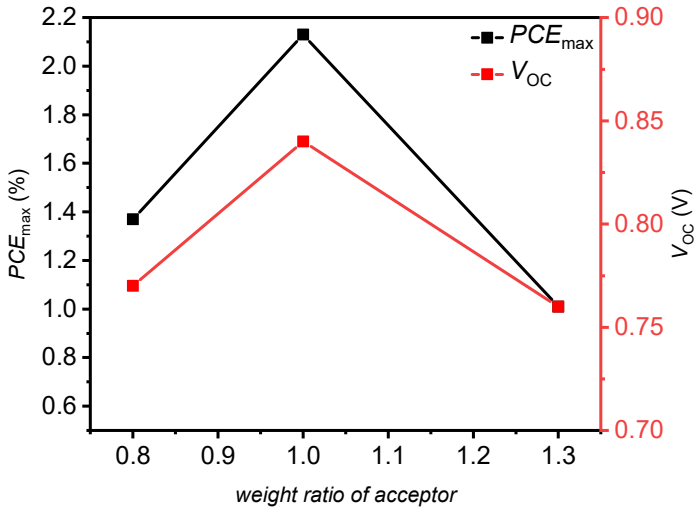

Figure 80: PCE^{Max} (black) and V_{OC} (red) of **PCE-10:4** based OPV in ITO|ZnO|BHJ|MoO_3|Al architecture. The polymer concentration was kept at 7.5 mg mL^{-1} in chlorobenzene as solvent, while the mass ratio of the acceptor was changed. The OSCs were measured under inert conditions and under AM 1.5G irradiation.

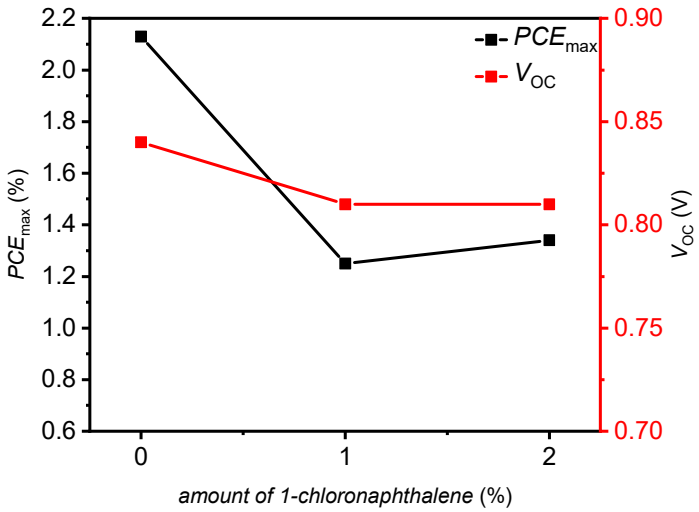

Figure 81: PCE^{Max} (black) and V_{OC} (red) of **PCE-10:4** based OPV in ITO/ZnO/BHJ/MoO_3/Al architecture. The total concentration was kept at 15 mg mL^{-1} in 1:1 ratio in chlorobenzene as solvent, while 1-chloronaphthalene was added prior to the spin-coating process. The OSCs were measured under inert conditions and under AM 1.5G irradiation.

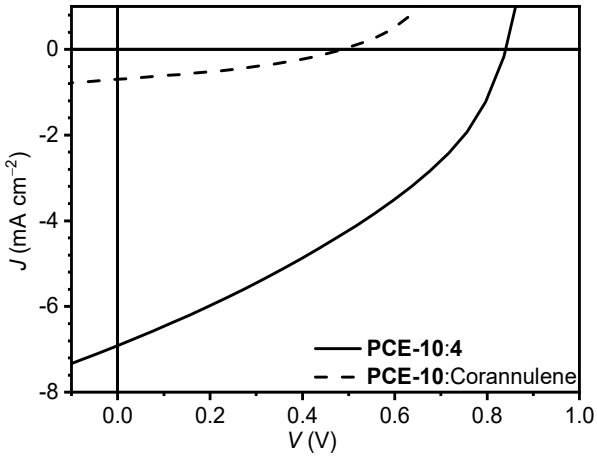

Figure 82: *J-V* curves of ITO|ZnO(30 nm)|BHJ|MoO_3(10 nm)|Al(100 nm) of **4** (solid) and corannulene (dashed) in 1:1 ratio with donor **PCE-10** measured under inert conditions and under AM 1.5G irradiation.

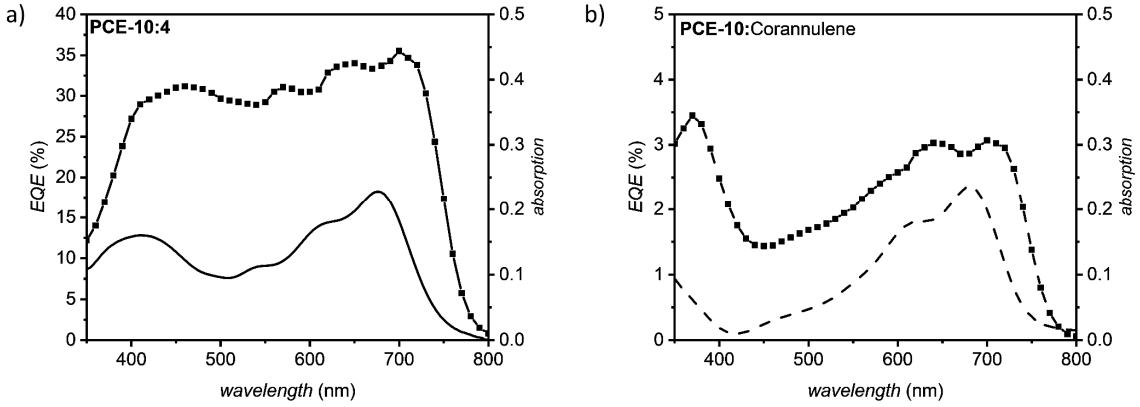

Figure 83: EQE (symbol) and UV-Vis (solid line)-spectra of **PCE-10:4** (a) and **PCE-10**:corannulene (b) based OSC in ITO|ZnO|BHJ|MoO_3|Al architecture, which were measured under inter conditions under AM 1.5G irradiation.

Table 25: Photovoltaic parameters of OSCs based on **PCE-10:4** and **PCE-10**:corannulene in 1:1 ratio in the architecture ITO|ZnO|BHJ|MoO_3|Al.

Donor	Acceptor	J_{SC} (mA cm^{-2})	V_{OC} (V)	*FF* (%)	PCE (%)	PCE^{Max} (%)
PCE-10	**4**	−6.71 ± 0.1	0.82 ± 0.02	36 ± 1	2.0 ± 0.1	2.1
PCE-10	Corannulene	−0.63 ± 0.1	0.37 ± 0.04	33 ± 2	0.07 ± 0.01	0.1

6.5.7 OTFT Data

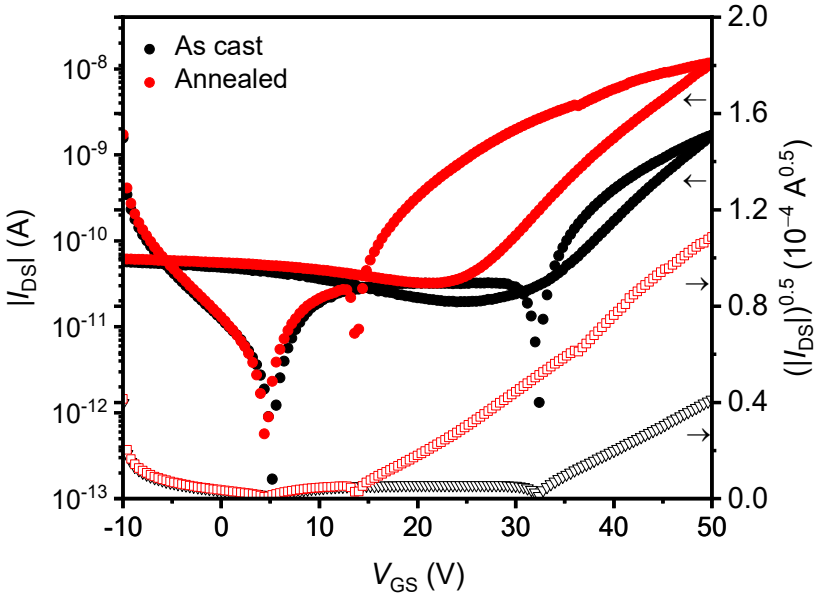

Figure 84: Transfer curves (filled circle) and square root plot (open square) of Si|SiO_2|OTES|**4**|Au based OTFT (L = 20 µm, W = 1 mm, V_{DS} = 50 V) before (black) and after (red) an annealing step at 100 °C for 5 min.

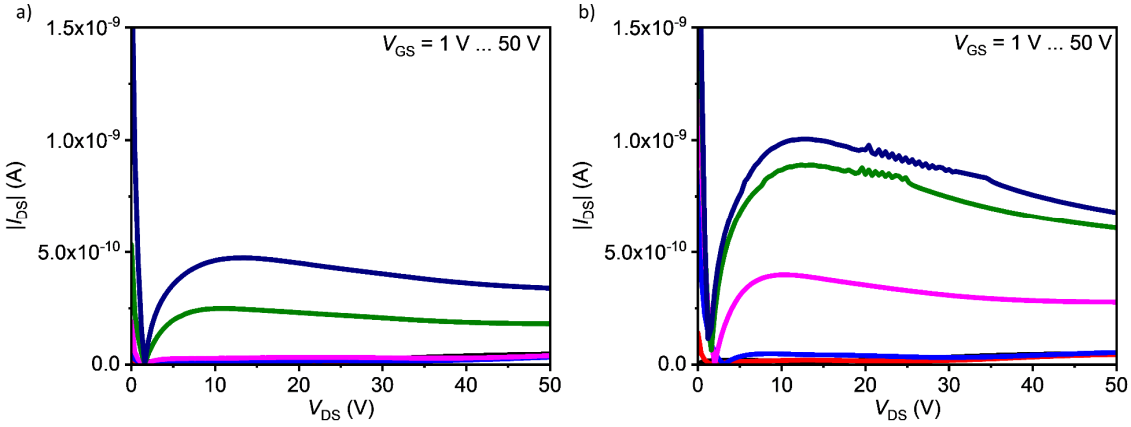

Figure 85: Output curves of Si|SiO_2|OTES|**4**|Au based OTFT (L = 20 µm, W = 1 mm, V_{DS} = 50 V) before (a) and after (b) an annealing step at 100 °C for 5 min.

6.5.8 AFM Morphology

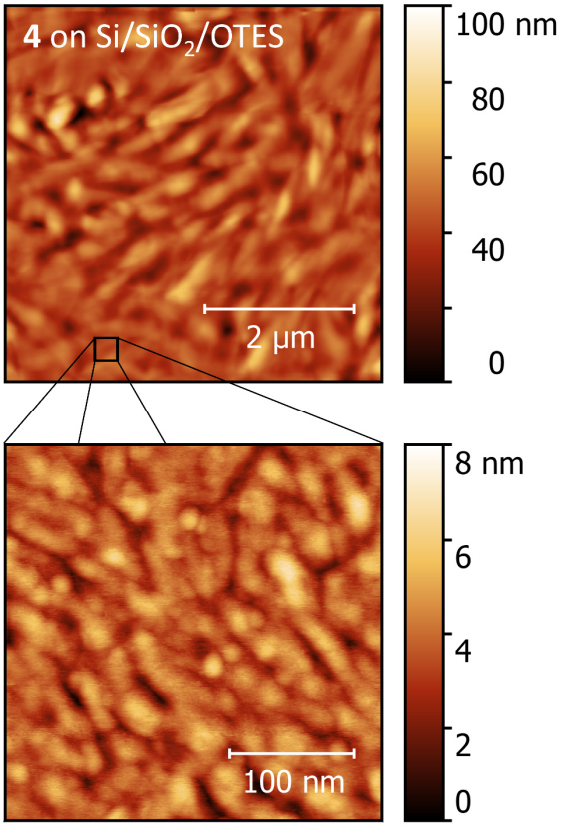

Figure 86: AFM-height image of a spin-coated thin film of **4** on top of an OTES-treated Si|SiO_2 substrate.

Chapter VII: Sterically Shielded Polycyclic Aromatic Dicarboximides as new Non-Fullerene Acceptors

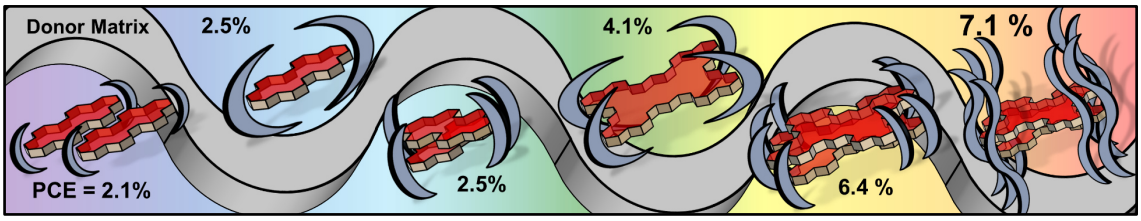

A new class of non-fullerene acceptors for organic solar cells namely sterically shielded polycyclic aromatic dicarboximides was studied by increasing the size of the π-surface from perylene bisimide to larger nanographene tetraimide. The latter afforded higher efficiencies of up to 7.1% in donor polymer-based organic solar cells, even without the formation of extended π-stacked domains.

The following people contributed to this chapter:

Kaan Menekşe:	Design of research, calculations, characterization in solution and polymer matrixes, organic solar cells and their characterization, writing.
Simon Soldner:	Synthesis and molecular characterization, crystal growth.
Magnus Mahl:	Synthesis and molecular characterization, crystal growth.
Tim Schembri:	Calculations.
Julius Albert:	Synthesis and molecular characterization.
Kazutaka Shoyama:	Crystallography.
Matthias Stolte:	Correction and coordination.
Frank Würthner:	Correction and coordination.

7.1 Abstract

Polycyclic aromatic dicarboximides based on perylene bisimides and on nanographene tetraimides were synthetically decorated with sterical demanding imide substituents to tune their self-assembly behavior in solution as well as their molecular packing in solid-state. These highly soluble materials combine high extinction coefficients of 90000 and 300000 $L\,mol^{-1}\,cm^{-1}$ with low reduction potentials at around −1 V, which render them as candidates for non-fullerene acceptors in bulk-heterojunction organic solar cells. By single-crystal X-ray diffraction we investigated the structure dependence of the imide substituents, which helps us to explain the optical changes, which were observed in polymer blended thin films. These findings were in line with the obtained solar cell efficiencies of these sterically shielded acceptors combined with the donor polymer **PM6**. Our investigations shed light onto the acceptor-acceptor interactions and their impact on the solar cell performance. Most interestingly, we could observe that extended π-stacked domains of individual acceptor molecules are not mandatory to obtain power conversion efficiencies over 7%.

7.2 Introduction

In the field of organic electronics, the tuning and control of intermolecular interactions between independent molecules to form functional materials is the key construction principle towards tailor-made efficient devices.[17,204-208] These interactions can be demonstrated in organic solar cells (OSCs), where the balance between donor-donor (D-D)[209,210], donor-acceptor (D-A)[211,212] and acceptor-acceptor interactions (A-A)[83,213] correlates strongly with the resulting device performance. By a closer view on the elementary processes in OSCs, it became clear that every step is connected to intermolecular interactions, which direct the structural, morphologic, and energetic properties in the OSCs device. The D-D interactions in blends with fullerenes are well elucidated by various aggregation studies for small molecules as well as polymeric donors in solution and thin films, which showed that intermolecular interactions guide the formation of the extended π-stacked donor domains.[209,214] These donor domains in combination with an respective acceptor are then responsible for the photovoltaic performance. Generally, these domains consist of molecules, where the respective π-surfaces are

in direct π-contact to those of neighboring molecules, which leads to pronounced exciton- as well as charge-transport properties. At the interface, the most important D-A interaction can be described with the help of the respective charge-transfer (CT) state. Several groups verified the photocurrent contribution of the CT state with the external quantum efficiency (EQE) spectrum on the one hand and by its electroluminescence properties on the other hand, which allows conclusions to be drawn about the energy loss factors.[215,216] Unlike the D-D and D-A interactions so far, the A-A interactions are not studied yet so much in detail for the various classes of new non-fullerene acceptors (NFAs). Still, several intermolecular interactions are present as for the variety of the most efficient ADA dyes, where a slip-stacked J-aggregation leads to the formation of a grid-like structure with two- or even three-dimensional percolation pathways for exciton and charges.[17,75,217] State-of-the-art ADA NFAs show minimal π-surface overlap with neighboring donor polymers or acceptors in the solid state due to the bulky donor group in the center unit of the typical ADA scaffold guiding the slip-stack packing arrangement. In contrast to these NFAs, several groups focus on polycyclic aromatic dicarboximides (PADIs) due to their low lying lowest unoccupied molecular orbital (LUMO) levels, high tinctorial strengths as well as large π-surfaces, which show excellent interactions with the respective donor materials combined with outstanding tunable morphologic as well as energetic properties.[50,180,218] The main drawback of these large and often highly symmetric π-systems is their tendency for the formation of too large π-stacked crystalline domains (over-aggregation), which significantly reduce their solubility and lead to the formation an inferior interface to the donor counterpart. This drawback can be overcome by introducing sterically demanding substituents to fine-tune the material's morphological aspects.[105,219-221] For the newest generation of PADI molecules, photovoltaic performances were observed even without the formation of an extended π-stacked arrangements.[50,94,176] Generally, these molecules are based on the perylene bisimide (PBI) structural motif and are then further functionalized *via* the extension of the π-surface to finally obtain a three dimensional structures.[222-225] Due to the lack of π-π contacts, which either results from the distorted large π-surface[50,176] or from the introduction of sterically shielding substituents,[226,227] different exciton- and charge-transport pathways have to be present in the bulk heterojunction (BHJ). So far, in literature these

pathways are not elucidated in detail yet. To gain a deeper understanding into the photophysical processes that take place for this class of NFAs, we designed a series of sterically shielded PADIs. Just recently, we demonstrated a PADI, which we decorated with bulky sterically demanding imide substituents[115] and could show a variety of structures of the PADI acceptor and small molecule donors, which revealed the well-pronounced D-A interactions. We could also demonstrate that these dyes are able to interact with themselves *via* dimerization (A_2) which encouraged us to launch a systematic study of the use of these sterically shielded PADIs in BHJ OSCs.

Here, we focus on two series of two chromophore classes with different sizes namely the parent perylene bisimides (PBIs; **1a**-**d**) with a π-surface area of about 55 nm^2 and the almost square-shaped nanographene tetraimides (NGTIs; **2a**-**d**) with π-surface area of about 148 nm^2, respectively, which we decorate with different bulky imide substituents (Figure 87). To further control the interaction between the respective acceptor and donor molecules and to overcome the strong tendency for over-aggregation of the NFA, we decided to implement multiple *tert*-butyl or *iso*-propyl groups at different positions of the imide substituents.[228,229]. Hence, we tune the access of the donor polymer and of neighboring acceptor molecules.

After the successful synthesis and purification of these dyes, we investigate the solid-state structures of these dyes and compare the packing motifs with the optical properties of the NFAs in thin films using a poly(methyl methacrylate) matrix (PMMA).[230] The different molecular arrangements in the solid state have a direct

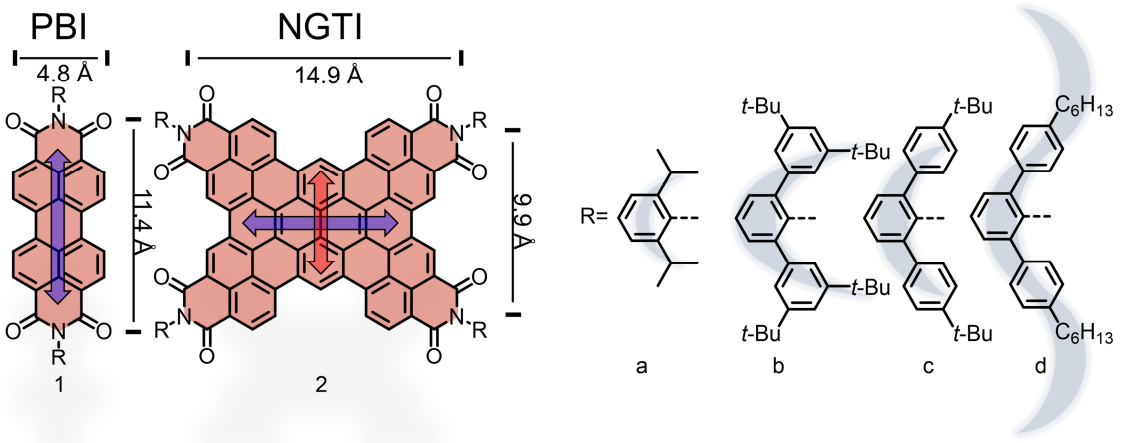

Figure 87: Chemical structures of sterically shielded PBIs **1a-d** and NGTIs **2a-d** combined with the direction of the respective transition dipole moments.

impact on the resulting OSC performance, which we analyze by a closer view on the characteristic photovoltaic parameters. Finally, we could show that domains of extended π-stacked molecules are not necessarily required, when the respective π-surface is big enough to enable efficient exciton and electron transport. With this new knowledge, we were able to obtain a high power conversion efficiency (PCE) of up to 7.1% even from as-cast thin films with donor polymer **PM6**, without the need of additives or post-treatment steps.

7.3 Results and Discussion

7.3.1 Synthesis and Molecular Properties

Detailed synthetic procedures for the investigated NFAs are described in Chapter 6.5.1 (for **1d**, **2b** and **2d**, Scheme 3) or in the corresponding literature (for **1b**[111], **1c**[111], **2a**[114], **2c**[115]). For our studies, we used 2,6-di-*iso*-propylphenyl (**1a/2a**) or 2,6-bisphenylphenyl moieties, which were further functionalized with two *tert.*-butyl groups in meta position (2,6-bis(3,5-di *tert*-butylphenyl)phenyl; **1b/2b**), one *tert.*-butyl group in para position (2,6(4-*tert*-butylphenyl)phenyl; **1c/2c**), or a linear hexyl chain in para position (2,6-bis(4-*n*-hexylphenyl)phenyl; **1d/2d**) as imide substituents. While the PBIs are synthesized by the respective ortho-substituted amine with perylene tetracarboxylic acid tetramethylester, the synthesis of the NGTIs was performed *via* the formation of the respective dibromo naphthalimide precursor, which was then coupled with the tetraboronated pyrene core by a Suzuki cross-coupling reaction and subsequent oxidative dehydrogenation. For the hexyl-substituted molecules **1d**[112] and **2d**, literature-unknown amines and dibromo naphthalimides were employed.

The sterical demand of the respective imide substituents is shown in Figure 88 for the PBIs (Figure 107 for all materials). The DFT-calculated structures show, that PBI

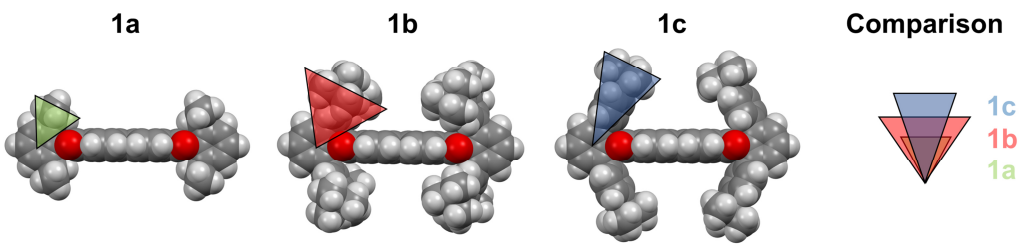

Figure 88: Sterical demand of the imide substituents **a**, **b** and **c** of the chromophores and the comparison between the respective demand.

1c is forming a void on top of the π-surface, while the π-surface of the heavily shielded PBI **1b** is almost covered, due to the multiple *tert.*-butyl groups in the meta-position. These *tert.*-butyl groups are in shorter distance to the π-surface in comparison with **1c**, which prevents the formation of voids. Also, the apparently least shielded molecule **1a** shows a slight coverage of the π-surface due to the remaining H-atom at the *iso*-propyl group.

The PBIs show the same optical features in CH_2Cl_2 solution with high molar extinction coefficients (ε_{Max}) of around 90000 L mol^{-1} cm^{-1} of their S_0-S_1 transition located at 527 nm (λ_{Max}) with a well-resolved vibronic structure with an ratio of the respective intensities of the A_{00} and A_{01} transition of 1.60, while the NGTIs exhibit significantly higher ε_{Max} of around 300000 L mol^{-1} cm^{-1} with a more complex band shape resulting from their two perpendicularly polarized transition dipole moments (μ_{eg}) with maxima at 584 and 489 nm, respectively (Figure 89, Table 26). The $A_{00}\,A_{01}^{-1}$ ratio for the absorption band at around 498 nm ranges from 3.57-3.70, while the other absorption band about 584 nm exhibit ratios of about 2.00-2.17. The stronger (ε_{Max}) and broader absorption (λ_{Max}) characteristics of NGTIs already implies that they might be more suitable acceptors in BHJ OSCs compared to the PBIs. While the PBIs inherit a μ_{eg} of 8.5 D for the short-wavelength transition polarized along the long *N,N´* axis, the NGTIs exhibits two orthogonal polarized μ_{eg} along the short and the long molecular axis of the π-system, respectively (Figure 87). While μ_{eg} along the long axis corresponds to the absorption at 490 nm (11.6 D) the short axis can be related to the absorption at 590 nm (8.8 D).[114] A closer look at the rise of the absorption spectra of the NGTIs in CH_2Cl_2 (Figure 89b) reveals a small

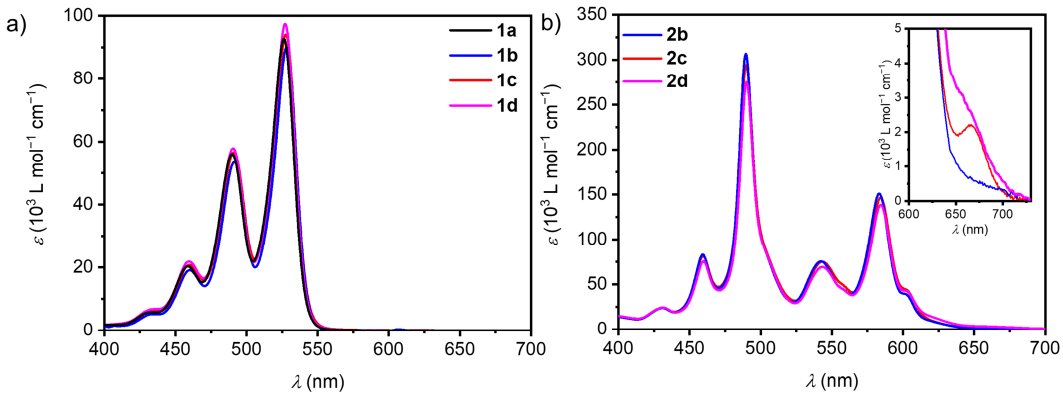

Figure 89: UV-Vis absorption spectra of **1a-d** (a; 1×10^{-4} mol L^{-1})[112] and **2a-d** (b; 4×10^{-6} mol L^{-1}) in CH_2Cl_2 solution with zoom in to the UV-Vis absorption spectra in solution for the NGTIs from 600-750 nm.

additional absorption band at around 680 nm only for **2c** and **2d**, which indicates aggregation even in highly diluted solutions (4×10^{-6} mol L^{-1}) at room temperature. It can be assumed, that aggregation also takes place at higher concentrations of the NGTIs, while it was already presented for the PBIs by our group before.[112] Especially for the PBIs, the aggregation can be also traced with the help of ^{1}H-NMR spectra of the PBI **1b** and **1c**, which were reported by us before.[111] While the most shielded derivative **1b** displays well-resolved NMR spectra already at room temperature, the less shielded derivative **1c** exhibits broad signals indicating aggregation at room temperature, which required us to record the ^{1}H-NMR spectra at elevated temperature of 80 °C in $C_2D_2Cl_4$ (Figure 114).

The steady state fluorescence spectra in CH_2Cl_2 solution are shown in Figure 100. As expected from our previous studies[111], the imide substituents have only a minor impact and all PBIs show a mirror-like emission spectrum with Stokes shifts ($\Delta\tilde{\nu}_{Stokes}$) of around 200-300 cm^{-1}, fluorescence quantum yields (Φ_{Fl}) between

Table 26: Optical properties of **1a-d** and **2a-d** in CH_2Cl_2 solution, which were obtained via UV-Vis absorption and fluorescence studies. Data for **1b**[111], **1c**[111], **1d**[112], **2a**[114] and **2c**[115] were taken from the respective literature.

	λ_{Abs}[a] (nm)	ε_{Max}[a] (L mol^{-1} cm^{-1})	$A_{00}A_{01}^{-1}$[a] (1)	$\Delta\tilde{\nu}_{Stokes}$[b] ($cm^{-1}$)	λ_{Em}[b] (nm)	τ_1[c] (ns)	τ_2[c] (ns)	Φ_{Fl}[d] (%)
1a	526	93000	1.66	320	535	3.8	-	100
1b[111]	528	87000	1.66	250	533	3.7	-	96
1c[111]	527	91000	1.66	250	534	3.8	-	97
1d[112]	528	90000	1.66	250	535	3.9	-	97
2a[114]	489 (584)	278000 (141000)	3.70 (2.00)	670	608	13.4	-	67
2b	489 (583)	307000 (150000)	3.70 (2.00)	700	608	13.5	-	73
2c[115]	490 (585)	320000 (163000)	3.57 (2.17)	540	604	12.0	-	68
2d	490 (584)	274000 (138000)	3.57 (2.00)	670	608	12.4	5.0	62

[a] λ_{Abs}, ε_{Max} and the A_{00} A_{01}^{-1} ratio were obtained for UV-Vis experiments in CH_2Cl_2 solution (PBIs: 1×10^{-4} mol L^{-1}; NGTIs: 4×10^{-6} mol L^{-1}); [b] $\Delta\tilde{\nu}_{Stokes}$, λ_{Em} were obtained from fluorescence experiments in the same solution while the PBIs and NGTIs were excited at 480 nm and at 550 nm, respectively; [c] The respective excited state lifetimes were collected by a TCSPC set up while exciting the PBIs and NGTIs at 505.8 nm and measuring the emission at λ_{Em}. The lifetimes were calculated by fitting a monoexponential decay and a biexponential decay for **2d**; [d] Fluorescence quantum yields were measured absolute in an integration sphere.

96-100% and fluorescence lifetimes (τ) of 3.7-3.9 ns (Table 26). In comparison to the PBIs, the NGTIs exhibit slightly larger $\Delta\tilde{\nu}_{Stokes}$ of 540-700 cm^{-1}, lower Φ_{Fl} in the range of 62-73% but longer τ between 12.0-13.4 ns. Energetically, both classes of materials show almost identical first reduction potentials of −1.02 V (PBIs[231]) and −0.99 V (NTGIs[114]) as determined by cyclic voltammetry, which render them suitable NFA candidates in combination with typical p-type semiconducting materials.

7.3.2 Solid-State Structures

To get insights into the possible packing arrangements which are formed during the rapid spin-coating process while the solar cells fabrication we analyzed single crystals by X-ray diffraction. Either the crystal structures were already literature-known like for **1a**[232], **1b**[111], **2a**[114] and **2c**[115] or we analyzed single crystals, which we have grown using the diffusion method followed by slowly evaporation of the residual solvent for **1c**, **2b** (Table 33). For **1d** and **2d**, it was not possible to grow suitable crystals for the X-ray analysis, presumably due to the flexible hexyl chains which induce significant structural disorder. As weak interactions to the packing neighbor prevail for most of these dyes, we like to emphasize that different structures may be present in thin films and that other polymorphic crystals might be formed under different conditions of crystallization. For instance, solvent or other additives like small molecule donors (e.g. coronene for **2c**) may occupy the cavity and thereby direct the resulting structure. To qualitatively assess the impact of the residual solvent to the respective aggregate structure, we performed DFT calculation of monomers and π-stacked dimers using B3LYP as functional and 6-31g-d,p as basis set.

The respective monomer and dimer structures of molecules in the crystal structure compared with calculated monomers and dimer of the PBIs (**1a-c**) are shown in Figure 90. From the calculational point-of-view **1a** with the di-*iso*-propyl-phenyl imide substituents could not form crossed-stacked dimers, due to large π-distances for about 6 Å, which indicates only weak attractive π-π interactions. According to this the crystal structure of PBI **1a**[232] (Figure 90a, Figure 91a) exhibits rather isolated molecules, whose closest contact originates from edge-to-edge contacts to four neighboring ones, which are aligned in the same layer, but are tilted by 22° with

respect to its *N,N´*axis. The next layer shows a distance towards the first one of 7.3 Å, without any close π-π interactions, as predicted from the DFT-calculation. The even higher π-π distance, which was obtained by the single crystal in comparison to the calculation can be traced back to embedded solvent molecules (CH_2Cl_2) between two chromophores. This structure can be described with the formation of layers by individual edge-to-edge connected monomers.

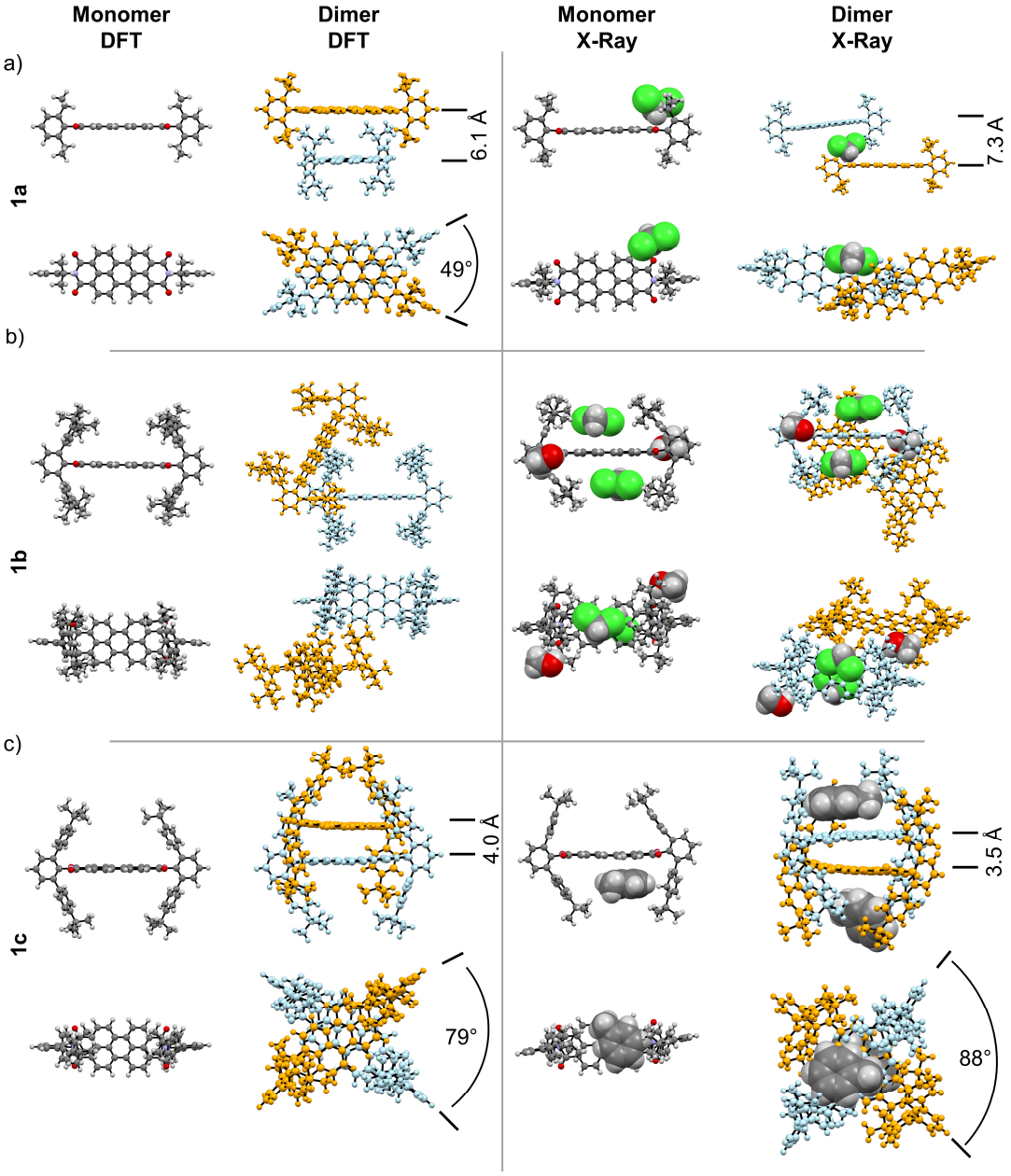

Figure 90: Calculated monomer and dimer structures based on PBI **1a** (a), **1b** (b) and **1c** (c) compared with their respective crystal structure under addition of solvent molecules. Color code: grey – carbon, light grey – hydrogen, red – oxygen, blue – nitrogen. For dimeric structures, the respective PBIs were uniformly colored in orange and light blue. Respective solvent molecules are depicted in spacefill model.

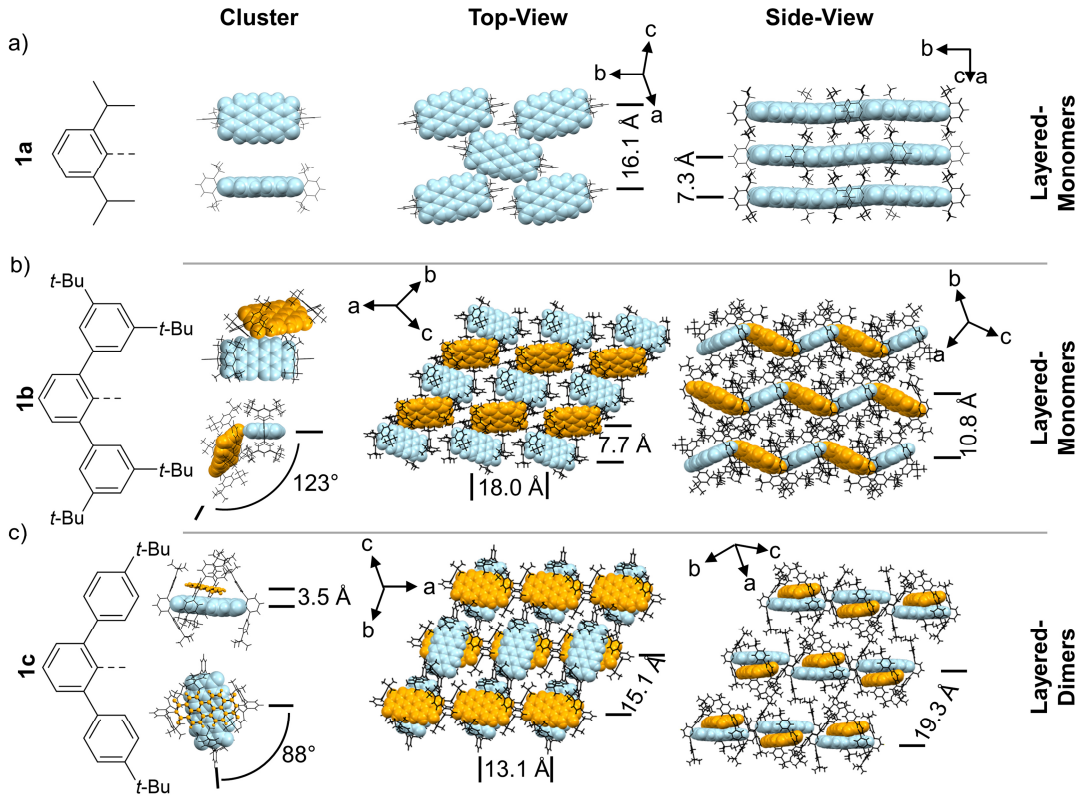

Figure 91: Solid-state molecular packing determined by X-ray crystal structure analysis for PBIs **1a** (a), **1b** (b) and **1c** (c). Illustration of the central molecule and the next neighbors which differ in their planarity (orange, blue) in space-filling, while the imide substituents are displayed in wireframe. The packing motif of the two-dimensional layers and the packing orthogonal to the two-dimensional layers are additionally depicted. Hydrogen atoms are omitted and solvent molecules as well as molecular disorder of the imide substituents are neglected.

The most shielded **1b**[111] does not show any π-stack in the DFT dimer geometry (Figure 90b). Large voids are observable too, due to the most cumbersome imide substituents. In the respective crystal structure of **1b** (Figure 90b, Figure 91b), two individual molecules are present while one molecule shows a planar π-surface (blue) in comparison to the second one which is highly distorted from planarity. Due to the voids, solvent molecules are located either on top of the chromophore (CH_2Cl_2) or next to one carbonyl group per side (MeOH). This leads to discrete edge-to-edge contact of individual chromophores, while the neighbor is tilted towards the central molecule by 123°. Therefore, ribbons are formed as it can be seen in Figure 91b with a molecular distance of 7.7 Å (center-to-center). The next ribbon in the plane shows a distance of even 18.0 Å towards the first one, through which a two-dimensional layer is formed. These layers exhibit a distance between each other of about 12.8 Å.

In contrast to **1a** and **1b**, the geometry optimization yield a cross-stacked dimer structure of **1c** by DFT calculation, which reveal a π-π distance of only 4.0 Å and a tilt angle of 79° towards the *N*,*N*' axis (Figure 90c). As proposed from the DFT calculations we could observe distinct cross-stacked dimers for **1c** in the crystal structure (Figure 91c) with a rotational twist of 88° with respect to their *N*,*N´* axes. While one molecule (blue) shows a planar π-system, the other one shows heavy distortion (as for **1b**). The distortion can be traced back to the bulky *tert.*-butyl groups, which seem to hamper the dimerization process. Nevertheless, the two molecules exhibit a π-π distance of 3.5 Å and thereby form a defined dimer. Even after the dimer formation, large voids are observable in the crystal structure, which are filled with solvent molecules (toluene). Each crossed-stacked dimer is further coordinated with two toluene molecules. The next neighboring dimer shows either the same orientation with a short distance between these dimers of 13.1 Å or a twisted orientation with a slightly increased distance of 15.1 Å. As a result, a two-dimensional layer of dimers is formed with a layer distance of 19.3 Å. As **1d** with more flexible hexyl-chains shows similar substitution pattern like **1c**, we assume, that **1d** is forming a similar packing arrangement in the solid state.

When comparing the respective X-ray structures of these sterically shielded PBIs, **1b** seems to be the most shielded one, which efficiently prevent any π-π interactions to itself. On the first glance, one could think, that **1a** should show the highest tendency for the formation of crossed-stacked dimers due to the smaller di-*iso*-propylphenyl substituents. In reality, it shows a lower tendency towards dimer formation than **1c**, which presumably can be traced back to stabilizing phenyl···H interactions originating from the additional phenyl groups of the imide-substituent of **1c.** This attractive interaction does not lead to dimerization in the case of **1b** due to the *tert.*-butyl groups in meta position, which reduce the size of the void.

The respective calculated monomers and dimers of NGTIs **2a-c** compared with their crystal structures are shown in Figure 92, while their packing arrangements are displayed in Figure 93. They show similarities (**2a-b**) as well as well as differences (**2c**) to their PBI-based counterparts **1a-c**. From the calculational point-of-view **2a** (Figure 92a) should form not form a crossed-stacked dimers. Indeed, like in the case of **1a**, the apparently least-shielded NTGI **2a**[114] (Figure 93a) shows isolated

individual molecules, which form a two-dimensional layer with the two neighboring edge-to-edge connected molecules. The larger π-π distance of 6.8 Å in comparison to the calculated dimer originate from solvent molecules (CH_3Cl), which are located in close proximity next to the chromophores. The formation of edge-to-edge connected chromophores instead of dimers can be traced back to the already mentioned missing phenyl···H interactions. In z-direction two individual layers are formed, leading to alternating A-B packing motif. As in the case of **1a**, the structure can be described by the formation of layers, which consist of individual monomers with edge-to-edge contacts to two neighboring molecules.

For the most sterically shielded NTGI **2b** (Figure 92b and Figure 93b), it was not possible to calculate a discrete π-stacked dimer, due to the large imide substituents. In the respective crystal structure, the resulting large voids between the molecules are filled with several molecules like toluene, methanol and chloroform. The packing of **2b** is characterized by isolated monomers that are surrounded by four edge-to-edge connected neighbors, which lie parallel to each other. Interestingly, because less residual solvent is present in-plane, the distances between the molecules are even smaller compared with **2a**. Towards the next two-dimensional layer, a distance of 12.8 Å can be observed, which is significantly larger than for **2a** due to the bigger imide substituents and the already mentioned solvent inclusion.

Like in the case of **1c**, **2c** (Figure 92c, Figure 93c,d) shows in accordance to the X-ray structures crossed-stacked dimer from the DFT optimization with a π-π distance of 4.1 Å and a tilt angle of 47°. From the crystallographic point-of-view, it was able the obtain two different polymorphs for **2c**.[115] One, where several solvent molecules are present, leading to an monomeric growth and the other one, where coronene was added as a small donor, leading to a dimeric growth. The monomer-like structure exhibits several solvent molecules like toluene and chloroform surrounding the chromophore. Additionally, two other individual chromophores are connected to a central chromophore *via* edge-to-edge contacts (blue/orange/green). The complicated three-dimensional (3D) network can be understood as ribbons, where alternating molecular orientations are present. These ribbons exhibit a distance of 12.5 Å. To the over and underlying plane, these ribbons are connected *via* the green marked molecule leading to a non π-stacked 3D

network. The dimeric structure shows a π-π distance of 4.1 Å, which is the exact calculated value from the DFT experiments. Only a different tilt angle of 34° was obtained, which is lower than the calculated value of 47°. Similar as observed dimeric structure for **1c**, interdigitated dimers of **2c** are formed. The main difference between these structures is that the **2c** dimers an edge-to-edge contact to neighboring dimers leading to a ribbon-like structure, which is missing for **1c**. To the next ribbon, a distance of 12.2 Å was observed, which leads to a layered-like structure consisting of individual dimeric strands.

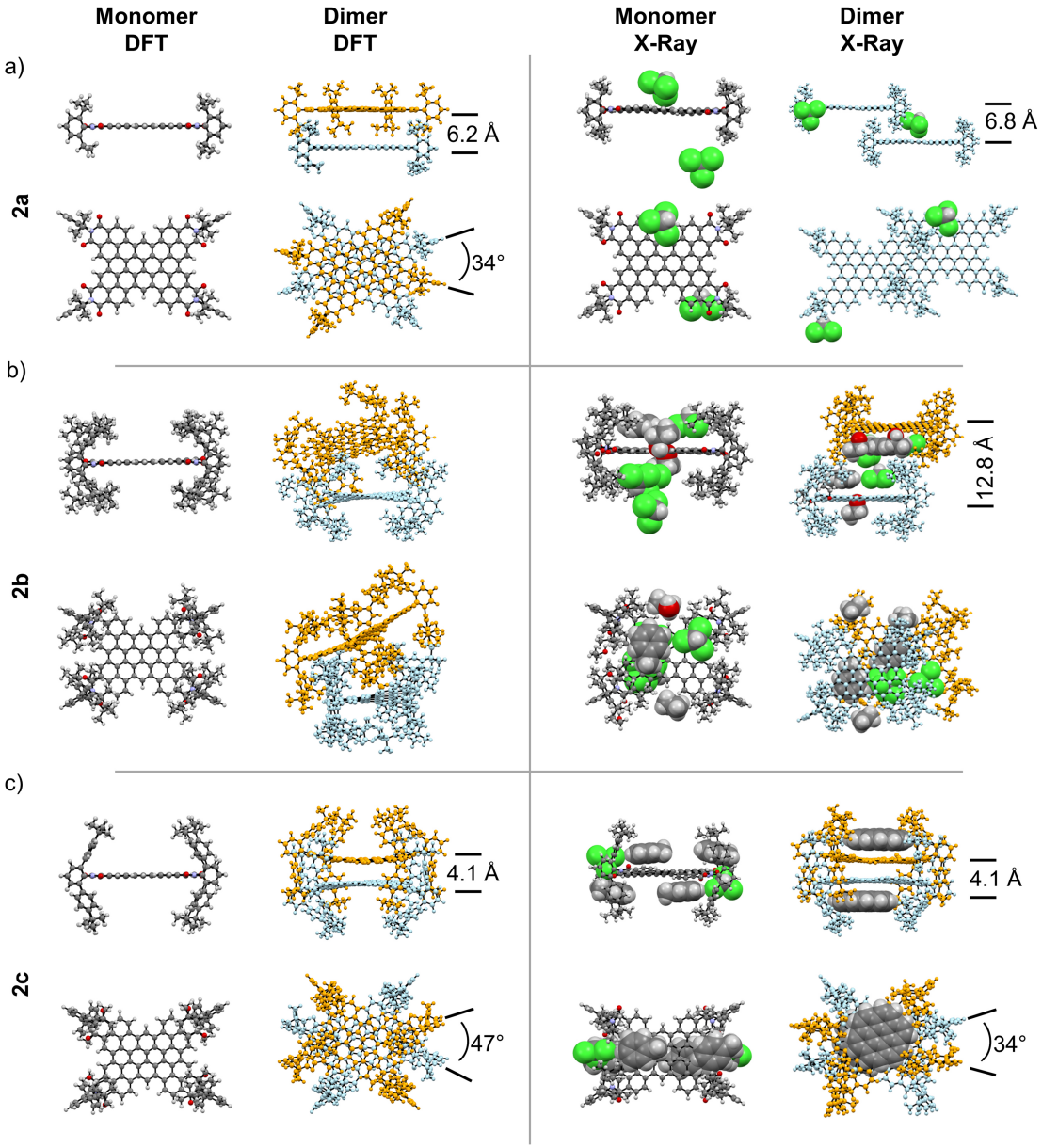

Figure 92: Calculated monomer and dimer structures based on NGTI **2a** (a), **2b** (b) and **2c** (c) compared with their respective crystal structure under addition of solvent molecules. Color code: grey – carbon, light grey – hydrogen, red – oxygen, blue – nitrogen. For dimeric structures, the respective NGTIs were uniformly colored in orange and light blue. Respective solvent molecules are depicted in spacefill model. For **2c** the monomeric and the dimeric structure are shown.

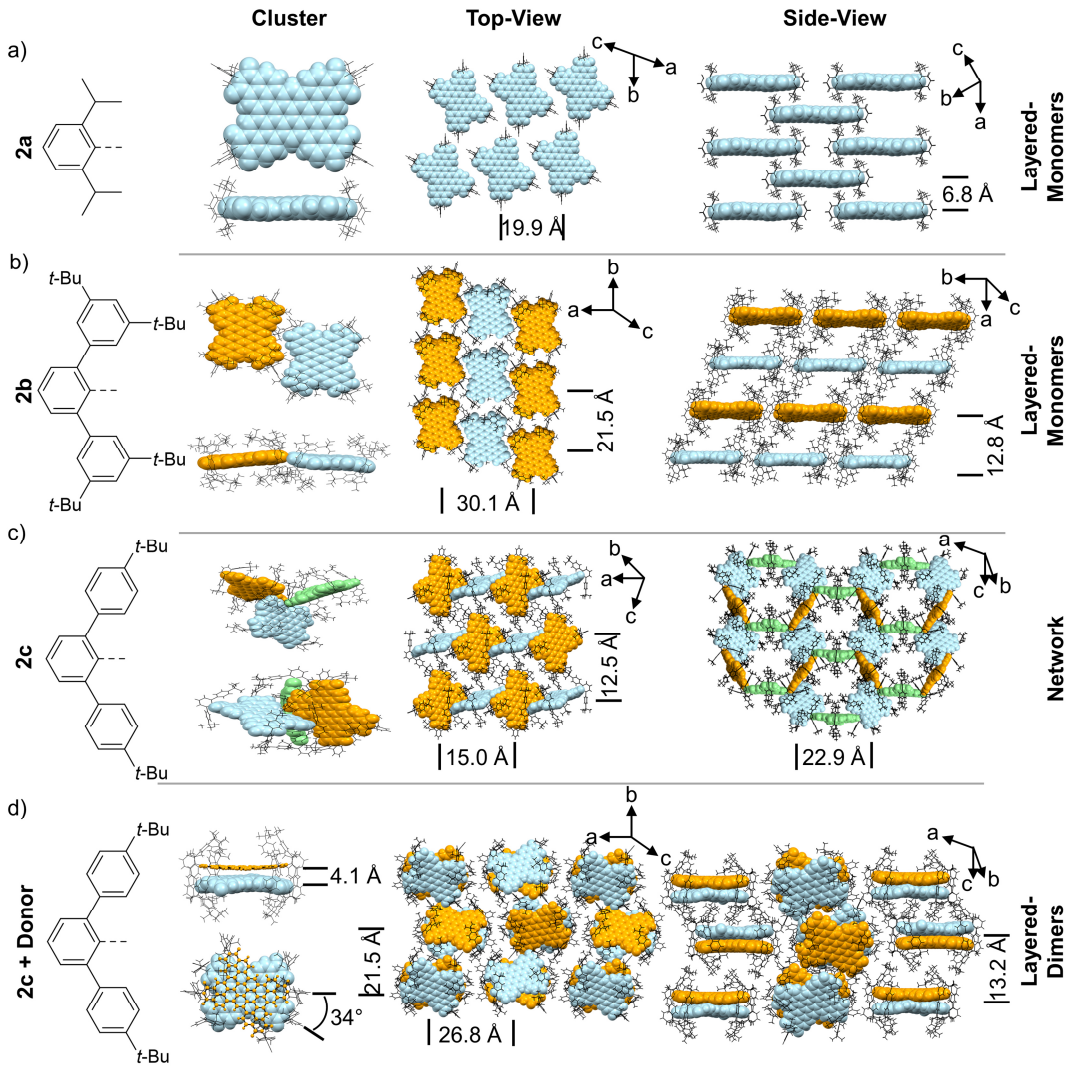

Figure 93: Solid-state molecular packing determined by X-ray crystal structures of the NGTIs **2a** (a)**, 2b** (b) and **2c** (c,d). Illustration of the central molecule and the next neighboring which differ in their planarity (orange, blue, green) in space-filling, while the imide substituents are displayed in wireframe. The packing motives of the two-dimensional layers and the packing orthogonal to the two-dimensional layers are additionally depicted. Hydrogen atoms are omitted and solvent or additional donor molecules as well as molecular disorder of the imide substituents are neglected. For d) a co-crystal structure was used, where the small molecular donor (coronene) was neglected to demonstrate the variety of structures. As these dyes do not shows long ranging supramolecular forces, short ranging forces direct the resulting structures and solvent as well as small donors have a major impact on the structure.

When having a closer view on the molecule-molecule contacts in the crystal structures, mainly two different intermolecular interactions appear to be of relevance for which direct the variety of the solid-state packing motif, namely the π-π interactions towards the dimeric structures and the CH···O interactions leading to an edge-to-edge interaction as shown in Figure 108. Considering, that only weak interactions direct the resulting structure, several polymorphic structures can be possibly formed during the rapid spin-coating process. Nevertheless, it can be concluded that the heavily shielded molecules **1b** and **2b** and the non-shielded

chromophores **1a** and **2a** rather stay in a monomeric species, while the void-forming molecules **1c**, **1d**, **2c** and **2d** should also form dimers in the thin film.

7.3.3 Optical Signatures in Polymer-based Thin Films

The optical changes, which are induced by the presented molecular packing arrangements, were investigated in polymer-based thin films. In line with studies by Zhang *et al.*, we used mixed thin films of the respective acceptor and PMMA[230] for our optical studies instead of **PM6** (OSCs donor polymer) to avoid during the spectroscopic studies parasitic **PM6** absorption on the one hand and to simulate the BHJ morphology of the real device on the other hand. In all shown thin-film samples we used a polymer:acceptor blend solution (1:0.6) with a total concentration of 12 mg mL^{-1} in chlorobenzene without the addition of any additives, which was spin-cast at 750 rpm for 60 s onto quartz substrates. The thin films (Figure 101) were investigated without any post-treatment in accordance with the later OSC fabrication. This allows us to transfer the finding of the PMMA-based layers to the respective active layers of the OSCs. The replacement of PM6 by PMMA had almost no impact on the UV-Vis absorption properties of the acceptors, as it was checked by additional UV-Vis studies (Figure 103).

As mentioned before, the impact of the aggregation can be observed already in solution, like for **1c.** Therefore, the different thin-film absorption spectra on quartz substrates of the PBIs **1a-d** exhibit several changes in comparison with the respective solution spectra (Figure 94, Table 27), which originate from the coupling of μ_{eg} of the respective molecules in close proximity. As μ_{eg} of the PBI´s S_0-S_1 transition is polarized along the *N*,*N´* axis, these materials serve as a tool kit to understand the more complicated changes in absorption band shapes for the NGTIs, which originate from their two orthogonally polarized μ_{eg}.

When discussing the respective UV-Vis absorption as well as fluorescence spectra (for additional information see Figure 102, Figure 104 and Figure 105), one must notice, that UV-Vis experiments resemble quantitative information about the respective absorbing species, while the emission spectra only give qualitative information due to different quantum yields of the respective emitting species and due to possible electron/energy transfer processes between them. All here shown

dyes are mainly present as monomers in the solid state, leading to an Förster resonance energy transfer (FRET) from the monomer to the aggregate as it was described by Zhang *et al*. for similar dyes.[230]

The absorption spectrum of the most heavily shielded PBI **1b** (Figure 94b) with 2,6-di-*tert*-butylphenyl substituents suggests that isolated individual PBI chromophores prevail in the polymer matrices which do not or only slightly interact with each other. Therefore, only a small solid-state blue shift of 1 nm (70 cm^{-1}) was observed. However, weak H-type interaction between the chromophores[233,234] can be deduced from the ratio between the absorption intensities of the first and the second vibronic bands of the S_0-S_1 transition ($A_{00}\,A_{01}^{-1}$) of 1.56, which is reduced compared to the solution value of 1.69. While the absorption spectrum predominantly shows monomeric absorption features, the fluorescence spectrum of this dye in the PMMA matrix showed two clearly distinguishable emission bands – one narrow-band emission at 536 nm and a second broadband emission at about 588 nm ($\Delta\tilde{\nu}_{Stokes}$ = 2000 cm^{-1}). Therefore, predominantly two species within the respective acceptor domain in the PMMA matrix are formed. The narrow emission

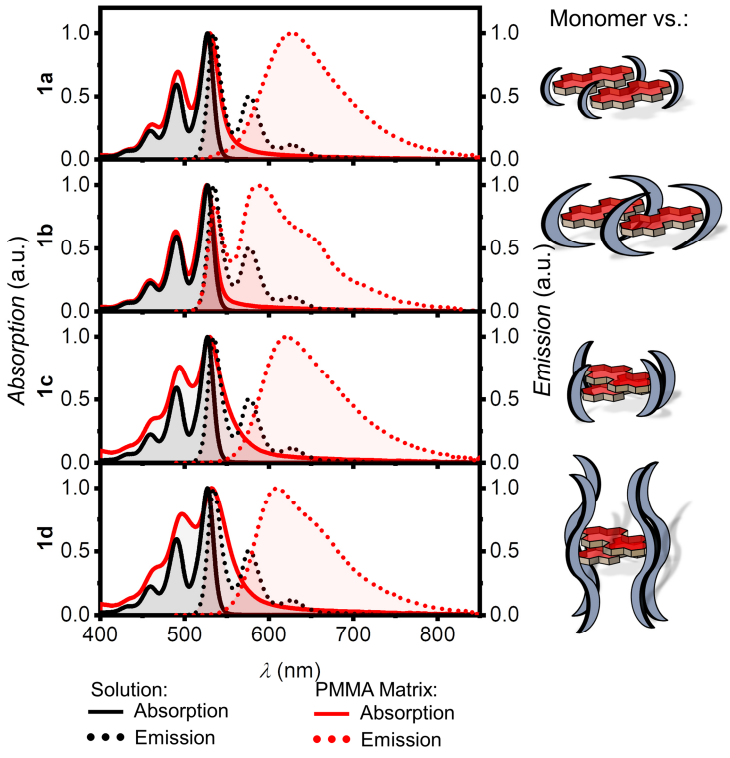

Figure 94: Normalized UV-Vis absorption (solid) and fluorescence (dotted) spectra in CH_2Cl_2 solution (black) and in PMMA matrix spin-casted on quartz substrates (red) of PBIs **1a-d**. For the respective emission spectrum, the acceptors were excited at 550 nm.

bands at 536 nm presumably originates from a rather monomer-like species with short lifetimes (τ_1 = 1.1 ns; Figure 102), while the other emission band can be attributed to individual molecules in close proximity which are connected in an edge-to-edge manner like it was shown in the respective crystal structure (τ_2 = 4.5 ns; Figure 102b).

A similar behavior is observed for the least soluble dye **1a** with the 2,6 di-*iso*-propylphenyl substituents, which shows only a minor solid-state red shift of −4 nm (−140 cm^{-1}) as well as a broadening of the spectra, which we trace back to the formation of a dense edge-to-edge packing under the rapid deposition conditions. In the fluorescence traces of monomer emission is still present, while the main broad and structureless emission at 625 nm ($\Delta\tilde{\nu}_{Stokes}$ = 2800 cm^{-1}) originates from an aggregate species with highly increased lifetime (τ_2 = 12.7 ns; Figure 102a).

In stark contrast, the absorption properties for the less shielded derivatives **1c** and **1d** with para *tert.*-butyl and *n*-hexyl groups at the imide phenyl moiety are drastically altered displaying clear H-type aggregate characteristics.[233,234] In both cases, solid-state red shifts of −3 nm (−110 cm^{-1}) and −5 nm (−140 cm^{-1}) and a large tailing into the long wavelength region compared to **1a** and **1b** were observed. A similar tailing was described by Zhang *et al*. for sterically shielded PBIs, which form crossed-stack packing arrangements.[230,235] Combined with the strongly reduced $A_{00}\,A_{01}^{-1}$ ratio (**1c**: 1.31; **1d**: 1.26) vs. 1.66 (solution)) and the already mentioned

Table 27. Characteristic values for UV-Vis and fluorescence experiments of thin-film samples of the respective acceptor embedded in a PMMA matrix (1:0.6).

	λ_{Abs}[a] (nm)	$A_{00}\,A_{01}^{-1}$ [a] (1)	$\Delta\lambda$[a] (nm / cm^{-1})	$\Delta\lambda$[a] (H or B)	$\Delta\tilde{\nu}_{Stokes}$[b] ($cm^{-1}$)	λ_{Em}[b] (nm)	τ_1[c] (ns)	τ_2[c] (ns)
1a	530	1.42	−4 / −140	B	2800	625	3.5	12.7
1b	526	1.56	2 / 70	H	2000	588	1.1	4.5
1c	530	1.31	−3 / −110	B	2760	621	0.3	6.6
1d	532	1.26	−4 / −140	B	2400	610	4.6	11.1

[a] The maximum absorption wavelength (λ_{Abs}), the ratio of the intensities for the A_{01} and A_{00} transition and its shift ($\Delta\lambda$) by the transition from CH_2Cl_2 solution to the solid state in the PMMA matrix (H – hypsochromic / positive values; B – bathochromic / negative values) were collected from UV-Vis absorption spectroscopy. [b] The Stokes shift ($\Delta\tilde{\nu}_{Stokes}$) and the emission maximum (λ_{Em}) were collected by excitation of the thin-film samples at 480 nm and at 550 nm, respectively. [c] The respective excited state lifetimes were collected by a TCSPC set up while exciting the PBIs and NGTIs at 505.8 nm and measuring the emission at 618 nm (**1a**), 618 nm (**1b**), 588 nm (**1c**) and 610 nm (**1d**). The lifetimes were calculated by fitting a biexponential decay to the respective decay curve.

NMR and UV-Vis experiments (*vide supra*) which indicate H-type coupling of stacked chromophores, we conclude the formation of cross-stacked dimers in the thin-film. In the fluorescence spectra, broad excimer-like emission bands located at 717 nm ($\Delta\tilde{\nu}_{Stokes}$ = 2800 cm^{-1}) and 754 nm ($\Delta\tilde{\nu}_{Stokes}$ = 2400 cm^{-1}) with lifetimes of 6.6 ns and even 11.1 ns (Figure 102), respectively, were observed.

To get further insights into the Coulomb and CT-coupling, which are strongly connected to the respective molecular arrangement in the dimer, impacted by the imide substituents, we used the already shown dimer structures of **1b** and **1c** (Figure 90). According to our previous work,[116] we calculated the impact of the resulting connection motive (π-stacked dimer or edge-to-edge monomer) on the optical properties *via* the respective coupling strength (Table 32). The overall coupling of the respective μ_{eg} (S_0-S_1) is positive (H-type) but low for **1c** (16 meV) and negligible for **1b** (6 meV). The coupling mainly originates from Coulombic coupling $J_{Coulomb}$ of the dimeric structure of **1c**. In both cases, the charge-transfer coupling J_{CT} is almost 0 meV due to minute charge-transfer integrals for both electron and hole transport (t_- and t_+), respectively. Overall, this leads to weak H-type coupling in the case of the dimeric structure for **1b** and a neglectable coupling for **1c**, which correlates well to the optically described $A_{00}A_{01}^{-1}$ values. Due to the same substitution motifs and the same optical changes, we assume similar coupling strength for the dimer of **1d**.

Due to low solubility and concomitant aggregation of acceptor **2a** it was not possible to obtain a thin-film sample in the desired quality for the UV-Vis absorption experiments (Figure 111). Analogue to **1b**, **2b** shows an almost monomer-like absorption in the thin-film (Figure 95, Table 27). Still, minor changes in position and intensity in the thin-film UV-Vis absorption spectrum are still observable. The second absorption band at around 490 nm, which correspond to the μ_{eg} polarized along the long molecular axis, has a similar shape in the thin film as in solution. This underpins the $A_{00}A_{01}^{-1}$ (490 nm) ratio of 3.13 in the thin film compared with 3.70 in solution. Furthermore, a small solid-state blue shift of only 2 nm (80 cm^{-1}) was observed. Similarly, the $A_{00}A_{01}^{-1}$ ratio of the absorption band polarized along the short axis at 580 nm of 1.82 compares with 2.00 in solution and for the solid-state blue shift is minor with 1 nm (30 cm^{-1}). This leads to the conclusion, that NGTI **2b,**

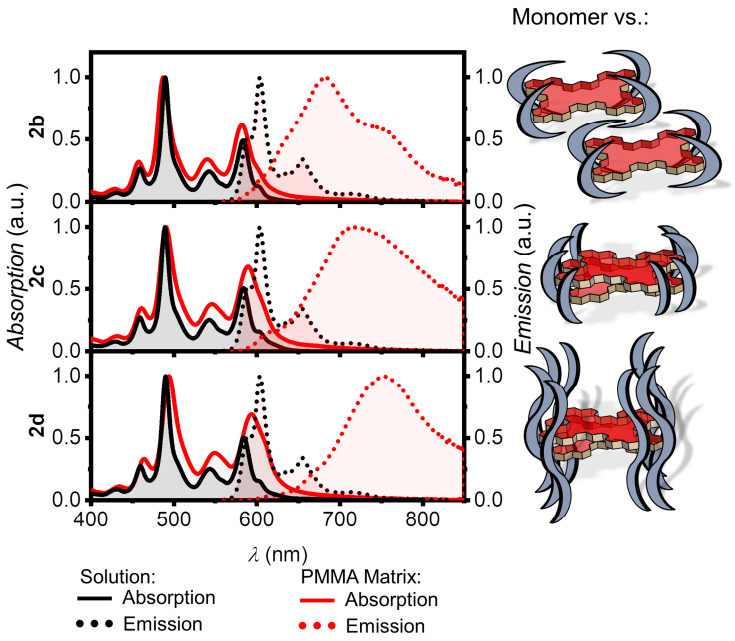

Figure 95. Normalized UV-Vis absorption (solid) and fluorescence (dotted) spectra in CH_2Cl_2 solution (black) and in PMMA matrix spin-casted on quartz substrates (red) of NGTIs **2b-d**. **2a** was not investigated due to inferior film-formation properties. For the respective emission spectrum, the acceptors were excited at 550 nm.

like PBI **1b,** rather forms an edge-to-edge arrangement as it was shown in the crystal structure, due to the two bulky *tert*-butyl groups at each meta position of the imide phenyl units, which successfully shield the chromophore core. Therefore, the Coulomb coupling between the μ_{eg} of neighboring molecules is low due to the large distances in the solid state and an almost monomer-like absorption is retained. As in the case of **1b**, an ensemble of emission bands at around 610 nm, 700 nm and 750 nm were obtained for **2b** in PMMA matrix in the fluorescence experiment. The weaker one at around 610 nm can be traced back to mainly remaining monomers, while the rest correspond to the already described edge-on neighboring molecules (682 nm; $\Delta\tilde{\nu}_{Stokes}$ = 2520 cm^{-1}).

When reducing the bulkiness of the imide substituent as for **2c** and **2d**, the optical changes can be traced back to the formation of discrete dimers as for **1c** and **1d**. This can be underlined with the help of the solid-state red shifts, the tailing as well as excimer emission at 717 nm ($\Delta\tilde{\nu}_{Stokes}$ = 3000 cm^{-1}) and 754 nm ($\Delta\tilde{\nu}_{Stokes}$ = 3800 cm^{-1}). Respective increased excimer-like fluorescence lifetimes of 8.7 ns and 13.3 ns compared with the lifetime of 5.7 ns of the most shielded derivative **2b** cooperate this finding (Table 28, Figure 102). Due to the successive bathochromic shift of the emission maximum and the increased lifetimes of the **2c**

Table 28. Characteristic values for UV-Vis and fluorescence experiments of thin-film samples of the respective acceptor embedded in a PMMA matrix (1:0.6).

	λ_{Abs}[a] (nm)	$A_{00}\,A_{01}^{-1}$[a] (1)	$\Delta\lambda$[a] (nm / cm^{-1})	$\Delta\lambda$[a] (H or B)	$\Delta\tilde{\nu}_{Stokes}$[b] ($cm^{-1}$)	λ_{Em}[b] (nm)	τ_1[c] (ns)	τ_2[c] (ns)
2b	487	3.13	2 / 80	H	2520	682	2.0	5.7
	582	1.82	1 / 30	H				
2c	490	2.86	0 / 0	0	6500	717	1.9	8.7
	589	1.79	−4 / −120	B				
2d	491	2.94	−1 / −50	B	3800	754	2.8	13.3
	586	1.56	−2 / −60	B				

[a] The maximum absorption wavelength (λ_{Abs}), the ratio of the intensities for the A_{01} and A_{00} transition and its shift ($\Delta\lambda$) by the transition from CH_2Cl_2 solution to the solid state in the PMMA matrix (H – hypsochromic / positive values; B – bathochromic / negative values) were collected from UV-Vis absorption spectroscopy. [b] The Stokes shift ($\Delta\tilde{\nu}_{Stokes}$) and the emission maximum (λ_{Em}) were collected by excitation of the thin-film samples at 480 nm and at 550 nm, respectively. [c] The respective excited state lifetimes were collected by a TCSPC set up while exciting the PBIs and NGTIs at 505.8 nm and measuring the emission at 717 nm (**2b**), 682 nm (**2c**) or 754 nm (**2d**). The lifetimes were calculated by fitting a biexponential decay to the respective decay curve.

and **2d**, compared with the heavily shielded derivative **2b**, we assume, that the π-stacked dimer formation is strongly favored for **2d** followed by **2c** and is almost impossible for the most shielded **2b**, which is in line with the respective X-ray data.

Furthermore, the TD-DFT calculated couplings (Table 32) for the heavily shielded **2b** showed only a weak J-type Coulomb coupling (−22 meV) for the μ_{eg}, which is oriented along the long molecular axis and a neglectable H-type coupling (9 meV) for the μ_{eg} oriented along the short molecular axis. An opposite behavior was obtained for dimers of **2c**, which revealed weak H-type Coulomb coupling (36 meV) for the μ_{eg} which is oriented along the long molecular axis and weak J-type coupling (−29 meV) for μ_{eg} oriented on the short-axis. This correlates to the spectral changes of the thin film, where μ_{eg} of the short and the long axis behave differently.

Accordingly, our UV-Vis absorption and fluorescence studies showed that we are able to fine-tune the capability for self-aggregation into dimers of these dyes in the thin film with the help of the different bulky substituents. We assume that most of the respective chromophore is still present in a monomer species, which can be traced back to the almost monomer-like absorption properties. Nevertheless, for both series of chromophores a Förster resonance energy transfer takes place from the monomer to the respective aggregate species.

7.3.4 Organic Solar Cells

Based in their strong absorption and appropriate redox properties all PBIs and NGTIs should be well-suited to serve as acceptor compounds in polymer-based OSCs with the donor polymer **PM6** (Figure 96a). Just by comparing the two spectral ranges of the absorbed light of the PBI:**PM6** and NGTI:**PM6** mixtures, we would expect a similar short-circuit current density (J_{SC}) (Figure 96b). However, as the NGTIs exhibit significantly higher molar extinction coefficients per mass, the resulting J_{SC} for the NGTIs should be higher. The respective combination covers a spectral range from about 400 nm to 700 nm. For the robust screening procedure, a reliable inverted device architecture was chosen, which consists of ITO|ZnO|**PM6**:NFA(1:0.6)|MoO_3|Al (Figure 97a). Energetically, an interesting circumstance can be observed (Figure 96c). As all the here investigated dyes possess their first reduction potential at around −1 V in solution, they should also show similar open-circuit voltages (V_{OC}), if the respective energy loss factor (E_{Loss}) in the BHJ is the same (Additional information see Figure 106 and Table 31). This would allow gaining insights into the relationships of V_{OC} to the molecular isolation and arrangement in the solid state. As the NFAs show different solubility, all solar cells were spin-coated (750 rpm, 60 s) from chlorobenzene solution with a blend ratio of 1:0.6 (m_D:m_A) and a total concentration of 12 mg mL^{-1} to obtain almost equal layer thicknesses of approximately 90 nm each. The combination with additives or any post-processing step was deliberately avoided but also had no positive effect on the device efficiency. The respective *J-V* curves of all OSCs are shown in Figure 97b (dark curves are shown in Figure 109), while the characteristic values are listed in Table 29. Most of the dyes showed indeed an appropriate diode-like behavior, which is remarkable since the rigid bulky imide substituents prohibit the close contacts

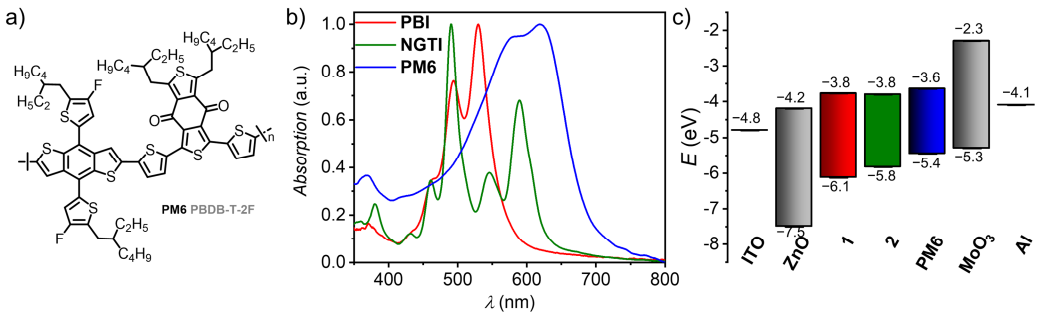

Figure 96. a) Chemical structure of donor polymer **PM6** also known as **PBDB-TF**. b) Normalized UV-Vis absorption spectra of thin films of **1b** and **2b** compared with the donor polymer **PM6**. c) Schematic energy diagram of all OPV materials.

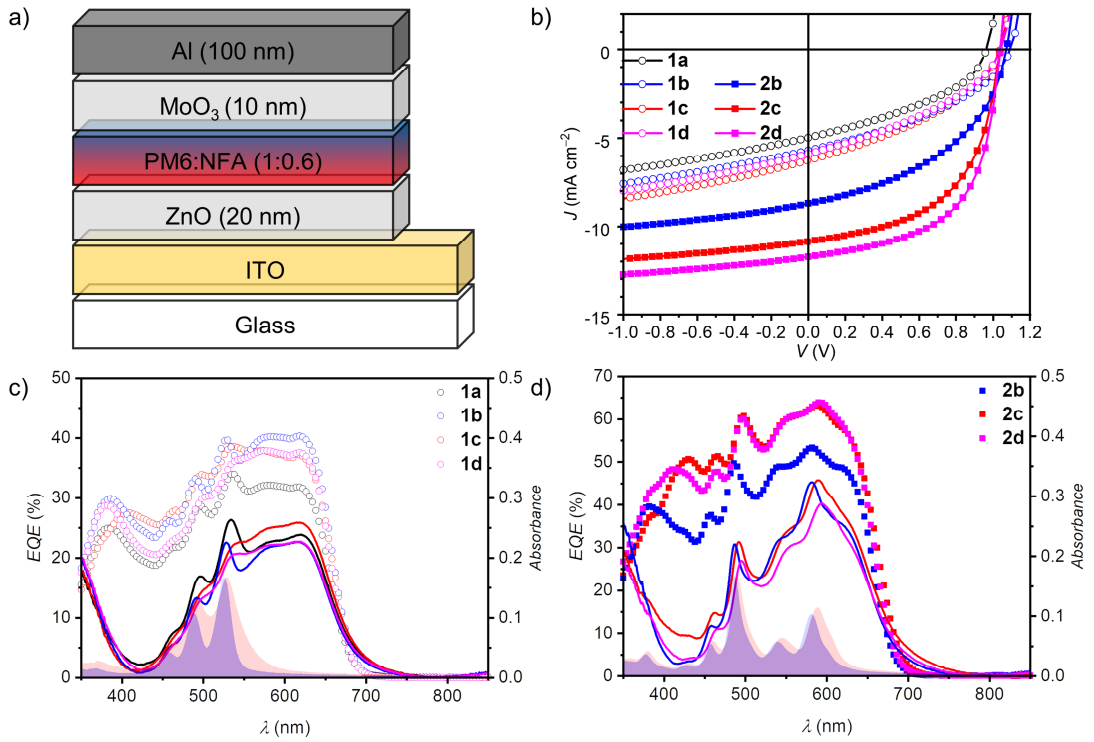

Figure 97. a) Schematic representation of the device architecture of the inverted OSCs. b) *J*-*V* curves of shielded NFAs containing OSCs in combination with **PM6** as donor material, which were measured under inert conditions and AM1.5G irradiation. EQE (symbols) and UV-Vis absorption (solid) spectra of the BHJ OSCs based on PBIs (c) and NGTIs (d). For clarification the absorption spectra of PMMA-based films of **1b**, **1c**, **2b** and **2c** were displayed in c) and d) to further represent the impact of the packing to the spectroscopic changes.

between the π-surface of the NFAs to enable charge transport. Only for **2a**, no diode-like behavior was observed due to its insufficient solubility and strong phase separation from the donor polymer after spin-coating. The diode-like behavior for all other devices can be quantified with the $J_{(-1\ V)}\ J_{SC}^{-1}$ ratio. An ideal solar cell would exhibit a value of 1. For the here shown OSCs, the values decrease from about 1.33-1.39 for the PBIs down to 1.09 for the NGTIs **2c** and **2d**. On the first glance, it seems that an increased size of the π-surface lead to a better diode-like behavior.

Interestingly, all PBIs showed almost the same J_{SC} value of around −5.5 to −5.7 mA cm^{-2} although they display different absorption spectra. Therefore, it can be concluded, that the imide substituents for the shielded PBIs have only a minor impact on overall photon collection, exciton migration and resultant respective J_{SC} value. The EQE spectra of these acceptors revealed a broadband photocurrent contribution ranging from 300-700 nm with maximum EQE values of around 40%. When comparing the different EQE and UV-Vis absorption spectra of these OSCs (Figure 97c) and with the spectra of the PBIs in the PMMA matrix (Figure 94) it can be concluded, that both species, the monomers and dimers contribute to the

Table 29. Photovoltaic parameters of the inverted BHJ OPVs in ITO|ZnO|**PM6**:NFA|MoO_3|Al architecture. All parameters (expect of J_{SC}^{EQE}) were collected from a *J-V* measurement under inert and AM1.5G conditions. For the statistics, 15 individually operating devices were measured.

NFA	J_{SC}^{EQE} (mA cm^{-2})	J_{SC} (mA cm^{-2})	$J_{(-1\,V)}J_{SC}^{-1}$ (1)	V_{OC} (V)	V_{OC}^{Max} (V)	E_{Loss} (V)	FF (%)	PCE (%)	PCE^{Max} (%)
1a	−4.9	−5.0 ±0.2	1.37	0.95 ±0.01	0.96	0.70	40 ±1	1.9 ±0.1	2.1
1b	−5.5	−5.7 ±0.1	1.33	1.09 ±0.02	1.12	0.54	38 ±1	2.4 ±0.1	2.5
1c	−5.5	−5.5 ±0.1	1.39	1.02 ±0.02	1.04	0.62	37 ±1	2.1 ±0.2	2.5
1d	−6.0	−5.7 ±0.2	1.36	1.03 ±0.01	1.04	0.62	37 ±1	2.2 ± 0.1	2.4
2b	−7.7	−8.6 ±0.2	1.15	1.08 ±0.01	1.08	0.60	44 ±1	4.1 ±0.1	4.2
2c	−9.6	−10.7 ±0.5	1.09	1.02 ±0.02	1.04	0.64	54 ±1	6.0 ±0.2	6.4
2d	−9.7	−10.8 ±0.5	1.09	1.04 ±0.01	1.04	0.64	56 ±1	6.3 ±0.5	7.1

photocurrent. The calculated short-circuit current density, which was obtained by integrating the EQE (J_{SC}^{EQE}), exhibits the same trend.

As expected, all NGTIs **2b-d** exhibit significant higher J_{SC} values of −8.59 (**2b**), −10.75 (**2c**) and −10.79 (**2d**) mA cm^{-2} in combination with the donor polymer **PM6** compared to their PBI counterparts. It seems to be, that the edge-to-edge connected monomers as in the case of **2b** show a significantly higher recombination rate as the preassembled dimers in the case of **2c** and **2d**. Therefore, a closer look on the respective EQE spectra is needed. In the case of the NGTIs small changes in the EQE and absorption maxima for **2c** and **2d** again can be traced back to the formation of dimers. Therefore, not only the isolated monomer species of **2c** and **2d** contributes to the photocurrent generation but also the respective aggregate, namely the dimer.

When comparing the V_{OC} of the different PBIs values from 0.96 V up to 1.12 V were observed. Surprisingly, the largest V_{OC} of 1.12 V was measured for the most enwrapped PBI **1b**, while the other derivatives exhibit values of 1.04 V (**1c**/**1d**) and 0.96 V (**1a**). We assume, that the V_{OC} value can be directly related to the respective

molecular arrangement in the NFA domains. Monomeric arrangements lead to high V_{OC} values (**1b**), while the formation of dimers yield lower values (**1c**/**1d**). The lowest V_{OC} for **1a** could be related to a non-suitable interface to the donor polymer, due to its low solubility, which disturbs the spin-coating process. For the NGTIs, similar V_{OC} values were observed ranging from 1.04 V for **2c** and **2d** to up 1.08 V for **2b**. These observations are in line with the PBIs. The lower V_{OC} for **2b** in comparison to **1b** originates from the larger π-surface, which less shielded than the smaller one from the PBIs.

The third parameter to be discussed is the fill-factor (FF), which gives information about a balanced electron and hole mobility as well as recombination pathways in the respective OSCs. Here, most PBI-based devices showed a medium FF between 37-40%, while for the NGTI-based devices an increase in FF from 44% for **2b** even to up to 57% for **2d** was observed. This indicates that an increasing size of the π-surface of the NFA as well as a packing arrangement with more intermolecular contacting possibilities between the acceptor dyes (for **2c** and **2d**) in the BHJ seems to facilitate the electron transport for the NGTIs.

The main figure of merit for an OSCs is the power conversion efficiency (PCE). While the PBI-based devices showed a PCE of about 2.1-2.5%, the NGTI-based devices showed significantly increased efficiencies. NGTI **2b** with the most shielded π-surface showed the lowest PCE of up to 4.4%, while **2c** reaches 6.4%. The highest PCE was obtained for **2d** with up to 7.1%, due to its increased V_{OC} and J_{SC}.

To get further insights into the charge-transport properties of the active layers, we processed space-charge-limited current devices (SCLC) in ITO|PEDOT:PSS|BHJ|MoO_3|Al (hole-only device; HOD) and in ITO|ZnO|BHJ|PDINO|Al (electron-only device, EOD) architecture with the same active layer as in the OSC experiments (Figure 98). While the hole-mobility, which is connected to the polymer **PM6**, is overall high and in the range from 10^{-4} to 10^{-3} cm^2 V^{-1} s^{-1} the electron mobility differs significantly for the NFAs. While all PBIs show an overall low electron mobility of about 10^{-9} to 10^{-8} cm^2 V^{-1} s^{-1} the NGTIs exhibit an increased mobility ranging from 10^{-8} up to 10^{-6} cm^2 V^{-1} s^{-1} from **2b** over **2c** to **2d**. Therefore, it can be concluded that the NGTI core unit is more capable to facilitate electron transport than the PBI analogues. Furthermore, we are

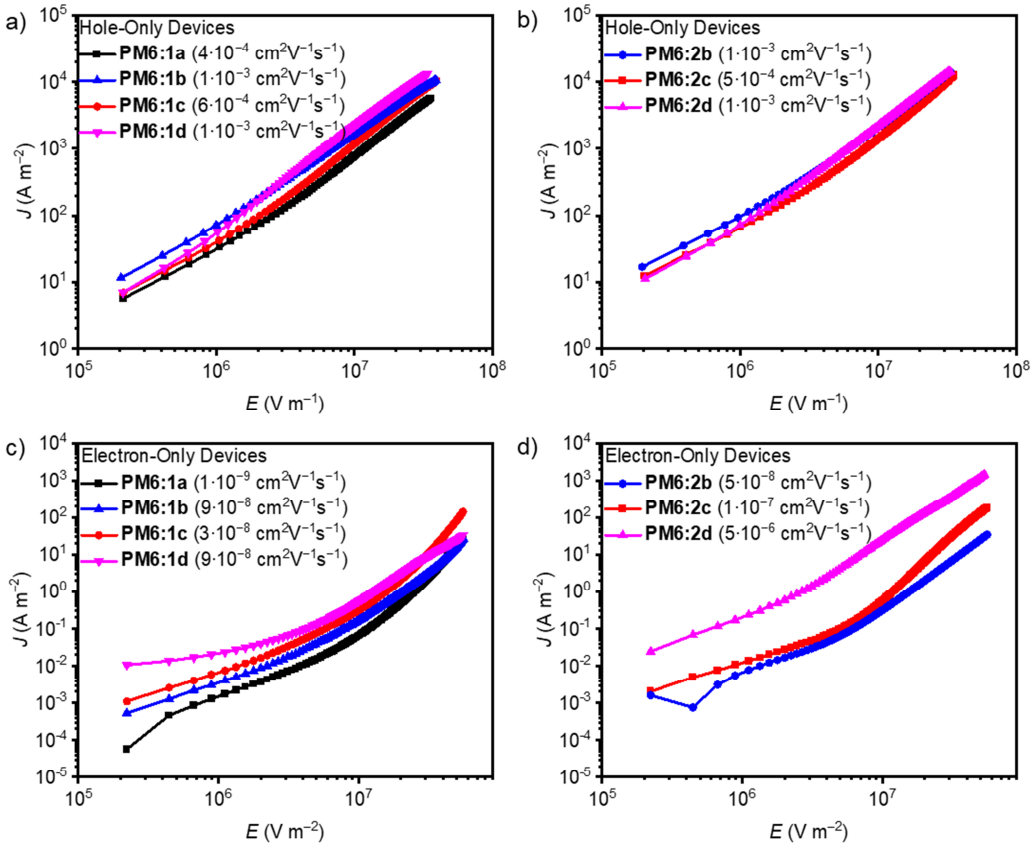

Figure 98: SCLC plots in *J-E* format with the respective charge carrier mobility. Hole-only devices were processed in ITO|PEDOT:PSS|BHJ|MoO_3|Al architecture (a,b), while for the electron-only devices ITO|ZnO|BHJ|PDINO|Al (c,d) was chosen. The calculation of the mobility.

able to identify the *n*-hexylphenyl substituents of **1d** and **2d** as the most potent substituents for best film-forming ability as well as NFA packing arrangement for optimal charge-transport, followed by the *tert*-butylphenyl and the di-*tert*-butylphenyl substituent. Whilst the percolation pathways for electron transport in the respective acceptor domains cannot be attributed to a continuous π-stack of NFAs, we hypothesize that edge-to-edge contacts of residual monomers as shown in Figure 108, can to certain extend enable the observed mobilities even without an orbital overlap between acceptor molecules. Investigations of the morphology of all blends by AFM (Figure 110), did not reveal distinguishable separated donor or acceptor domains. Instead, overall low surface roughnesses in root mean squares of only 2-3 nm at a 10×10 mm^2 surface area the active layer exhibits a very homogenous and well mixed BHJ with presumable nanometer-scaled acceptor domains.

While we assume, that the exciton diffusion in the respective NFA domain is performed by FRET, the recombination pathways limiting the device's performance are not clear so far. Therefore, we performed a recombination analysis analogue to Li *et al.*[215] by measuring the dependence of J_{SC} and V_{OC} to the incident light power (P_{Light}), which is shown in Figure 99. For analyzing J_{SC} *vs.* P_{Light}, the obtained J_{SC} values are fitted with the power-law equation:

$$J_{SC} \propto P_{Light}^{\alpha}. \tag{3}$$

The power factor α is used for describing the mechanism of the recombination. If α is close to unity, only bimolecular recombination takes place, while monomolecular recombination can be neglected. In the case of the shielded PBIs (Figure 99a), α is determined to around 0.83-0.88, which lead us to the presumption that both monomolecular and bimolecular recombination pathways are possible. In the case of the NGTIs (Figure 99b) α increases up to 0.94 (**2d**) and accordingly a part of the monomolecular recombination can be avoided. This can be traced back to the large available π-surface as well as the formation of the variety of possible structures,

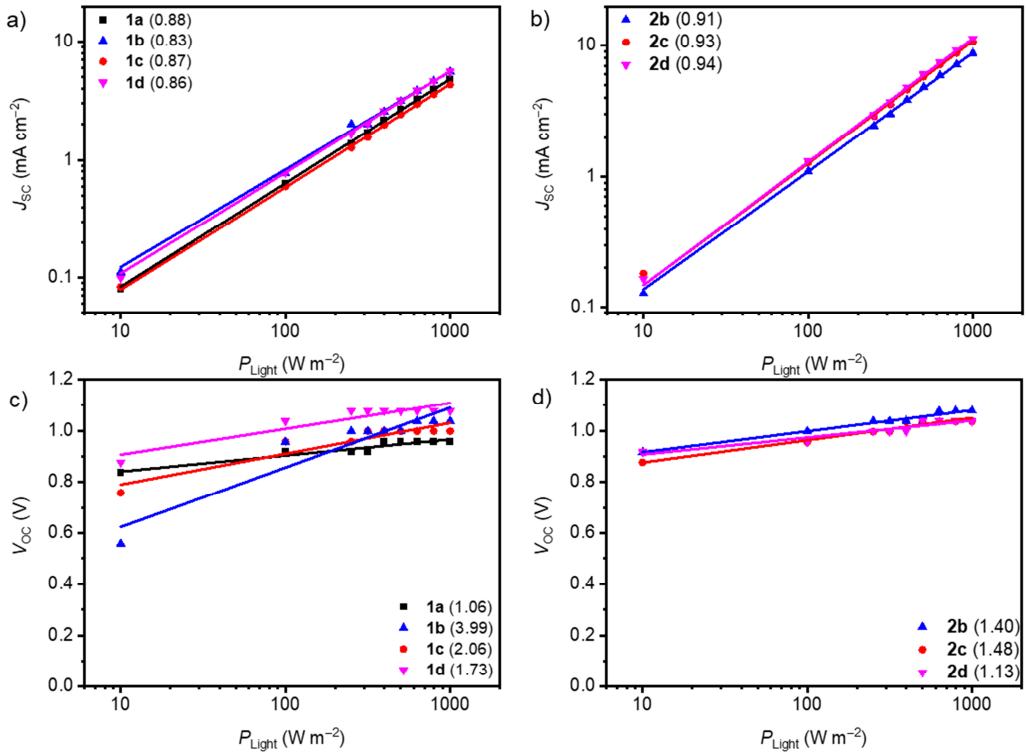

Figure 99: J_{SC} *vs.* P_{Light} dependence for PBIs (a) and NGTIs (b). The data was fitted using the power-law equation. The α-value is given in brackets. V_{OC} *vs.* P_{Light} dependence for PBIs (c) and NGTIs (d). The n-value is given in brackets.

which forms a good interface to the polymer **PM6**. The V_{OC} *vs.* P_{Light} dependence can be described with a linear dependence of ln(P_{Light}) to V_{OC} with a slope of nk_BTq^{-1}. k_B is the Boltzmann constant, T the temperature and q the elementary charge. The ideality factor n represents in combination to the J_{SC} vs. P_{Light} plot the recombination mechanism. n is close to 1, when bimolecular recombination takes place, while higher values are obtained for trap-assisted recombination. For the PBI-based OSCs n ranges from almost 1 to almost 4 (Figure 99c).With an increased sterically demand of the imide-substituents, higher n values were obtained, which can be traced back to the formation of energetic traps within the BHJ probably caused by a too intense shielding. For **1a** almost the whole π-surface is accessible, which leads to a low trap density and therefore a low n value of only 1.06. In the case of **1b** the π-surface is almost completely blocked, which generates several trap states and a very high n value of 3.99. **1c** and **1d** are due to the different substitution motive in-between these extremes. Nevertheless, the n factor is high with values of almost 2, which suggests that trap states are still dominating. Better ideality factors were obtained for the NGTIs (Figure 99d). Here, **2b** and **2c** showed a similar value of around 1.4, which still indicates a trap-assisted recombination pathway. For **2d** the lowest value of 1.13 was observed, which implies the best interface to the polymer as well as a lower trap density. Therefore, it can be summarized that the main recombination pathways of those shielded acceptors are trap-assisted recombination events in the BHJ.

Table 30: Summarized mobility (μ_h, μ_e) values, which were obtained *via* SCLC measurements in ITO|PEDOT:PSS|BHJ|MoO_3|Al architecture for hole-only devices and ITO|ZnO|BHJ|PDINO|Al for the electron-only and recombination parameters α and n, which were obtained by J_{SC} *vs.* P_{Light} and V_{OC} *vs.* P_{Light} measurements.

NFA	μ_h ($cm^2\ V^{-1}\ s^{-1}$)	μ_e ($cm^2\ V^{-1}\ s^{-1}$)	α (1)	n (1)
1a	4×10^{-4}	1×10^{-9}	0.88	1.06
1b	1×10^{-3}	9×10^{-8}	0.83	3.99
1c	6×10^{-4}	3×10^{-8}	0.87	2.06
1d	1×10^{-3}	9×10^{-8}	0.86	1.73
2b	1×10^{-3}	5×10^{-8}	0.91	1.40
2c	5×10^{-4}	1×10^{-7}	0.93	1.48
2d	1×10^{-3}	5×10^{-6}	0.94	1.13

The here shown OSCs exhibit unique pathways for electrons and excitons in the NFA domains, which are the reason that also these shielded NFAs show an OSC performance. While excitons are transferred by an Förster resonance energy transfer, the electrons are transported *via* an edge-to-edge transport between individual chromophores. This transport mechanism finally led to the observed performances, which reached up to 7.1% for **2d**. This demonstrates the favorable effect of the π-stacked dimerization as well as a presumably 3D percolation network among these dimers. The maximum PCE of 7.1% for NTGI **2d** is indeed remarkably high considering that no classical percolation pathways with π-orbital overlap are present inside the respective acceptor domains

7.4 Conclusion

In this chapter, we demonstrated the application of a series of new non-fullerene acceptor molecules based on shielded polycyclic aromatic dicarboximides, namely perylene bisimides and nanographene tetraimides, which we decorated with different rigid imide substituents. These sterically demanding substituents shield specific parts of the chromophore's surface, which strongly prevent over-aggregation. We summarized their optical properties in solution, investigated their solid-state structures and the impact on the optical signatures in the thin film blended with a polymer. With the help of UV-Vis absorption and fluorescence spectroscopy in combination with (TD-)DFT-calculations and the respective crystal structures we were able to gain an in-depth view in the molecular arrangement within the respective acceptor domains. Our work showed that small optical changes in the thin film can be traced back to the formation of edge-to-edge connected monomers or π-stacked dimers. We assume, that a part of the acceptor material is undergoing a preorganization process already in solution, while the other part is still present as monomers. The position of this monomer-dimer-equilibrium can be changed by varying the size of the void, which is formed due to the sterical demand of the imide substituents. In organic solar cells, the monomer and the dimer absorb light and generate photocurrent. The exciton transport probably occurs over an Förster resonance energy transfer in the NFA domains. After the efficient charge separation, the chromophore's size plays a crucial role in terms of the charge transport, due to the lack of extended π-stacked molecules in

the NFA domains. We were able to proof, that the large nanographene tetraimides exhibit an improved charge-transport behavior than their smaller perylene bisimide counterparts. Generally, the charge-transport of these dyes is conducted *via* an edge-to-edge transport leading to good diode-like behaviors in OSCs. We could also demonstrate that the open-circuit voltages are strongly connected to the aggregation behavior of the respective acceptor molecule enabling values up to 1.12 V for PBIs, which tend to stay in a monomeric phase. NFAs, which are able to undergo dimerization exhibit V_{OC} values of 1.04 V. We could show that the best materials in our study (NGTI **2d**) exhibit dimer formation as well as a three-dimensional edge-to-edge packing motif, which increases the solar cell performance to a maximum PCE value of 7.1% in combination with **PM6** in inverted BHJ solar cells. The efficiency of the here shown devices is limited, due to the charge-carrier mobilities and due to the recombination pathways at energetic traps. Both could be overcome with the help of even larger π-systems, which would also allow absorption up to the NIR-region to increase the photocurrent.

7.5 Supporting Information for CHAPTER VII

7.5.1 Materials and Methods

Synthesis: **1a** was purchased from BASF, the synthesis of **1b**[111], **1c**[111], **2a**[114] and **2c**[115] was published before. The synthetic procedures for the new materials **1d**[112], **2b** and **2d** as well as their characterization is reported in Chapter 7.5.2.

Measurements and Characterization: UV-Vis absorption spectroscopy in CH_2Cl_2 was measured at room temperature on a Jasco V770 spectrophotometer in 10 mm cuvettes (SUPRASIL®, Hellma® Analytics). For the thin-film spectra on quartz substrates (SUPRASIL®, Hellma® Analytics) as well as of the active layer of the OSCs, a Perkin Elmer Lambda 950 spectrometer with an integration sphere was used. The PMMA-based thin films of the investigated compounds were fabricated by spin coating a blend of poly(methyl methacrylate) (PMMA) and the respective NFA on quartz substrates (1:0.6, c_{Total} = 12 mg mL^{-1} in CB, 750 rpm, 60 s). Fluorescence spectroscopy in CH_2Cl_2 solution (10^{-6} M, A_{max} < 0.2, spectroscopic grade, Uvasol®, Merck) as well as in the thin film were measured at room temperature on an Edinburgh Instruments FLS980-D2D2-ST spectrometer and were corrected against the photomultiplier sensitivity and the lamp intensity. Fluorescence lifetimes were determined with an EPL picosecond pulsed diode laser (λ_{Ex} = 505.8 nm) for time correlated single photon counting (TCSPC) with the same spectrometer. Fluorescence quantum yields were measured in CH_2Cl_2 on a Hamamatsu Absolute PL Quantum Yield Measurement System CC9920-02. NMR-Spectroscopy was performed on a Bruker Avance III HD 400 MHz NMR spectrometer relative to residue undeuterated solvent signals. The chemical shifts (δ) are listed in parts per million (ppm). Multiplicities for proton signals are abbreviated as s, d, t and m for singlet, doublet, triplet and multiplet, respectively. Mass spectrometry was performed in the negative mode via MALDI-TOF on a Bruker Daltonics UltrafleXtreme with 2-[(2E)3-(4-*tert*-butylphenyl)-2-methylprop-2-enylidene]malononitrile) (DCBT) as matrix or *via* ESI on a Bruker Daltonics micrOTOF focus.

Single Crystal Structure: Single crystal X-ray diffraction for compounds **1c**, **2c** was measured at 100 ± 1 K on a Bruker D8 Quest Kappa diffractometer with a Photon II CMOS detector and multi-layered mirror with monochromated CuK_a radiation. The

solved structure was obtained with Fourier techniques and the Shelx software package.

DFT calculations for HOMO and LUMO energies as well as for the ground state dipole moments were performed using the Gaussian 09 program package.[155] Starting structures were energy minimized using the B3LYP[156-157] functional and a 6-31G** basis set[159-161].The DFT-optimized dimer structures were used for further quantum chemical calculations of intermolecular couplings. For the respective dimer of NGTIs **2b** and **2c**, the imide substituents were replaced with 2,6-dimethylphenyl units to significantly reduce the calculation time while leaving the π-system unchanged. The long-range Coulomb coupling $J_{Coulomb}$ was calculated using time-dependent DFT (TD-DFT) in the Gaussian 09 program package with the long-range corrected hybrid density functional ωB97X-D[236] and a def2-SVP basis set.[237] The resulting transition density was then fitted to the Mulliken atomic transition charges by electron excitation analysis for the dominant excited state(s) using the Multiwfn software package[238] and $J_{Coulomb}$ finally calculated using the transition charge method.[239] Hereby, the Mulliken transition charges were accordingly scaled by 0.88 [PBI S_1], 0.79 [NGTI (μ_{eg} along short axis)] and 0.87 [NGTI (μ_{eg} along short axis)] due to an overestimation of μ_{eg} from TD-DFT. The short-range charge-transfer coupling J_{CT} was calculated at the perturbative limit[234,240] with an estimated energy difference in the charge transfer and local Frenkel state of 1600 cm^{-1} and with the effective electron and hole transfer integrals t_- and t_+, respectively, as determined using the Amsterdam Density Functional (ADF) program[162-164] with the PW91 functional[166] and a TZP basis set.[165] The resulting total coupling $J_{Coupling}$ was finally calculated as the sum of $J_{Coulomb}$ and J_{CT}.

Organic Solar Cells were processed on ITO-glass substrates (Soluxx GmbH), which were cleaned by sonication with acetone, detergent solution (mucasol®), deionized water and isopropanol followed by an UV/ozone treatment for 30 min. Afterwards the ZnO layer was applied by spin coating a colloidal solution of ZnO (according to Sun *et al.*[73]) and annealed for 1 h at 200 °C. The ITO|ZnO Substrates were transferred to a nitrogen filled glovebox (M. Braun Inertgas Systeme GmbH; $c(O_2)$ < 0.1 ppm, $c(H_2O)$ < 0.1 ppm), where the active layers were deposited *via* spin coating. Therefore, the blend solutions were prepared at room temperature by dissolving

the respective NFA molecule in chlorobenzene (CB, 4.5 mg mL^{-1}; 3 h). The acceptor was mixed (1:0.6) with the donor polymer **PM6** (7.5 mg mL^{-1}, Brilliant Matters Inc) and stirred overnight. Spin coating was performed at 750 rpm for 60 s. To complete the solar cells, MoO_3 (d = 10 nm, r = 0.2 Å s^{-1}, ω_{rot} = 10 rpm, $p < 10^{-6}$ mbar) was deposited as hole-transporting layer and aluminum (d = 100 nm, r = 2-3 Å s^{-1}, ω_{rot} = 0 rpm, $p < 10^{-6}$ mbar) as electrode material using the OPTIvap-XL from CreaPhys GmbH. The resulting solar cells were measured as cast and under inert conditions. *J-V* measurements were performed after calibration with a standard silicon solar cell with a KG filter (ISE Freiburg) under an AM1.5 G Oriel Sol3ATM Class AAA solar simulator (Newport®) by a parameter analyzer (Botest Systems GmbH). EQE measurements were carried out with a Quantum Efficiency/IPCE Measurement Kit (Newport®) by using a 300 W Xe lamp and a Cornerstone monochromator with a SR810 Lock-In Amplifier for detection. Hole-only and electron-only devices for calculating the SCLC mobility were fabricated with the same procedure for the active layer as for the OSC manufacture. While the hole-only devices (HOD) structures consists of ITO|PEDOT:PSS|BHJ|MoO_3|Al the electron-only devices (EOD) were fabricated in ITO|ZnO|BHJ|PDINO|Al architecture. PEDOT:PSS (Heraeus, Clevios O VO Ak 4083) were deposited onto ITO substrates (2500 rpm, 60 s) followed by an annealing step at 150 °C for 15 min. PDINO was synthesized according to Zhang *et al.*[72] and solubilized in methanol (1 mg mL^{-1}) and deposited onto the BHJ layer (3000 rpm, 60 s). The calculation of the respective mobilities was performed analogue to Zhu *et al.*[241] The remaining layers (MoO_3, ZnO, Al) were fabricated according to the OSC manufacture. The *J-V* characteristics of the HOD- and EOD-devices were measured using an Agilent 4055C parameter analyzer on a Cascade EPS150 probe station.

AFM Morphologies of thin films were investigated with NT-MDT Next Solver System in semi-contact mode by using a SCOUT 350 RAI (Nu Nano Ltd) silicon cantilever (spring constant = 42 N m^{-1}; resonance frequency = 350 kHz).

7.5.2 Synthesis

The synthetic procedure is shown in Scheme 3. The experimental details for obtaining the new derivatives **1d**[112], **2b** and **2d** can be found on the following pages,

while all others were already previously described by us (**1a** supported by BASF, **1b**[111], **1c**[111], **2a**[114] and **2c**[115]).

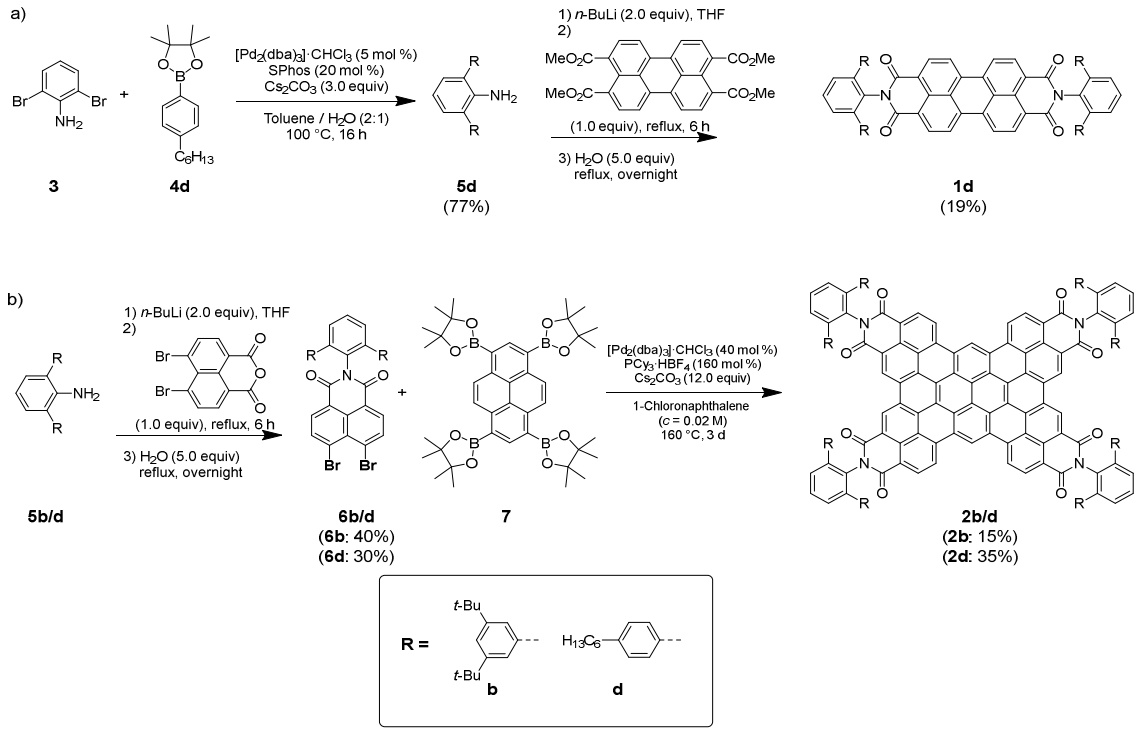

Scheme 3: Synthetic routes for the formation of PBI **1d** and NGTIs **2b** and **2d**.

2,6-Bis(4-hexylphenyl)aniline (5d)[112]

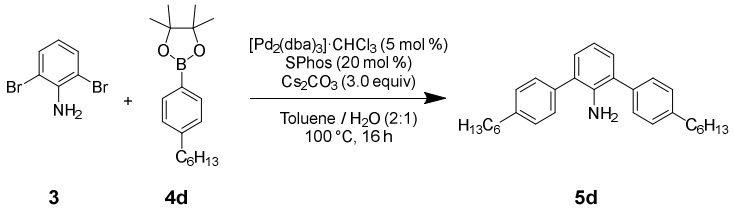

Scheme 4: Synthesis of **5d**.

2,6-Dibromo aniline (88.4 mg, 352 µmol, 1.0 eq), 2-(4-hexylphenyl)-4,4,5,5-tetramethyl-1,2,3-dioxaborolane (234 g, 810 µmol, 2.3 eq), cesium carbonate (344 g, 1.06 mmol, 3.0 eq), $Pd_2(dba)_3{\cdot}CHCl_3$ (18.2 mg, 17.6 µmol, 5 %), SPhos (28.9 mg, 70.5 µmol, 20%) were solubilized in THF (dry, degassed, 26 mL) and water (13 mL) and stirred for 16 h at 100 °C. After cooling to room temperature, the mixture was extracted with CH_2Cl_2, washed with water and dried over $MgSO_4$. The residual solvent was removed under reduced pressure and the raw product was purified via column chromatography (silica, CH_2Cl_2:cyclohexane – 1:9 to 3:7).

Yield: 112 mg (77%) of a yellow-brownish oil.

^{1}H-NMR (400 MHz, CD_2Cl_2, 298 K): δ/ppm = 7.52 (d, *J* = 7.86 Hz, 4 H), 7.36 (d, *J* = 8.32 Hz, 4 H), 7.21 (d, *J* = 6.94 Hz, 2 H), 6.95 (t, *J* = 8.32 Hz, 1 H), 3.95 (s, 2 H), 2.76 (t, *J* = 6.98 Hz, 4 H), 1.77 (quin, *J* = 7.00 Hz, 4 H), 1.51-1.39 (m, 12 H), 1.02 (t, *J* = 5.58 Hz, 6 H).

^{13}C-NMR (100 MHz, CD_2Cl_2, 298 K): δ/ppm = 142.4 141.4, 137.4, 129.8, 129.4, 129.2, 128.1, 118.2, 36.0, 32.11, 31.91, 29.44, 23.0, 14.24.

HRMS (ESI-TOF): m/z: calcd. for $C_{30}H_{40}N^+$ $[M + H]^+$: 414.31553; found: 414.31726.

N,N`-bis[2,6-bis(4-hexylphenyl)phenyl]perylene-3,4:9,10-bis(dicarboximide) (1d)[112]

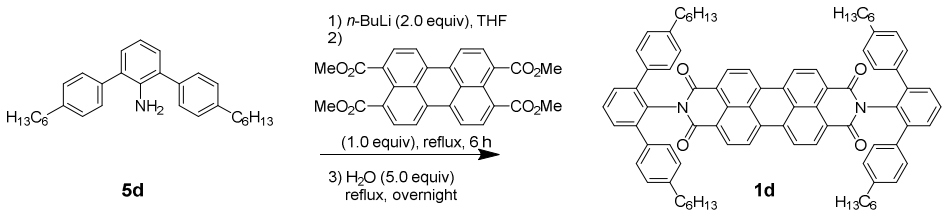

Scheme 5: Synthesis of **1d**.

2,6-Bis(4-hexylphenyl)aniline (**5d**; 59.8 mg, 145 µmol, 2.0 eq) was solubilized in THF (dry, 2 mL) and cooled down to −78 °C, while *n*-butyl lithium in *n*-hexane (2.5 M, 116 µL, 18.5 mg, 289 µmol, 4.0 eq) was added dropwise under stirring (1 h). The mixture was allowed to come to room temperature and 3,4,9,10-perylene tetracarboxylic acid tetramethylester (35.0 mg, 72.3 µmol, 1.0 eq) was added, followed by heating up to 90 °C for 6 h. After cooling down, the residual solvent was removed under reduced pressure, followed by purification with HPLC (CH_2Cl_2:EtOAc – 99:1) and recrystallization in CH_2Cl_2 and methanol.

Yield: 16.5 mg (19%) of a crystalline red solid.

Melting Point: 240-242 °C

^{1}H-NMR (600 MHz, $C_2D_2Cl_2$, 373 K): δ/ppm = 8.29 (d, *J* = 7.12 Hz, 4 H), 8.24-7.95 (m, 4 H), 7.53 (t, *J* = 7.91 Hz, 2 H), 7.44 (d, *J* = 7.91 Hz, 4 H), 7.21 (d, *J* = 7.91 Hz, 8 H), 6.89

(d, *J* = 7.91 Hz, 8 H), 2.33 (t, *J* = 7.15 Hz, 8 H), 1.31 (quin, *J* = 8.17 Hz, 8 H), 1.01 (s, 24 H), 0.60 (t, *J* = 7.15 Hz, 12 H).

^{13}C-NMR (100 MHz, $C_2D_2Cl_2$, 373 K): δ/ppm = 163.4, 142.1, 142.0, 136.8, 134.5, 132.1, 131.2, 130.0, 129.5, 128.9, 128.6, 127.9, 126.4, 123.4, 122.8, 120.6, 35.5, 31.6, 30.9, 28.7, 22.5, 13.9.

HRMS (MALDI-TOF, neg. Mode, DCM): m/z: calcd.: 1182.62801; found: 1182.62844.

UV-Vis (CH_2Cl_2; 1×10^{-5} mol L^{-1}): λ_{max} (nm) (ε (L mol^{-1} cm^{-1}) = 528 (90300).

Fluorescence ($CHCl_3$): λ_{Em}^{Max} (nm) (Φ_{Fl}(%)) = 535 (97 ± 2).

N-(2,6-Bis-(3,5-(di-*tert*-buyl)-phenyl)phenyl)-4,5-dibromo-1,8-naphthalimid (**6b**)

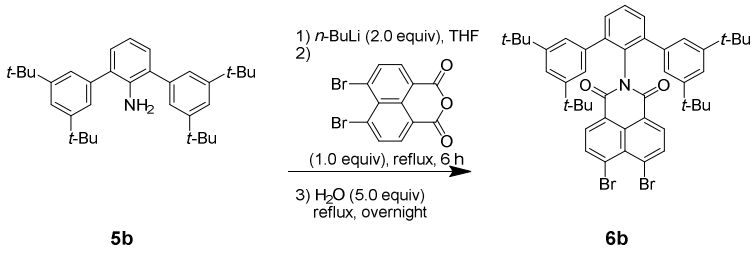

5b **6b**

Scheme 6: Synthesis of **6b**.

2,6-Bis(3,5-di-*tert*-butylphenyl)anilin (**5b**) (50.0 mg, 106 µmol, 1.0 eq.) was solubilized in THF (100 mL, dried) and cooled to −78 °C. To this solution, *n*-butyl lithium in hexane (133 µL, 1.6 M in *n*-hexane, 212 µmol, 2.0 eq.) was added dropwise followed by stirring for 1 h. After heating to room temperature, 4,5-dibromonaphthalin-1,8-dicarboxylic acid anhydride (37.9 mg, 106 µmol, 1.0 eq.) was added and the mixture was stirred for 6 h at 75 °C, followed by the addition of water (0.58 mL) and by additional 16 h of stirring at 75 °C. After cooling down to room temperature, the mixture was filtered over silica and washed with CH_2Cl_2. The residual solvent was removed under reduced pressure and the raw product was purified using column chromatography (silica, CH_2Cl_2/cyclohexane from 1:2 to 1:1) and recrystallized from CH_2Cl_2/methanol.

Yield: 34.6 mg (40%) of a white solid.

Melting Point: 256-257 °C.

^{1}H-NMR (400 MHz, $CDCl_3$, 298 K): δ/ppm = 8.14 (d, J = 8.0 Hz, 2 H, Ar-*H*), 8.05 (d, J = 8.0 Hz, 2 H, Ar-*H*), 7.58–7.63 (m, 1 H, Ar-*H*), 7.50–7.54 (m, 2 H, Ar-*H*), 7.16 (d, J = 1.9 Hz, 4 H, Ar-*H*), 7.09 (t, J = 1.9 Hz, 2 H, Ar-*H*), 1.06 (s, 36 H, Alkyl-*H*).

^{13}C-NMR (101 MHz, $CDCl_3$, 298 K): δ/ppm = 163.0, 150.0, 142.5, 138.2, 135.9, 131.6, 131.22, 131.21, 129.7, 129.2, 127.9, 127.5, 123.1, 123.0, 120.9, 34.8, 31.3.

HRMS (ESI-TOF, pos. mode, acetonitrile/chloroform 1/1): calcd. for $C_{46}H_{49}Br_2NO_2Na$: 828.2028; found: 828.2022 $[M+Na]^+$.

UV–Vis ($CHCl_3$): λ_{Max} (nm) (ε (L mol^{-1} cm^{-1})) = 377 (17200).

N-[2,6-bis(4-hexylphenyl)phenyl]-4,5-dibromo-naphthalene-1,8-dicarboximide (6d)

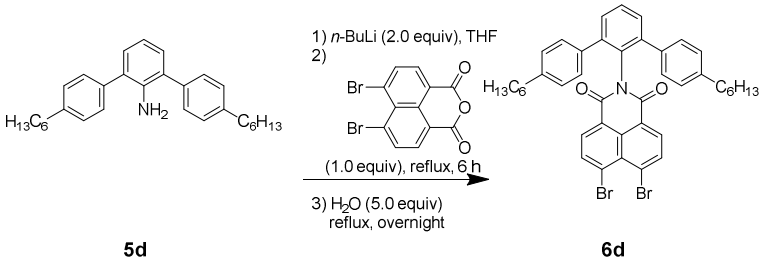

Scheme 7: Synthesis of **6d**.

To a solution of 2,6-bis(4-hexylphenyl)aniline (**5d**) (8.5 g, 21 mmol) in THF (400 mL) was added *n*-butyllithium (1.6 M in hexane, 25.7 mL, 41.1 mmol) at −78 °C. The mixture was stirred for 1 hour and allowed to warm-up to room temperature. 4,5-dibromonaphthalene-1,8-dicarboximide (**2**) (7.31 g, 20.6 mmol) was added and refluxed for 6 h. Water (1.85 mL, 103 mmol) was added to the resulting mixture and additionally refluxed for additional 16 h. After cooling to room temperature, the mixture was filtered and washed with CH_2Cl_2. The filtrate was washed with water and extracted with CH_2Cl_2. The organic layers were combined and concentrated under reduced pressure. The crude product was purified by silica-gel column chromatography (cyclohexane / CH_2Cl_2 = 1:4).

Yield: 4.7 g (30%) of a yellow solid.

Melting point: 164-165°C.

^{1}H-NMR (400 MHz, $CDCl_3$): δ 8.19 (d, *J* = 8.3 Hz, 2H), 8.08 (d, *J* = 8.0 Hz, 2H), 7.58 (t, *J* = 7.7 Hz, 1H), 7.46 (d, *J* = 7.7 Hz, 2H), 7.18 (d, *J* = 8.1 Hz, 4H), 6.93 (d, *J* = 8.1 Hz, 4H), 2.41 (t, *J* = 7.8 Hz, 4H), 1.45–1.36 (m, 4H), 1.20–1.05 (m, 12H), 0.81 (t, *J* = 7.0 Hz, 6H).

^{13}C-NMR (100 MHz, $CDCl_3$): δ 163.3, 142.1, 141.7, 136.4, 136.1, 131.6, 131.4, 131.0, 130.2, 129.3, 128.2, 128.1, 127.7, 122.8, 35.5, 31.7, 31.1, 28.8, 22.7, 14.2.

HRMS (ESI): Calcd for $C_{42}H_{41}Br_2NNaO_2^+$ [M + Na]$^+$: 772.13962. Found: 772.13766.

N,*N*',*N*'',*N*'''-Tetrakis[2,6-Bis-(3,5-(di-*tert*-butyl)-phenyl)phenyl] tetranaphtho[8,8a,1,2-*abc*:2',1',8a',8'-*efg*:8'',8a'',1'',2''-*lmn*:2''',1''',8a''',8'''-*pqr*]ovalene-3,4:7,8:14,15:18,19-tetrakis(dicarboximide) (2b)

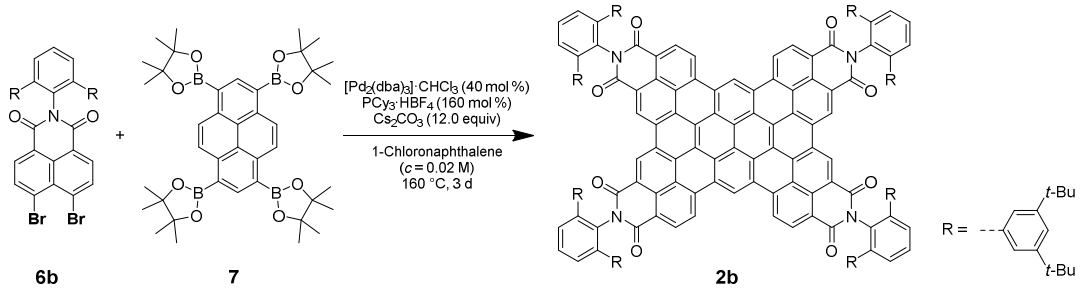

6b 7 2b

Scheme 8: Synthesis of **2b**.

A Schlenk-tube was charged with the respective imide **6b** (4.4 eq.), **7** (1.0 eq.), *tris*(dibenzylideneacetone)dipalladium(0)-chloroform adduct $[Pd_2(dba)_3]\cdot CHCl_3$ (40 mol%), $PCy_3\cdot HBF_4$ (160 mol%), Cs_2CO_3 (12.0 eq.) and 1-chloronaphthalene as a solvent under a nitrogen atmosphere at room temperature and heated to 160 °C for 20 h. The reaction mixture was allowed to cool to room temperature, and the mixture was filtered over a pad of silica gel to remove 1-chloronaphthalene and the crude product was eluated with dichloromethane. The crude product was purified by column chromatography, followed by size exclusion chromatography (BioBeads SX1 or SX3, $CHCl_3$), recycling gel permeation chromatography ($CHCl_3$) and precipitation.

Yield: 6.5 mg (15%) of a dark purple solid.

Melting Point: > 300 °C

^{1}H-NMR (400 MHz, CD_2Cl_2, 298 K): δ/ppm =11.65 (*s*, 2 H, Ar-*H*). 10.63 (*s*, 4 H, Ar-*H*), 10.19 (*d*, *J* = 8.5 Hz, 4 H, Ar-*H*), 9.46 (*d*, *J* = 8.5 Hz, 4 H, Ar-*H*), 7.83-7.92 (*m*, 28, Ar-*H*), 7.46-7.48 (*m*, 8, Ar-*H*), 7.34-7.39 (*m*, 32, Ar-*H*), 7.05-7.10 (*m*, 32 H, Ar-*H*), 6.90-6.95 (*m*, 16, Ar-*H*).

^{13}C-NMR (151 MHz, $CDCl_3$, 298 K): δ/ppm = 164.9, 164.6, 142.0, 141.4, 140.5, 140.4, 134.6, 132.5, 130.6, 129.9, 129.8, 128.7, 127.6, 127.4, 127.0, 126.62, 126.56, 125.0, 124.7, 124.4, 124.3, 123.8, 123.0, 122.9 121.5.

HRMS (MALDI-TOF, neg. mode, DCTB in chloroform): calcd. for $C_{232}H_{130}N_4O_8$: 3098.9889, found: 3098.9932 $[M]^-$.

UV-Vis (CH_2Cl_2; 4×10^{-6} M): λ_{Max} (nm) (ε (L mol^{-1} cm^{-1}) = 489.5 (281000), 583.5 (138000).

Fluorescence ($CHCl_3$): $\lambda_{Em}{}^{Max}$ (nm) (Φ_{Fl} (%)): 608 (73 ± 3).

N,*N*',*N*'',*N*'''-Tetrakis[2,6-bis(4-hexylphenyl)phenyl)]tetranaphtho[8,8a,1,2-*abc*:2',1',8a',8'-*efg*:8'',8a'',1'',2''-*lmn*:2''',1''',8a''',8'''-*pqr*]ovalene-3,4:7,8:14,15:18,19-tetrakis(dicarboximide) (2d)

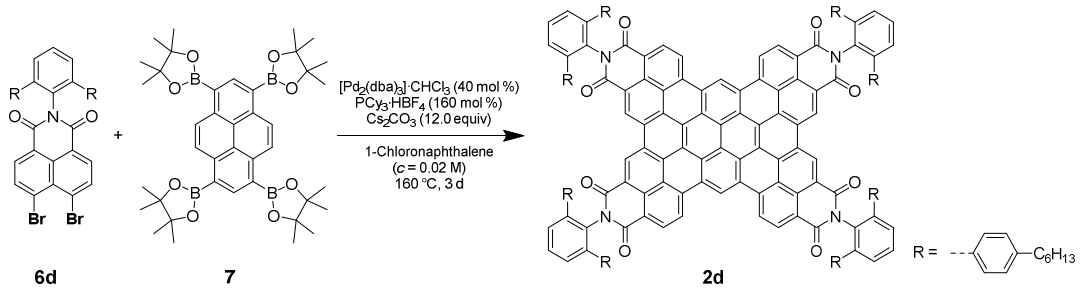

Scheme 9: Synthesis of 2d.

A Schlenk-tube was charged with *N*-[2,6-bis(4-hexylphenyl)phenyl]-4,5-dibromo-naphthalene-1,8-dicarboximide (**6d**) (93.7 mg, 125 µmol, 4.4 eq.), pyrene-1,3,6,8-tetraboronic acid tetrakis(pinacol)ester (**7**) (20.00 mg, 28.3 µmol, 1.0 eq.), tris(dibenzylideneacetone) dipalladium(0)-chloroform adduct $[Pd_2(dba)_3]\cdot CHCl_3$ (11.6 mg, 22.6 µmol, 40 mol %), $PCy_3\cdot HBF_4$ (16.6 mg, 90.4 µmol, 160 mol %), and Cs_2CO_3 (110 mg, 339 µmol, 12.0 eq.) under a nitrogen atmosphere. Subsequently, 1-chloronaphthalene (1.4 mL) was added and the mixture was stirred at 160 °C for 3 days. The reaction mixture was cooled down to room temperature and passed

through a pad of silica-gel using cyclohexane/dichloromethane = 3:7 as an eluent to remove 1-chloronaphthalene and dichloromethane/methanol = 9:1 to collect fractions containing the product. The crude product was purified by column chromatography (gradient of cyclohexane/dichloromethane from 7:3 to 0:1) and precipitation from dichloromethane/methanol followed by washing with methanol and *n*-hexane.

Yield: 25.0 mg (35%) of a red solid.

Melting Point: 250-252 °C.

^{1}H-NMR (400 MHz, $CDCl_3$): δ 11.66 (s, 2H), 10.79 (s, 4H), 10.17 (d, *J* = 8.5 Hz, 4H), 9.43 (d, *J* = 7.8 Hz, 4H), 7.69 (dd, *J* = 7.0, 7.0 Hz, 4H), 7.62–7.58 (m, 8H), 7.46 (d, *J* = 8.2 Hz, 16H), 6.97 (d, *J* = 8.2 Hz, 16H), 2.25 (t, *J* = 7.8 Hz, 16H), 1.27–1.17 (m, 16H), 0.92–0.72 (m, 48H), 0.33 (t, *J* = 7.0 Hz, 24H).

^{13}C-NMR (100 MHz, $CDCl_3$): δ 164.6, 164.4, 142.0, 141.9, 136.7, 134.6, 131.7, 130.4, 130.0, 129.9, 129.4, 129.1, 128.4, 128.3, 127.7, 126.7, 124.7, 124.6, 124.4, 124.0, 123.2, 122.9, 121.6, 119.7, 35.4, 31.4, 30.9, 28.57, 22.3, 13.8.

HRMS (MALDI TOF): Calcd. for $C_{184}H_{162}N_4O_8^+$ (M^+): 2555.23872. Found: 2555.24008.

UV-Vis (CH_2Cl_2; 4×10^{-6} M): λ_{Max} (nm) (ε (L mol^{-1} cm^{-1}) = 490 (279000), 854.5 (140000).

Fluorescence (CH_2Cl_2): λ_{Em}^{Max} (nm) (Φ_{Fl} (%)): 608 nm (62 ± 1).

7.5.3 UV-Vis and Fluorescence Data

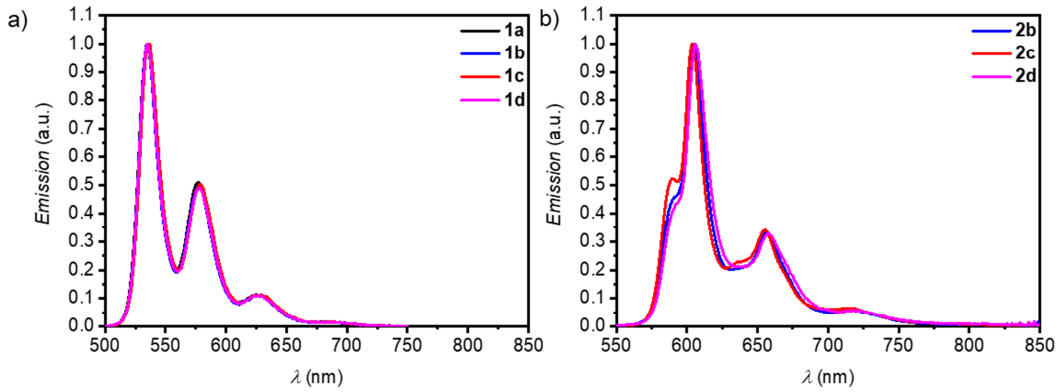

Figure 100: Fluorescence spectra of **1a-d** (a; 1×10^{-4} mol L^{-1}) and **2b-d** (b; 4×10^{-6} mol L^{-1}) in CH_2Cl_2 solution measured at room temperature. For the PBIs and NGTIs were excited at 480 nm and at 550 nm, respectively.

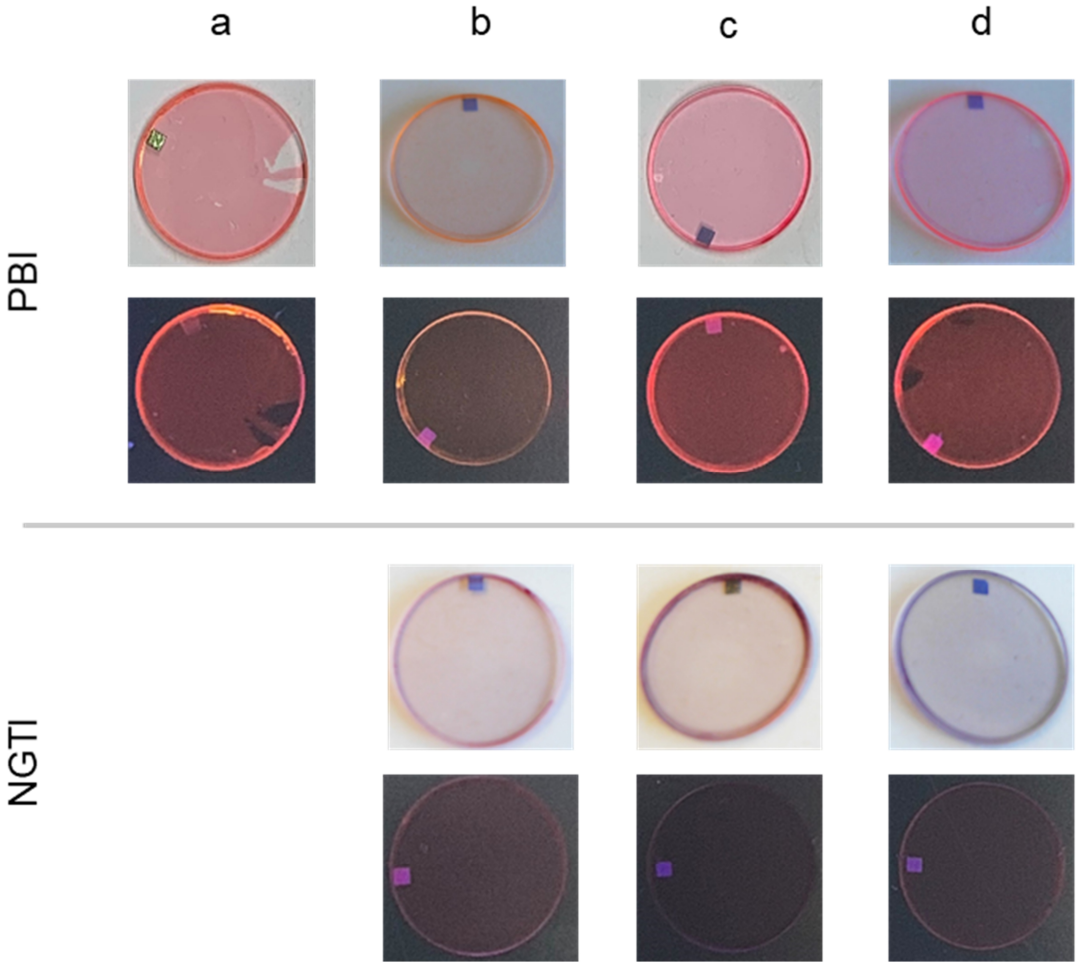

Figure 101: Photographs of the described NFAs in PMMA matrix under ambient light as well as UV-light irradiation.

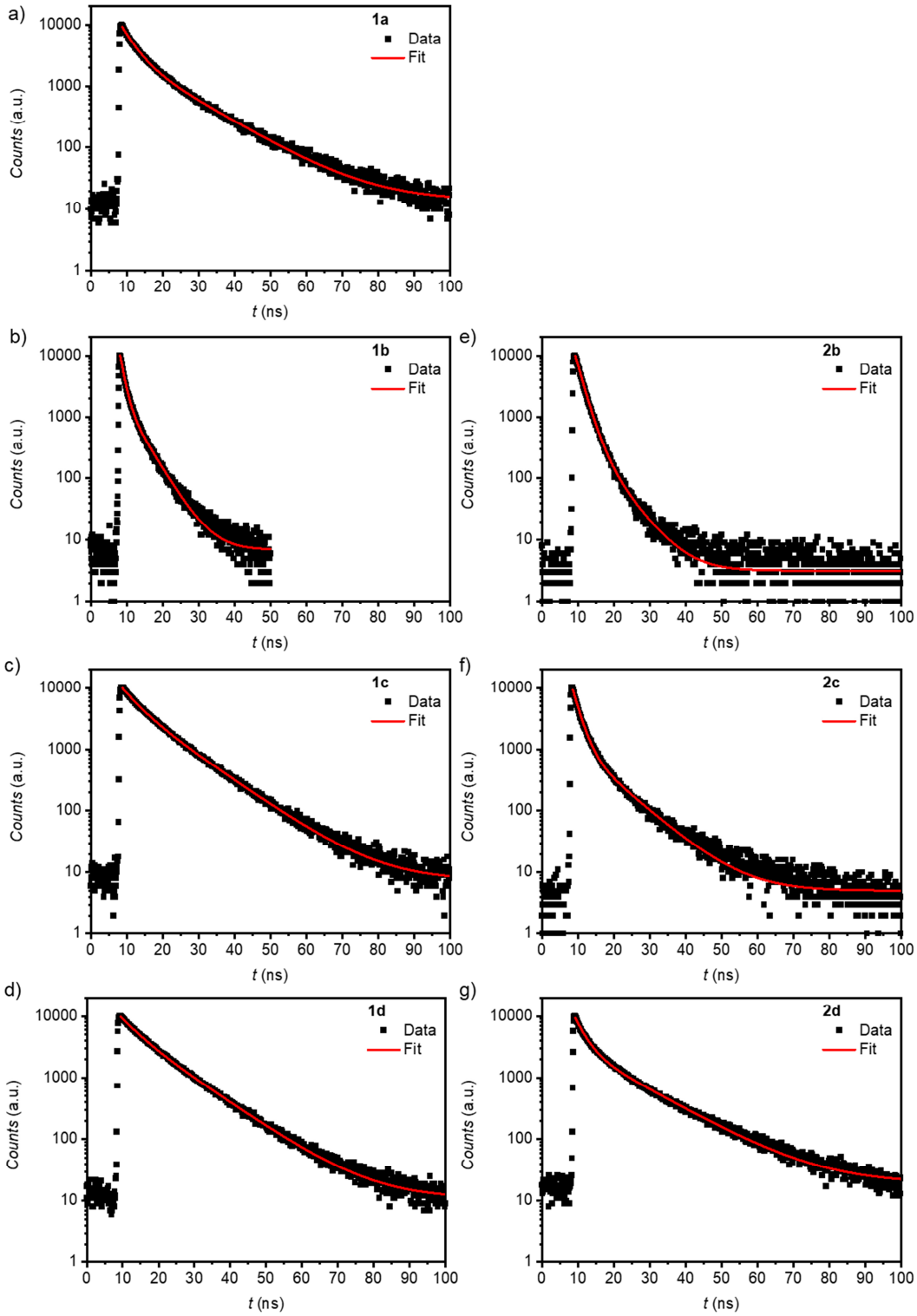

Figure 102: Fluorescence decay curves (black solid) and the respective biexponential fit (red) of the PBIs **1a** (a), **1b** (b), **1c** (c), **1d** (d) and of the NGTIs **2b** (e), **2c** (f), **2d** (g) in PMMA matrix (1:0.6). For all compound an excitation wavelength of 505.8 nm was chosen, and the emission decay detected at 618 nm (**1a**), 618 nm (**1b**), 588 nm (**1c**), 610 nm (**1d**), 717 nm (**2b**), 682 nm (**2c**), 754 nm (**2d**), respectively. For **2a** it was not possible to obtain a thin film in the desired quality, due to insufficient solubility.

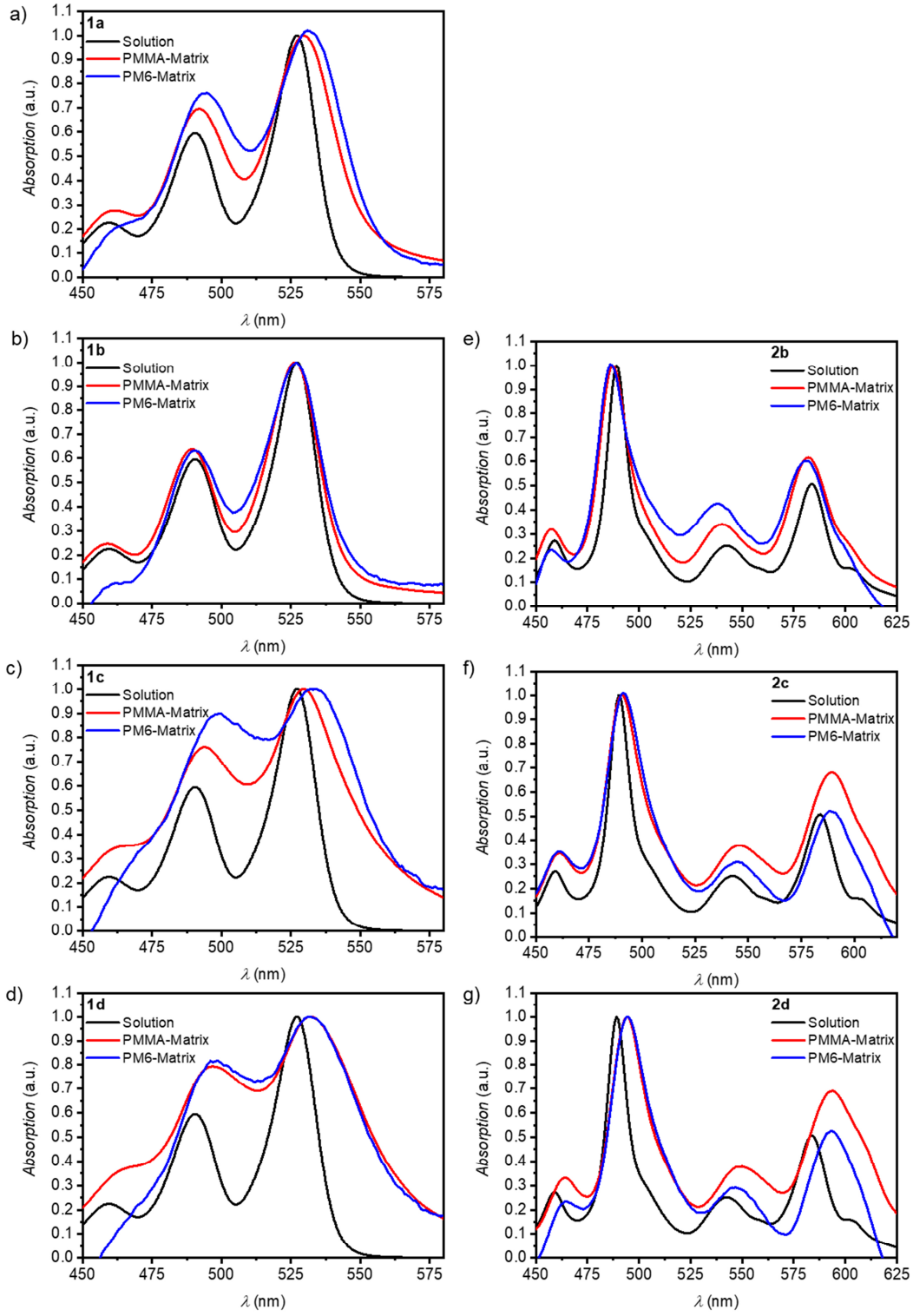

Figure 103: Normalized UV-Vis spectra of **1a** (a) **1b** (b), **1c** (c), **1d** (d), **2b** (e), **2c** (f), **2d** (g) in CH_2Cl_2 solution (black), in PMMA matrix (red), and in **PM6** matrix (blue). For the spectra in **PM6** matrix, the absorption of the neat donor polymer layer was subtracted. For **2a** it was not possible to obtain a thin film in the desired quality, due to insufficient solubility.

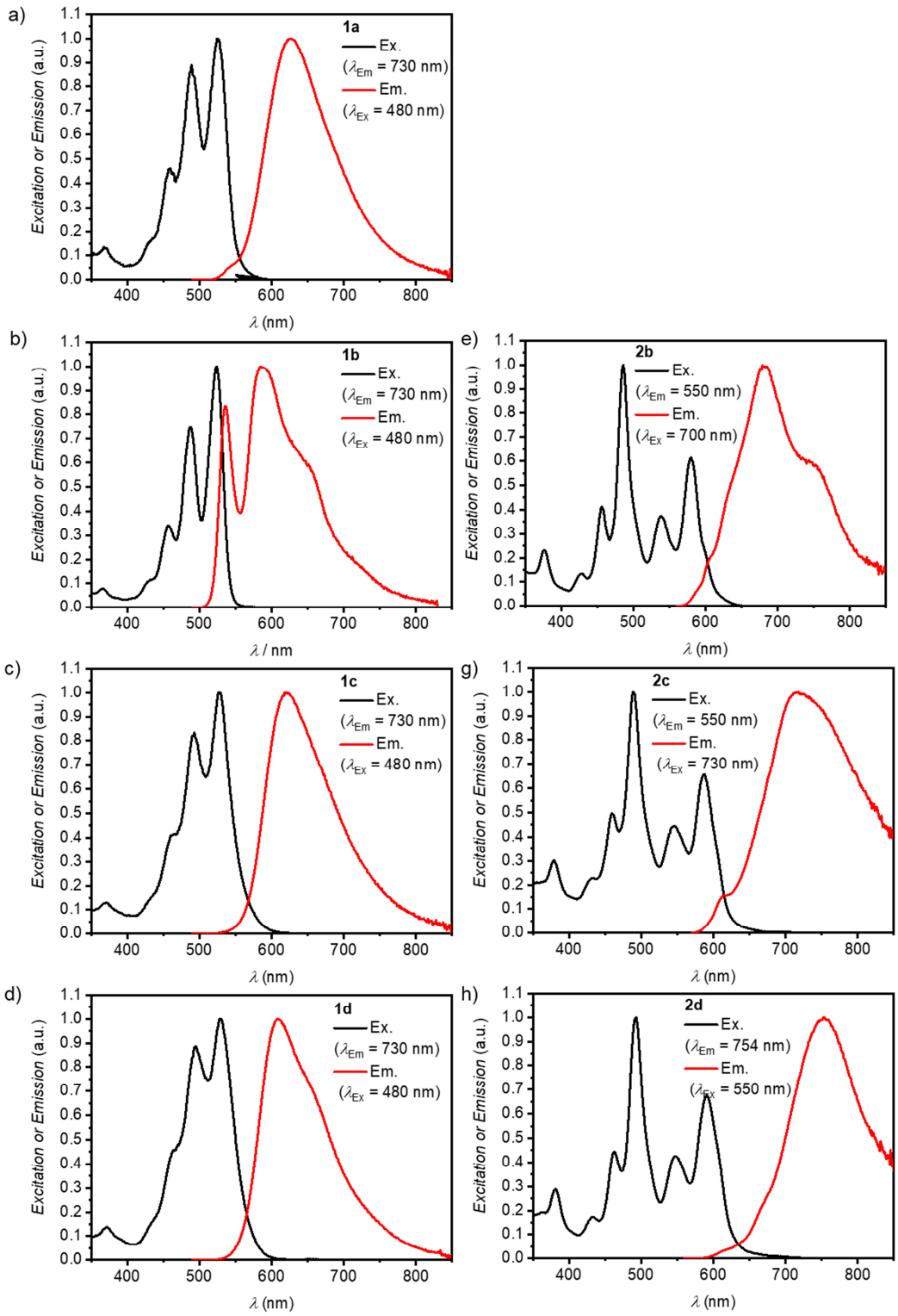

Figure 104: Excitation (black) and emission (red) spectra of **1a** (a) **1b** (b), **1c** (c), **1d** (d), **2b** (e), **2c** (f), **2d** (g) in PMMA matrix. The individual excitation and emission wavelengths are denoted in the respective figure. For **2a** it was not possible to obtain a thin film in the desired quality, due to insufficient solubility.

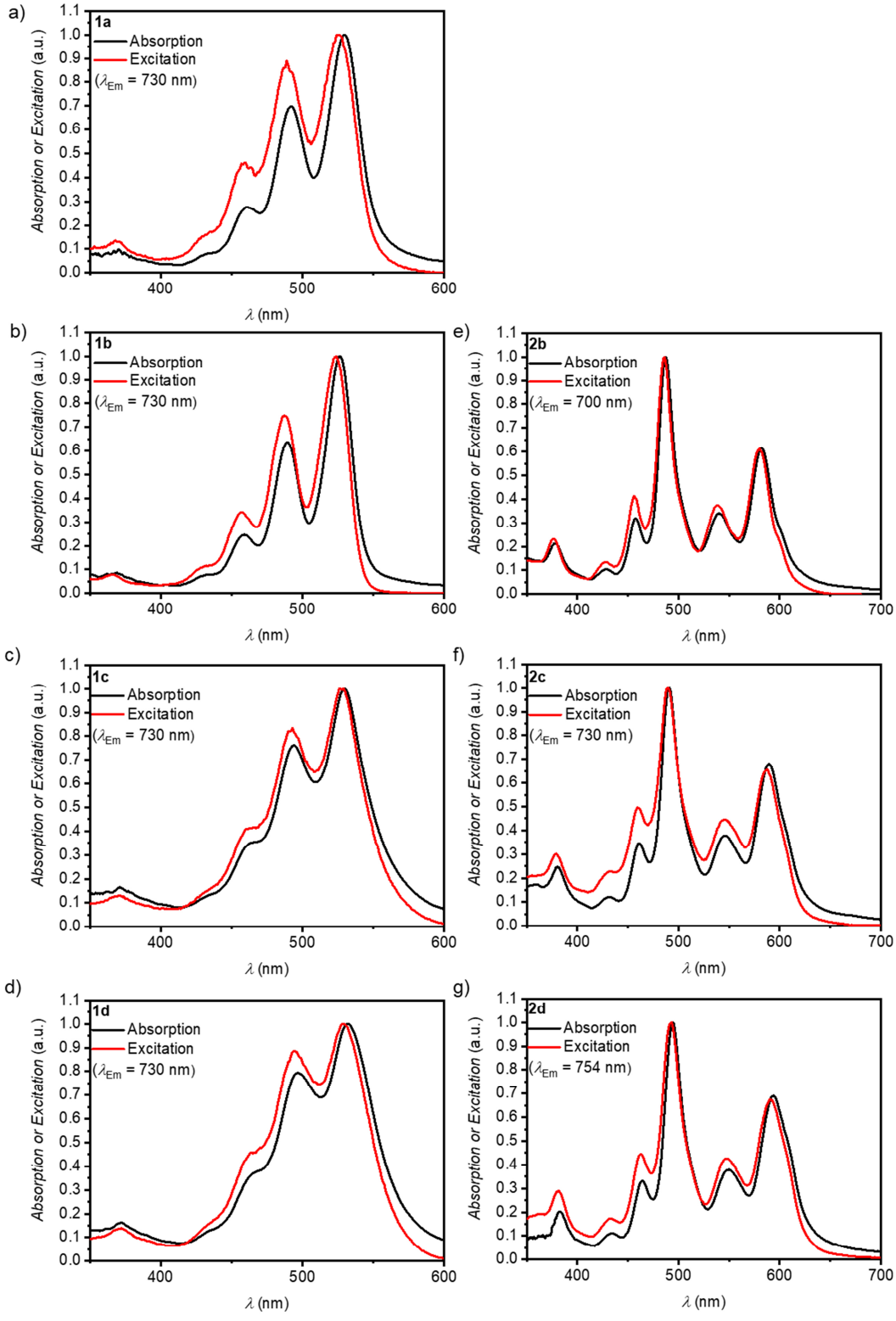

Figure 105: Normalized UV-Vis absorption spectra **1a** (a) **1b** (b), **1c** (c), **1d** (d), **2b** (e), **2c** (f), **2d** (g) in PMMA matrix (black) compared with their excitation spectra (red). For **2a** it was not possible to obtain a thin film in the desired quality, due to insufficient solubility.

7.5.4 DFT-Calculations

Table 31: Calculated HOMO and LUMO energies as well as internal reorganization energies (λ_{Reorg}) for all NFAs via DFT compared with the literature data, which were obtained from cyclic voltammetry.

Acceptor	λ_{Reorg} (eV)	$E^{DFT}{}_{HOMO}$ (eV)	$E^{DFT}{}_{LUMO}$ (eV)	$E^{CV}{}_{HOMO}$ (eV)	$E^{CV}{}_{LUMO}$ (eV)
1a	~0.30	−6.01	−3.48	−6.13[231]	−3.79[231]
1b		−5.88	−3.35		
1c		−5.90	−3.37		
1d		−5.86	−3.33		
2a	~0.15	−5.85	−3.63	−3.81[114]	−6.06[114]
2b		−5.71	−3.48		
2c		−5.72	−3.50		
2d		−5.69	−3.46		

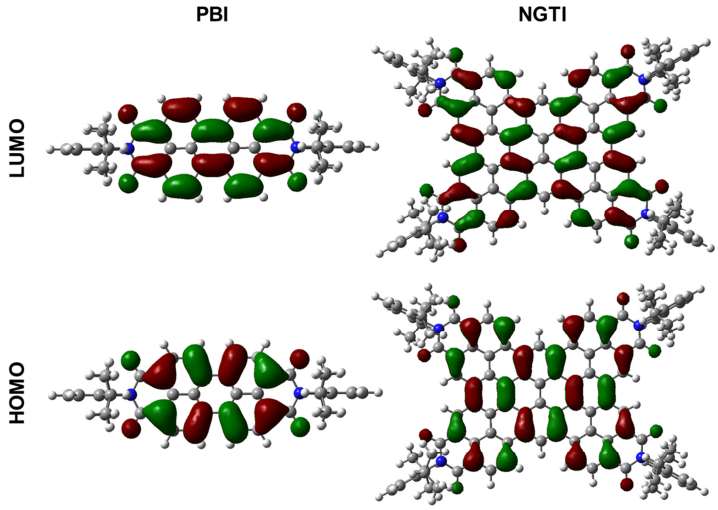

Figure 106: Calculated HOMO and LUMO for the PBI and the NGTI chromophores.

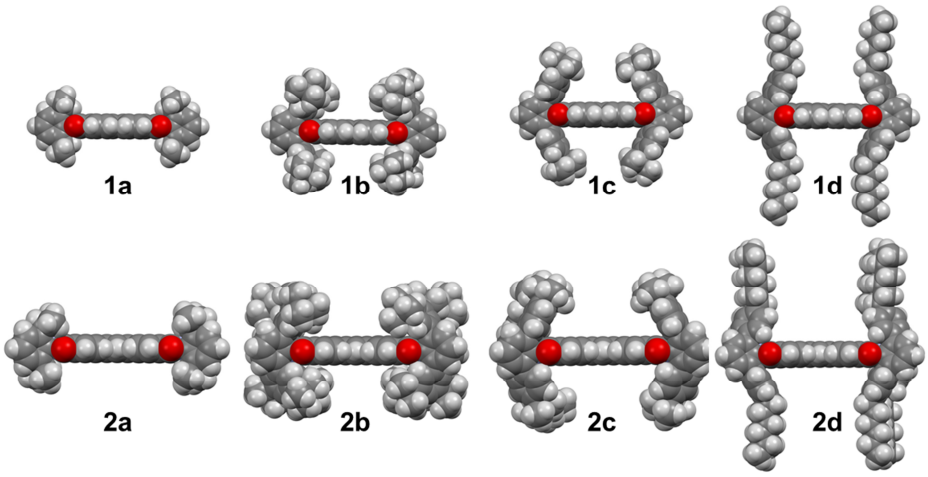

Figure 107: Energy minimized structures (B3LYP, 6-31-d,p) of NFAs in spacefill model (side-view).

Table 32: Coupling strength of respective transition dipole moments in the dimer. Positive values resemble hypochromic shifts and negative value lead to a bathochromic shift.

	t_+ (meV / cm^{-1})	t_- (meV / cm^{-1})	J_{CT} (meV / cm^{-1})	$J_{Coulomb}$ (meV / cm^{-1})	$J_{Coupling}$ (meV / cm^{-1})
1b	1 / 7	0 / 0	0 / 0	6 / 45	6 / 45 (H)
1c	1 / 4	36 / 288	0 / 2	16 / 131	16 / 130 (H)
2b	0 / 0	0 / 2	0 / −1	9 / 76[a] −22 / −179[b]	9 / 76[a] (H) −22 / −179[b] (J)
2c	24 / 191	21 / 169	−5 / −40	−24 / −194[a] 41 / 334[b]	−29 / −234[a] (J) 36 / 294[b] (H)

[a] Transition dipole moment along the short molecular axis. [b] Transition dipole moment along the long molecular axis.

7.5.5 X-Ray Data

Table 33: X-ray structure characteristics for PBI **1c** and NGTI **2b**.

	1c	**2b**
Empirical formula	$C_{76}H_{66}N_2O_4$	$C_{200}H_{194}N_4O_8$
Wavelength (Å)	1.54178	1.54178
T (K)	101	100
Description of the crystal		
Crystal System	Triclinic	Triclinic
Space group	P–1	P–1
Unit cell dimension		
a (Å)	16.5447	21.2988
b (Å)	18.7892	23.2102
c (Å)	23.3659	23.6180
α (°)	82.920	114.246
β (°)	83.513	102.882
γ (°)	77.185	91.032
Volume (Å^3)	7001.1	10301.7
Z	4	1
$p_{calc.}$ (g cm^{-3})	1.104	1.167
F(000)	2472.1	3875.4
Range of θ (°)	2.424-73.461	2.120-79.282
Goodness of Fit	1.077	1.030
CCDC	2011168	2011165

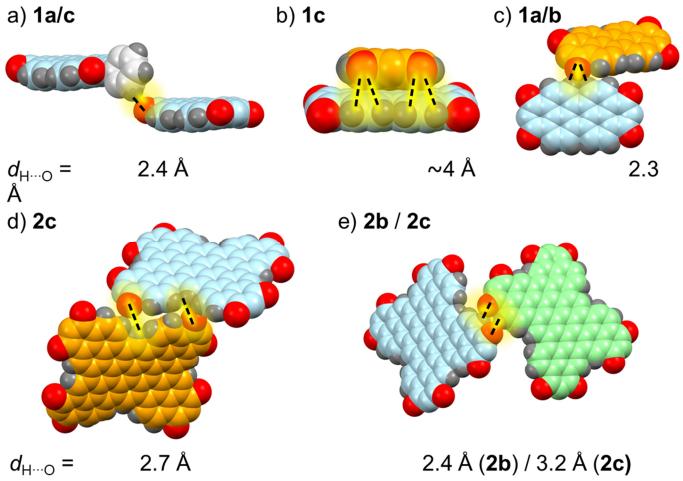

Figure 108: Schematic depiction of the structure directing intermolecular contacts for the respective crystal structures. For clarification the same molecular color code was used as in **Figure 91** and **Figure 93**. Additionally, all hydrogen atoms are marked in grey while all oxygen atoms are marked in red. a) H···O bonding from the perylene oxygen to the imide-substituent hydrogen. b) H···O bonding from perylene oxygen to π-stacked perylene hydrogen. c) CH···O bonding from carbonyl oxygen to the perylene core in edge-to-edge orientation. d) CH···O bonding from NTGIs carbonyl oxygen to pyrene core hydrogen in edge-to-edge orientation. e) CH···O bonding from NTGIs carbonyl oxygen to naphthalene hydrogen in edge-to-edge orientation.

7.5.6 OSC Data

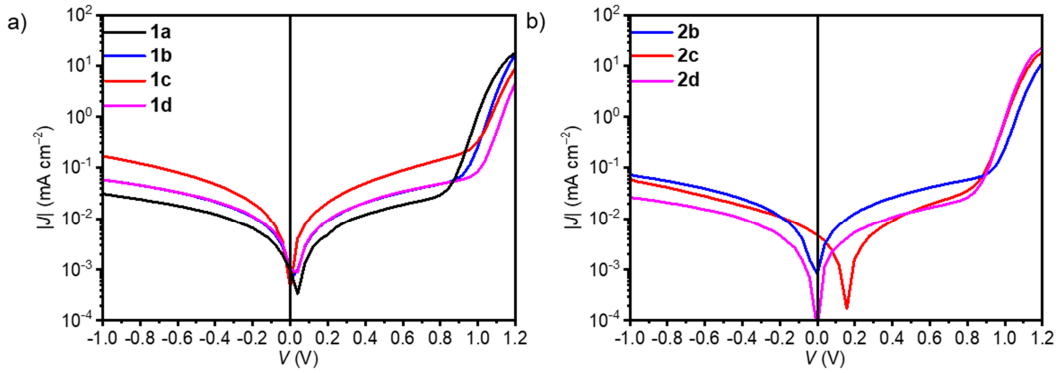

Figure 109: *J-V* dark curves of OSCs in ITO|ZnO|**PM6**:NFA|MoO_3|Al architecture for a) PBIs **1a-d** and b) NGTIs **2c-d**.

7.5.7 AFM Studies

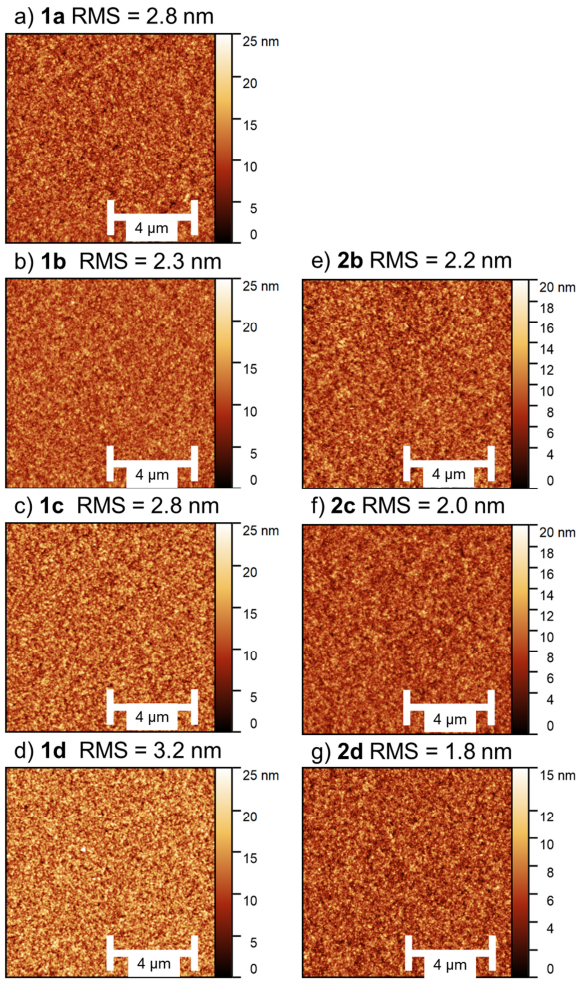

Figure 110: AFM studies of the respective **PM6:**NFA bulk-heterojunction deposited on ITO|ZnO.

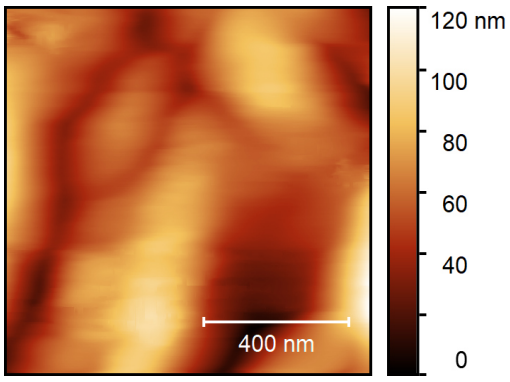

Figure 111: AFM-study of **2a** embedded in PMMA Matrix. Root mean square = 18.2 nm. s

7.5.8 ^{1}H-NMR Spectra

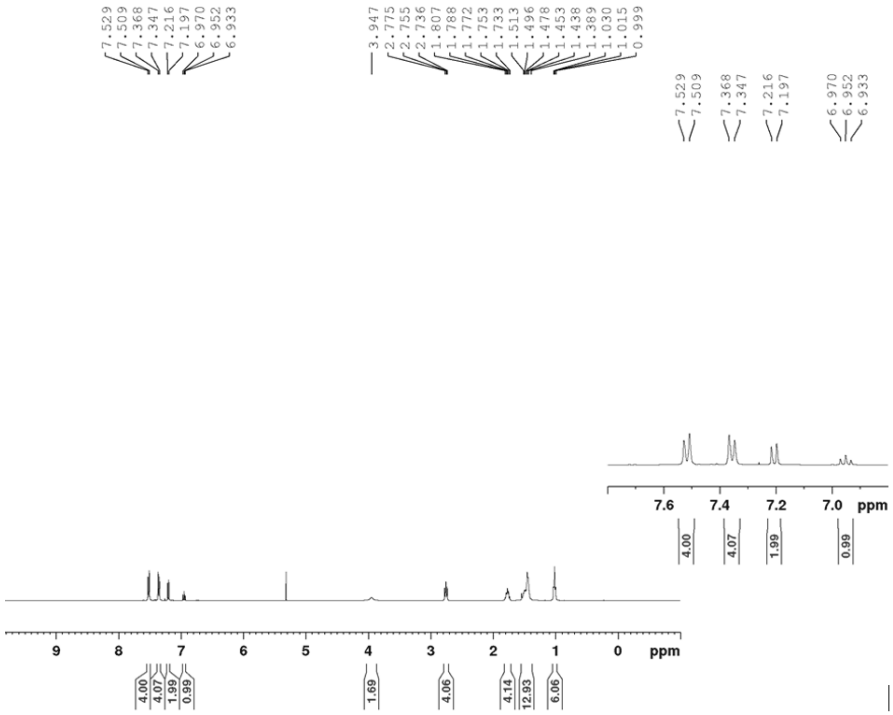

Figure 112: 400 MHz ^{1}H-NMR spectrum of compound **5d** in CD_2Cl_2 at 298 K**.**

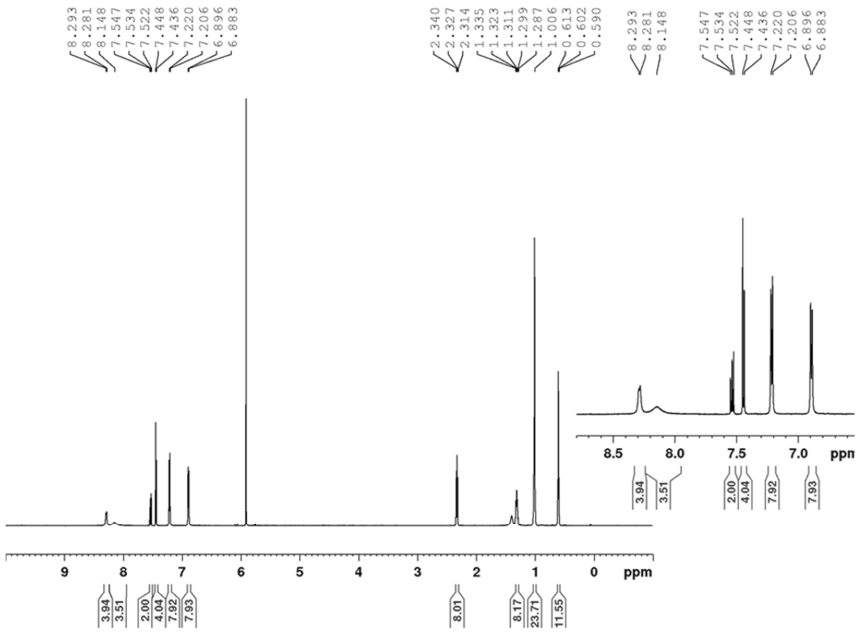

Figure 113: 400 MHz ^{1}H-NMR spectrum of compound **1d** in $C_2D_2Cl_2$ at 373 K**.**

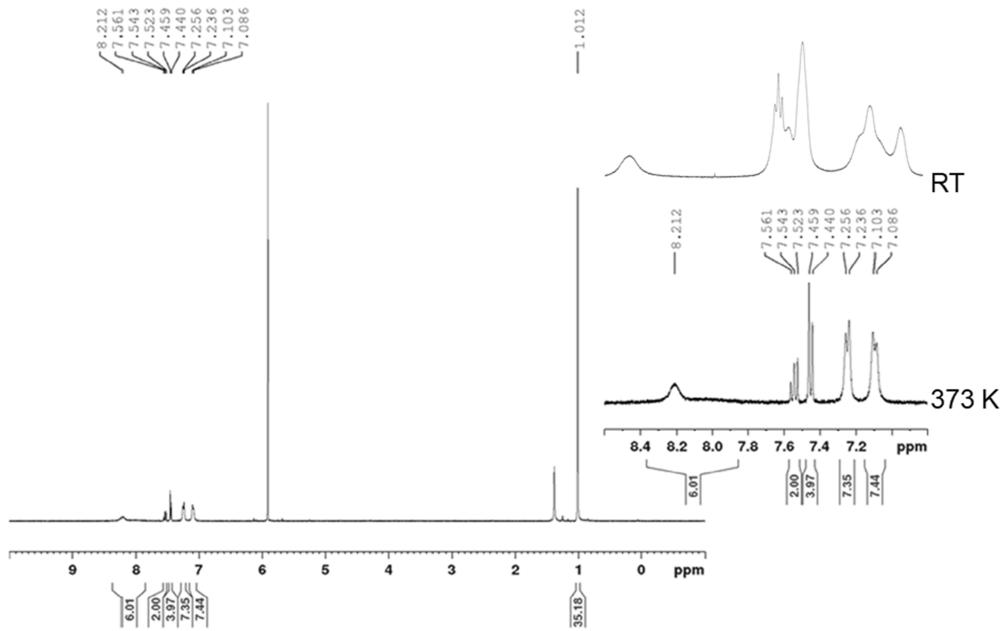

Figure 114: 400 MHz ^{1}H-NMR spectrum of compound **1b**. Inset: Zoom into 6.8-8.6 ppm for **1b** measured at room temperature and at 373 K in $C_2D_2Cl_2$.

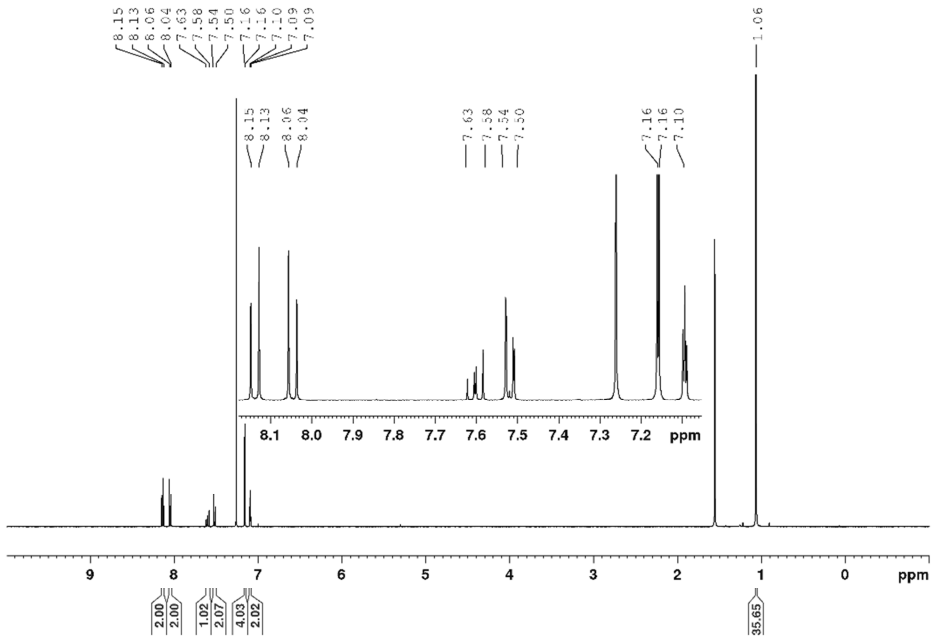

Figure 115: 400 MHz ^{1}H-NMR spectrum of compound **6b** in $CDCl_3$ at 298 K**.**

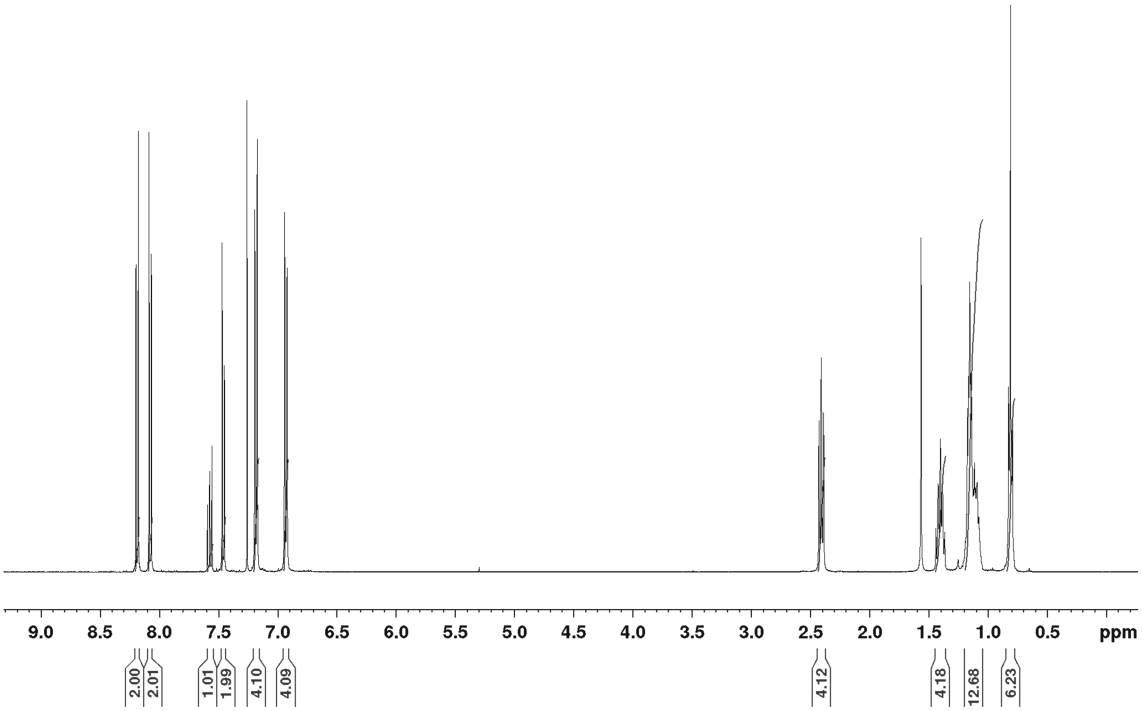

Figure 116: 400 MHz ^{1}H-NMR spectrum of compound **6d** in $CDCl_3$ at 298 K.

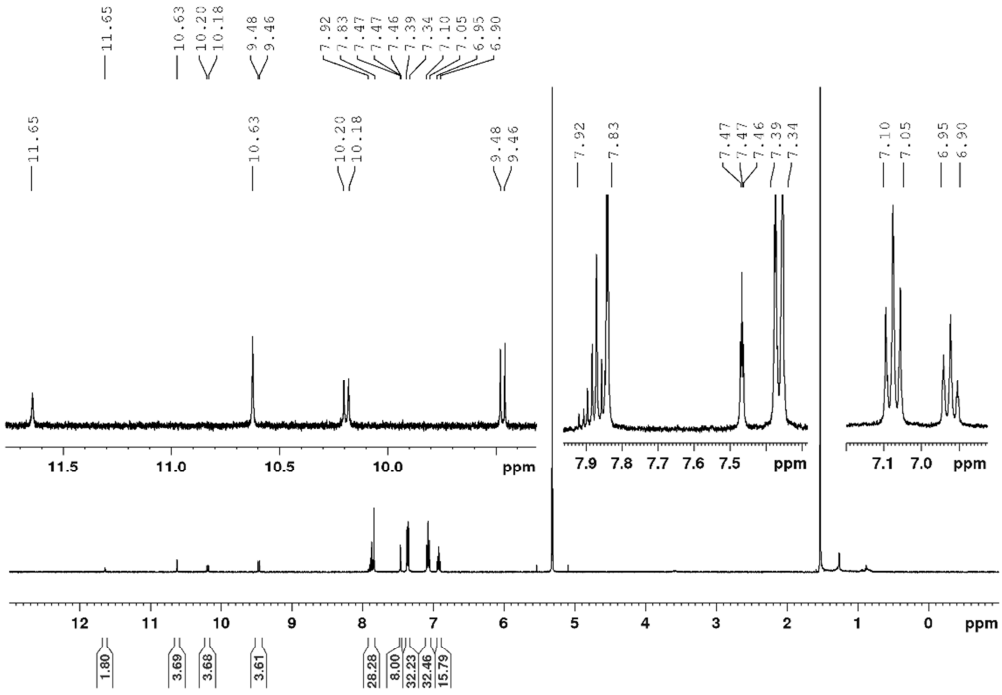

Figure 117: 400 MHz ^{1}H-NMR spectrum of compound **2b** CD_2Cl_2 at 298 K.

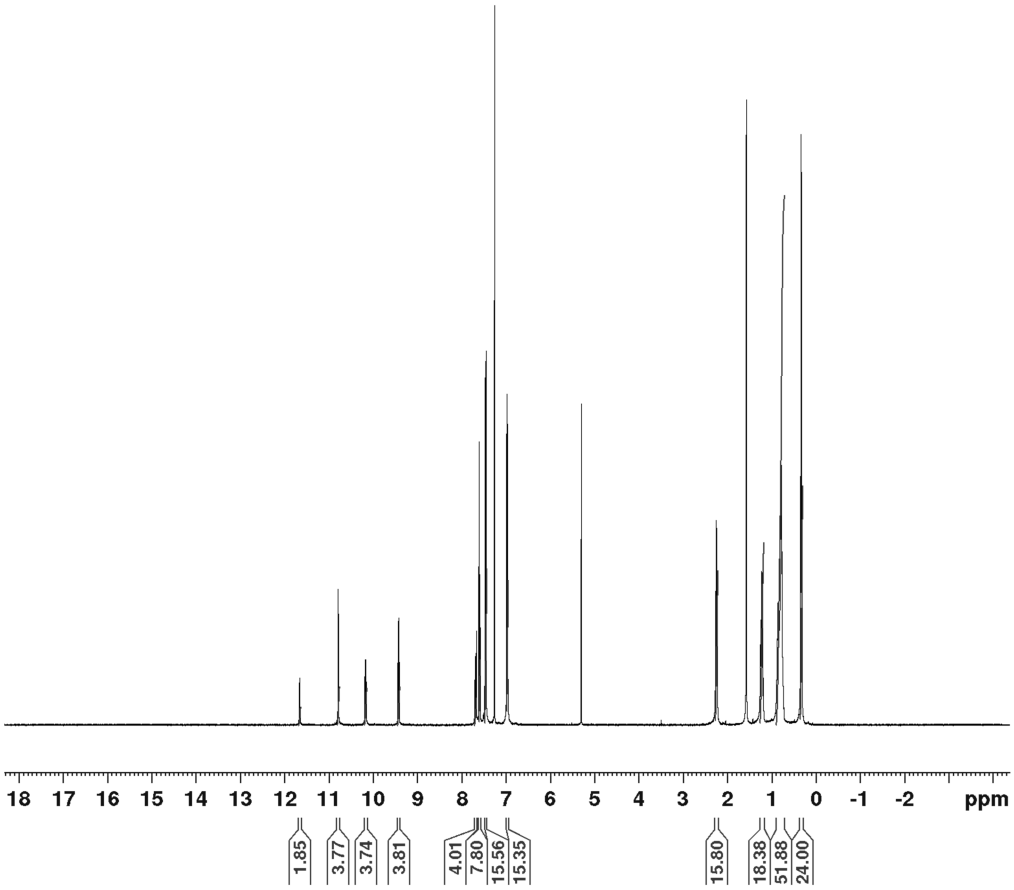

Figure 118: 400 MHz ^{1}H-NMR spectrum of compound **2d** in $CDCl_3$ at 298 K.

7.5.9 ^{13}C-NMR Spectra

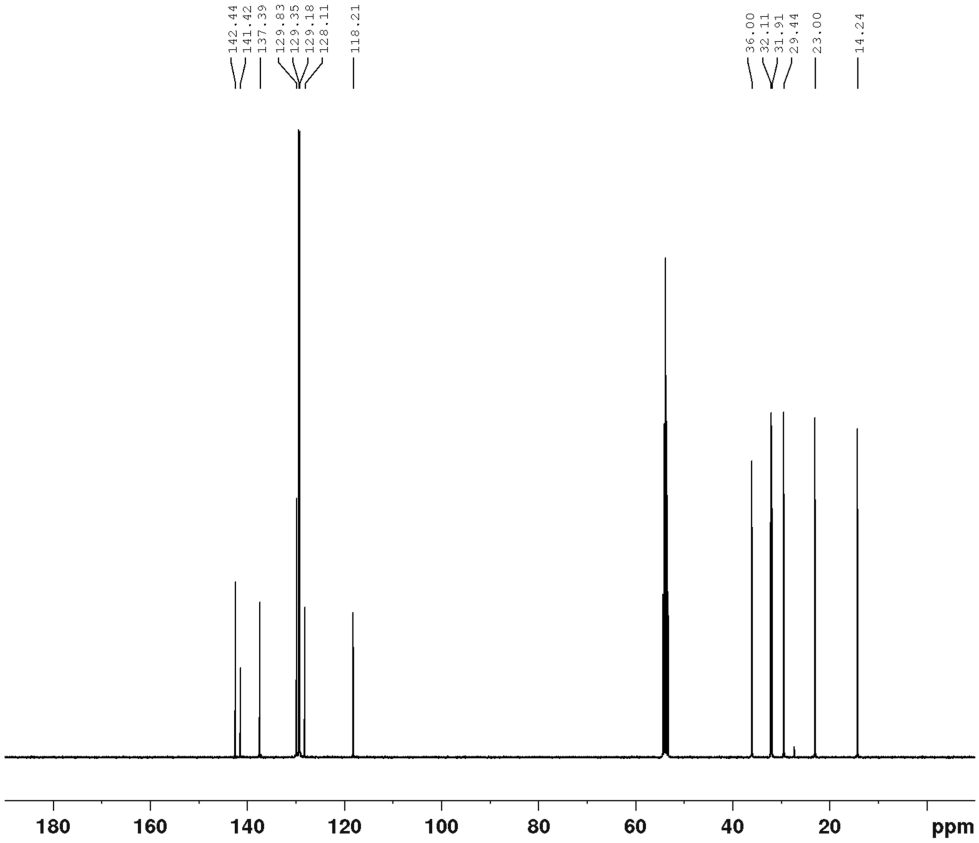

Figure 119: 100 MHz ^{13}C-NMR spectrum of compound **5d** CD_2Cl_2 at 298 K.

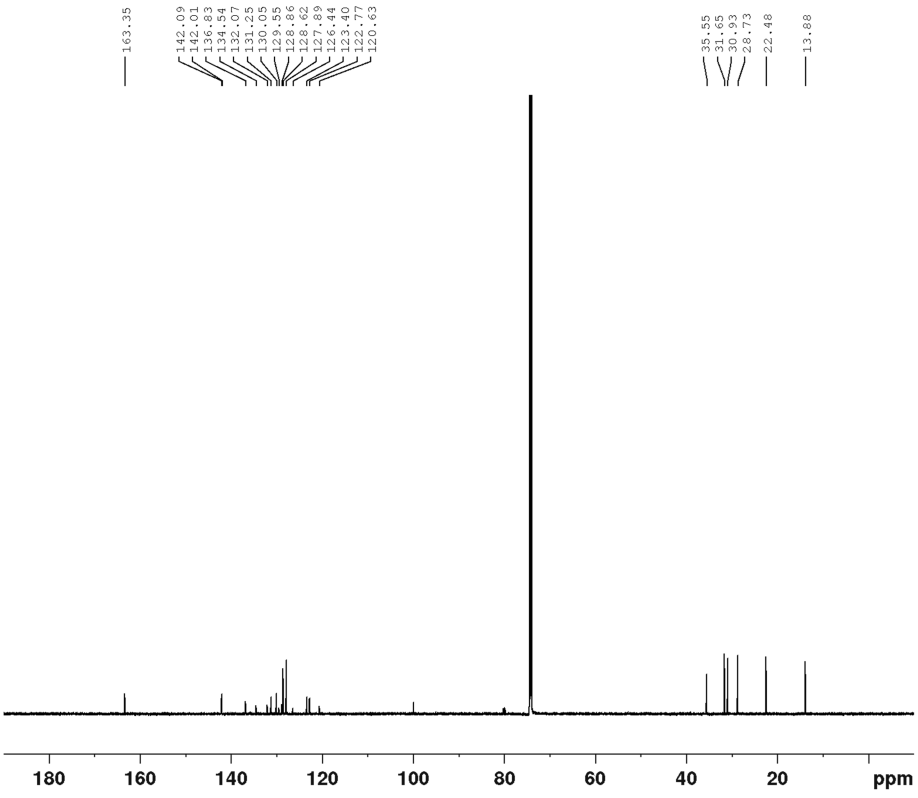

Figure 120: 100 MHz ^{13}C-NMR spectrum of compound **1d** in CD_2Cl_2 at 373 K.

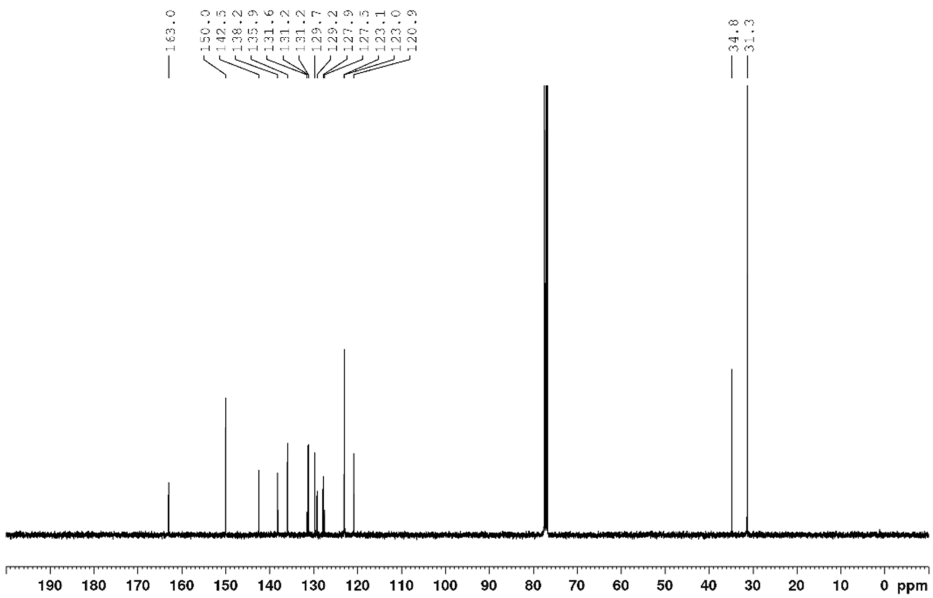

Figure 121: 101 MHz ^{13}C-NMR spectrum of compound **6b** in $CDCl_3$ at 298 K**.**

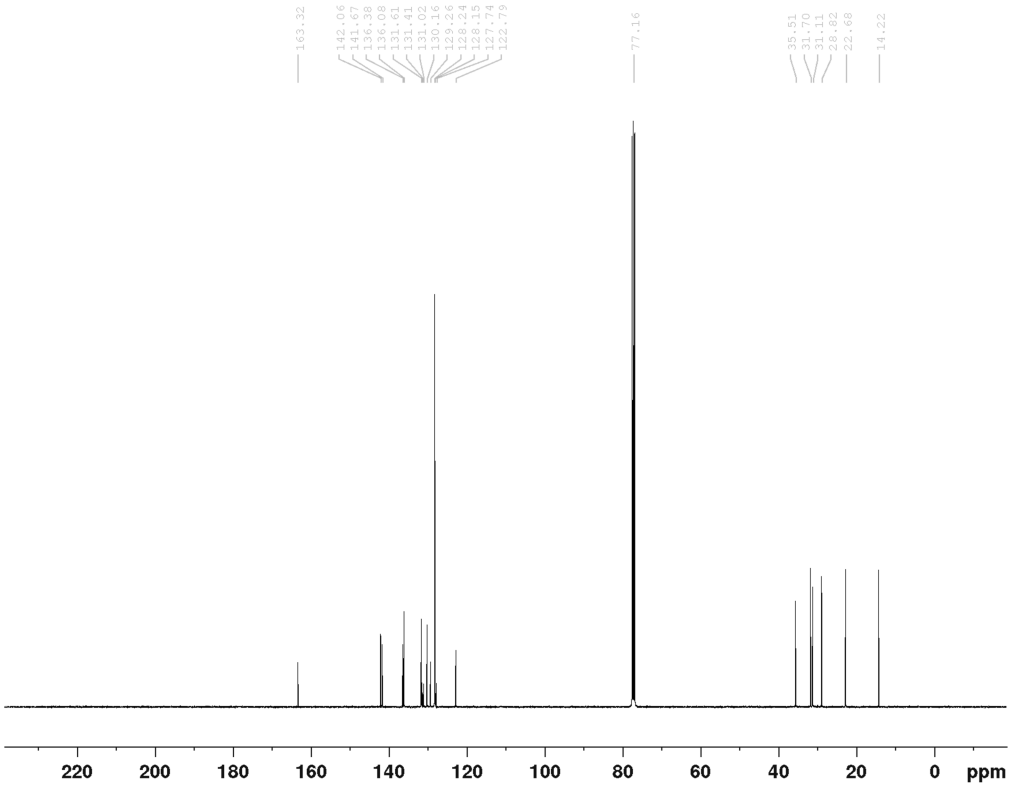

Figure 122: 100 MHz ^{13}C-NMR spectrum of compound **6d** $CDCl_3$ at 298 K.

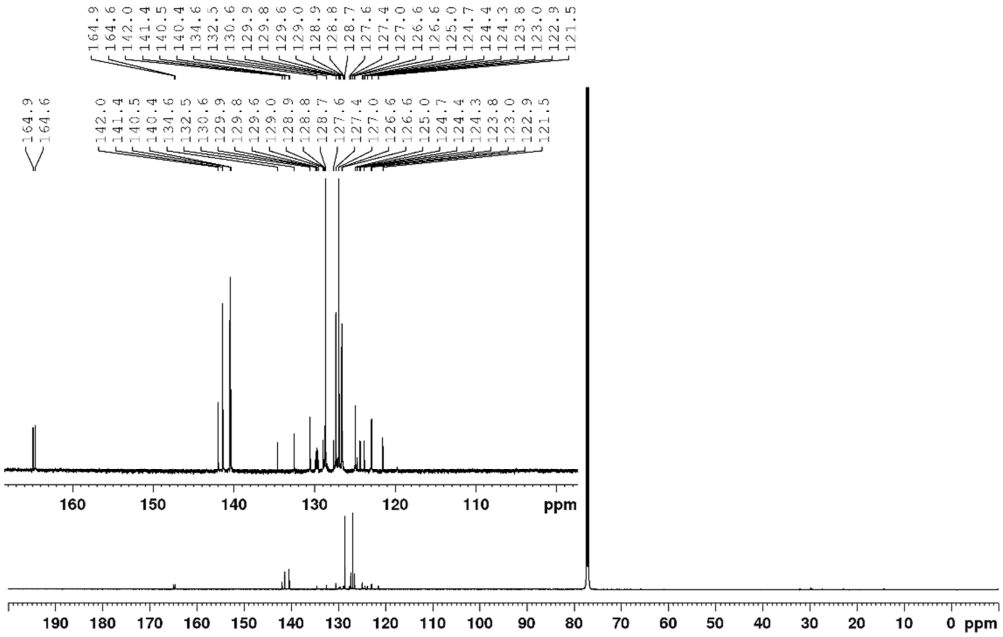

Figure 123: 151 MHz ^{13}C-NMR spectrum of compound **2c** $CDCl_3$ at 298 K.

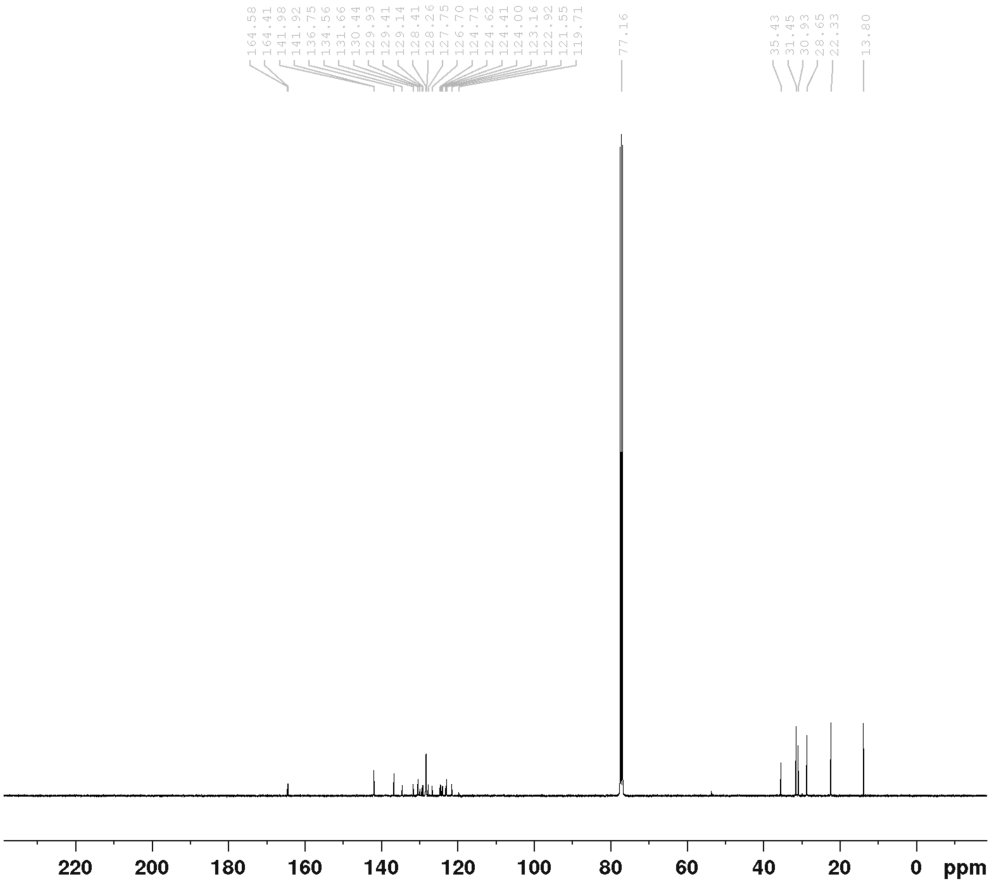

Figure 124: 100 MHz ^{13}C-NMR spectrum of compound **2d** in $CDCl_3$ at 298 K.

7.5.10 High-Resolution Mass Spectra

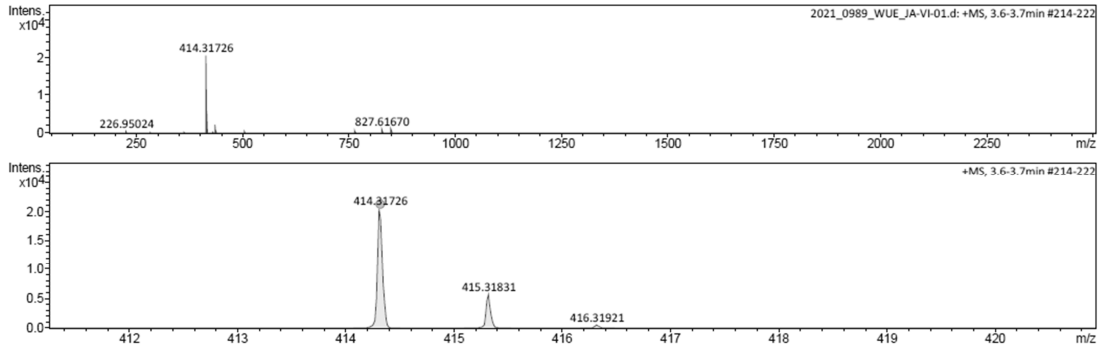

Figure 125: ESI-TOF HRMS spectrum of compound **5d**.

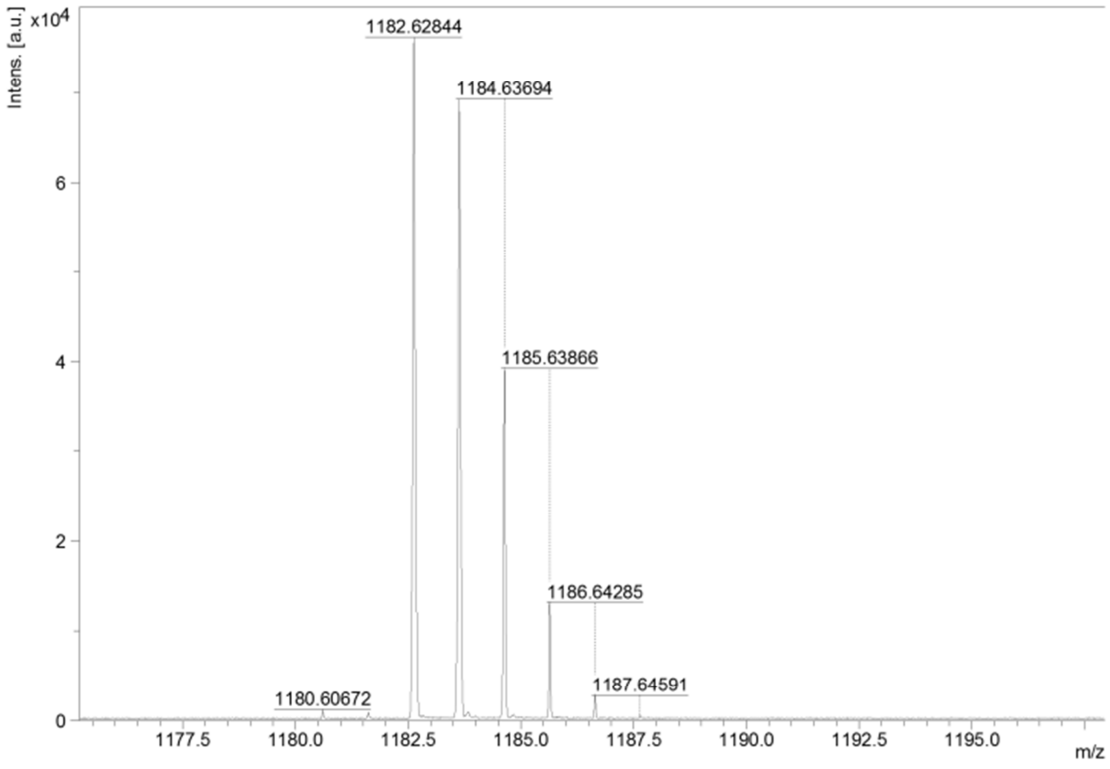

Figure 126: MALDI-TOF HRMS spectrum of compound **1d**.

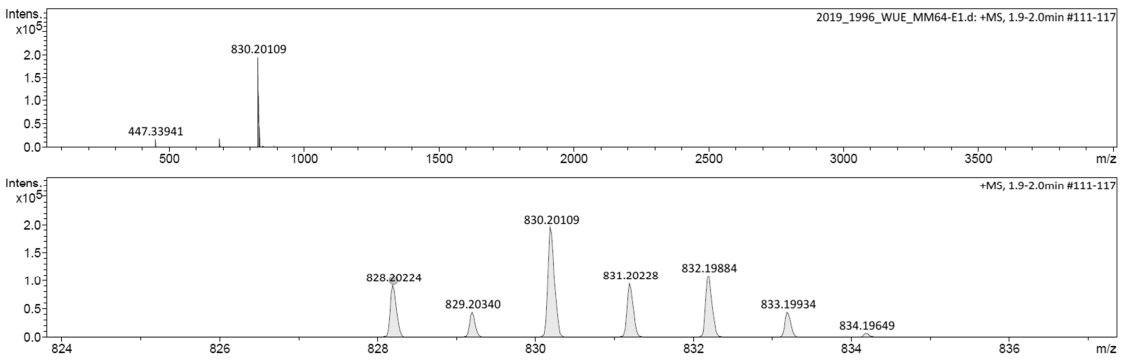

Figure 127: ESI-TOF HRMS spectrum of compound **6c**.

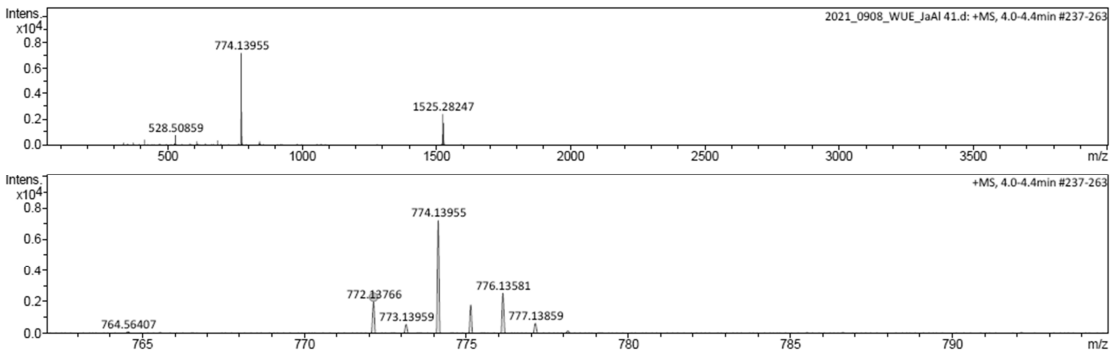

Figure 128: ESI-TOF HRMS spectrum of compound **6d**.

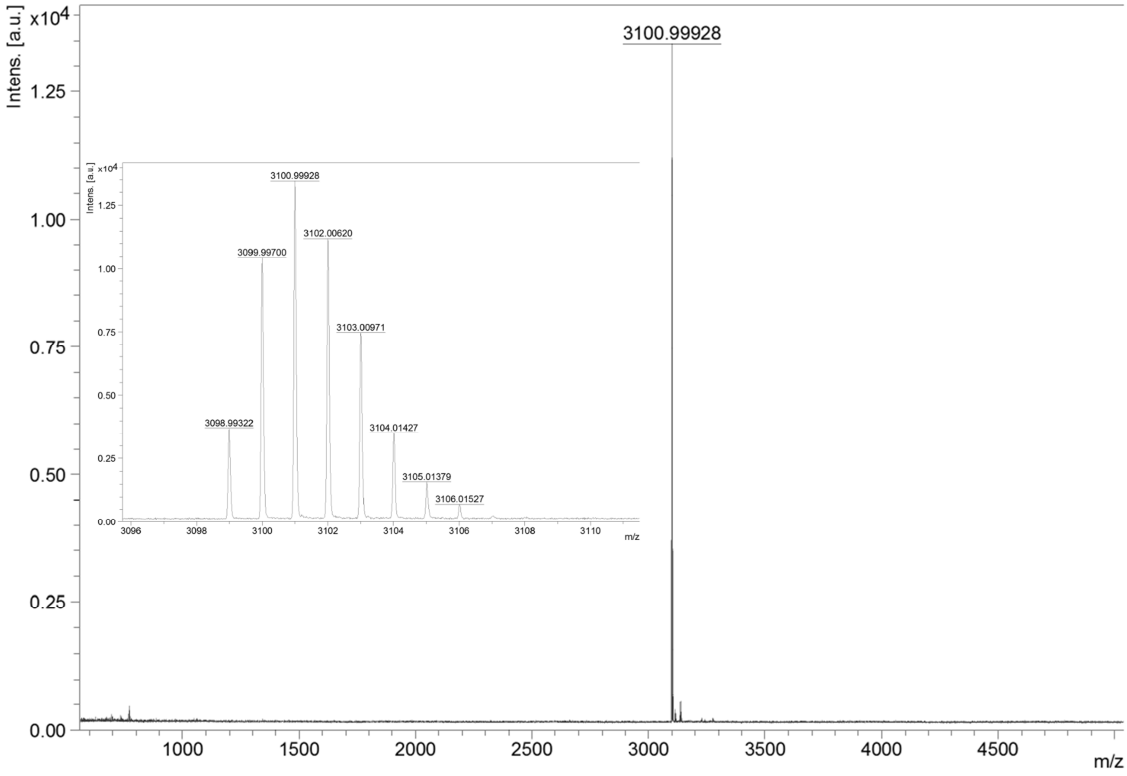

Figure 129: MALDI-TOF HRMS spectrum of compound **2c**.

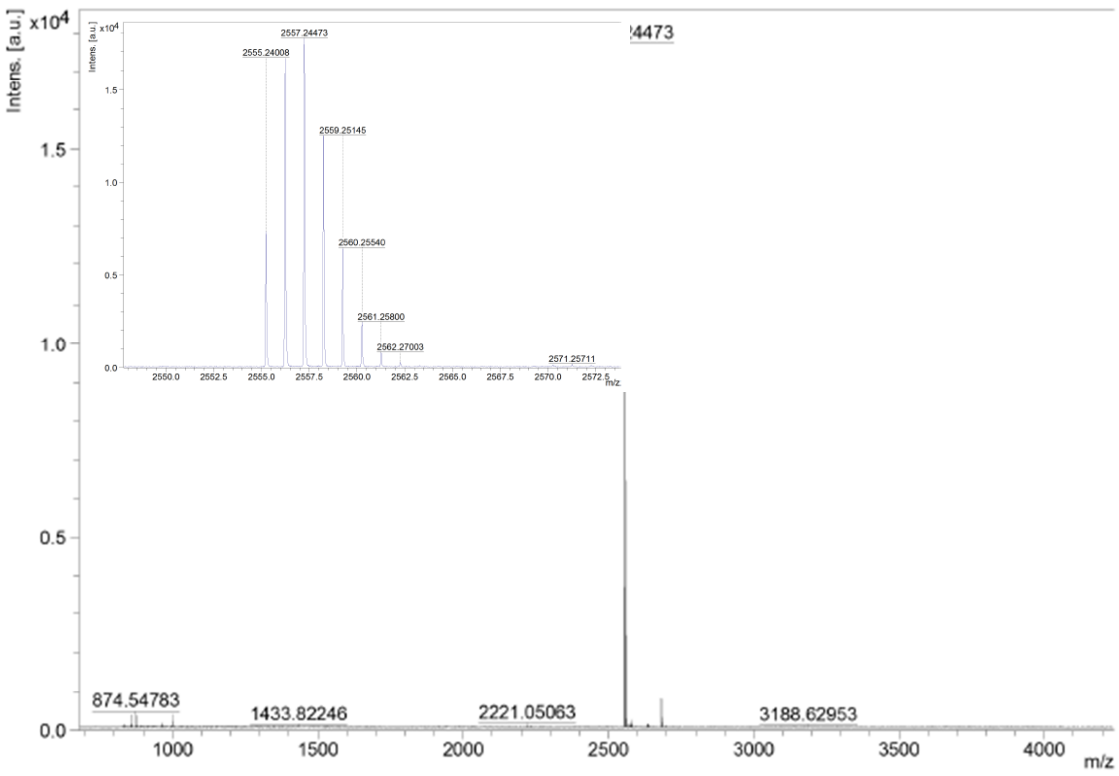

Figure 130: MALDI-TOF HRMS Spectrum of compound **2d**.

Chapter VIII: Summary and Conclusion

In this PhD thesis new acceptor molecules for solution- as well as vacuum-processed organic solar cells with special focus on their intermolecular acceptor-acceptor interactions were investigated. To achieve this goal, the new evaporation device OPTIvap-XL (Figure 131) in combination with a glovebox line was taken into operation, which enable now state-of-the-art multilayer device manufacture and characterization under complete inert conditions.

After the calibration of the OPTIvap-XL, the reproducibility of organic electronic devices such as organic solar cells (OSCs) and organic thin-film transistors (OTFTs) was investigated. Literature-reported OTFTs can be now successfully reproduced using the evaporation device OPTIvap-XL. Furthermore, fullerene-based and fullerene-free bulk-heterojunction OSCs can be processed in the conventional as well as inverted device architecture using solution as well as vacuum techniques. For the OSC devices, the whole glovebox line in combination with the OPTIvap-XL is needed for processing and characterization. With the successful calibration and reproduction of several literature-known OSCs in combination with the gained knowledge in processing these types of devices, the OPTIvap-XL is ready for the investigation of new materials. However, the extensive reproduction work cannot be limited to OTFTs and OSCs. A larger variety of organic devices such as phototransistors, photodiodes or light-emitting diodes can be also manufactured, which is done now by other group members.

To elucidate the intermolecular interactions of non-fullerene acceptors (NFAs), suitable candidates first had to be identified. For this purpose, more than 90 materials synthesized in the group were investigated by new and efficient laboratory-intern screening methods regarding their suitability. For vacuum-processable materials 18 compounds exhibited a charge-carrier mobility of

Figure 131: Photo of the evaporation device OPTIvap-XL.

10^{-3} cm^2 V^{-1} s^{-1} or higher, while six of them showed an OSCs efficiency of 0.5% or higher. For these OSCs suitable fill factors and open-circuit voltages were obtained. The main bottleneck in most of the cases towards efficient devices were low short-circuits current densities, which limited the device performance, probably due to recombination losses.

For solution-processed OSCs 14 materials yielded an efficiency of 2.0% or higher in polymer-based devices. The performance of these devices was often limited due to low short-circuit current density, probably due to recombination pathways analogue to the vacuum-deposited materials. Also, the fill factor needs to be optimized to compete with literature-known NFAs. Nevertheless, surprisingly high open-circuit voltages often over 1 V could be achieved, indicating suitable energetics of the NFA candidates to the commercially available donor polymer **PCE-10**, **PBDB-T** and **PM6**.

However, based on these screening results, a promising series of quinoidal dicyanomethylene-endcapped cyclopentadithiophenes was found (Figure 132). These new materials with their high tinctorial strength exhibit n-type

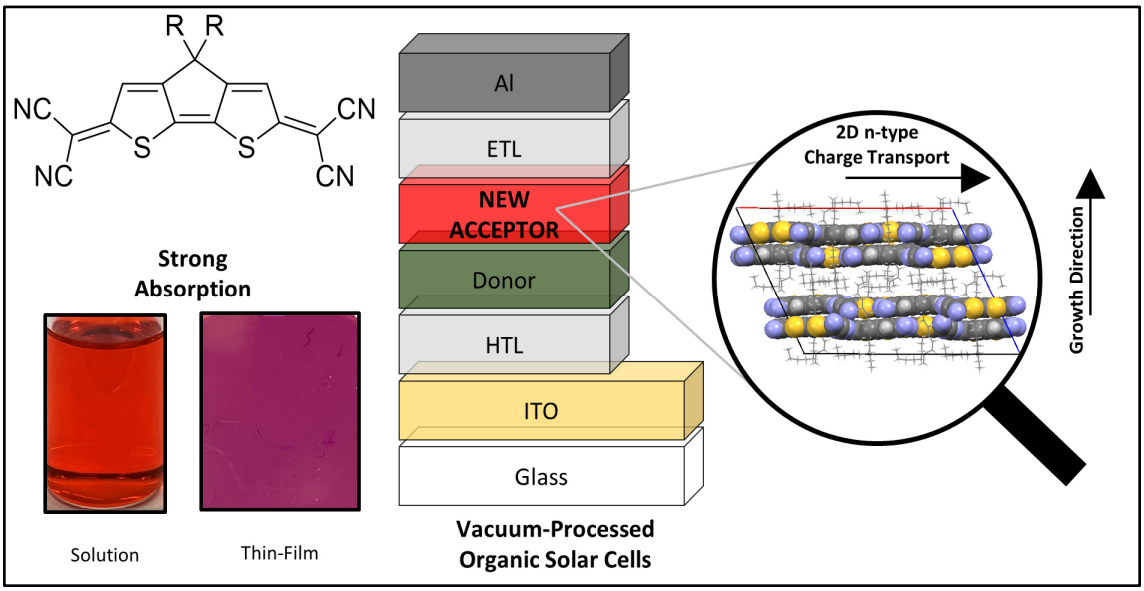

Figure 132: Quinoidal dicyanomethylene-endcapped cyclopentadithiophenes as vacuum-processable n-type semiconductors.

semiconductance in OTFTs with mobilities up to 10^{-2} cm^2 V^{-1} s^{-1} and an OSC efficiency of 0.64% in combination with a merocyanine-based donor material. These results further show, that for planar-heterojunction (PHJ) OSCs, the π-π contact of the acceptor is mandatory for fabricating an operating device. The bulk mobility of the acceptor, which can be understood as the charge-transport over several domains, takes on a great deal of importance of PHJ architectures. While charges were able to be extracted, it was not able for excitons generated within the acceptor domain to reach the respective donor-acceptor interface, either due to the demonstrated solid-state structures or due to an inferior film formation. Thus, the search towards efficient NFAs for vacuum-processed OSCs need to be continued and more small molecular materials based on different structural motifs need to be tested. For example, also known p-type semiconductors can be used as NFAs in vacuum-deposited OSCs, as it was shown in the screening procedure. A donor material with even higher energetics is needed. As already mentioned before, the moderate efficiencies achieved so far in this field give hope that many new materials can be identified. Furthermore, to my knowledge, no NFA-based vacuum-deposited bulk-heterojunction (BHJ) OSCs are known in the literature, which could significantly increase the efficiency of such devices. Therefore, it can be assumed that there is still a lot of potential in this field, which could revolutionize research on OSCs.

One of the acceptor candidates for solution-processed OSCs was a literature-unknown naphthalimide-annulated corannulene, which was decorated with solubilizing aliphatic chains (Figure 133). Its optical and electrochemical properties and its aggregation behavior in solution and in thin film showed a preorganization process, which occurs in highly concentrated solutions as they were used for solar cell fabrication. During this process discrete stacked dimers of the corannulene derivative are formed, which are then responsible for the photocurrent contribution in polymer-based BHJ OSCs, leading to an efficiency of up to 2.1% in combination with the donor polymer **PCE-10**. Until then, this was the highest efficiency of a corannulene-based acceptor, but higher efficiencies have since been reported in literature, which present the capability of the corannulene unit.[50] Hence, new corannulene derivatives with self-assembly propensity could be designed, to further boost the solar cell efficiency. Additionally, to the investigation in binary solar cells, the application of corannulene derivatives could be studied in ternary solar cells in combination with fullerenes. The respective corannulene could form a supramolecular complex in combination with fullerenes, which then could be used as acceptor materials.

Beyond the corannulene-based material, it was observed during the screening procedure that many materials cannot show a classical π-π contact, due to their sterically demanding substituents. Nevertheless, they still exhibit an appropriate solar cell efficiency of up to 7% in combination with the above-mentioned donor polymers. This seems to contradict the common doctrine in OSC, where an intimate

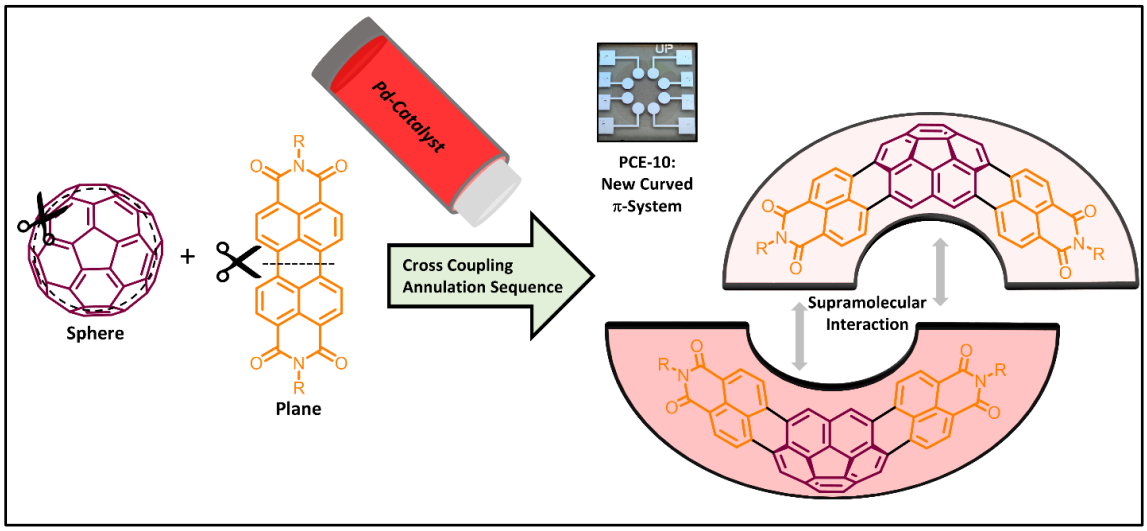

Figure 133: Bowl-shaped naphthalimide annulated corannulene as non-fullerene acceptor in organic solar cells.

π-π contact is mandatory for a sufficient exciton- and charge-transport to enable efficient devices. To further elucidate this circumstance, a series of sterically different shielded perylene bisimides and nanographene tetraimides with very high solubility was investigated (Figure 134). By studying their optical properties in solution and in a polymer-based thin film, we showed that a part of the molecules in the thin film remain in a monomeric phase, while the other part is forming defined aggregates namely dimers. The shape of the respective aggregate is changing by the sterical demand of the imide substituent. Therefore, either π-stacked dimers or edge-to-edge connected monomers are formed during the rapid film formation process. Extended π-stacked molecules in a NFA domain are not needed for efficient devices with PCEs of up to 7.1%, if the π-surface of the respective chromophore is large enough. Therefore, the future perspective of this project is the further enlargement of the chromophore's π-systems, while still preventing aggregation by tuning the imide substituents size. The enlarging of the π-systems could have two major benefits: First, the electron mobility would be increased, which allow higher fill factors and therefore higher efficiencies. Secondly, the absorption bands should shift towards higher wavelengths or even in the NIR, which allow better complementary absorption properties in combination with the respective donor polymer. Additionally, the larger π-surface could decrease the observed trap density, which is limiting the device's performance so far. As the open-circuit voltage of these materials is mainly connected to the aggregation type, it could be possible to maintain the high voltage, while increasing the short-circuit current density and the fill factor of the resulting device.

For the Chapters **V-VII**, it was necessary to study the intermolecular acceptor-acceptor interactions to draw structure-property relationships and to explain the observed OSC performance. While for PHJ OSCs the π-π contact of individual acceptor molecules is mandatory, for polymer-based BHJ OSCs, the classical

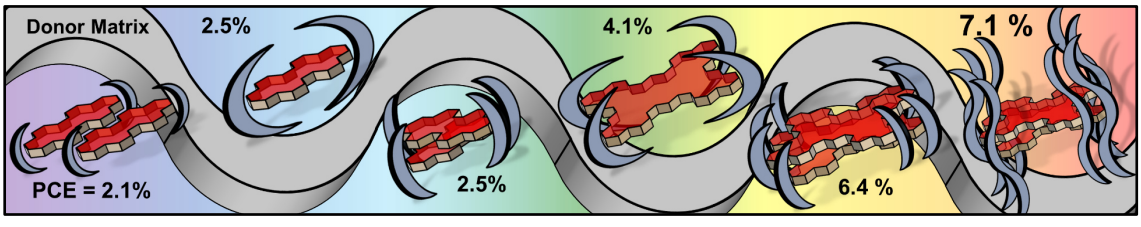

Figure 134: Sterically shielded polycyclic aromatic dicarboximides as new non-fullerene acceptors.

π-stacked molecules in a NFA domains seems not to be needed, especially when larger NFA chromophores are involved.

In the future, more research is needed to clarify which specific properties are needed for an acceptor material and what such a molecule would have to look like. Finally, modern synthetic methods could lead to the next generation of materials, and therefore to an extensive commercial application of NFA-based OSCs.

Chapter IX: Zusammenfassung und Fazit

In dieser Doktorarbeit wurden neue Akzeptormoleküle für lösungs- und vakuumprozessierte organische Solarzellen mit besonderem Augenmerk auf intermolekulare Akzeptor-Akzeptor Wechselwirkungen untersucht. Dazu wurde zunächst eine neue Aufdampfanlage (OPTIvap-XL, Abbildung 135) in Kombination mit einer aus Handschuhboxen bestehenden Solarzellenfabrikationslinie in Betrieb genommen, die die Fertigung und die Charakterisierung dieser aus mehreren Schichten aufgebauten Bauelemente unter inerten Bedingungen erlaubt. Anschließend wurde die Reproduzierbarkeit der Bauelemente untersucht, welche neben den organischen Solarzellen (*engl.: Organic solar cells; OSCs*) auch organische Dünnschichttransistoren (*engl.: Organic thin-film transistors; OTFTs*) beinhalten. Hierbei konnte zeigt werden, dass unterschiedliche literaturbekannte OTFTs durch die Aufdampfanlage OPTIvap-XL erfolgreich reproduziert werden konnten. Des Weiteren wurde die Herstellung von fullerenhaltigen und nichtfullerenhaltigen mischphasenheteroübergangbasierten (*engl.: bulk heterojunction; BHJ*) OSCs in konventioneller und invertierter Architektur präsentiert. Dabei wurden Lösungs- und Vakuumtechniken angewandt. Für die Fertigung und Charakterisierung von OSCs wurde dazu die vollständige Fertigungslinie in Kombination mit der OPTIvap-XL genutzt. Durch die erfolgreiche Kalibrierung der Anlage und der Reproduktion von literaturbekannten OSCs in Verbindung mit dem erworbenen Wissen über die Herstellung ebendieser, ist die OPTIvap-XL nun bereit für die Untersuchung von neuen Materialien. Nichtsdestotrotz kann die aufwendige Reproduktionsarbeit auch auf weitere organische Bauteilelemente wie Fototransistoren, Fotodioden oder lichtemittierende Dioden angewandt werden, die derzeit durch andere Gruppenmitglieder untersucht werden.

Abbildung 135: Foto der Aufdampfanlage OPTIvap-XL zur Fertigung von organischen Bauteilelementen.

Um die zwischenmolekularen Wechselwirkungen von Nichtfullerenakzeptoren (NFAs) aufzuklären, müssen zuerst passende molekulare Kandidaten identifiziert werden. Dazu wurden über 90 in der Gruppe synthetisierte Materialien in neuen und effizienten laborinternen Rastermethoden hinsichtlich ihrer Eignung untersucht. 18 vakuumprozessierte Materialien wiesen hierbei eine Ladungsträgermobilität von 10^{-3} cm^2 V^{-1} s^{-1} oder höher auf, während sechs von ihnen eine OSCs Effizienz über 0.5 % erzielten. Für viele der hergestellten OSCs wurden gute Füllfaktoren und Leerlaufspannungen beobachtet. Problematisch hingegen war in den meisten Fällen die beobachteten niedrigen Kurzschlussstromdichten, die möglicherweise auf Rekombinationsverluste zurückgeführt werden können.

14 Materialien für lösungsprozessierte OSCs erzielten Effizienzen über 2.0 % in polymerbasierten Bauteilen. Deren Leistung ist oft durch geringe Kurzschlussstromdichten limitiert, die ebenfalls auf Rekombinationswege zurückgeführt werden können. Des Weiteren müsste zusätzlich der Füllfaktor optimiert werden, um mit den besten literaturbekannten NFAs mithalten zu

können. Nichtsdestotrotz wurden beachtlich hohe Leerlaufspannungen von über 1 V erzielt, was auf eine passende Energetik der NFA-Kandidaten in Kombination mit den kommerziell erhältlichen Donorpolymeren **PCE-10**, **PBDB-T** und **PM6** hindeutet.

Basierend auf den Ergebnissen der Rasteruntersuchung wurde die vielversprechende Serie der dicyanomethylen-funktionalisierten Cyclopentadithiophene gefunden (Abbildung 136). Diese neuen Materialien mit ihrer hohen Farbstärke weisen n-Kanal Halbleitung in OTFTs mit Mobilitäten bis zu 10^{-2} cm^2 V^{-1} s^{-1} auf. Dazu konnte in vakuumprozessierten OSCs in Kombination mit einem Merocyanin als Donor eine Effizienz von bis zu 0.64 % beobachtet werden. In diesen planaren Heteroübergängen (*engl.: planar heterojunction; PHJ*) konnte daher gezeigt werden, dass ein intimer π-π Kontakt obligatorisch für die Fertigung von funktionierenden Bauteilen ist. Des Weiteren spielt die makroskopische Mobilität des Akzeptors, die den Ladungstransport über mehrere Domänen beschreibt, eine große Rolle für PHJ-basierte Architekturen. Während Ladungen extrahiert werden konnten, war es in diesem Fall nicht möglich, die vom Akzeptor generierten Exzitonen zur Donor-Akzeptor Grenzfläche zu transportieren, was entweder auf die jeweilige Festkörperstruktur oder auf eine unzureichende Filmbildung zurückgeführt werden konnte. Für den Weg in Richtung höherer Effizienzen für NFA-basierte vakuumprozessierte OSCs, müssten noch mehr kleine Moleküle auf

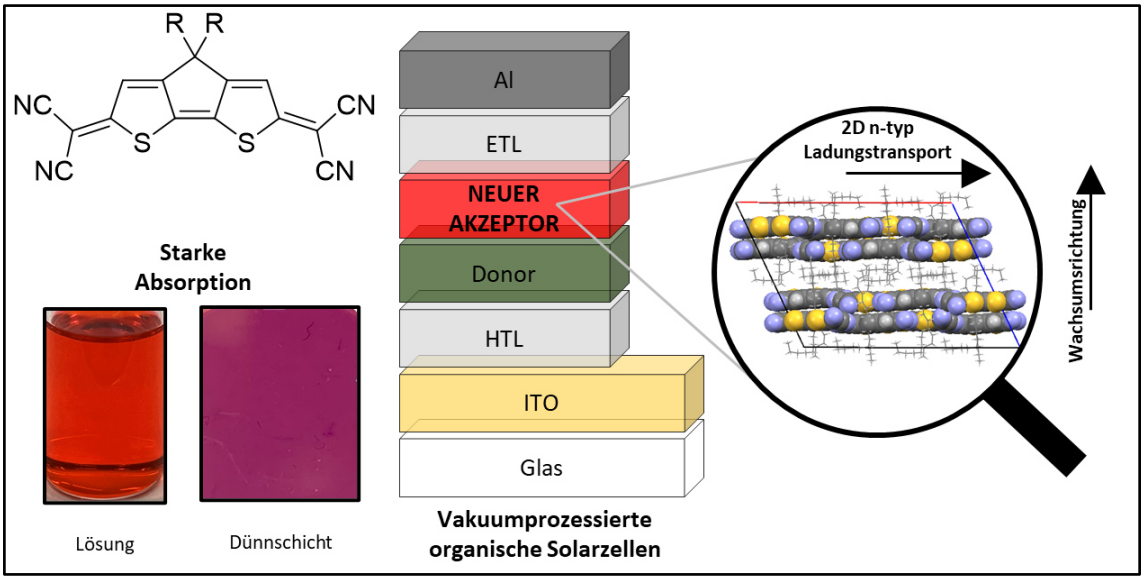

Abbildung 136: Chinoidale dicyanomethylen-funktionalisierte Cyclopentadithiophene als vakuumprozessierbare n-Kanal Halbleiter.

Basis von neuen Strukturmotiven getestet werden. Beispielsweise konnte im Rahmen der Rasterprozedur gezeigt werden, dass sich ebenfalls p-Kanal halbleitende Materialien als NFAs eignen, sofern ein Donormaterial mit passender Energetik genutzt wird. Die bisher geringen Effizienzen, die in diesem Gebiet erzielt wurden, geben Hoffnung, dass noch weitere Materialien identifiziert werden können. Des Weiteren ist nach meiner Erkenntnis keine BHJ-basierte vakuumprozessierte OSCs bekannt, die NFAs verwendet. Dies könnte die Effizienzen in neue Bereiche vorstoßen lassen. Daher kann davon ausgegangen werden, dass ein großes Zukunftspotential in dem Feld der vakuumprozessierbaren NFAs steckt, was die Forschung an OSCs revolutionieren könnte.

Einer der untersuchten Akzeptormaterialien für lösungsprozessierte OSCs war ein literaturunbekanntes Naphthalimid-annuliertes Corannulen, das mit aliphatischen Löslichkeitsketten funktionalisiert wurde (Abbildung 137). Die Charakterisierung der optischen und elektrochemischen Eigenschaften des Moleküls sowie seines Aggregationsverhaltens in Lösung und in der Dünnschicht zeigen einen Präorganizationsprozess, der in hochkonzentrierten Lösungen auftritt, wie sie in der Solarzellenherstellung genutzt werden. Während dieses Prozesses bilden sich diskrete gestapelte Dimere des Corannulenderivats, die in der resultierenden polymerbasierten BHJ-Solarzelle zum generierten Fotostrom beitragen. Dies führt zu einer Effizienz von bis zu 2.1 % in Kombination mit dem Donorpolymer **PCE-10**. Bis dato, war dies die höchste literaturbekannte Effizienz, die auf Basis eines

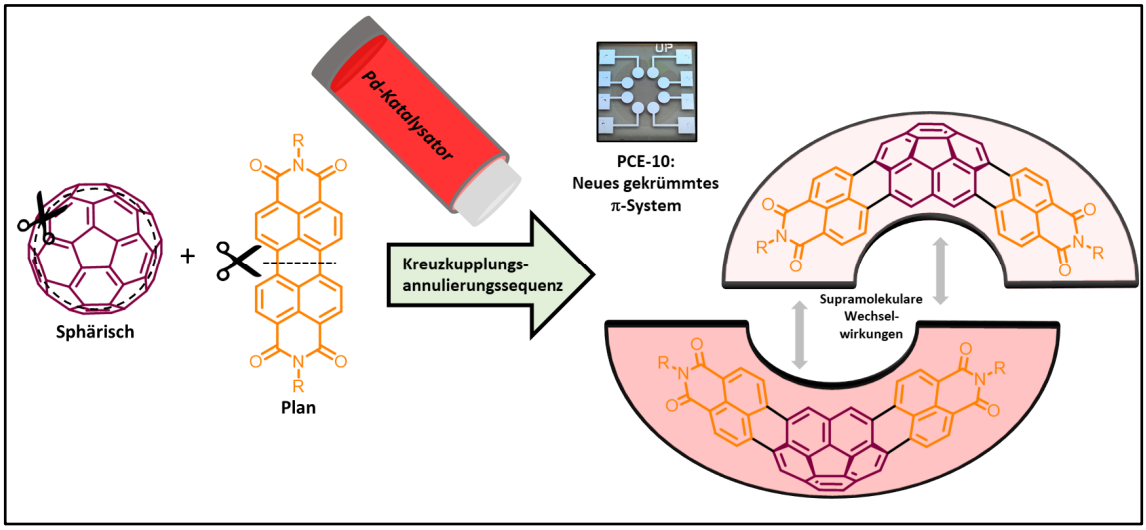

Abbildung 137: Schüsselförmiges Naphthalimid-annuliertes Corannulen als Nichtfullerenakzeptor in organischen Solarzellen.

Corannulenderivats erzielt werden konnte. Jedoch wurden mittlerweile bereits höhere Effizienzen erzielt, was die Nutzung von Corannulenderivaten in OSCs als aussichtsreich erscheinen lässt.[50] So könnten zum Beispiel neue Corannulenderivate mit Selbstassemblierungseigenschaften entworfen werden, um höhere Effizienzen zu erzielen. Aufgrund ihrer Form, eigenen sich Corannulenderivate jedoch nicht nur für binäre Systeme. In Kombination mit Fullerenen wären ebenfalls ternäre Systeme denkbar, die anschließend in der Form eines supramolekularen Komplexes als Akzeptormaterial genutzt werden können.

Neben dem Corannulenderivat wurde während der Rasteruntersuchung beobachtet, dass sich ebenfalls Materialien als NFAs eigenen, die aufgrund ihrer sterisch anspruchsvollen Substituenten keinen klassischen π-π Kontakt aufweisen können. Nichtsdestotrotz zeigen sie dennoch gute Effizienzen bis zu 7.1 % in Kombination mit den zuvor erwähnten Donorpolymeren in lösungsprozessierten BHJ OSCs. Dies scheint der klassischen Betrachtungsweise von NFAs in der organischen Elektronik entgegenzustehen, die davon ausgeht, dass ein intimer π-π Kontakt der Akzeptormoleküle Voraussetzung für einen guten Ladungs- und Exzitonentransport und daher für hohe Effizienzen ist. Um dieses Verhalten aufzuklären, wurde eine Serie an unterschiedlich sterisch abgeschirmten Perylenbisimiden und Nanographentetraimiden mit hoher Löslichkeit untersucht (Abbildung 138). Durch das Studium der optischen Eigenschaften in Lösung und in polymerbasierten Dünnschichten konnte gezeigt werden, dass ein Teil der Moleküle in der Dünnschicht immer noch als Monomer vorliegt, wohingegen sich ein anderer Teil in einer definierten aggregierten Form als Dimer befindet. Die Menge der aggregierten Form hängt dabei vom jeweiligen sterischen Anspruch des Imidsubstituenten ab. So bilden sich während der schnellen Rotationsbeschichtung entweder π-gestapelte Dimere oder Kante an Kante verbundene Monomere. Mit Effizienzen von bis zu 7.1 % trotz Abwesenheit ausgedehnter π-gestapelter

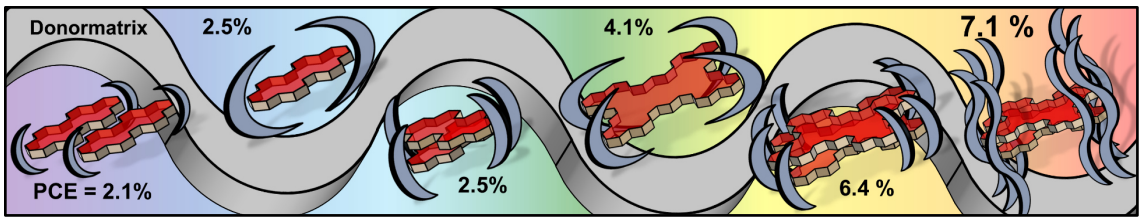

Abbildung 138: Sterisch abgeschirmte polycyclisch aromatische Dicarboximide als neue Nichtfullerenakzeptoren.

Akzeptordomänen konnte gezeigt werden, dass für große π-Systeme kein intimer π-π Kontakt notwendig ist. Zukünftig könnten daher noch größere π-Gerüste synthetisiert werden, wobei weiterhin große abschirmende Substituenten eingesetzt werden, um eine Aggregation zu verhindern. Die Vergrößerung der π-Fläche hätte zwei Vorteile. Einerseits würde die Elektronenmobilität erhöht werden, was zu einem erhöhten Füllfaktor und daher zu einer erhöhten Effizienz führt. Andererseits würde die Absorptionsbande des NFAs in Richtung höherer Wellenlängen verschoben, wodurch eine bessere spektrale Abdeckung des Sonnenlichts bis ins NIR mit dem jeweiligen Donorpolymer gegeben wäre. Zusätzlich könnten durch die größere π-Fläche die Anzahl an Fallenzuständen reduziert werden, was derzeit die Leistung der OSCs limitiert. Da die Leerlaufspannung bei diesen Materialien hauptsächlich durch den Aggregationstyp bestimmt wird, könnte es möglich sein, die hohen beobachteten Leerlaufspannungen beizubehalten, während die Kurzschlussstromdichte und der Füllfaktor erhöht werden.

Für die Kapitel V-VII war es notwendig, die intermolekularen Akzeptor-Akzeptor Wechselwirkungen zu studieren, um Struktur-Eigenschaftsbeziehungen aufzustellen und die beobachtetet OSC Effizienzen zu erklären. Während für PHJ-OSCs ein intimer π-π Kontakt zwischen den jeweiligen Akzeptormaterialien obligatorisch ist, können polymerbasierte BHJ OSCs auch ohne π-gestapelte Moleküle in den NFA-Domänen effizient sein, sofern die Chromophore genügend groß sind.

In Zukunft ist jedoch mehr Forschung notwendig, um genauer zu erörtern, welche spezifischen Eigenschaften ein Akzeptormaterial aufweisen muss und wie dieses auszusehen hat. Schlussendlich könnte durch moderne synthetische Methoden eine neue Generation an effizienten NFAs hergestellt werden, die sich auch industriell einsetzen lässt.

List of Publications

1. K. Menekşe, P. Chen, B. Mahlmeister, O. Anhalt, A. Kudzus, M. Stolte, F. Würthner

   Journal of Material Chemistry C, **2020**, *8*, 15303-15311.

   Quinoidal Dicyanomethylene-endcapped Cyclopentadithiophenes as Vacuum-Processable n-Type Semiconductors

2. K. Menekşe, R. Renner, B. Mahlmeister, M. Stolte, F. Würthner

   Organic Materials, **2020**, *3*, 229-234.

   Bowl-Shaped Naphthalimide-Annulated Corannulene as Nonfullerene Acceptor in Organic Solar Cells

3. J. M. Farrell, C. Mützel, D. Bialas, M. Rudolf, K. Menekşe, A.-M. Krause, M. Stolte, F. Würthner

   Journal of the American Chemical Society **2019**, *141,* 22, 9096-9104.

   Tunable Low-LUMO Boron-Doped Polycyclic Aromatic Hydrocarbons by General One-Pot C-H Borylations

4. M. Wolf, K. Menekşe, A. Mundstock, R. Hinterding, F. Nietschke, O. Oeckler, A. Feldhoff

   Journal of Electronic Materials **2019**, *48*, 7551-7561.

   Low Thermal Conductivity in Thermoelectric Oxide-Based Multiphase Composites

Contributions

For the included manuscripts of this thesis, the respective author agrees with the respective individual contributions as well as with the reprint.

Chapter V: Quinoidal Dicyanomethylene-Endcapped Cyclopentadithiophenes as Vacuum-processable n-type Semiconductors

K. Menekşe (K.M.), P. Chen (P.C.), B. Mahlmeister (B.M.), O. Anhalt (O.A.), A. Kudzus (A.K.), M. Stolte (M.S.) and F. Würthner (F.W.).

Method	K.M.	P.C.	B.M.	O.A.	A.K.	M.S.	F.W.	Σ
Design of research	-	-	-	-	-	2.5%	2.5%	5%
Synthesis and Purification	-	10%	2.5%	2.5%	-	-	-	5%
Characterization of molecular properties	7.5%	2.5%	-	-	-	-	-	10%
Characterization of solid-state properties	10%	-	-	-	-	-	-	10%
Calculations	5%	-	-	-	-	-	-	5%
Single-crystal growth and X-ray methods	2.5%	-	-	2.5%	-	-	-	5%
Organic thin-film transistors	10%	-	5%	-	-	-	-	15%
Organic solar cells	10%	-	-	-	5%	-	-	15%
Publication writing	8%	-	-	-	-	-	-	8%
Publication correction	2%	-	-	-	-	2.5%	2.5%	7%
Publication coordination	-	-	-	-	-	2.5%	2.5%	5%
Σ	55%	12.5%	7.5%	5%	5%	7.5%	7.5%	**100%**

Chapter VI: Bowl-Shaped Naphthalimide Annulated Corannulene as Non-Fullerene Acceptor in Organic Solar Cells

K. Menekşe (K.M.), R. Renner (R.R.), B. Mahlmeister (B.M.), M. Stolte (M.S.) and F. Würthner (F.W.).

Method	K.M.	R.R.	B.M.	M.S.	F.W.	Σ
Design of research	-	-	-	2.5%	2.5%	5%
Synthesis and purification	-	25%	-	-	-	25%
Characterization of molecular properties	-	10%	-	-	-	10%
Characterization of solid-state properties	10%	-	-	-	-	10%
Organic solar cells	20%	-	5%	-	-	25%
Organic thin-film transistors	5%	-	-	-	-	5%
Publication writing	5%	-	5%	-	-	10%
Publication correction	-	-	-	2.5%	2.5%	5%
Publication coordination	-	-	-	2.5%	2.5%	5%
Σ	40%	40%	5%	7.5%	7.5%	100%

Bibliography

[1] Y. Xia, J. Yu, *Chem.* **2020**, *6*. 1035-1042.

[2] J. Penuelas, J. Sardans, M. Estiarte, R. Aogaya, J. Carnicer, M. Coll, A. Barbeta, A. Rivas-Ubach, J. LLusia, M. Garbulsky, I. Filella, A. Jump, *Glob. Change Biol.* **2013**, *19*, 2303-2338.

[3] S. R. Loarie, P. B. Duffy, H. Hamilton, G. P. Asner, C. B. Field, D. D. Ackerly, *Nature* **2009**, *462*, 1052-1055.

[4] C. Rosenzweig, M. L. Parry, *Nature* **1994**, *367*, 133-138.

[5] https://www.bundesregierung.de/breg-de/themen/klimaschutz/klimaschutzprogramm-2030-1673578 (accessed: May 2022).

[6] V. M. Dolkart, L. V. Pronina, *Russ. Electr. Eng.* **2007**, *78*, 548-553.

[7] J. H. Park, D. Y. Kim, E. F. Schubert, J. Cho, J. K. Kim, *ACS Energy Lett.* **2018**, *3*, 655-662.

[8] R. W. Miles, G. Zoppi, I. Forbes, *Mater. Today* **2007**, *10*, 20-27.

[9] H. Gruber, *Res. Policy* **2000**, *29*, 725-740.

[10] T. L. Jester, *Prog. Photovolt.: Res. Appl.* **2002**, *10*, 99-106.

[11] S. J. S. Flora, *J. Occup. Health* **2000**, *42*, 105-110.

[12] E. K. Atibu, P. Lacroix, P. Sivalingam, N. Ray, G. Giuliani, C. M. Mulaji, J.-P. Otamonga, P. T. Mpiana, V. I. Slaveykova, J. Poté, *Chemosphere* **2018**, *191*, 1008-1020.

[13] M. Mamada, C. Pérez-Bolívar, P. Anzenbacher, *Org. Lett.* **2011**, *18*, 4882-4885.

[14] B. Heyne, *Photochem. Photobiol. Sci.* **2016**, *15*, 1103-1114.

[15] a) F. Würthner, T. E. Kaiser, C. R. Saha-Möller, *Angew. Chem. Int. Ed.* **2011**, *50*, 3376-3410; b) F. Würthner, T. E. Kaiser, C. R. Saha-Möller, *Angew. Chem.* **2011**, *123*, 3436-3473.

[16] N. J. Hestand, F. C. Spano, *Chem. Rev.* **2018**, *118*, 7069-7163.

[17] J. H. Kim, T. Schembri, D. Bialas, M. Stolte, F. Würthner, *Adv. Mater.* **2021**, 2104678.

[18] S. Haq, W. Rehman, M. Waseem, R. Javed, M. Mahfooz-ur-Rehman, M. Shahid, *Appl. Nanosci.* **2018**, *8*, 11-18.

[19] V. Coropceanu, J. Cornil, D. A. da Silva Filho, Y. Olivier, R, Silbey, J.-L. Brédas, *Chem. Rev.* **2007**, *107*, 926-952.

[20] H. Ehrenreich, *Phys. Rev.* **1960**, *120* (6), 1951-1963.

[21] M. Riede, D. Spoltore, K. Leo, *Adv. Energy Mater.* **2011**, *11*, 2002653.

[22] S. Philipps, W. Warmuth, PSE Projects GmbH, Photovoltaics report, https://www.ise.fraunhofer.de/content/dam/ise/de/documents/publications/studies/Photovoltaics-Report.pdf (accessed: May 2022).

[23] Heliatek, Whitepaper, Organic Photovoltaics – Truly Green Energy: Ultra-Low Carbon Footprint, https://www.heliatek.com/en/news/detail/whitepaper-organic-photovoltaics-truly-green-energy-ultra-low-carbon-footprint/ (accessed: May 2022).

[24] Heliatek, https://www.heliatek.com/en/news/detail/solar-refresh-for-an-industrial-facade/ (accessed: May 2022).

[25] Y. Li, X. Guo, Z. Peng, B. Qu, H. Yan, H. Ade, M. Zhang, S. R. Forrest, *Proc. Natl. Acad. Sci. U. S. A.* **2020**, *117* (35), 21147-21154.

[26] Y. Xie, R. Xia, T. Lei, L. Ye, X. Zhan, H.-L. Yip, Y. Sun, *Small Methods* **2019**, *3*, 1900424.

[27] G. Han, Y. Yi, *Adv. Theory Simul.* **2009**, *2*, 1900067.

[28] U. Hörmann, C. Lorch, A. Hinderhofer, A. Gerlach, M. Gruber, J. Kraus, B. Sykora, S. Grob, T. Linderl, A. Wilke, A. Opitz, R. Hansson, A. S. Anselmo, Y. Ozawa, Y. Nakayama, H. Ishii, N. Koch, E. Moons, F. Schreiber, W. Brütting, *J. Phys. Chem. C* **2014**, *118*, 26462-26470.

[29] B. Qi, J. Wang, *Phys. Chem. Chem. Phys.* **2013**, *15*, 8972-8982.

[30] C. W. Tang, *Appl. Phys. Lett.* **1986**, *48* (2), 183-185.

[31] D. W. Zhao, P. Liu, X. W. Sun, S. T. Tan, L. Ke, A. K. K. Kway, *Appl. Phys. Lett.* **2009**, *95*, 153304.

[32] K. Leo, *Elementary Processes in Organic Photovoltaics*, 1. Ed., Springer International Publishing, Switzerland **2017**.

[33] Y. Zhang, M. T. Sajjad, O. Blaszczyk, A. J. Parnell, A. Ruseckas, L. A. Serrano, G. Cooke, I. D. W. Samuel, *Chem. Mater.* **2019**, *31*, 6548-6557.

[34] H. Bin, J. Wang, J. Li, M. M. Wienk, R. A. J. Janssen, *Adv. Mater.* **2021**, *33*, 2008429.

[35] M.-H. Jao, H.-C. Liao, W.-F. Su, *J. Mater. Chem. A* **2016**, *4*, 5784-5801.

[36] L. J. A. Koster, S. E. Shaheen, J. C. Hummelen, *Adv. Energy Mater.* **2012**, *2*, 1246-1253.

[37] J. Kwon, J.-P. Hong, S. Noh, T.-M. Kim, J.-J. Kim, C. Lee, S. Lee, J.-I. Hong, *New. J. Chem.* **2012**, *23*, 1813-1818.

[38] D. Natali, M. Sampietro, *J. Appl. Phys.* **2002**, *92* (9), 5310-5318.

[39] C. B. Nielsen, S. Holliday, H.-Y. Chen, S. K. Cryler, I. McCulloch, *Acc. Chem. Res.* **2015**, *48*, 2803-2812.

[40] E. M. Speller, A. J. Clarke, J. Luke, H. K. H. Lee, J. R. Durrant, N. Li, T. Wang, H. C. Wong, J.-S. Kim, W. C. Tsoi, T. Li, *J. Mater. Chem. A* **2019**, *7*, 23361-23377.

[41] C. Yan, S. Barlow, Z. Wang, H. Yan, A. K.-Y. Jen, S. R. Marder, X. Zhan, *Nat. Rev. Mater.* **2018**, *3*, 18003.

[42] D. Li, X. Zhang, D. Liu, T. Wang, *J. Mater. Chem. A* **2020**, *8*, 15607-15619.

[43] N. Liang, D. Meng, Z. Wang, *Acc. Chem. Res.* **2021**, *54* (4), 961-975.

[44] P. Heremans, D. Cheyns, B. P. Rand, *Acc. Chem. Res.* **2009**, *42* (11), 1740-1747.

[45] Y. Liu, X. Wan, B. Yin, J. Zhou, G. Long, S. Yin, Y. Chen, *J. Mater. Chem.* **2010**, *20*, 2464-2468.

[46] A. L. Jones, C. H. Y. Ho, P. R. Riley, I. Angunawela, H. Ade, F. So, J. R. Reynolds, *J. Mater. Chem. C* **2020**, *8*, 15459-15469.

[47] C. McDowell, M. Abdelsamie, M. F. Toney, G. C. Bazan, *Adv. Mater.* **2018**, *30*, 1707114.

[48] J.-L. Wang, K.-K. Liu, J. Yan, Z. Wu, F. Liu, F. Xiao, Z.-F. Chang, H.-B. Wu, Y. Cao, T. P. Russell, *J. Am. Chem. Soc.* **2016**, *138*, 7687-7697.

[49] L. Zhu, M. Zhang, J. Xu, C. Li, J. Yan, G. Zhou, W. Zhong, T. Hao, J. Song, X. Xue, Z. Zhou, R. Zeng, H. Zhu, C.-C. Chen, R. C. I. MacKenzie, Y. Zou, J. Nelson, Y. Zhang, Y. Sun, F. Liu, *Nat. Mater.* **2022**, *21*, 656-663.

[50] S. Chen, D. Meng, J. Huang, N. Liang, Y. Li, F. Liu, H. Yan, Z. Wang, *CCS Chem.* **2021**, *3*, 78-84.

[51] S. Steinberger, A. Mishra, E. Reinold, J. Levichkov, C. Uhrich, M. Pfeiffer, P. Bäuerle, *Chem. Commun.* **2011**, *47*, 1982-1984.

[52] T.-Y. Li, J. Benduhn, Z. Qiao, Y. Liu, Y. Li, R. Shivhare, F. Jaiser, P. Wang, J. Ma, O. Zeika, D. Neher, S. C. B. Mannsfeld, Z. Ma, K. Vandewal, K. Leo, *J. Phys. Chem. Lett.* **2019**, *10*, 2684-2691.

[53] Y.-H. Chen, L.-Y. Lin, C.-W. Lu, F. Lin, Z.-Y. Huang, H.-W. Lin, P.-H. Wang, Y.-H. Liu, K.-T. Wong, J.-Wen, D. J. Miller, S. B. Darling, *J. Am. Chem. Soc.* **2012**, *134*, 13616-13623.

[54] N. M. Kronenberg, V. Steinmann, H. Bürckstümmer, J. Hwang, D. Hertel, F. Würthner, K. Meerholz, *Adv. Mater.* **2010**, *22*, 4193-4197.

[55] Y. Zhou, J. Holst, Y. Zhang, R. J. Holmes, *J. Mater. Chem. A* **2014**, *2*, 12397-12402.

[56] R. Fitzner, E. Mena-Osteritz, A. Mishra, G. Schulz, E. Reinold, M. Weil, C. Körner, H. Ziehlke, C. Elschner, K. Leo, M. Riede, M. Pfeiffer, C. Uhrich, P. Bäuerle, *J. Am. Chem. Soc.* **2012**, *134*, 11064-11067.

[57] C.-C. Lee, W.-C. Su, Y.-S. Shu, W.-C. Chang, B.-Y. Huang, Y.-Z. Lee, T.-H. Su, K.-T. Chen, S.-W. Liu, *RSC Adv.* **2015**, *5*, 5617-5626.

[58] D. Wynands, M. Levichkova, M. Riede, M. Pfeiffer, P. Bäuerle, R. Rentenberger, P. Denner, K. Leo, *J. Appl. Phys.* **2010**, *107*, 014517.

[59] F. Grote, Master Thesis, Julius-Maximilians Universität Würzburg, **2019**.

[60] Y. Li, J.-D. Lin, X. Liu, Y. Qu, F.-P. Wu, F. Liu, Z.-Q. Jiang, S. R. Forrest, *Adv. Mater.* **2018**, *30*, 1804416.

[61] K. Cnops, B. P. Rand, D. Cheyns, B. Verreet, M. A. Empl, P. Heremans, *Nat. Commun.* **2014**, *5*, 3406.

[62] T. Schembri, Bachelor Thesis, Julius-Maximilians-Universität Würzburg, **2018**.

[63] Z. Xiao, K. Sun, J. Subbiah, T. Qin, S. Lu, B. Purushothaman, D. J. Jones, A. B. Holmes, W. W. H. Wong, *Poly. Chem.* **2015**, *6*, 2312-2318.

[64] P. Müller-Buschbaum, *Adv. Mater.* **2014**, *26*, 7692-7709.

[65] K. S. Sree Harsha, *Principles of Vapor Deposition of Thin Films*, 1. Ed., Elsevier Science, **2006**.

[66] M. Campione, M. Cartotti, E. Pinotti, A. Sassella, A. Borghesi, *J. Vac. Sci. Technol. A* **2014**, *22* (3), 482-486.

[67] J. Lee, J. H. Kim, S. Im, *J. Appl. Phys.* **2004**, *95* (7), 3733-3736.

[68] R. Hofmockel, Z. Zschieschang, U. Kraft, R. Rödel, N. H. Hansen, M. Stolte, F. Würthner, K. Takimiya, K. Kern, J. Pflaum, H. Klauk, *Org. Electron.* **2013**, *14*, 3213-3221.

[69] M. Stolte, S.-L. Suraru, F. Würthner, J. H. Oh, Z. Bao, J. Brill, M. Könemann, J. Qu, U. Zschieschang, H. Klaus, *Proc. of SPIE* **2010**, *7778,* 777804.

[70] Y. Qiao, Y. Guo, C. Yu, F. Zhang, W. Xu, Y. Liu, D. Zhu, *J. Am. Chem. Soc.* **2012**, *134*, 4084-4087.

[71] D. Qian, L. Ye, M. Zhang, Y. Liang, L. Li, Y. Huang, X. Guo, S. Zhang, Z. Tan, J. Hou, *Macromolecules* **2012**, *45*, 9611-9617.

[72] Z.-G. Zhang, B. Qi, Z. Jin, D. Chi, Z. Qi, Y. Li, J. Wang, *Energy Environ. Sci.* **2014**, *7*, 1966-1973.

[73] Y. Sun, J. H. Seo, C. J. Takacs, J. Seifter, A. J. Heeger, *Adv. Mater.* **2011**, *23*,1679-1683.

[74] S. Nam, J. Seo, S. Woo, W. H. Kim, H. Kim, D. D. C. Bradley, Y. Kim, *Nat. Commun.* **2015**, *10*, 8929.

[75] T. J. Aldrich, M. Matta, W. Zhu, S. M. Swick, C. L. Stern, G. C. Schatz, A. Facchetti, F. S. Melkonyan, T. J. Marks, *J. Am. Chem. Soc.* **2019**, *141*, 3274-3287.

[76] Y. Ito, A. A. Virkar, S. Mannsfeld, J. H. Oh, M. Toney, J. Locklin, Z. Bao, *J. Am. Chem. Soc.* **2009**, *131*, 9396-9404.

[77] R. Hecht, Doctoral Thesis, Julius-Maximilians-Universität Würzburg, **2018**.

[78] C. Uhrich, R. Schueppel, A. Petrich, M. Pfeiffer, K. Leo, E. Brier, P. Kilickiran, P. Bäuerle, *Adv. Funct. Mater.* **2007**, *17*, 2991-2999.

[79] P. Sullivan, G. E. Gallis, L. A. Rochford, J. F. Arantes, P. Kemppinen, T. S. Jones, K. N. Winzenberg, *Chem. Commun.* **2015**, *51*, 6222-6225.

[80] Q. Yue, S. Liu, S. Xu, G. Liu, Y. Jiang, Y. Wang, X. Zhu, *J. Mater. Chem. C* **2022**, *10*, 2569-2574.

[81] A. N. Bartynski, M. Gruber, S. Das, S. Rangan, S. Sonya, C. Trinh, S. E. Bradflorth, K. Vandewal, A. Salleo, R. A. Bartynski, W. Brütting, M. E. Thompson, *J. Am. Chem. Soc.* **2015**, *137*, 5397-5405.

[82] A. Nowak-Król, R. Wagener, F. Kraus, A. Mishra, P. Bäuerle, F. Würthner, *Org. Chem. Front.* **2016**, *3*, 545-555.

[83] K. Menekşe, P. Chen, B. Mahlmeister, O. Anhalt, A. Kudzus, M. Stolte, F. Würthner, *J. Mater. Chem. C* **2020**, *8*, 15303-15311.

[84] A. Sahin, Doctoral Thesis, Universität zu Köln, 2020.

[85] J. Cao, S. Liu, W. Hu, Y. Xu, Y. Zhou, Y. Zeng, J. Yu, Z. Tang, *Synth. Met.* **2018**, *240*, 15-20.

[86] T. M. Pappenfuss, B. J. Hermanson, T. J. Helland, G. G. W. Lee, S. M. Drew, K. R. Mann, K. A. McGee, S. C. Rasmussen, *Org. Lett.* **2008**, *10* (8), 1553-1556.

[87] Q. Zhou, Y. Jiang, T. Du, Z. Wang, Z. Liang, Y. Han, Y. Deng, H. Tian, Y. Geng, *J. Mater. Chem. C* **2019**, *7*, 13939-13946.

[88] A. Yassin, T. Rousseau, P. Leriche, A. Cravino, J. Roncali, *Sol. Energy Mater. Sol. Cells* **2011**, *95*, 462-468.

[89] C. Mützel, Doctoral Thesis, Julius-Maximilians-Universität Würzburg, planned for **2022**.

[90] C. Ottohal, Bachelor Thesis, Julius-Maximilians-Universität Würzburg, **2019**.

[91] J. M. Farrell, C. Mützel, D. Bialas, M. Rudolf, K. Menekşe, A.-M. Krause, M. Stolte, F. Würthner *J. Am. Chem. Soc.* **2019**, *141* (22), 9096-9104.

[92] a) C. Mützel, J. M. Farrell, K. Shoyama, F. Würthner *Angew. Chem. Int. Ed.* **2022**, *61*, e202115746; b) C. Mützel, J. M. Farrell, K. Shoyama, F. Würthner *Angew. Chem.* **2022**, *134*, e202115746.

[93] R. Renner, B. Mahlmeister, O. Anhalt, M. Stolte, F. Würthner, *Chem. Eur. J.* **2021**, *27*, 11997-12006.

[94] B. Mahlmeister, R. Renner, O. Anhalt, M. Stolte, F. Würthner, *J. Mater. Chem. C* **2022**, *10*, 2581-2591.

[95] J. Sakai, T. Taima, T. Yamanari, K. Saito, *Sol. Energy Mater. Sol. Cells* **2009**, *93*, 1149-1153.

[96] S. Trost, K. Zilberberg, A. Behrendt, A. Polywka, P. Görrn, P. Reckers, J. Maibach, T. Mayer, T. Riedl, *Adv. Energy Mater.* **2013**, *11*, 1437-1444.

[97] a) M. Gsänger, J. H. Oh, M. Könemann, H. W. Höffken, A.-M. Krause, Z. Bao, F. Würthner, *Angew. Chem. Int. Ed.* **2010**, *49*, 740-743; b) M. Gsänger, J. H. Oh, M. Könemann, H. W. Höffken, A.-M. Krause, Z. Bao, F. Würthner, *Angew. Chem.* **2010**, *122*, 752-755.

[98] M.-M. Ling, Z. Bao, P. Erk, M. Könemann, M. Gomez, *Appl. Phys. Lett.* **2007**, *90*, 093508.

[99] Z. Xie, V. Stepanenko, B. Fimmel, F. Würthner, *Mater. Horiz.* **2014**, *1*, 355-359.

[100] M. Stolte, R. Hecht, Z. Xie, L. Liu, C. Kaufmann, A. Kudzus, D. Schmidt, F. Würthner, *Adv. Optical Mater.* **2020**, *8*, 2000926.

[101] E. Mayerhöfer, Bachelor Thesis, Julius-Maximilians-Universität Würzburg, **2019**.

[102] A. Arjona-Esteban, J. Krumrain, A. Liess, M. Stolte, L. Huang, D. Schmidt, V. Stepanenko, M. Gsänger, D. Hertel, K. Meerholz, F. Würthner, *J. Am. Chem. Soc.* **2015**, *137* (42), 13524-13434.

[103] T. Maeda, A. Liess, A. Kudzus, A.-M. Krause, M. Stolte, H. Amitani, S. Yagi, H. Fujiwara, F. Würthner, *Chem. Commun.* **2020**, *56*, 9890-9893.

[104] R. Singh, E. Aluicio-Sarduy, Z. Kan, T. Ye, R. C. I. MacKenzie, P. E. Keivanidis, *J. Mater. Chem. A* **2014**, *2*, 14348-14353.

[105] P. E. Hernett, E. A. Margulies, H. S. S. Ramakrishna Matte, M. C. Hersam, T. J, Marks, M. R. Wasielewski, *Chem. Mater.* **2016**, *28*, 3928-3936.

[106] Y. Cai, L. Huo, X. Sun, D. Wie, M. Tang, Y. Sun, *Adv. Energy Mater.* **2015**, *5*, 1500032.

[107] H. Wang, L. Chen, Y. Xiao, *J. Mater. Chem. A* **2017**, *5*, 22288-22296.

[108] D. Meng. G. Liu, C. Xiao, Y. Shi, L. Zhang, L. Jiang, K. K. Baldridge, Y. Li, J. S. Siegel, Z. Wang, *J. Am. Chem. Soc.* **2019**, *141* (13), 5402-5408.

[109] J. Feng, H. Fu, W. Jiang, A. Zhang, H. S. Ryu, H. Y. Woo, Y. Sun, Z. Wang, *ACS Appl. Mater. Interfaces* **2020**, *12* (26), 29516-29519.

[110] C. Kaufmann, Master Thesis, Julius-Maximilians-Universität Würzburg, **2015**.

[111] a) M. Mahl, K. Shoyama, A.-M. Krause, D. Schmidt, F. Würthner, *Angew. Chem. Int. Ed.* **2020**, *59*, 13401-13405; b) M. Mahl, K. Shoyama, A.-M. Krause, D. Schmidt, F. Würthner, *Angew. Chem.* **2020**, *132*, 13503-13507.

[112] S. Soldner, Master Thesis, Julius-Maximilians-Universität Würzburg, **2021**.

[113] K. Shoyama, M. Mahl, S. Seifert, F. Würthner, *J. Org. Chem.* **2018**, *83*, 5339-5346.

[114] a) S. Seifert, K. Shoyama, D. Schmidt, F. Würthner, *Angew. Chem. Int. Ed.* **2016**, *55*, 6390-6395; b) S. Seifert, K. Shoyama, D. Schmidt, F. Würthner, *Angew. Chem.* **2016**, *128*, 6500-6505.

[115] M. Mahl, M. A. Niyas, K. Shoyama, F. Würthner, *Nat. Chem.* **2022**, *14*, 457-462.

[116] C. Kaufmann, D. Bialas, M. Stolte, F. Würthner, *J. Am. Chem. Soc.* **2018**, *140*, 9986-9995.

[117] a) B. Teichmann, A.-M. Krause, M.-J. Lin, F. Würthner, *Angew. Chem. Int. Ed.* **2022**, *61*, e202117625; b) B. Teichmann, A.-M. Krause, M.-J. Lin, F. Würthner, *Angew. Chem.* **2022**, 134, e202117625.

[118] M. Schulze, Doctoral Thesis, Julius-Maximilians-Universität Würzburg, **2016**.

[119] K. Menekşe, R. Renner, B. Mahlmeister, M. Stolte, F. Würthner, *Org. Mater.* **2020**, *2*, 229-234.

[120] a) B. Pigulski, K. Shoyama, F. Würthner, *Angew. Chem. Int. Ed.* **2020**, *59*, 15908-15912; b) B. Pigulski, K. Shoyama, F. Würthner, *Angew. Chem.* **2020**, *132*, 16042-16046.

[121] B. Pigulski, K. Shoyama, M.-J. Sun, F. Würthner, *J. Am. Chem. Soc.* **2022**, *144*, 5718-5722.

[122] W. Helfrich, W. G. Schneider, *Phys. Rev. Lett.* **1965**, *14* (7), 229-231.

[123] Q. Liu, Y. Jiang, K. Jin, J. Qin, J. Xu, W. Li, J. Xiong, J. Liu, Z. Xiau, K. Sun, S. Yang, X. Hang, L. Ding, *Sci. Bull.* **2020**, *65,* 272-275.

[124] A. Wadsworth, M. Moser, A. Marks, M. S. Little, N. Gasparini, C. J. Brabec, D. Baran, I. McCulloch, *Chem. Soc. Rev.* **2019**, *48*, 1596-1625.

[125] Y. Lin, X. Zhan, *Mater. Horiz.* **2014**, *1*, 470-488.

[126] a) X. Wen, A. Nowak-Krol, O. Nagler, F. Kraus, N. Zhu, N. Zheng, M. Müller, D. Schmidt, Z. Xie, F. Würthner, *Angew. Chem. Int. Ed.* **2019**, *58*, 13051-13055;

b) X. Wen, A. Nowak-Krol, O. Nagler, F. Kraus, N. Zhu, N. Zheng, M. Müller, D. Schmidt, Z. Xie, F. Würthner, *Angew. Chem.* **2019**, *131*, 13185-13189.

[127] X. Che, Y. Li, Y. Qu, S. R. Forrest, *Nat. Energy* **2018**, *3*, 422-427.

[128] X. Che, X. Xiao, J. D. Zimmerman, D. Fan, S. R. Forrest, *Adv. Energy Mater.* **2014**, *4*, 1400568.

[129] R. Meerheim, C. Körner, B. Oesen, K. Leo, *Appl. Phys. Lett.* **2016**, *108*, 103302.

[130] X. Gao, Y. Hu, *J. Mater. Chem. C* **2014**, *2*, 3099-3117.

[131] M. M. Mandoc, L. J. A. Koster, P. W. M. Blom, *Appl. Phys. Lett.* **2007**, *90*, 133504.

[132] S. M. Menke, N. A. Ran, G. C. Bazan, R. H. Friend, *Joule* **2018**, *2*, 25-35.

[133] T. Linderl, T. Zechel, M. Brendel, D. Mosequi Gonzales, P. Müller-Buschbaum, J. Pflaum, W. Brütting, *Adv. Energy Mater.* **2017**, *7*, 1700237.

[134] V. Vohra, K. Kawashima, T. Kakara, T. Koganezawa, I. Osaka, K. Takimiya, H. Murata, *Nat. Photon.* **2015**, *9*, 403-408.

[135] S. Dai, J. Zhou, S. Chandrabose, Y. Shi, G. Han, K. Chen, J. Xin, K. Liu, Z. Chen, Z. Xie, W. Ma, Y. Yi, L. Jiang, J. M. Hodgkiss, X. Zhan, *Adv. Mater.* **2020**, *32*, 2000645.

[136] E. F. Manley, T. Harschneck, N. D. Eastham, M. J. Leonardi, N. Zhou, J. Strzalka, R. P. H. Chang, L. X. Chen, T. J. Marks, *Chem. Mater.* **2019**, *31* (20), 8308-8319.

[137] T. Harschneck, N. Zhou, E. F. Manley, S. J. Lou, X. Yu, M. R. Butler, A. Timalsina, R. Turrisi, M. A. Ratner, L. X. Chen, R. P. H. Chang, A. Facchetti, T. J. Marks, *Chem. Commun.* **2014**, *50*, 4099-4101.

[138] D. Demeter, T. Rousseau, P. Leriche, T. Cauchy, R. Po, J. Roncali, *Adv. Funct. Mater.* **2011**, 21, 4379-4387.

[139] A. Mishra, D. Popvic, A. Vogt, H. Kast, T. Leitner, K. Walzer, M. Pfeiffer, E. Mena-Osteritz, P. Bäuerle, *Adv. Funct. Mater.* **2014**, *26*, 7217-7223.

[140] Y. A. Getmanenko, T. A. Purcell, D. K. Hwang, B. Kippelen, S. R. Marder, *J. Org. Chem.* **2012**, *77*, 10931-10937.

[141] J. Lie, X. Qiao, Y. Xiong, W. Hong, X. Gao, H. Li, *J. Mater. Chem. C* **2013**, *1*, 5128-5132.

[142] S. Vegiraju, G.-Y. He, C. Kim, P. Priyanka, Y.-J. Chiu, C.-W. Liu, C.-Y.- Huang, J.-S. Ni, Y.-W. Wu, Z. Chen, G.-H. Lee, S.-H. Tung, C.-L. Liu, M.-C. Chen, A. Facchetti, *Adv. Funct. Mater.* **2017**, *27*, 1606761.

[143] a) T. Du, R. Gao, Y. Deng, C. Wang, Q. Zhou, Y. Geng, *Angew. Chem. Int. Ed.* **2020**, *59*, 221-225; b) T. Du, R. Gao, Y. Deng, C. Wang, Q. Zhou, Y. Geng, *Angew. Chem.* **2020**, *132*, 227-231.

[144] C. Zhang, D. Yuan, H. Wu, E. Gann, L. Thomsen, C. R. McNeill, C.-A. Di, X. Zhu, D. Zhu, *J. Mater. Chem. C* **2017**, *5*, 1935-1943.

[145] K. Yamamoto, S. Jinnai, T. Takehara, T. Suzuki, Y. Ie, *Org. Lett.* **2020**, *22*, 547-551.

[146] L. Shen, X. Wang, H. Liu, X. Li, *Phys. Chem. Chem. Phys.* **2018**, *20*, 5975-5802.

[147] a) H. Bürckstümmer, E. V. Tulyakova, M. Deppisch, M. R. Lenze, N. M. Kronenberg, M. Gsänger, M. Stolte, K. Meerholz, F. Würthner, *Angew. Chem. Int. Ed.* **2011**, *50*, 11628-11632; b) H. Bürckstümmer, E. V. Tulyakova, M. Deppisch, M. R. Lenze, N. M. Kronenberg, M. Gsänger, M. Stolte, K. Meerholz, F. Würthner, *Angew. Chem.* **2011**, *123*, 11832-11836.

[148] a) P. Wonner, A. Dreger, L. Vogel, E. Engelage, S. M. Huber, *Angew. Chem. Int. Ed.* **2019**, *58*, 16923-16927; b) P. Wonner, A. Dreger, L. Vogel, E. Engelage, S. M. Huber, *Angew. Chem.* **2019**, *131*, 17079-17083.

[149] M. Gsänger, E. Kirchner, M. Stolte, C. Burschka, V. Stepanenko, J. Pflaum, F. Würthner, *J. Am. Chem. Soc.* **2014**, *136*, 2351-2362.

[150] Y. Suzuki, M. Shimawaki, E. Miyazaki, I. Osaka, K. Takimiya, *Chem. Mater.* **2011**, *23*, 795-804.

[151] S. Handa, E. Miyazaki, K. Takimiya, *Chem. Commun*. **2009**, *26*, 3919-3921.

[152] F. Würthner, M. Stolte, *Chem. Commun.* **2011**, *47*, 5109-5115.

[153] K. Horiuchi, T. Kato, S. Hashii, A. Hashimoto, T. Sasaki, N. Aoki, Y. Ochiai, *Appl. Phys. Lett.* **2005**, *86*, 153108.

[154] N. M. Kronenberg, M. Deppisch, F. Würthner, H. W. A. Lademann, K. Deing, K. Meerholz, *Chem. Commun.* **2008**, *48*, 6489-6491.

[155] Gaussian 09, Revision D.01, M. J. Frisch, G. W.Trucks, H. B. Schlegel, G. E. Scuseria, M. A. Robb, J. R. Cheeseman, G. Scalmani, V. Barone, B. Mennucci, G. A. Petersson, H. Nakatsuji, M. Caricato, X. Li, H. P. Hratchian, A. F. Izmaylov, J. Bloino, G. Zheng, J. L. Sonnenberg, M. Hada, M. Ehara, K. Toyota, R. Fukuda, J. Hasegawa, M. Ishida, T. Nakajima, Y. Honda, O. Kitao, H. Nakai, T. Vreven, J. A. Montgomery, J. E. Peralta, F. Ogliaro, M. Bearpark, J. J. Heyd, E. Brothers, K. Kudin, V. N. Staroverov, T. Keith, R. Kobayashi, J. Normand, K. Raghavachari, A. Rendell, J. C. Burant, S. S. Iyengar, J. Tomasi, M. Cossi, N. Rega, J. M. Millam, M. Klene, J. E. Knox, J. B. Cross, V. Bakken, C. Adamo, J. Jaramillo, R. Gomperts, R. E. Stratmann, O. Yazyev, A. J. Austin, R. Cammi, C. Pomelli, J. W. Ochterski, R. L. Martin, K. Morokuma, V. G. Zakrzewski, G. A. Voth, R. Salvador, J. J.

Dannenberg, S. Dapprich, A. D. Daniels, O. Farkas, J. B. Foresman, J. V. Ortiz, J. Cioslowski and D. J. Fox, Gaussian, Inc., Wallingford CT, 2013.

[156] A. D. Becke, *Phys. Rev. A* **1988**, *38*, 3098-3100.

[157] C. Lee, W. Yang, R. G. Parr, *Phys. Rev. B* **1988**, *37*, 785-789.

[158] A. D. Becke, *J. Chem. Phys.* **1993**, *98*, 5648-5652.

[159] R. Krishnan, J. S. Binkley, R. Seeger, J. A. Pople, *J. Chem. Phys.* **1980**, *72*, 650-654.

[160] T. Clark, J. Chandrasekhar, G. W. Spitznagel, R. v. R. Schleyer, *J. Comput. Chem.* **1983**, *4*, 294-301.

[161] M. J. Frisch, J. A. People, J. S. J. Binkley, *Chem. Phys.* **1984**, *80*, 3265-3269.

[162] G. te Velde, F. M. Bickelhaupt, E. J. Baerends, C. Fonseca Guerra, S. J. A. van Gibsbergen, J. G. Snijders, T. J. Ziegler, *Comput. Chem.* **2001**, *22*, 931-967.

[163] C. Fonseca Guerra, J. G. Snijders, E. J. Baerends, *Theor. Chem. Acc*. **1998**, *99*, 391-403.

[164] ADF2013, SCM, Theoretical Chemistry, Vrije Universiteit, Amsterdam, The Netherlands, http://www.scm.com.

[165] P. L. Barbieri, P. A. Fantin, F. E. Jorge, *Mol. Phys.* **2006**, *104*, 2945-2954.

[166] J. P. Perdew, K. Burke, Y. Wang, *Phys. Rev. B* **1996**, *54*, 16533-16539.

[167] G. Sheldrick, *Acta Cryst. A* **2008**, *64*, 112-122.

[168] G. Zotti, G. Schiavon, A. Berlin, G. Fontana, G. Pagani, *Macromolecules* **1994**, *27*, 1938-1942.

[169] Z. Zhu, D. Waller, R. Gaudiana, M. Morana, D. Mühlbacher, M. Scharber, C. Brabec, *Macromolecules* **2007**, *40*, 1981-1986.

[170] H. Hanamura, N. Nemoto, *Polymer* **2014**, *55*, 6672-6679.

[171] Z. Ma, T. Winands, N. Liang, D. Meng, W. Jiang, N. L. Doltsinis, Z. Wang, *Sci. China Chem.* **2020**, *63*, 208-214.

[172] X.-Y. Wang, X. Yao, K. Müllen, *Sci. China Chem* **2019**, *62*, 1099-1144.

[173] Y.-T. Wu, J. S. Siegel, *Chem. Rev.* **2006**, *116*, 4843-4867.

[174] a) C. Duan, G. Zango, M. García Iglesias, F. J. M. Colberts, M. M. Wienk, M. V. Martínez-Díaz, R. A. J. Janssen, T. Torres, *Angew. Chem. Int. Ed.* **2017**, *56*, 148-152; b) C. Duan, G. Zango, M. García Iglesias, F. J. M. Colberts, M. M. Wienk, M. V. Martínez-Díaz, R. A. J. Janssen, T. Torres, *Angew. Chem.* **2017**, *129*, 154-158.

[175] K. M. Magiera, V. Aryal, W. A. Chalifoux, *Org. Biomol. Chem.* **2020**, *18*, 2372-2386.

[176] D. Meng, G. Liu, C. Xiao, Y. Shi, L. Zhang, L. Jiang, K. K. Baldridge, J. S. Siegel, Z. Wang, *J. Am. Chem. Soc.* **2019**, 141, 5402-5408.

[177] X. Huang, M. Hu, X. Zhao, C. Li, Z. Yuan, X. Liu, C. Cai, Y. Zhang, Y. Hu, Y. Chen, *Org. Lett.* **2019**, *21*, 3382-3386.

[178] Z. Luo, T. Liu, W. Cheng, K. Wu, D. Xie, L. Huo, Y. Sun, C. Yang, *J. Mater. Chem. C* **2018**, *6*, 1136-1142.

[179] A. D. Handsbee, J.-P. Sun, W. K. Law, H. Yan, I. G. Hill, D. M. Spasyuk, G. C. Welch, *Chem. Mater.* **2016**, *28*, 7098-7109.

[180] Y. Zhong, M. T. Trinh, R. Chen, G. E. Purdum, P. P. Khlyabich, M. Sezen, S. Oh, H. Zhu, B. Fowler, B. Zhang, W. Wang, C. Y. Nam, M. Y. Black, C. T. Black, M. L. Steigerwald, Y. L. Loo, F. Ng, X. Y. Zhu, C. Nucholls, *Nat. Commun.* **2015**, *6*, 8242.

[181] T. Huang, H. Chen, J. Feng, A. Zhang, W. Jiang, F. He, Z. Wang, *ACS Mater. Lett.* **2019**, *1*, 404-409.

[182] B. Verreet, B. P. Rand, D. Cheyn, A. Hadipour, T. Aernouts, P. Heremans, A. Madina, C. G. Claessens, T. Torres, *Adv. Energy Mater.* **2011**, *1*, 565-586.

[183] W. E. Barth, R. G. Lawton, *J. Am. Chem. Soc.* **1966**, *88* (2), 380-381.

[184] E. Nestoros, M. C. Stuparu, *Chem. Commun.* **2018**, *54*, 6503-6519.

[185] R. Chen, R.-Q. Lu, K. Shi, F. Wu, H.-X. Fang, Z.-X. Niu, X.-Y. Yan, M. Luo, X.-C. Wang, C.-Y. Yang, X.-Y. Wang, B. Xu, H. Xia, J. Pei, X.-Y. Cao, *Chem. Commun.* **2015**, *51*, 13768-13771.

[186] K. Shi, T. Lei, X.-Y. Wang, J.-Y. Wang, J. Pei, *J. Chem. Sci.* **2014**, *5*, 1041-1045.

[187] R.-Q. Lu, Y.-N. Zhou, X.-Y. Yan, K. Shi, Y.-Q. Zheng, M. Luo, X.-C. Wang, J. Pei, H. Xia, L. Zoppi, K. K. Baldridge, J. S. Siegel, X.-Y. Cao, *Chem. Commun.* **2015**, *51*, 1681-1684.

[188] J. Mack, P. Vogel, D. Jones, N. Kaval, A. Sutton, *Org. Biomol. Chem.* **2007**, *5*, 2448-2452.

[189] G. Valenti, C. Bruno, S. Rapino, A. Fiorani, E. A. Jackson, L. T. Scott, F. Paolucci, M. Marcaccio, *J. Phys. Chem. C* **2010**, *114*, 19467-19472.

[190] J. Li, A. Terec, Y. Wang, J. Joshi, Y. Lu, H. Sun, M. C. Stuparu, *J. Am. Chem. Soc.* **2017**, *139* (8), 3089-3094.

[191] J. E. Anthony, *Chem. Mater.* **2011**, *23*, 583-590.

[192] R. Chen, R.-Q. Lu, P. C. Shi, X.-Y. Cao, *Chin. Chem. Lett.* **2016**, *27*, 1175-1183.

[193] V. Rajeshkumar, C. Marc, F. Fichou, M. C. Stuparu, *Synlett* **2016**, *27*, 2101-2104.

[194] Y. Deng, B. Xu, E. Castro, O. Fernandez-Delgado, L. Echegoyen, K. K. Baldridge, J. S. Siegel, *Eur. J. Org. Chem.* **2017**, *29*, 4338-4342.

[195] R. Q. Lu, Y. Q. Zheng, N. Y. Zhou, X. Y. Yan, T. Lei, K. Shi, Y. Zhou, J. Pei, L. Zoppi, K. K. Baldridge, J. S. Siegel, X. Y. Cao, *J. Mater. Chem. A* **2014**, *2*, 20515-20519.

[196] K. Shoyama, D. Schmidt, M. Mahl, F. Würthner, *Org. Lett.* **2017**, *19*, 5328-5331.

[197] R. Renner, M. Stolte, F. Würthner, *ChemistryOpen* **2019**, *9*, 32-39.

[198] K. Shoyama, F. Würthner, *J. Am. Chem. Soc.* **2019**, *141* (33), 13008-13012.

[199] J. Gershberg, F. Fennel, T. H. Rehm, S. Lochbrunner, F. Würthner, *Chem. Sci.* **2016**, *7*, 1729-1737.

[200] M. C. Cardona, W. Li, A. E. Kaifer, D. Stockdale, G. C. Bazan, *Adv. Mater.* **2011**, *23*, 2367-2371.

[201] F. Würthner, K. Meerholz, *Chemistry* **2010**, *16*, 9366-9373.

[202] D. M. Meng, Y. Z. Tang, J. F. Wei, X. Y. Shi, M. Y. Yang, *Chem. Commun.* **2017**, *53*, 5744-5747.

[203] F. Fennel, J. Gershberg, M. Stolte, F. Würthner, *Phys. Chem. Chem. Phys*. **2018**, *20*, 7612-7620.

[204] T. A. Barendt, M. L. Ball, Q. Xu, B. Zhang, B. Fowler, A. Schattman, V. C. Ritter, M. L. Steigerwald, C. Nuckolls, *Chem. Eur. J.* **2020**, *26*, 3744-3748.

[205] K. M.-C. Wong, M. M.-Y. Chan, V. W.-W. Yam, *Adv. Mater.* **2014**, *26*, 5558-5568.

[206] Y. Yao, Q. Qu, K. Wang, H. Peng, F. Fang, Y. Shi, Y. Wang, D. I. Asperilla, Z. Shuai, P. Samorí, *Nat. Commun.* **2021**, *12*, 3667.

[207] W. He, M. Pang, D. H. Yeh, J. Huang, C. R. Menyuk, P. St. J. Russell, *Nat. Commun.* **2019**, *10*, 5756.

[208] A. S. Tayi, A. Kaeser, M. Matsumoto, T. Aida, S. I. Stupp, *Nat. Chem.* **2015**, 7, 281-294.

[209] S. Zhang, Y. Qin, M. A. Uddin, B. Jang, W. Zhao, D. Liu, H. Y. Woo, J. Hou, *Macromolecules* **2016**, *49*, 2993-3000.

[210] E. Wang, L. Hou, Z. Wang, S. Hellström, F. Zhang, O. Inganäs, M. R. Andersson, *Adv. Mater.* **2010**, *22*, 5240-5244.

[211] J. Lee, E. M. Go, S. Dharmapurikar, J. Xu, S. M. Lee, M. Jeong, K. C. Lee, J. Oh, Y. Cho, C. Zhang, M. Xiao, S. K. Kwak, C. Yang, *J. Mater. Chem. C* **2019**, *7*, 18468-18479.

[212] a) S. J. Kang, J. B. Kim, C.-Y. Chiu, S. Ahn, T. Schiros, S. S. Lee, K. G. Yager, M. F. Toney, Y.-L. Loo, C. Nuckolls, *Angew. Chem. Int. Ed*. **2012**, *51*, 8594-8597; b) S. J. Kang, J. B. Kim, C.-Y. Chiu, S. Ahn, T. Schiros, S. S. Lee, K. G. Yager, M. F. Toney, Y.-L. Loo, C. Nuckolls, *Angew. Chem.* **2012**, *124*, 8722-8725.

[213] B. Gao, H. Yao, B. Jang, J. Zhu, R. Yu, Y. Cui, F. Wang, H. Y. Woo, J. Hou, *J. Mater. Chem. A* **2018**, *6*, 2664-2670.

[214] H. Chen, D. Hu, Q. Yang, J. Gao, J. Fu, K. Yang, H. He, S. Chen, Z. Kan, T. Duan, C. Yang, J. Ouyang, Z. Xiao, K. Sun, S. Lu, *Joule* **2019**, *3*, 3034-3047.

[215] T.-Y. Li, J. Benduhn, Y. Li, F. Jaiser, D. Spoltore, O. Zeika, D. Neher, K. Vandewal, K. Leo, *J. Mater. Chem. A* **2018**, *6*, 18583-18591.

[216] K. Tvingstedt, K. Vandewal, A. Gadisa, F. Zhang, J. Manca, O. Inganas, *J. Am. Chem. Soc.* **2009**, *131*, 11819-11824.

[217] W. Zhu, A. P. Spencer, S. Mukherjee, J. M. Alzola, V. K. Sangwan, S. H. Amsterdam, S. M. Swick, L. O. Jones, M. C. Heiber, A. A. Herzing, G. Li, C. L. Stern, D. M. DeLongchamp, K. L. Kohlstedt, M. C. Hersam, G. C. Schatz, M. R. Wasielewski, L. X. Chen, A. Facchetti, T. J. Marks, *J. Am. Chem. Soc.* **2020**, *142*, 14532-14547.

[218] B. Wang, W. Liu, H. Li, J. Mai, S. Liu, X. Lu, H. Li, M. Shi, C.-Z. Li, H. Chen, *J. Mater. Chem. A* **2017**, *5*, 9396.

[219] P. E. Hartnett, A. Timalsina, H. S. S. Ramakrishna Matte, N. Zhou, X. Guo, W. Zhao, A. Facchetti, R. O. H. Chang, M. C. Hersam, M. R. Wasielewski, T. J. Marks, *J. Am. Chem. Soc.* **2014**, *136*, 16345-16356.

[220] Y. Cai, L. Huo, X. Sun, D. Wei, M. Tang, Y. Sun, *Adv. Energy Mater.* **2015**, *5*, 1500032.

[221] M. Stolte, T. Schembri, J. Süß, D. Schmidt, A.-M. Krause, M. O. Vysotsky, F. Würthner, *Chem. Mater.* **2020**, *32*, 6222-6236.

[222] N. Zink-Lorre, E. Font-Sanchis, A. Sastre-Santos, F. Fernández-Lázaro, *Chem. Commun.* **2020**, *56*, 3824-3838.

[223] J. Zhang, Y. Li, J. Huang, H. Hu, G. Zhang, T. Ma, P. C. Y. Chow, H. Ade, D. Pan, H. Yan, *J. Am. Chem. Soc.* **2017**, *123*, 16092-16095.

[224] H. Hu, Y. Li, J. Zhang, Z. Peng, L.-K. Ma, J. Xin, J. Huang, T. Ma, K. Jiang, G. Zhang, W. Ma, H. Ade. H. Yan, *Adv. Energy Mater.* **2018**, *8*, 1800234.

[225] M. Wu, J.-P.Yi, L. Chen, G. He, F. Chen, M. Y. Sfeir, J. Xia, *ACS Appl. Mater. Interfaces* **2018**, *10*, 27894-27901.

[226] I. Bronshtein, M. A. Iron, B. Rybtchinski, *J. Mater. Chem. C* **2018**, *6*, 10597-10602.

[227] X. Wen, Y. Zhang, G. Xie, R. Rausch, N. Tang, N. Zheng, L. Liu, F. Würthner, Z. Xie, *Adv. Funct. Mater.* **2022**, 2111706.

[228] J. Gierschner, M. Ehni, H.-J. Egelhaaf, B. M. Medina, D. Beljonne, H. Benmansour, G. C. Bazan, *J. Chem. Phys.* **2005**, *123*, 144914.

[229] J. Gierschner, J. Shi, B. Milián-Medina, D. Roca-Sanjuán, S. Varghese, S. Y. Park, *Adv. Optical Mater.* **2021**, *9*, 2002251.

[230] B. Zhang, H. Soleimaninejad, D. J. Jones, J. M. White, K. P. Ghiggino, T. A. Smith, W. H. Wong, *Chem. Mater.* **2017**, *29*, 8395-8403.

[231] A. Nowak-Król, K. Shoyama, M. Stolte, F. Würthner, *Chem. Commun*. **2018**, *54*, 13763-13772.

[232] L. Lei, Y.-J. Hong, D.-Y. Chen, M.-J. Lin, *Chem. Eur. J.* **2017**, *23*, 16612-16620.

[233] D. Bialas. E. Kirchner, M. I. S. Röhr, F. Würthner, *J. Am. Chem. Soc.* **2021**, *143*, 4500-4518.

[234] N. J. Hestand, F. C. Spano, *Acc. Chem. Res.* **2017**, *50*, 341-350.

[235] a) E. Sebastian, A. M. Philip, A. Benny, M. Hariharan, *Angew. Chem*. *Int. Ed.* **2018**, *57*, 15696-15701; b) E. Sebastian, A. M. Philip, A. Benny, M. Hariharan, *Angew. Chem*. **2018**, *130*, 15922-15927.

[236] J.-D. Chai, M. Head-Gordon, *Phys. Chem. Chem. Phys.* **2008**, *10*, 6615-6620.

[237] F. Weigend, R. Ahlrichs, *Phys. Chem. Chem. Phys.* **2005**, *7*, 3297-3305.

[238] T. Lu, F. Chen, *J. Comput. Chem.* **2012**, *33*, 580-592.

[239] J. C. Chang, *J. Chem. Phys.* **1977**, *67*, 3901-3909.

[240] G. D. Scholes, K. P. Ghiggino, *J. Phys. Chem.* **1994**, *98*, 4580-4590.

[241] W. Zhu, J. M. Alzola, T. J. Aldrich, K. L. Kohlstedt, D. Zheng, P. E. Hartnett, N. D. Eastham, W. Huang, G. Wang, R. M. Young, G. C. Schatz, M. R. Wasielewski, A. Facchetti, F. S. Melkonyan, T. J. Marks, *ACS Energy Lett.* **2019**, *4* (11), 2695-2702.